Dissertation

submitted to the

Combined Faculty of Natural Sciences and Mathematics

of Heidelberg University, Germany

for the degree of

Doctor of Natural Sciences

Put forward by

Jan-Lukas Tirpitz

born in: Braunschweig

Oral examination: 23.06.2021

Enhancing MAX-DOAS atmospheric remote sensing by multispectral polarimetry

Referees: Prof. Dr. Ulrich Platt

Prof. Dr. Andreas Quirrenbach

Die Anwendung von multispektraler Polarimetrie in der atmosphärischen Fernerkundung durch die MAX-DOAS Methode

Die Multi-Axiale differentielle optische Absorptionsspektroskopie (MAX-DOAS) ist eine etablierte Fernerkundungsmethode zum Nachweis von atmosphärischen Aerosolen und Spurengasen. Sie basiert auf der Analyse von Himmelslichtspektren im ultravioletten und sichtbaren Spektralbereich. Die Kombination von mehreren unter verschiedenen Sichtgeometrien aufgenommenen Spektren („Multi-Axial“) ermöglicht es, Vertikalverteilungen von Aerosolen und Spurengasen sowie Aerosoleigenschaften abzuleiten. Letzteres geschieht unter Anwendung von numerischen Inversionsverfahren. Es ist bereits länger bekannt, dass der Polarisationszustand des Himmelslichts zusätzliche Informationen über den atmosphärischen Zustand liefern kann. Dies wurde in bisherigen MAX-DOAS Messungen jedoch nicht ausgenutzt. Hauptziel der vorgestellten Arbeit war es, das Potenzial polarimetrischer MAX-DOAS Messungen abzuschätzen. Zu diesem Zweck wurden ein polarisationsempfindliches MAX-DOAS-Instrument (PMAX-DOAS) und ein entsprechender Inversionsalgorithmus (RAPSODI) entwickelt, die sowohl die Erfassung als auch die Verarbeitung polarimetrischer Informationen erlauben. RAPSODI ermöglicht außerdem als erster MAX-DOAS Inversions-Algorithmus die Bestimmung von mikrophysikalischen Aerosoleigenschaften. Im Vergleich zu herkömmlichen MAX-DOAS-Messungen, die keine Polarisation berücksichtigen, konnte für die polarimetrischen Messungen ein signifikanter Informationszuwachs bzgl. des atmosphärischen Zustands festgestellt werden: unter typischen Sichtgeometrien erhöht sich die Anzahl ableitbarer Freiheitsgrade für Aerosolprofile und Aerosoleigenschaften um etwa 50 % bzw. 70 %, für Spurengasprofile um etwa 10 %. Unter der Annahme idealer Messbedingungen, prognostizieren die Studien anhand synthetischer Daten eine Verbesserung der Messgenauigkeit (mittlere quadratische Abweichung zum wahren Wert) von etwa 60 %, 40 % und 10 % für vertikale Aerosolsäulen, Aerosoleigenschaften und vertikale Spurengassäulen.

Enhancing MAX-DOAS atmospheric remote sensing by multispectral polarimetry:

Multi-AXis Differential Optical Absorption Spectroscopy (MAX-DOAS) is a well-established remote sensing technique for the detection of atmospheric aerosol and trace gases. Ultra-violet and visible radiation spectra of skylight are analysed to obtain information on different atmospheric parameters. An appropriate set of spectra recorded under different viewing geometries ("Multi-Axis") allows to infer aerosol and trace gas vertical distributions as well as aerosol properties by applying numerical inversion methods. It is well known but not yet used in MAX-DOAS applications that, besides the spectra, the polarisation state of skylight provides additional information on the atmospheric conditions. The major aim of the presented work was to assess the potential of polarimetric MAX-DOAS observations. For this purpose, a novel polarization-sensitive MAX-DOAS instrument (PMAX-DOAS) and a corresponding inversion algorithm (RAPSODI) were developed, capable to record and process polarimetric information. Furthermore, RAPSODI is the first MAX-DOAS inversion algorithm allowing to retrieve aerosol microphysical properties. Compared to conventional non-polarimetric MAX-DOAS approaches, the information on the atmospheric state contained in polarimetric observations is strongly enhanced: assuming typical viewing geometries, the degrees of freedom of signal increase by about 50 % and 70 % for aerosol vertical distributions and aerosol properties, respectively, and by approximately 10 % for trace gas vertical profiles. For an ideal atmosphere, the studies on synthetic data predict an improvement in the results' accuracy (root-mean-square differences to the true values) of about 60 %, 40 % and 10 % for aerosol vertical columns, aerosol properties and trace gas vertical columns, respectively.

Contents

Part I

Background

1 Introduction and motivation

Comprehensive and accurate observations of atmospheric aerosol and trace gases are crucial to understand physical and chemical processes in the Earth's atmosphere. Despite their low abundance compared to the main gaseous atmospheric constituents, trace gases play a crucial role for life on Earth as we know it. Prominent examples are the green-house gases or the stratospheric ozone layer. But also phenomena like urban photochemical smog or acid deposition are attributed to trace gases. Atmospheric aerosol plays an important role e.g. regarding air quality, heterogeneous chemistry and the radiative balance of our planet. Many of the related chemical and physical processes are not yet completely understood. In particular aerosols still contribute the largest uncertainty to recent radiative forcing estimates (IPCC, 2014).

In the recent decades, passive spectroscopic remote sensing of atmospheric constituents from ground-based and air-borne platforms as well as satellites has made great progress. Many of the corresponding approaches record and analyse spectra of direct or scattered solar radiation, exploiting the fact that different atmospheric species alter the extraterrestrial solar spectrum in a characteristic manner, depending on their absorption and scattering properties. In contrast to in-situ sampling methods, remote sensing allows contact-free detection of atmospheric constituents averaged over considerable spatial scales (up to hundreds of km) and, particularly in the case of satellites, allows to achieve extensive temporal and spatial coverage.

Multi-AXis Differential Optical Absorption Spectroscopy (MAX-DOAS) (e.g. Hönninger and Platt, 2002; Hönninger et al., 2004; Wagner et al., 2004; Heckel et al., 2005; Frieß et al., 2006; Platt and Stutz, 2008; Irie et al., 2008; Clémer et al., 2010; Wagner et al., 2011; Vlemmix et al., 2015) is a versatile passive remote sensing technique for the simultaneous detection of aerosol and trace gases. The typical MAX-DOAS instrument consists of a motorised telescope and a spectrometer unit, allowing to record ultraviolet (UV)- and visible (Vis) radiation spectra of scattered sunlight in different viewing directions ("Multi-Axis"). The spectra are analysed using Differential Optical Absorption Spectroscopy (DOAS, Platt and Stutz, 2008), to obtain information on different atmospheric parameters, integrated over the effective light path from the top of the atmosphere (TOA) to the instrument. An appropriate set of spectra allows to retrieve tropospheric aerosol and trace gas vertical distributions as well as aerosol properties by applying inverse modelling approaches, implemented in the form of so-called "retrieval algorithms". Throughout this thesis we focus on the ground-based application of MAX-DOAS. It is meanwhile widely applied all around the world, not least because it allows to confine the atmospheric state at rather low financial and logistic effort with relatively simple

instrumentation.

Due to limitations in the design of instruments and retrieval algorithms, present MAX-DOAS measurements do not exploit the full information contained in skylight observations. Particularly, the polarisation state of the light and its spectral dependence have largely been ignored (apart from few investigations e.g. by Seidler (2008) and Bernal (2017)), even though it is well known that its consideration enhances the sensitivity of passive remote sensing to aerosol abundances and properties (e.g. Herman et al., 1971; Mishchenko and Travis, 1997; Boesche et al., 2006; Hasekamp and Landgraf, 2007; Hansen and Travis, 1974). In fact, in the recent decades polarimetry has already been extensively utilized for aerosol detection with radiometers/polarimeters, most prominently in the *Aerosol Robotic Network* (AERONET Holben et al., 1998; Li et al., 2009) and the *POLarization and Directionality of Earth's Reflectances* (POLDER) satellite instrument (Deschamps et al., 1994).

Nevertheless, the application of polarimetry for MAX-DOAS measurements comes along with novel aspects, challenges and possibilities, arising from fundamental differences between the MAX-DOAS technique and radiometer observations. First, in contrast to radiometers/polarimeters, MAX-DOAS instruments are typically not radiometrically calibrated and therefore do not provide absolute radiances. Instead, observations performed at different viewing directions are evaluated against each other to obtain "differential" quantities. A second major difference are the instruments' spectral resolutions: polarimeters focus on broadband spectral features of skylight. They apply optical bandpass filters at few individual wavelengths, typically covering a broad spectral range (approximately from 400 to 1000 nm). In contrast, MAX-DOAS focusses on the detection of atmospheric trace gases with characteristic narrow-band absorption features that require a much higher spectral resolution (≈ 1 nm) to be resolved. Information on atmospheric aerosol is inferred indirectly by analysing narrow-band absorption features of proxy gases with well known vertical distributions (Wagner et al., 2004; Frieß et al., 2006). The high resolution is achieved with dispersive techniques (typically one or more grating spectrometers with spectral coverage of ≈ 150 nm each).

The major aim of this thesis is to investigate the potential of polarimetry for the retrieval of atmospheric trace gas and aerosol vertical distributions as well as aerosol properties from ground-based MAX-DOAS observations. For this purpose we developed the "PMAX-DOAS" (Polarimetric MAX-DOAS) instrument, and the "RAPSODI" (Retrieval of Atmospheric Parameters from Spectroscopic Observations using DOAS Instruments) retrieval algorithm. The key component of the PMAX-DOAS is a motorised linear polariser inside the telescope unit, which allows to record skylight spectra at arbitrary polarisation orientations (in the following referred to as "polarimetric spectra"). The key feature of the RAPSODI algorithm is its capability to process these polarimetric observations and to exploit the corresponding information.

The thesis is divided into four parts. The first part provides an overview on the atmospheric constituents of relevance for the presented work and describes the basic principles of the MAX-DOAS technique. It further discusses the problem of

polarised radiative transfer in the atmosphere and introduces the RAPSODI retrieval algorithm. The second part presents investigations on the basis of synthetic data. Amongst others, the general potential of the polarimetric MAX-DOAS technique in comparison to the conventional non-polarimetric approach is assessed. The third part shows first retrieval results from polarimetric field data recorded with the PMAX-DOAS instrument. Part four summarises the major findings of the thesis.

2 Atmospheric constituents

The following chapter briefly introduces the atmospheric constituents of relevance for this work. Note, however, that this thesis focusses on the methodological aspects of MAX-DOAS measurements rather than the physics or chemistry of the detected species. We therefore keep the descriptions short. Most of this chapter is based on textbook knowledge, adapted from Seinfeld and Pandis (2016) and Finlayson-Pitts and Pitts Jr. (1999). For further details, the reader is referred to these textbooks.

The main gaseous constituents of the atmosphere are Nitrogen (78.08 %), Oxygen (20.95 %) and Argon (0.93 %), which account for > 99.9 % of atmospheric gases. The remaining constituents with volume mixing ratios (VMR) less than 0.1 % are typically referred to as "trace gases" (the exact definition varies throughout the literature, though). Among others, these include carbon dioxide (≈ 0.04 %) other noble gases than Argon (0.0025 %) and methane (0.00017 %). Also water vapour is often considered as a trace gas, even though its highly variable VMRs between up to few percent violate the above definition.

Neglecting changes in temperature, the air density is proportional to the pressure. The latter in good approximation decays exponentially with altitude with a scale height of about 8 km. Regarding the major components and trace gases with long residence times (e.g. carbon dioxide and methane), the atmospheric composition is relatively constant up to altitudes of ≈ 100 km. This can be very different for aerosols and trace gases with short atmospheric residence times: the vertical distribution then strongly depends on their origin (e.g. whether they are directly emitted or formed during chemical reactions), transport and sinks.

Ground based MAX-DOAS observations are most sensitive to the lowest kilometres of the atmosphere, hence to the lower part of the troposphere. The troposphere can be subdivided into two regimes, the "planetary boundary layer" (PBL) and the "free troposphere". The PBL is the lowest part (≈ 1 km) of the atmosphere, whose behaviour is directly influenced by its contact with the Earth's surface. Even though it only covers a small altitude range, it is subject to a large and diverse field of research. It is of particular scientific interest, since most short living pollutants and related chemistry are confined to this layer.

In principle any element in the periodic table can be found in the atmosphere when going to sufficiently low concentrations. However, in the following we will limit most of our considerations to the gases of relevance for this thesis, which are nitrogen dioxide (NO_2), formaldehyde (HCHO) and the oxygen collision complex (O_4). Furthermore, we discuss the role of aerosols (particles suspended in the atmosphere) as another relevant atmospheric constituent.

2.1 Nitrogen dioxide

Nitrogen dioxide (NO_2) is strongly chemically active and affects the abundance and partitioning of hydroxyl and peroxy radicals, which determine the atmosphere's oxidation capability. NO_2 is often regarded in conjunction with nitric oxide (NO) since both species are rapidly converted into each other. NO_2 and NO are typically summarised as "NO_x". During daytime, the partitioning of NO_x into NO_2 and NO is predominantly driven by the abundance of tropospheric ozone and the solar actinic flux (Leighton, 1961). Typical daylight partition ratios of $[NO]/[NO_2]$ vary between 0.5 and 1.0. Most of the tropospheric NO_x originates from emissions at the surface, predominantly in the form of NO. A major source is the combustion of fossil fuels, accounting for about 60 % of all NO_x emissions. Other sources are biomass burning, soil emissions and lightnings. Typical volume mixing rations of NO_x in the PBL vary between 0.02 ppb (remote areas) and several 100 ppb (urban areas). The lifetime of tropospheric NO_x is approximately 1 day. NO_2 is also present in the stratosphere at volume mixing rations of few ppb, originating from the photolysis of nitrous oxide (N_2O). Regarding the methodological aspects of this thesis, NO_2 is of particular interest since it exhibits significant radiation absorption features over a broad wavelength range from the UV to the Vis.

2.2 Formaldehyde

Formaldehyde (HCHO) appears in the atmosphere predominantly as intermediate in the oxidation of different hydrocarbons. Many of the latter originate from emissions at the Earth surface by biogenic, combustion and industrial processes and feature relatively short residence times. Consequently, highest HCHO volume mixing ratios are encountered in the PBL, typically between few and several tens of ppb. HCHO itself exhibits a residence time of a few hours only, since it is quickly removed from the atmosphere by photolysis and reaction with hydroxyl radicals. HCHO exhibits significant radiation absorption in the UV, at wavelengths $\lesssim 360$ nm.

2.3 Ozone and water vapour

Ozone (O_3) and water vapour (H_2O) are not target species of the retrievals performed in this thesis, but need to be considered in parts of the evaluation due to their absorbing properties. O_3 features strong absorption in the UV (the "Hartley" and the "Huggins band") but also in the Vis ("Chappuis band"). Approximately 90 % of O_3 is contained in the stratosphere, where it is produced through photolysis of O_2 molecules into single atoms that again react with O_2 to form O_3. Maximum volume mixing ratios are on the order of 5 ppm here. But O_3 is also present in the troposphere. A small fraction results from vertical transport of stratospheric O_3. However, particularly in urban regions and in the case of strong solar radiation, most of the tropospheric O_3 originates from chemical reactions involving pollutants

like hydrocarbons and NO_x. Typical tropospheric volume mixing ratios are on the order of several tens of ppb. The residence time of tropospheric O_3 varies between hours and months.

H_2O is mostly confined to the troposphere. Its concentrations are highly variable in the temporal as well as the spatial dimension. On a global scale tropospheric VMRs vary between 10^{-4} and few percent. Its residence time in the atmosphere is on the order of 10 days. H_2O exhibits strong radiation absorption bands in the infrared. Of relevance for this thesis, however, are its much weaker but still significant absorption bands in the UV and Vis.

2.4 Oxygen collision complex

A peculiar role for the MAX-DOAS technique plays the collisionally induced complex $(O_2)_2$ of oxygen molecules (Perner and Platt, 1980), in the following referred to as "O_4". Since it requires the collision of two O_2 molecules, its concentration is proportional to the square of the O_2 concentration $[O_2]^2$. The vertical distribution of the latter basically only depends on the rather weakly varying temperature and pressure profile of the atmosphere and is therefore well known. Note that the vertical profile of $[O_2]^2$ has only half the scale height ($\approx 4\,\mathrm{km}$) of the $[O_2]$ vertical profile. O_4 exhibits several radiation absorption bands over the solar spectral range. Neither the constant of proportionality between O_4 and $[O_2]^2$, nor the absorption cross-section of O_4 are exactly known. However, their product σ_{O_4} has been well determined (e.g. Greenblatt et al., 1990). Apart from a few peculiarities regarding the units, σ_{O_4} can mathematically be treated like an absorption cross-section, as it directly relates $[O_2]^2$ to the O_4 absorption coefficient (see Section 3.3.2 for further details). With the accurate knowledge on $[O_2]^2$ and σ_{O_4}, the magnitude of O_4 absorption features in a skylight spectrum are a proxy for the air mass traversed by the light. They thereby provide information on the light path distribution. In the atmosphere, the latter is mostly driven by the abundance and properties of aerosol. Accurate detection of O_4 absorption features therefore not only allows to confine the radiative transfer but also enables to retrieve aerosol vertical distributions and properties (Wagner et al., 2004; Frieß et al., 2006). In fact, in conventional MAX-DOAS profile inversions, O_4 absorption is the only source of information on atmospheric aerosol.

2.5 Aerosols

Aerosols (or "particulate matter") in the atmosphere originate from natural sources, like windborne dust, seaspray, volcanic emissions, but also from anthropogenic activities, like the combustion of fuels. Aerosols originate either from direct emission or from conversion of certain gases with the capability to condense as particles. Close to the ground, aerosols are mostly removed from the atmosphere by settling and dry deposition. At higher altitudes ($\gtrsim 100\,\mathrm{m}$), wet deposition is the dominant

removal process. Usual residence times are on the order of few days to few weeks and strongly depend on the aerosol size. Highest aerosol concentrations are encountered in the PBL: here, typical concentrations are on the order of 10 to 10000 cm^{-3} for small particles with radii $< 1\,\mu\mathrm{m}$ while for larger particles they are below $1\,\mathrm{cm}^{-3}$. Aerosols might either be solid or liquid and their chemical composition is versatile: main constituents of tropospheric aerosols are sulfate, ammonium nitrate, sodium, chloride, trace metals, carbonaceous material, crustal elements and water.

Aerosol sizes in the atmosphere are described by aerosol size distribution (for further details and different representations, see also Section 3.3.3). Typical size ranges cover radii of few Ångstrom to several hundred µm and throughout their life in the atmosphere, aerosols change in size and chemical composition mainly due to coagulation.

As a consequence of the different contributing sources as well as the coagulation and removal processes, aerosol size distributions can often be divided into different modes, as indicated in Figure 2.1. Particles in the "Aitken" or "nucleation mode" are formed through condensation of hot combustion vapours or the nucleation of certain atmospheric species. The main loss mechanism in this mode is coagulation with larger particles, "shifting" the aerosol to the "accumulation mode". The latter typically accounts for most of the aerosol in terms of surface area and a substantial part of the their mass. The name of this mode originates from the fact that removal mechanisms in this size range are least efficient. Particles in this mode therefore accumulate and achieve the longest atmospheric residence times. Coarse particles mostly originate from anthropogenic and natural dust-particles. Due to their considerable size, they exhibit large sedimentation velocities and quickly settle out of the atmosphere compared to accumulation mode aerosol. Throughout this thesis we typically assume bi-modal size distributions, considering the accumulation and the coarse mode only. In the solar spectral range, nucleation mode aerosol is basically invisible (see Section 3.3.3) and is therefore not considered in passive remote sensing applications based on sunlight.

It shall be noted that aerosol is also present in the stratosphere in the form of sulfuric acid droplets, originating from the photodissociation of long lived carbonyl sulfate diffusing into the stratosphere. Typical stratospheric aerosol optical thicknesses at 400 nm wavelengths are on the order of 10^{-4} to 10^{-3} but can increase significantly if strong volcanic eruptions inject large amounts of sulfuric compounds directly into the stratosphere. However, most of the time, the optical effect and the negligible sensitivity of MAX-DOAS observations to stratospheric altitudes allow to ignore stratospheric aerosol and we do so for the investigations performed in this thesis.

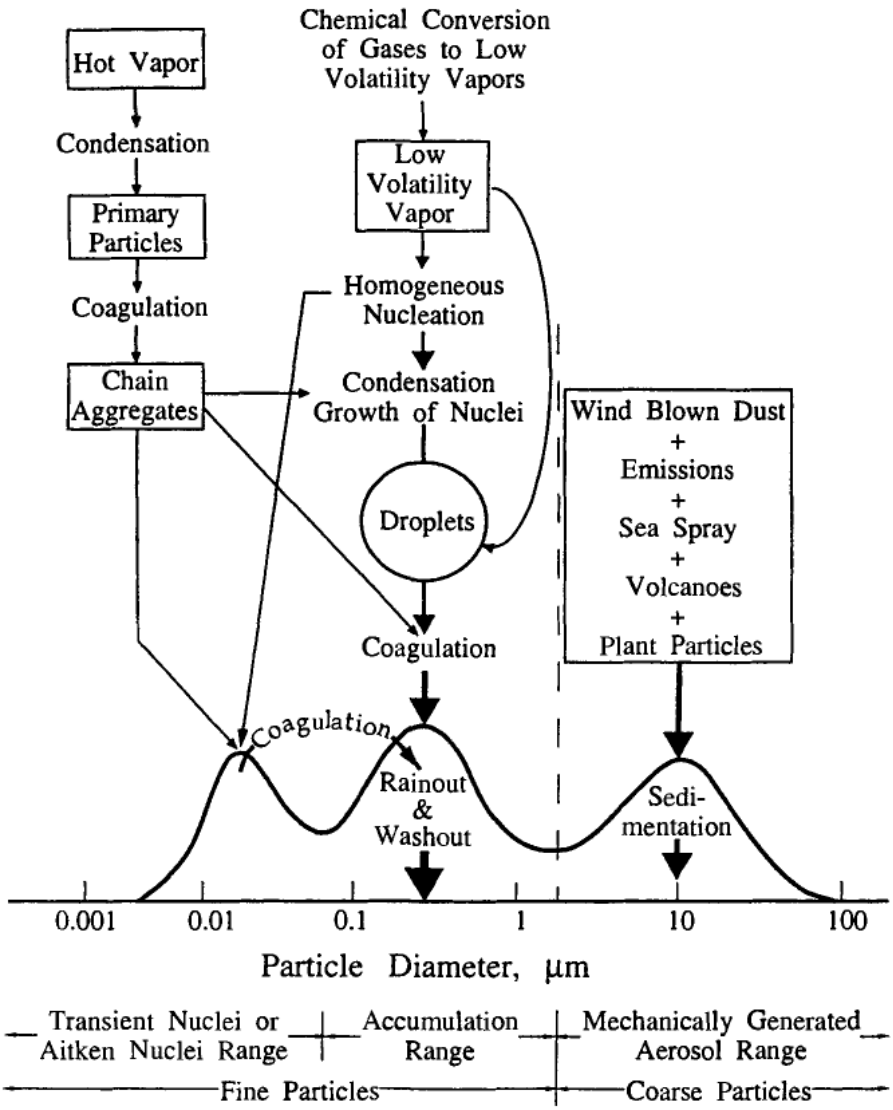

Figure 2.1: Idealised schematic of the aerosol size distribution (in terms of surface area) with its principal modes. Sources, coagulation and removal mechanisms are indicated (Seinfeld and Pandis, 2016).

3 Radiative transfer in the atmosphere

To understand the MAX-DOAS measurement principle and the approaches taken in this thesis, it is important to outline what in scientific literature and in the following is referred to as atmospheric *radiative transfer* (RT), namely the behaviour of electromagnetic radiation in the Earth's atmosphere. Most of this chapter's content is based on textbook knowledge, adapted from Petty (2006), Bohren and Huffman (2008) and Roedel and Wagner (2017).

Two major spectral regimes of radiation can be distinguished: the *solar radiation* arriving from the Sun and the *thermal radiation* emitted by the Earth's surface and the atmosphere. At the top of the atmosphere (TOA), solar radiation covers an approximate wavelength range between 0.2 and 2.5 µm with a spectral intensity maximum at about 0.5 nm, hence it comprises ultra violet (UV), visible (Vis) and near infrared (NIR) radiation, therefore frequently called "short-wave" radiation. Thermal radiation spectra at typical atmospheric and Earth surface temperatures (200 to 300 K) lie in the far infrared between 2.5 and 50 µm with maxima around 10 µm, therefore typically referred to as "long-wave" radiation. Both are subject to interactions with atmospheric constituents and the Earth's surface by absorption, scattering and (re-)emission processes.

The MAX-DOAS technique is primarily applied to in the UV and Vis spectral ranges. Therefore, for the discussion of RT and throughout this thesis, we will focus on short-wave solar radiation between 300 and 600 nm, even though, apart from a few approximations, the basic concepts apply to thermal radiation, either.

In Section 3.1 we will first introduce the "Stokes vector" (or "Stokes parameters"), a convenient concept to describe macroscopic radiative properties including the state of polarisation in radiative transfer calculations. Section 3.2 introduces the so called "Müller matrices", which mathematically describe the effect of different light-matter-interactions on the Stokes parameters. In Section 3 we will go into the details of short wave radiative transfer in the atmosphere, in particular discussing the various interactions of light with molecules and particles. Sections 3.3.5 and 3.4 conclude with a summary of the most important aspects and remarks on atmospheric radiative transfer models, respectively.

3.1 The stokes vector

For most electrodynamic problems, and also for our purposes, it is convenient to stick to the wave picture of electromagnetic (EM) radiation with plane waves being the "smallest unit" to consider. We avoid any considerations in terms of photons to not get stuck in the apparent contradictions between the quantum mechanic and the

wave picture. We will make use of the complex notation of EM-waves, as it allows to easily include phase information, which is particularly useful for the description of polarised light and any algebra that requires to keep track of phase differences and related interference effects. Note that the "physical" representation of the complex quantities can be obtained at any point by regarding only their real part.

In the atmosphere, we typically deal with large ensembles of mostly incoherent photons and thus radiative transport calculations are commonly carried out in terms of macroscopic quantities, such as radiances or irradiances. Nonetheless, it is illustrative to start by considering a single plane wave (monochromatic and fully polarised) described in terms of its electric field (E-field)

$$\mathbf{E} = \mathbf{E_0} e^{i\,(\mathbf{kr}-\omega t)}, \tag{3.1}$$

with t being time and $\mathbf{r}$ indicating a point in space. ω is the angular frequency, related to the radiation oscillation frequency ν, the speed of light in the traversed medium c and the radiation wavelength λ according to

$$\omega = 2\pi\nu = 2\pi\frac{c}{\lambda}. \tag{3.2}$$

The wave vector $\mathbf{k}$ is defined according to

$$\mathbf{k} = \frac{2\pi}{\lambda}\,\mathbf{e_k} = \frac{2\pi\nu}{c}\,\mathbf{e_k} \tag{3.3}$$

with $\mathbf{e_k}$ being the unit vector pointing in the wave's propagation direction (in the following example oriented along the x-axis). The complex vector

$$\mathbf{E_0} = \begin{pmatrix} 0 \\ E_{0y}\, e^{i\varphi_y} \\ E_{0z}\, e^{i\varphi_z} \end{pmatrix} \tag{3.4}$$

defines the amplitude and state of polarisation (SOP), the latter being determined by the phase difference $\varphi = \varphi_y - \varphi_z$ between the two transversal components as further described below. In the vacuum, the *instantaneous* energy transport in $\mathrm{W\,m^{-2}}$ through a plane perpendicular to the propagation direction is described by the Poynting vector

$$\mathbf{S} = \sqrt{\frac{\epsilon}{\mu}}\,\Re(\mathbf{E})^2\,\mathbf{e_k}, \tag{3.5}$$

with ϵ and μ being relative permittivity and permeability of the vacuum. Typically, not the instantaneous energy flux but the average over a time period $\gg 1/\nu$ of $\mathbf{S}$ is of interest. It is

$$\langle\mathbf{S}\rangle = \frac{1}{2}\sqrt{\frac{\epsilon}{\mu}}\,(\mathbf{E_0}\mathbf{E_0^*})\,\mathbf{e_k} = \frac{1}{2}\sqrt{\frac{\epsilon}{\mu}}\,(E_{0y}^2 + E_{0z}^2)\,\mathbf{e_k}. \tag{3.6}$$

The radiative flux through a surface - the *irradiance* F - in units of $[\mathrm{W\,m^{-2}}]$ can be considered as a sum of the energy transport of many plane waves i from different directions, each projected onto the surface's normal $\mathbf{e_n}$:

$$F = \sum_i \mathbf{S}_i \mathbf{e_n} \tag{3.7}$$

In the case of continuous fluxes of sufficiently large ensembles of plane waves, it is reasonable to replace the sum by an integral and to introduce the *radiance* $I(\Omega)$ in units of $[\mathrm{W\,sr^{-1}\,m^{-2}}]$, which might be considered as the temporally averaged value of Poynting vectors in a certain direction Ω. Equation 3.7 can then be expressed as

$$F = \int_\Omega I(\Omega')\, \mathbf{e_{\Omega'}}\, \mathbf{e_n}\, d\Omega'. \tag{3.8}$$

In polar coordinates the direction Ω is defined by the polar angle θ and the azimuth angle ϕ and the infinitesimal solid angle element is $d\Omega = \sin\theta\, d\theta\, d\phi$.

In the following F and I must be regarded spectrally resolved. They then depend on λ and are given in units of $[\mathrm{W\,m^{-2}\,nm^{-1}}]$ and $[\mathrm{W\,sr^{-1}\,m^{-2}\,nm^{-1}}]$, respectively.

For many applications it is sufficient to consider I simply as a scalar quantity. Sometimes, e.g. in this study, it is however necessary to not only keep track of the radiative energy, but also of the light's SOP. A common representation of radiance for this purpose are the *Stokes parameters*, often summarised in the *Stokes vector*

$$\boxed{\mathbf{I} = \begin{pmatrix} I \\ Q \\ U \\ V \end{pmatrix}} \tag{3.9}$$

While I is equal to the scalar radiance, Q, U and V carry the information on the SOP as described in more detail below. For a plane wave according to Equation 3.1 above, the stokes vector components in the y-z-plane are given by

$$I = E_{0y}^2 + E_{0z}^2 \tag{3.10}$$
$$Q = E_{0y}^2 - E_{0z}^2 \tag{3.11}$$
$$U = 2\, E_{0y}\, E_{0z} \cos(\varphi_y - \varphi_z) \tag{3.12}$$
$$V = 2\, E_{0y}\, E_{0z} \sin(\varphi_y - \varphi_z) \tag{3.13}$$

Note that from Equation 3.10 on we will drop the proportionality factor that ensures the equality between electric field and energy density (compare Eq. 3.6). Depending on the purpose, it is often convenient to normalise $\mathbf{I}$ to $I = 1$, anyway. In the case of the superposition of multiple plane waves of different phase and thus different

SOPs, the Stokes parameters can be expressed according to:

$$I = \langle \hat{E_y}^2 + \hat{E_z}^2 \rangle \tag{3.14}$$

$$Q = \langle \hat{E_y}^2 - \hat{E_z}^2 \rangle \tag{3.15}$$

$$U = \langle 2\,\hat{E}_y\,\hat{E}_z \cos(\hat{\varphi}) \rangle \tag{3.16}$$

$$V = \langle 2\,\hat{E}_y\,\hat{E}_z \sin(\hat{\varphi}) \rangle \tag{3.17}$$

with $\hat{E}_y$ and $\hat{E}_z$ being the instantaneous components of the total electromagnetic field vector resulting from the superposition of all incident plane waves, $\hat{\varphi}$ being their relative phase and $\langle\rangle$ indicating the temporal average. For the rest of this thesis we will not consider any plane waves but describe the state of light only in terms the macroscopic quantities I, Q, U and V. A major advantage of the stokes parameters (and probably the most intuitive access to their actual meaning) is that they can be calculated straightforward from a small set of radiance measurements I_δ using a linear polariser at different orientations $\delta =\in [0, 45, 90, 135°]$ (with respect to to a reference plane, here, the x-y-plane) and circular polarisers (right-hand and left-hand, represented by $\delta = RH$ and LH, respectively) according to:

$$\boxed{\begin{aligned} I &= I_{0°} + I_{90°} = I_{45°} + I_{135°} \\ Q &= I_{0°} - I_{90°} \\ U &= I_{45°} + I_{135°} \\ V &= I_{RH} + I_{LH} \end{aligned}} \tag{3.18–3.21}$$

It becomes particularly apparent here that Q and U carry the information on the linear and V on the circular polarisation. In general, any plane wave can be considered elliptically polarised, with linear and circular polarisation being special cases. The latter are illustrated in Figure 3.1 together with the corresponding stokes parameter vector. For unpolarised light, only I is non-zero while for fully polarised light it is $I^2 = Q^2 + U^2 + V^2$. Obviously, light beams consisting of many plane waves can be partially polarised (with some prevailing SOP). Thus in general it is

$$0 \leq Q^2 + U^2 + V^2 \leq I^2 \tag{3.22}$$

It is often useful to mathematically decompose I into a polarised (I_{pol}) and an unpolarised (I_{unpol}) component. The *degree of polarisation* (DOP) is defined as

$$D = \frac{I_{pol}}{I_{pol} + I_{unpol}} = \frac{\sqrt{Q^2 + U^2 + V^2}}{I} \tag{3.23}$$

Further, we can differentiate between the *degree of circular polarisation* $D_C = V/I$ and the *degree of linear polarisation* (DOLP)

$$\boxed{D_L = \frac{\sqrt{Q^2 + U^2}}{I}} \tag{3.24}$$

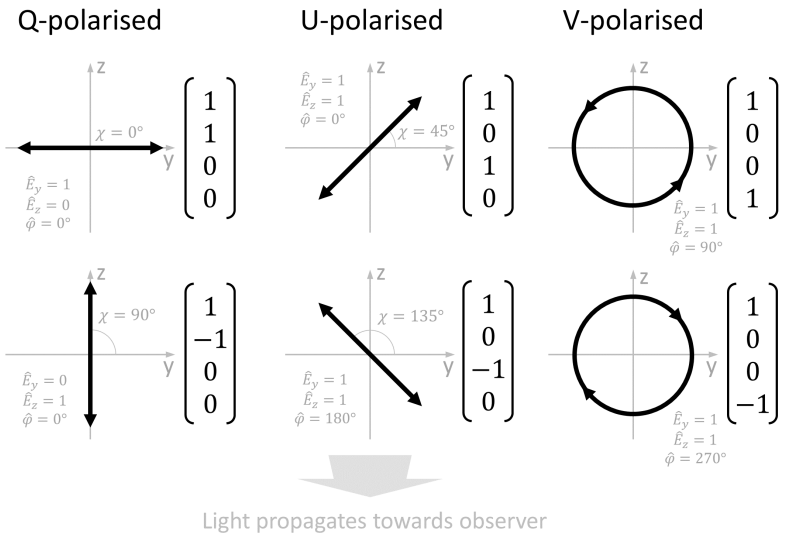

Figure 3.1: E-field oscillation patterns and corresponding normalised Stokes vectors for the six limiting cases of fully polarised radiation.

In the atmosphere, the degree of circular polarisation is negligible for our purposes ($D_C \lesssim 10^{-4}$, Kemp et al. (1971); Hansen (1971)) and in the following, we therefore focus on the DOLP as a measure for the polarisation strength. The angle of maximum polarisation is given by

$$\boxed{\chi = \frac{1}{2}\arctan\left(\frac{U}{Q}\right) + \begin{cases} 90°, & \text{if } Q \geq 0 \\ 0, & \text{if } Q < 0 \end{cases}} \tag{3.25}$$

Assuming $V = 0$, the radiation at a distinct location and direction in the atmosphere is fully described by three parameters and therefore we require three suitable measurements to determine the entire stokes vector. The PMAX-DOAS instrument, as described in detail in Section 11, basically consists of a telescope unit with a motorised linear polariser, accepting light of a distinct polarisation orientation only. With such a setup, and assuming that χ is not known prior to the measurement (in general this is the case, see Section 6.2), it is reasonable to perform radiance measurements I_δ at three linear polariser orientations δ in steps of $\Delta\delta = 60\,°$. In this study, these measured radiances are typically $I_{0°}$, $I_{60°}$ and $I_{120°}$. The observed intensity I_δ for a given incident stokes vector can be derived using Eq. 3.34 below to:

$$I_\delta = \frac{1}{2}(I + Q\cos 2\delta + U\sin 2\delta) \tag{3.26}$$

From this, it is straightforward to derive expressions for the quantities introduced

above in terms of the three measurements:

$$I = \frac{2}{3}(I_{0^\circ} + I_{60^\circ} + I_{120^\circ}) \tag{3.27}$$

$$Q = \frac{2}{3}(2I_{0^\circ} - I_{60^\circ} - I_{120^\circ}) \tag{3.28}$$

$$U = \frac{2}{\sqrt{3}}(I_{60^\circ} - I_{120^\circ}) \tag{3.29}$$

$$D_L = 2\,\frac{\sqrt{I_{0^\circ}^2 + I_{60^\circ}^2 + I_{120^\circ}^2 - I_{0^\circ}I_{60^\circ} - I_{0^\circ}I_{120^\circ} - I_{60^\circ}I_{120^\circ}}}{I_{0^\circ} + I_{60^\circ} + I_{120^\circ}} \tag{3.30}$$

$$\chi = \frac{1}{2}\arctan\left(\sqrt{3}\,\frac{I_{60^\circ} - I_{120^\circ}}{2I_{0^\circ} - I_{60^\circ} - I_{120^\circ}}\right) \tag{3.31}$$

As we shall see later (Section 6 and 9.3), under some conditions, the orientation of polarisation χ can be well predicted from simple geometric considerations. In this case, only two degrees of freedom are left in the Stokes parameters, and two measurements with δ perpendicular and parallel to the expected χ are sufficient to capture nearly the full information on the SOP.

3.2 Müller matrices

Any process altering the scalar radiance I can be described by multiplying I with a scalar factor. However, in the formalism for full stokes vector calculations, these factors become matrices - the *Müller matrices* - which, in contrast to scalar multiplication, account for the changes in all Stokes parameters. In the following, we will introduce a few basic Müller matrices. For further details please refer to the literature given above.

Generally, it is often necessary to rotate the Stokes reference frame by an angle γ, which can be achieved applying the matrix

$$\mathbf{M}_R(\gamma) = \begin{pmatrix} 1 & 0 & 0 & 0 \\ 0 & \cos(2\gamma) & \sin(2\gamma) & 0 \\ 0 & -\sin(2\gamma) & \cos(2\gamma) & 0 \\ 0 & 0 & 0 & 1 \end{pmatrix} \tag{3.32}$$

The Müller matrix of an optical attenuator acting equivalently on light of any SOP is given by

$$\mathbf{M}_A = A \begin{pmatrix} 1 & 0 & 0 & 0 \\ 0 & 1 & 0 & 0 \\ 0 & 0 & 1 & 0 \\ 0 & 0 & 0 & 1 \end{pmatrix} \tag{3.33}$$

with $0 < A < 1$ being the attenuation factor. The Müller matrix of an ideal linear

polariser at orientation δ is (Bohren and Huffman, 2008):

$$\mathbf{M}_{LP} = \frac{1}{2}\begin{pmatrix} 1 & \cos(2\delta) & \sin(2\delta) & 0 \\ \cos(2\delta) & \cos^2(2\delta) & \cos(2\delta)\sin(2\delta) & 0 \\ \sin(2\delta) & \cos(2\delta)\sin(2\delta) & \sin^2(2\delta) & 0 \\ 0 & 0 & 0 & 0 \end{pmatrix} \tag{3.34}$$

Applying it to an arbitrary Stokes vector according to $\mathbf{M}_{LP} \cdot (I, Q, U, V)^T$ and regarding I only, yields equation 3.26. We further introduce the matrix for a linear retarder (birefringent optical components):

$$\mathbf{M}_{LR} = \begin{pmatrix} 1 & 0 & 0 & 0 \\ 0 & \cos^2(2\delta) + \sin^2(2\delta)\cos(\Phi) & \cos(2\delta)\sin(2\delta)(1-\cos(\Phi)) & \sin(2\delta)\sin(\Phi) \\ 0 & \cos(2\delta)\sin(2\delta)(1-\cos(\Phi)) & \cos^2(2\delta)\cos(\Phi) + \sin^2(2\delta) & -\cos(2\delta)\sin(\Phi) \\ 0 & -\sin(2\delta)\sin(\Phi) & \cos(2\delta)\sin(\Phi) & \cos(\Phi) \end{pmatrix}, \tag{3.35}$$

(Bohren and Huffman, 2008), with δ being the orientation of the fast axis and Φ being the induced phase difference between fast and slow axis. Half- and quarter wave plates are special cases of the linear retarder with $\Phi = \pi$ and $\Phi = \pi/2$, respectively. Of particular interest are the Müller matrices describing scattering of light on air molecules and particles as they appear in the atmosphere. These are introduced in Section 3.3.2 and 3.3.3, respectively.

3.3 The radiative transfer equation

The effects of light-matter interactions determining the atmospheric radiative transport are succinctly summarised in the *radiative transfer equation* (RTE). Let's consider a beam of rays of wavelength λ and Stokes parameters $\mathbf{I}$ (we drop wavelength and direction dependencies for better readability), coming from a distinct direction Ω and penetrating an air volume element $dV = A \cdot ds$ with cross-sectional area A and length ds, oriented along Ω. Then, $\mathbf{I}$ along Ω is altered by different processes:

1. The incoming beam gets attenuated by absorption on molecules and particles.

2. Similarly the beam gets attenuated due to scattering of radiance out of its initial propagation direction Ω.

3. Beams from other directions $\mathbf{I}(\Omega')$ are potentially scattered into the direction Ω, resulting in an increase in radiance.

4. Thermal emission of the air parcel adds further radiance. However, this effect will in the following be neglected as its contribution is negligible in the UV and Vis spectral range at typical Earth surface and atmospheric temperatures.

The total change in radiance is described by the RTE:

$$\boxed{\frac{d\mathbf{I}}{ds} = -K^{(a)}\mathbf{I} - K^{(s)}\mathbf{I} + \frac{K^{(s)}}{4\pi}\int_{4\pi}\mathbf{P}(\Omega', \Omega)\mathbf{I}(\Omega')d\Omega'} \tag{3.36}$$

The first, second and third term account for the effects described in points 1 to 3 in the enumeration above, respectively. $K^{(a)}$ and $K^{(s)}$ are the wavelength dependent absorption- and scattering coefficient, respectively. The total effect of scattering and absorption is referred to as *extinction* and consequently we can define the extinction coefficient $K^{(e)} = K^{(a)} + K^{(s)}$. All three coefficients can be expressed as a sum over all contributing species i present in dV at number concentration c_i with absorption-, scattering- and extinction cross-sections $\sigma_i^{(a)}$, $\sigma_i^{(s)}$ and $\sigma_i^{(e)}$:

$$K^{(a)} = \sum_i \sigma_i^{(a)} c_i \qquad K^{(s)} = \sum_i \sigma_i^{(s)} c_i \qquad K^{(e)} = \sum_i \sigma_i^{(e)} c_i \tag{3.37}$$

Generally, $K^{(a)}$, $K^{(s)}$ and $K^{(e)}$ are Müller matrices, however, for randomly oriented molecules and particles as encountered in the atmosphere, their attenuating effects act equally on light of any SOP and therefore, according to Eq. 3.33, can be represented by a scalar multiplication. Another useful quantity is the air parcels single scattering albedo, defined as

$$\omega = \frac{K^{(s)}}{K^e}. \tag{3.38}$$

$\mathbf{P}(\Omega', \Omega)$ in the last term of Eq. 3.36 is the scattering phase matrix (in analogy to the *phase function* for the scalar radiance case), basically describing how much of the light $\mathbf{I}(\mathbf{\Omega'})$ incoming from any direction Ω' is scattered into the observer's direction Ω. It is normalised, such that integration of P_{11} over the full solid angle yields 4π.

In the atmosphere, light interacts with molecules and aerosols. Both contribute very differently to $K^{(a)}$, $K^{(s)}$ and $\mathbf{P}$. This will be discussed in detail in the following subsections.

3.3.1 General properties of scattering matrices

Single scattering processes in the atmosphere are most conveniently described, if the Stokes parameter reference frames of the incident as well as the scattered beam are oriented within the scattering plane, as illustrated in Figure 3.2. This significantly simplifies the scattering matrix structure and the matrix can be parametrised solely by the scattering angle Θ, which is the angle between the directions of incoming ($\mathbf{\Omega}$) and scattered ($\mathbf{\Omega'}$) beam. Any required reference frame rotation can be achieved by applying Eq. 3.32. Throughout this thesis, we assume atmospheric scatterers to be randomly oriented (Hulst and van de Hulst, 1981). This assumption is invalid only for few exceptions (e.g. levitating ice crystals). Given these assumptions, any

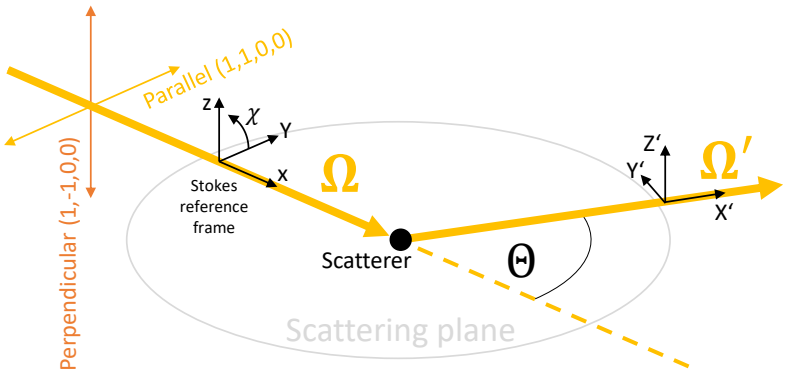

Figure 3.2: Coordinate systems and quantities for the description of scattering processes.

scattering process can be described by a matrix of the form

$$\mathbf{P}(\Theta) = \begin{pmatrix} P_{11}(\Theta) & P_{12}(\Theta) & 0 & 0 \\ P_{12}(\Theta) & P_{22}(\Theta) & 0 & 0 \\ 0 & 0 & P_{33}(\Theta) & P_{34}(\Theta) \\ 0 & 0 & -P_{34}(\Theta) & P_{44}(\Theta) \end{pmatrix} \tag{3.39}$$

with only six independent elements. For spherical particles (as they are assumed for molecular and Mie scattering), the matrix simplifies further, since $P_{11} = P_{22}$ and $P_{33} = P_{44}$. Note that P_{11} corresponds to the scattering phase function that is used in scalar RT calculations.

3.3.2 Extinction by molecules

Scattering of light by molecules is often referred to by *Rayleigh scattering*. It comprises several sub-processes and the exact definition of Rayleigh scattering slightly differs between communities and has raised confusion in the past (Young, 1982). In this thesis we refer by Rayleigh scattering to any scattering process on air molecules apart from vibrational Raman scattering, which is considered negligible for our applications (compare Lampel et al., 2015). Rayleigh scattering can then be subdivided into *Cabannes scattering* and *rotational Raman scattering*. Cabannes scattering describes elastic scattering, in the sense that it includes the processes causing radiation wavelength shifts of zero or much smaller than of relevance for our purposes. It comprises the Brillouin doublet (with wavelength shifts smaller than typical atmospheric Doppler-broadening) and the Gross or Landau-Plasczek line (Wang et al., 2003). Rotational Raman scattering is inelastic: in Rayleigh scattering events, there is a chance of typically 2 to 4% that photons loose or gain energy during scattering by increasing or decreasing the molecule's rotational quantum state (Raman, 1928), resulting in wavelength shifts up to $\approx 2\,\mathrm{nm}$.

Considering light in the solar spectral range, molecules have radii $r \ll \lambda$. In contrast to larger particles (see Section 3.3.3) molecules can therefore be regarded as being exposed to an temporally oscillating but spatially homogenous electric field. This significantly simplifies mathematical considerations, such that rather simple analytical expressions exist for the scattering cross-sections and phase matrices.

In this thesis we apply the Rayleigh scattering cross-section of air according to Bucholtz (1995):

$$\sigma_R(\lambda) = \frac{24\pi^3(n^2-1)^2}{\lambda^4 N^2(n^2+2)^2} F_K. \tag{3.40}$$

N is the molecule number density that can be obtained for a given pressure p and temperature T from the ideal gas law. n is the air refractive index and serves as the macroscopic description of the molecules' mean polarisability. Eq. 3.40 contains the well-known λ^{-4} wavelength dependence, but n and F_K also depend on λ and cause slight deviations from this simplified picture. F_K is the *King correction factor* that accounts for the depolarisation of scattered radiation due to anisotropies in the polarisability of air molecules. The values of F_K for N_2, O_2, Ar and CO_2 are given by Bates (1984) and allow to derive an expression for F_K for standard atmospheric compositions:

$$F_K(\lambda) = 1.046 + 5.036 \cdot 10^{-4}\,\mu\text{m}^2 \cdot \lambda^{-2} + 2.896 \cdot 10^{-5}\,\mu\text{m}^4 \cdot \lambda^{-4} \tag{3.41}$$

F_K is related to another parameter that is sometimes used in the literature:

$$\epsilon = \frac{9}{2}(F_K - 1). \tag{3.42}$$

ϵ is a more direct measure for the anisotropy of a molecule, as it directly compares its polarisability along the spatial axes (see Young (1982) for details). Typical effective values for F_K and ϵ in the atmosphere are around 1.05 and 0.22, respectively.

For the refractive index n_0 under standard conditions ($T = 15\,°\text{C}$, $p = 1013\,\text{hPa}$, dry air) we use the approximation by Ciddor (1996) for the UV-Vis spectral range:

$$10^8(n_0 - 1) = \frac{5792105\,\mu\text{m}^{-2}}{238.0185\,\mu\text{m}^{-2} - \lambda^{-2}} + \frac{167917\,\mu\text{m}^{-2}}{57.362\,\mu\text{m}^{-2} - \lambda^{-2}} \tag{3.43}$$

For arbitrary temperatures T, pressures p and water vapour pressure p_{H2O} the refractive index is

$$\begin{aligned}(n-1) = (n_0 - 1) \cdot \frac{104126\,\text{hPa}^{-1} \cdot p}{10^8 + 367100\,\text{K}^{-1} \cdot (T - 273.15\,\text{K})} \\ - \frac{p_{H2O} \cdot (4.292 - 0.0341\,\mu\text{m}^2 \cdot \lambda^{-2})}{10^8\,\text{hPa}}\end{aligned} \tag{3.44}$$

Table 3.1: Values for the constants in Eq. 3.45 for different scattering processes, adapted from Landgraf et al. (2004).

Scattering type	A	B	C	D
Rayleigh	$3(45+\epsilon)$	$30(9-\epsilon)$	36ϵ	$(180+40\epsilon)$
Cabannes	$3(180+\epsilon)$	$30(36-\epsilon)$	36ϵ	$40(18+\epsilon)$
Rotational Raman	3	-10	36	40

following Edlén (1966) and Ciddor (1996). For the scattering matrix we use the parametrisation by Landgraf et al. (2004). Rayleigh, Cabannes and rotational Raman scattering matrices share the same basic structure

$$\mathbf{P}_R(\Theta) = \frac{1}{D}\begin{pmatrix} A(1+\cos^2\Theta)+C & -A\sin^2\Theta & 0 & 0 \\ -A\sin^2\Theta & A(1+\cos^2\Theta) & 0 & 0 \\ 0 & 0 & 2A\cos\Theta & 0 \\ 0 & 0 & 0 & B\cos\Theta \end{pmatrix} \quad (3.45)$$

but require different values for A, B, C and D according to Table 3.1. Phase matrices for Rayleigh and Raman scattering are illustrated in the upper panels of Figure 3.8.

Absorption of light by atmospheric trace gases arises from the fact that molecules can exist in many different quantum-mechanical states in terms of their electron configuration (electronic states), their angular momentum (rotational states) and the vibration of their atoms relative to each other (vibrational states). Transitions between the states are mostly associated with the emission or absorption of photons of corresponding energy. However, within the altitude ranges of interest for our purposes, the collision frequency of air molecules is much larger than the inverse of typical natural lifetimes of the excited states. As a consequence, excited states relax mostly due to collisional quenching with the energy being dissipated into heat, rather than by emission of photons. We therefore assume the transitions to be solely absorbing and neglect fluorescence effects.

Many trace gas molecules feature electronic transitions with energy differences ($\approx 1\,\mathrm{eV}$) corresponding to photon wavelengths in the UV-Vis spectral range. Each electronic transition has an own set of vibrational transitions ($\approx 0.1\,\mathrm{eV}$) with each again featuring a set of rotational transitions (on the order of 10^{-3} to $10^{-2}\,\mathrm{eV}$). Consequently, an electronic transition actually 'produces' a pattern of many absorption lines of different strength. These line patterns - and thus the corresponding absorption cross-sections - have several remarkable properties that are crucial for the DOAS spectral analysis (see Section 4.2):

- The patterns are characteristic for the respective gas.
- They are spectrally quasi-continuous, in the sense that the distance between the lines is small compared to the resolving power of typical MAX-DOAS spectrometers.

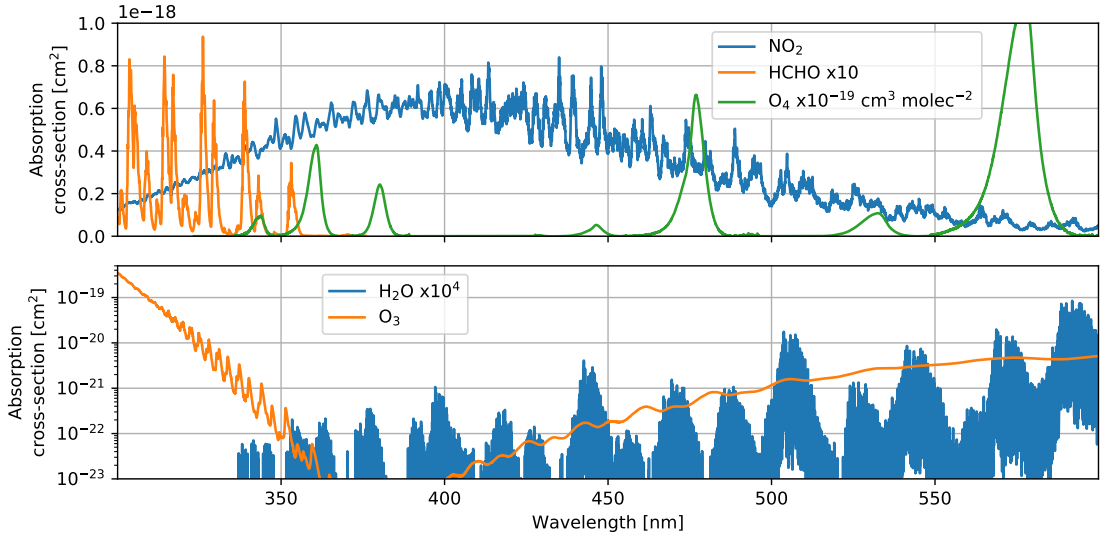

Figure 3.3: Literature absorption cross-sections for the trace gases most relevant in this thesis. The corresponding references are listed in Table 13.1. The unusual units of the O_4 cross-section and related peculiarities are discussed in the main text

.

- In contrast to most other light extinction processes in the atmosphere, they feature spectral narrow-band variations.

For many trace gases, there are literature absorption cross-sections available, derived from quantum-mechanical calculations or from lab measurements or a combination of both approaches. Absorption cross-sections of the trace gases most relevant for this thesis are shown in Figure 3.3. Recall that the O_4 absorption cross-section σ_{O_4} is not a conventional cross-section but directly relates the square of the oxygen concentration to the O_4 extinction coefficient (compare Section 2.4). As a consequence, related quantities have unusual units: σ_{O_4} is given in $\mathrm{cm}^5\,\mathrm{molec}^{-2}$ instead of cm^2 and the slant column densities (introduced in Section 4) have units of $\mathrm{molec}^2\,\mathrm{cm}^{-5}$ instead of cm^{-2}.

3.3.3 Extinction by aerosols

Before discussing the extinction of light on atmospheric aerosol, we introduce a few more useful quantities. The *size parameter*

$$\alpha = \frac{2\pi r}{\lambda} \tag{3.46}$$

compares the particle radius r to the radiation wavelength λ. The aerosol *extinction efficiency*

$$E = \frac{\sigma_{aer}^{(e)}}{\pi r^2} \tag{3.47}$$

compares the aerosol extinction cross-section per particle to its geometric cross-sectional area. In equivalence to the SSA introduced in Eq. 3.38, the aerosol SSA is defined as

$$\omega_{aer} = \frac{\sigma_{aer}^{(s)}}{\sigma_{aer}^{(s)} + \sigma_{aer}^{(a)}}. \tag{3.48}$$

The *asymmetry parameter* provides a useful quantification of the asymmetry of the scattering phase function and is defined as:

$$g = \frac{1}{2} \int_0^{\pi} \cos(\theta) P_{11}(\theta) \sin(\theta) d\theta. \tag{3.49}$$

It yields values $-1 \leq g \leq 1$. For $g < 0$, radiation is predominantly scattered backwards, i.e. at scattering angles $> 90°$. For $g > 0$, forward scattering prevails. Values for typical atmospheric aerosol are on the order of $g = 0.7$.

The Ångstrom exponent $å$ describes the wavelength dependence of the aerosol extinction $K^{(e)}$. It can be calculated from the extinction at two wavelength λ_1 and λ_1 according to

$$\frac{K^{(e)}(\lambda_1)}{K^{(e)}(\lambda_2)} = \left(\frac{\lambda_1}{\lambda_2}\right)^{-å} \tag{3.50}$$

The optical properties of spherical aerosol particles can be derived from the microphysical properties (size and material refractive index) using Mie theory (Mie, 1908). Throughout this thesis we make use the Mie model code introduced in more detail in Section 7. Going into the details of Mie theory, however, is out of the scope here.

For a first introduction of light extinction on aerosols we consider monodisperse aerosol, i.e. particles of a single size. The Mie theory yields that, for size parameters $\alpha \lesssim 1$, the extinction efficiency drops with decreasing particle size and $\sigma_{\text{aer}}^{(e)}$ approaches the Rayleigh extinction cross-section. Since particle concentrations in the atmosphere are many orders of magnitude smaller than molecule concentrations, particles with $\alpha \ll 1$ can be considered negligible in the context of RT. In contrast, the scattering efficiency E approaches two for $\alpha \gg 1$.

Figure 3.5 shows Mie caculations for the scattering matrix of monodisperse aerosol of different size parameters. For small α, the phase matrix is similar to the Rayleigh phase matrix. With increasing particle size, the phase matrix becomes more complex and scattering in the forward direction is increasingly pronounced. Regarding the signed DOLP, scattering on monodisperse aerosol in principle has the potential to strongly polarise light.

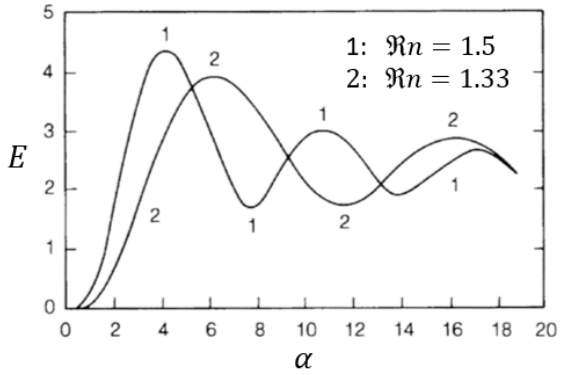

Figure 3.4: Dependence of the aerosol extinction efficiency E on the size parameter α for monodisperse aerosol of different refractive index $\Re n$. Figure is adapted from Roedel and Wagner (2017).

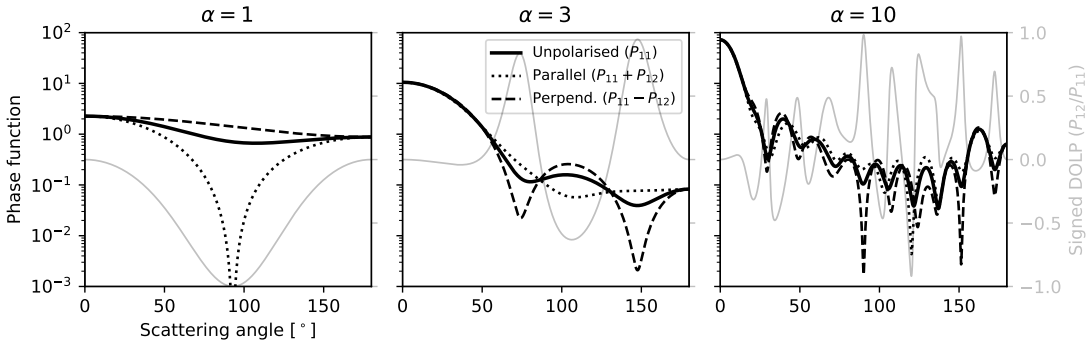

Figure 3.5: Illustration of scattering matrices for monodisperse aerosol with $n = 1.33{+}10^{-8}{\cdot}i$ and different size parameters α. The subplots show effective phase functions for unpolarised incoming light (matrix element P_{11}), as well as for polarisations parallel ($P_{11}+P_{11}$) and perpendicular ($P_{11}-P_{11}$) to the scattering plane. Grey lines and scales indicate the DOLP after a single scatter event of initially unpolarised light (P_{12}/P_{11}). It has a sign here: positive and negative values indicate polarisation perpendicular and parallel to the scattering plane, respectively.

But things change in the real atmosphere, where particles of multiple sizes coexist. Effective aerosol properties then need to be inferred by integration over *aerosol size distributions*. The latter are parametrised in different ways throughout the literature. Depending on the application it is for instance convenient to provide concentrations either in terms of particle number, surface area or volume. Also, the type of distribution may differ: most common are log-normal and gamma distributions. Further, the same distribution might be described by different sets of parameters. In the following, we will define the conventions and quantities used within this thesis and provide basic formulae to transform between the most common units and parametrisations.

The Mie code that we use (Spurr et al., 2012), which is also included in the RAPSODI algorithm (see Section 7), assumes a bi-modal aerosol number size distribution, with each mode described by a log-normal distribution. This approximation is generally considered appropriate for remote sensing applications in the solar spectral range (e.g. Whitby, 1978; Shettle and Fenn, 1979; Remer and Kaufman, 1998). The number of particles dN per radius interval dr is given by:

$$\begin{aligned}\frac{dN(r)}{dr} = n(r) = \frac{N_0}{\sqrt{2\pi}}\frac{1}{r}\left[\frac{f}{\sigma_1}\exp\left(-\frac{1}{2}\left(\frac{\ln r - \ln r_1}{\sigma_1}\right)^2\right)\right. \\ \left. + \frac{1-f}{\sigma_2}\exp\left(-\frac{1}{2}\left(\frac{\ln r - \ln r_2}{\sigma_2}\right)^2\right)\right]\end{aligned} \tag{3.51}$$

The first term in brackets represents the fine mode, described by r_1 and σ_1, while the second term represents the coarse mode described by r_2 and σ_2. r is the particle radius, $N_0 = N_{0,1} + N_{0,2}$ is the total number of particles, r_1 and r_2 are the mode median radii, σ_1 and σ_2 define the modal widths and $f = N_{0,1}/N_0$ is the fraction of particles residing within the fine mode. Instead of $dN(r)/dr$ sometimes $dN(r)/d\ln r$ is regarded instead. The latter can be derived from Eq. 3.51 through corresponding substitution of dr, which results in the removal of the factor $1/r$ in the first term. While maximum, mean and median are located at a common abscissa for normal distributions, they have different locations in the case of the log-normal distributions. The maxima of the single modes are located at the so-called "mode radii", which can be derived from r_m ($m \in [1, 2]$) according to

$$r_{mode,m} = r_m \cdot \exp\left(-\sigma_m^2\right). \tag{3.52}$$

The mean particle radii are given by

$$r_{mean,m} = \frac{1}{N_0}\int_0^\infty r n(r) dr = r_m \cdot \exp\left(\frac{\sigma_m^2}{2}\right). \tag{3.53}$$

In some studies and databases (e.g. AERONET, 2018) modes are characterised by the cross-sectional area weighted mean radius (or "effective radius") as first introduced by Hansen and Travis (1974)

$$r_{eff,m} = \frac{\int_0^\infty r\pi r^2 n(r) dr}{\int_0^\infty \pi r^2 n(r) dr} = r_m \cdot \exp\left(\frac{5}{2}\sigma_m^2\right), \tag{3.54}$$

with the advantage of being proportional to the aerosol extinction coefficient.

The log-normal distribution is convenient in the sense that the corresponding aerosol surface area and volume size distributions are also log-normal distributions with equal modal widths σ_m, however with different median radii. The area size distribution is obtained from Eq. 3.51 by replacing the total particle numbers of each mode, $N_{0,1} = f \cdot N_0$ and $N_{0,2} = (1-f) \cdot N_0$ by the corresponding total particle surface areas

$$A_{0,m} = 4\pi N_{0,m} \cdot r_m^2 \cdot \exp(2\sigma_i^2) \tag{3.55}$$

and replacing r_m by the area median radii

$$r_m^{(a)} = r_m \cdot \exp\left(2\sigma_m^2\right). \tag{3.56}$$

The volume size distribution is obtained equivalently by applying

$$V_{0,m} = \frac{4}{3}\pi N_{0,m} \cdot r_m^3 \cdot \exp\left(\frac{9}{2}\sigma_m^2\right) \tag{3.57}$$

and

$$r_m^{(v)} = r_m \cdot \exp(3\sigma_m^2). \tag{3.58}$$

For more details on the introduced equations and size distribution parametrisations in general the reader is referred to the very comprehensible document by Grainger (2012).

The effective properties of aerosol with a given size distribution $n(r)$ are in the following referred to as "bulk properties". They can be derived for any property $X(r)$ by integrating over the size distribution according to

$$\bar{X} = \frac{\int_0^\infty X(r)n(r)dr}{\int_0^\infty n(r)dr}. \tag{3.59}$$

For example the bulk extinction cross-section is given by

$$\bar{\sigma}_{\text{aer}}^{(e)} = \frac{\int_0^\infty \sigma_{\text{aer}}^{(e)}(r)n(r)dr}{\int_0^\infty n(r)dr}. \tag{3.60}$$

For many investigations throughout this thesis we assume microphysical properties for mixed aerosol (mixture of oceanic and industrial aerosol) as reported by Dubovik and King (2000a) for the Maldives. The exact values for the size distribution parameters and material refractive indexes are listed in Table 3.2. In the following we will refer to this aerosol as "standard mixed aerosol". The size distribution is illustrated in Figure 3.6. The bulk scattering phase matrix as calculated with the Mie model code is shown in Figure 3.8. Compared to calculations for monodisperse aerosol (see Figure 3.5), the phase matrix is strongly smoothed out over the scattering angle and its capability to produce polarised light is strongly reduced. The bulk optical properties and their dependence on wavelength are illustrated in Figure 3.7. All bulk properties change smoothly with λ, which is a crucial prerequisite for the DOAS spectral analysis (see Section 4.2). The Ångstrom exponent of the standard mixed aerosol is $\mathring{a} = 1.2$.

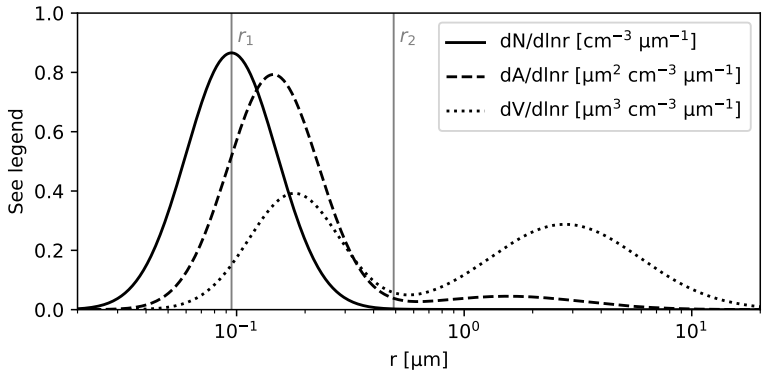

Figure 3.6: Mie aerosol size distribution in terms of normalised particle number (N), particle surface area (A) and particle volume (V) for the "standard mixed aerosol" case that is assumed for several investigations throughout this thesis (see Table 3.2). Vertical grey lines indicate the number size distribution mode median radii.

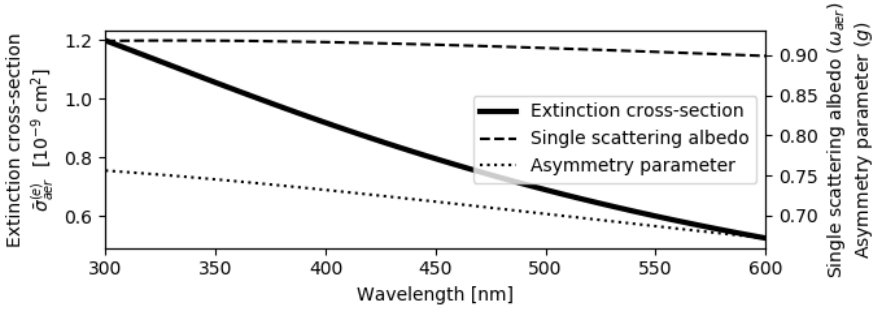

Figure 3.7: Bulk aerosol optical properties for the standard mixed aerosol (see Table 3.2).

Table 3.2: Number size distribution parameters and refractive index assumed for the "standard mixed aerosol" used for several investigations throughout this study. Values are adapted from Dubovik et al. (2002).

Parameter	Value
r_1	0.095 µm
r_2	0.49 µm
σ_1	0.46
σ_2	0.76
$\Re\, n$	1.44
$\Im\, n$	0.011
f	0.9983

Henyey-Greenstein approximation

Mie model calculations are rather complex and computationally expensive. An alternative and common approach to describe aerosol within RT simulations and inversion algorithms is the *Henyey-Greenstein* approximation. Here, properties are directly provided in terms of simplified optical properties. The scattering phase function is approximated as

$$P_{\mathrm{hg}}(\mu) = \frac{1 - g_{\mathrm{hg}}^2}{(1 + g_{\mathrm{hg}}^2 - 2\, g_{\mathrm{hg}}\, \mu)^{3/2}} \tag{3.61}$$

with μ being the cosine of the scattering angle. P_{hg} depends on a single parameter only, namely the asymmetry parameter g_{hg}. We assume the HG scattering matrix to be $P_{\mathrm{hg}} \cdot \mathbf{1}$, hence, we assume that single scattering on HG aerosol will not affect the polarisation state of the incoming radiation. In this case, the scattering matrix at a single wavelength is fully described by two optical parameters: the asymmetry parameter g_{hg} and the single scattering albedo ω_{hg}. The extinction capability is typically quantified in terms of the extinction coefficient and its wavelength dependence is described by the Ångstrom exponent $\mathring{a}_{\mathrm{hg}}$ (according to Equation 3.50).

3.3.4 Boundary conditions for the radiative transfer

Besides the atmosphere itself, it is necessary to consider the optical properties of the atmosphere's boundaries, namely the incoming radiation at TOA and the Earth's surface reflective properties at BOA. Extraterrestrial sunlight is unpolarised. Approximating the Sun as a point source, the downwelling stokes parameters at TOA are therefore:

$$\mathbf{I}_S^{\downarrow}(\Omega) = (F_S\, \delta(\Omega - \Omega_S), 0, 0, 0). \tag{3.62}$$

Here, F_S is the solar constant, hence, the irradiance for a plane perpendicular to the direction Ω_S of the incoming solar radiation and δ is the Dirac delta function.

In the case of scalar radiances, reflective properties of surfaces can be fully described by the *bidirectional reflectance distribution function* (BRDF). Similar to the scattering phase function, it describes which amount of radiation coming from a direction Ω is reflected into direction Ω'. For vectorised radiances, the BRDF is a Müller matrix. Two particular cases of the BRDF are specular and *Lambertian* reflection. In the former case, radiation obeys Snell's law and the Fresnel equations. In this study, however, we will only make use of the Lambertian case. It assumes that, independent of Ω, light is reflected isotropically into any direction of the upper half-space and gets fully depolarised. In this case, the surface optical properties are described solely by the surface albedo $\omega_{surf}(\lambda)$, which represents the fraction of incoming light that is actually reflected and not absorbed by the surface.

3.3.5 Concluding remarks

Figure 3.8 illustrates typical scattering phase functions for the processes described in Section 3.3.2 and 3.3.3. It provides insight on the dominant scattering directions and the potential of different processes to polarise initially unpolarised light. It is further of interest to quantify the processes' capabilities to depolarise light. For this purpose, we introduce the "average remaining DOLP" that we define as the intensity weighted average DOLP

$$\frac{\sum_\chi \sqrt{Q_\chi^2 + U_\chi^2}}{\sum_\chi I_\chi} \qquad \text{with} \qquad \chi \in [0, 45, 90, 135\,^\circ] \tag{3.63}$$

calculated from the stokes parameters I_χ, Q_χ and U_χ, that one obtains after scattering of initially linearly polarised light of polarisation angle χ. The results are illustrated in Figure 3.9. It is further worth noting that, for all elastic scattering processes, the SOP is maintained in the forward scattering direction: For scattering angles up to 30°, the difference in the normalised Stokes parameters between incoming and outgoing beam is $< 15\,\%$, for incoming light of arbitrary linear SOP.

Regarding the polarisation of skylight under typical atmospheric conditions, it is worth to summarise a few qualitative key facts:

1. The incoming sunlight at TOA is initially unpolarised.

2. Circular polarisation does not play a role in the atmosphere.

3. The only significant source of linear polarisation is Cabannes (except forward and backward scattering), particularly at scattering angles around $90\,^\circ$.

4. Once a ray travelling along a distinct geometrical path is polarised, it is unlikely to get depolarised again by single scattering events in the atmosphere. Significant depolarisation is only achieved by inelastic scattering or scattering on aerosol at large scattering angles, both rather unlikely to occur (few % probability per scattering event). It shall be pointed out, however, that the

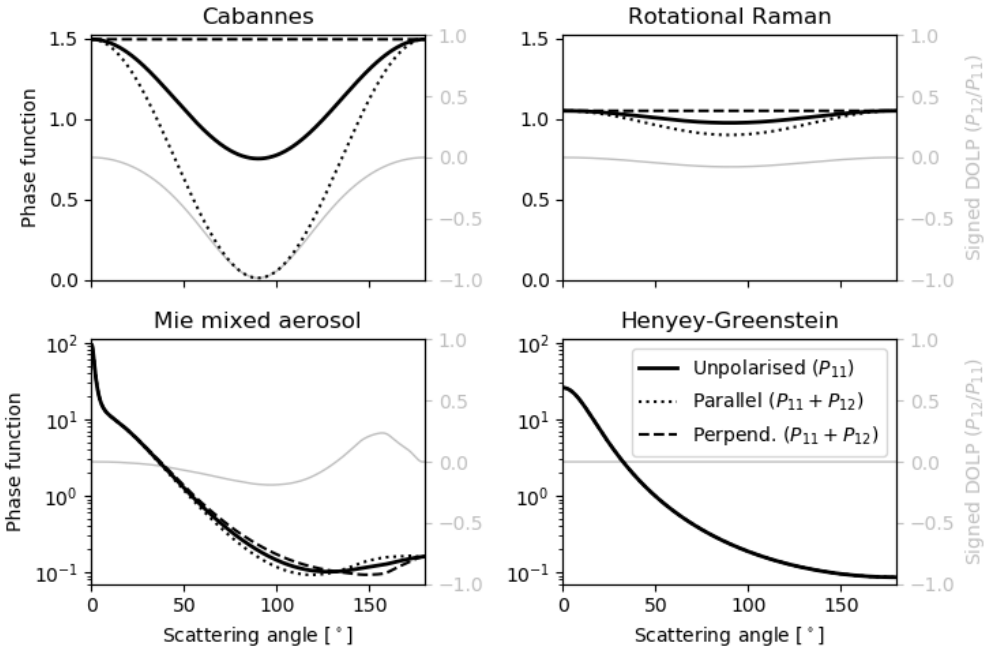

Figure 3.8: Illustration of scattering matrices for different scattering processes on molecules (top panels) and aerosols (lower panels). The Mie calculations were performed at $\lambda = 400\,\mathrm{nm}$ for the standard mixed aerosol as defined in Table 3.2. The HG phase matrix assumes an asymmetry parameter of $g_{\mathrm{hg}} = 0.74$. The data shown is similar to Figure 3.5.

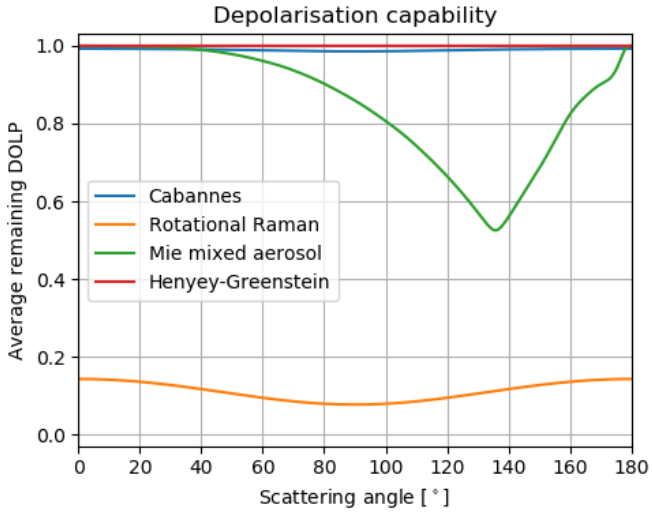

Figure 3.9: Average remaining DOLP after single scattering of initially linearly polarised light for different scattering processes. See text for the detailed definition.

superposition of several beams of different SOPs ultimately has a depolarising effect.

5. For elastic scattering at small scattering angles, the SOP is conserved.

Note that we ignored the Earth's surface here. In reality, the surface is capable to either produce significant amounts of polarised light (consider specular reflection on water surfaces close to the Brewster angle) or depolarise light (consider snow, with high albedo and a nearly Lambertian BRDF in the UV-Vis (Gibbs et al., 1993)). Further, in contrast to Mie aerosol as assumed within this thesis, non-spherical aerosol (e.g. desert dust) can have a rather strong depolarising effect (Dubovik et al., 2002).

3.4 Radiative transport models

With the knowledge from Section 3.3.2 and 3.3.3, we can, from the composition of an air volume dV, predict its optical properties in terms of effective values for $K^{(a)}$, $K^{(s)}$ and $\mathbf{P}(\Omega', \Omega)$. The actual mathematical challenge is to solve the RTE for the entire atmosphere, considering multiple scattering and given boundary conditions according to Section 3.3.4. RTM codes are readily available doing exactly this using a number of different approaches.

Monte Carlo models for instance explicitly simulate trajectories for large ensembles of photons (Kattawar and Plass, 1968) and derive the macroscopic radiation quantities applying statistics over the results. Their major advantage is the capability to simulate arbitrary atmospheres, notably with 3-dimensional aerosol and trace gas distributions and directly including Earth's sphericity.

Besides Monte Carlo, there are a number of semi-analytical approaches. An overview can be found, for instance, in Lenoble et al. (2013). Most prominent are the *successive order of scattering* approach (Hammad and Chapman, 1939), the *discrete ordinate* method (Chandrasekhar, 1947, 2013), and the *doubling-adding* method (Van de Hulst and Grossman, 1968). In contrast to Monte Carlo simulations, they only provide solutions for atmospheres consisting of optically homogeneous horizontal layers. Earth's sphericity is typically taken into account using a *pseudo-spherical* correction (e.g. Dahlback and Stamnes, 1991), which assumes a curved atmosphere only for the rather simple calculations of direct and singly scattered radiation fields, while calculations for the multiple-scattering field are performed in the plane-parallel approximation.

In this study, we use the vectorised linearised discrete-ordinate radiative transfer model (VLIDORT) (Spurr, 2006, 2008). The mathematical details of discrete-ordinate models are out of the scope of this study (the reader is referred to the literature given above), however, the very basic idea is to discretise the full solid angle into a finite number of directions. The azimuthal dependence of the radiation field is expressed in terms of a Fourier series. The polar angle is discretised into a distinct number of polar angles typically referred to as *discrete ordinates* or

streams. Likewise, the scattering phase matrices are expressed in terms of Legendre-Polynomial expansions. This discretisation allows to turn the integral in the RTE (Eq. 3.36) into a sum, allowing to express the RT problem in terms of a solvable set of coupled linear first-order differential equations. The number of streams and the associated order of the Legendre expansions are crucial parameters regarding the simulation performance and need to be chosen carefully (see Section 8.1).

4 Ground-based MAX-DOAS

Ground-based Multi-AXis Differential Optical Absorption Spectroscopy (MAX-DOAS) (e.g. Hönninger and Platt, 2002; Hönninger et al., 2004; Wagner et al., 2004; Heckel et al., 2005; Frieß et al., 2006; Platt and Stutz, 2008; Irie et al., 2008; Clémer et al., 2010; Wagner et al., 2011; Vlemmix et al., 2015) is versatile passive remote sensing technique for the simultaneous detection of aerosol and trace gases. As already briefly described Section 1, the typical MAX-DOAS measurement procedure can be subdivided into three major steps:

1. Acquisition of spectral data: The typical MAX-DOAS instrument consists of a motorised narrow field of view telescope and a spectrometer unit, allowing to record ultraviolet (UV)- and visible (Vis) radiation spectra of scattered sunlight in a multitude of viewing directions ("Multi-Axis") and in the scope of this thesis, at different polarisation orientations.

2. Spectral analysis: The spectra are analysed using "Differential Optical Absorption Spectroscopy" (DOAS) to obtain information on different atmospheric absorbers and scatterers, integrated over the light's effective path through the atmosphere.

3. Inversion procedure: inverse modelling approaches involving RTMs are used to infer the atmospheric state from the data acquired in the steps before. Such inversion schemes are frequently and in the following referred to as "retrieval algorithms".

The full procedure is qualitatively illustrated and outlined in Figure 4.1. The individual steps are described in detail in the following subsections.

For this thesis we focus on the detection of HCHO and NO_2. Other gases that have been analysed with MAX-DOAS in the UV and Vis spectral range are nitrous acid (HONO), water vapour (H_2O), sulfur dioxide (SO_2), ozone (O_3), glyoxal (CHOCHO) and halogen oxides (e.g. BrO, OClO). As already described in Section 2.4, the oxygen collision induced absorption (in the following treated as if being an additional trace gas species O_4) can be used to infer information on aerosols: since the concentration of O_4 is proportional to the square of the O_2 concentration, its vertical distribution is well known. The O_4 absorption signal can therefore be utilized as a proxy for the light path that strongly depends on the atmosphere's aerosol content. O_4 absorption measurements therefore allow to infer information on the aerosol vertical distribution as well as aerosol properties (Wagner et al., 2004; Frieß et al., 2006). In fact, in most conventional MAX-DOAS retrieval algorithms, O_4 absorption is used as the only source of information on aerosol.

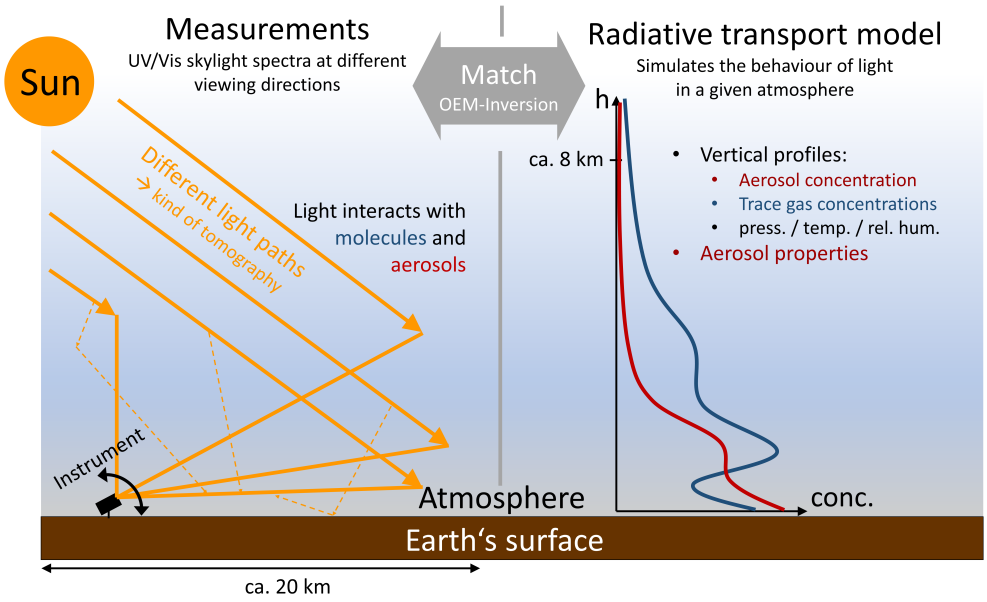

Figure 4.1: Illustration of the MAX-DOAS measurement procedure. Left: spectra of skylight recorded under different viewing directions contain information on the atmospheric state integrated along the effective light paths, the latter indicated by the thick yellow arrows. The paths are strongly simplified, as they are actually superpositions of a multitude of light paths, potentially involving multiple scattering in the atmosphere and on the Earth's surface, as illustrated by the dashed thin arrows. Right: Once measurements have been performed and spectrally analysed, an RTM is used to reproduce the observations in an artificial atmosphere. The model parameters are adapted to bring modelled and actual observations into closure, thereby approaching the real atmospheric state.

4.1 Acquisition of spectral data

Currently, a large number of different MAX-DOAS instrument prototypes exist, all different in the detailed implementation and sometimes optimised for distinct purposes. However, most of them share essential properties that have been established over recent years and shall be outlined here. The typical MAX-DOAS instrument consists of a telescope and a grating spectrometer unit. The telescope features a narrow field of view (FOV), with full aperture angles of approximately 0.5° (10 mrad). It is motorised to automatically realise multiple viewing directions in rather quick succession ($\approx$ 1 min per viewing direction). 1D-MAX-DOAS instruments are installed at a fixed viewing azimuth angle (VAA), automatically changing the viewing elevation angle (EA), while 2D-MAX-DOAS instruments have motors for both, VAA and EA. There are different approaches to guide the gathered light from the telescope to the spectrometer, the most common being to use fused silica optical fibres. Typical spectral coverage and resolving powers of the spectrometers applied are on the order of 150 nm and 10^3, respectively. It is not unusual to apply multiple spectrometers, commonly two, dedicated to the UV and the Vis spectral ranges with typical coverages of $300 - 400$ nm and $400 - 500$ nm, respectively. Further details on the instrumental implementation can be learned from Section 11, in the course of the description of the PMAX instrument. Note that DOAS instruments are typically not radiometrically calibrated. Therefore, any observed radiances I will in the following be assumed to have arbitrary units.

4.2 DOAS spectral analysis

In the following by "DOAS spectral analysis" we refer to the procedure of evaluating the raw spectral data, using the methods outlined below. It shall be noted that it is generally applicable to a number of different DOAS-techniques beside MAX-DOAS, some even using artificial light sources and folded light paths (see e.g. Platt and Stutz, 2008). Discussing those in detail is out of the scope of this study, but they all have in common that characteristic trace gas absorption features need to be identified in spectral data.

4.2.1 Beer-Lambert law

First, consider a beam with radiance spectrum $I_0(\lambda)$ traversing a volume of length L along the beam's direction. If no further light sources are present and multiple scattering in the volume is neglected, the integral term in the RTE (Eq. 3.36) is zero and the beam's attenuation at position s along L is described by the Beer-Lambert law

$$\frac{dI(\lambda)}{ds} = -K(\lambda, s)I(\lambda). \tag{4.1}$$

with $K(\lambda, s)$ being the extinction coefficient of the traversed volume as already introduced in Eq. 3.37 (we skip the (e)-label here for readability). Recall that $K(\lambda, s)$ includes the absorption and scattering capabilities of different constituents in terms of their absorption and scattering cross-sections $\sigma_i^{(a)}$ and $\sigma_i^{(s)}$.

Eq. 4.1 can be integrated over the beam path L to obtain the attenuated radiance $I(\lambda)$, observed by a detector behind the volume:

$$I(\lambda) = I_0(\lambda) \exp\left(-\int_0^L K(\lambda, s)ds\right) = I_0(\lambda) \exp(-\tau(\lambda)). \tag{4.2}$$

Here, $\tau(\lambda)$ is the volume's "optical thickness" (OT) along the beam's path, defined as

$$\tau(\lambda) = -\int_0^L K(\lambda, s)ds = \ln\left(\frac{I_0(\lambda)}{I(\lambda)}\right). \tag{4.3}$$

4.2.2 Slant optical thickness

Now consider a ground-based MAX-DOAS instrument, pointing into direction $\Omega = \{\theta, \phi, \alpha\}$, with θ, ϕ and α being the SZA, the RAA and EA, respectively. The instrument detects the skylight spectrum $I(\lambda, \Omega)$, which corresponds to the extraterrestrial spectrum $I_{\mathrm{TOA}}(\lambda)$, altered by the RT effects introduced in Section 3. In contrast to the simple example of beam attenuation in a volume, the light now travels from TOA to the instrument along an infinite number of possible geometrical paths, each with a contribution probability that itself is a function of the atmospheric state, particularly of the aerosol abundance.

Despite these complicating aspects, the total effect on the spectrum can still be expressed in terms of an OT, the "slant optical thickness" (SOT)

$$\tau(\lambda, \Omega) = \ln\left(\frac{I_{\mathrm{TOA}}(\lambda)}{I(\lambda, \Omega)}\right) \tag{4.4}$$

along a virtual *effective light path*. Note that $\tau(\lambda, \Omega)$ no longer describes attenuating effects alone, but now also includes changes in radiance arising from the spectral dependence of single and multiple scattering processes.

Recalling Section 3, there is a crucial prerequiste for the DOAS analysis: in contrast to trace gas absorption, all elastic scattering processes solely change the broad band shape of the spectrum. This allows to model $\tau(\lambda, \Omega)$ in good approximation as

$$\tau(\lambda, \Omega) \approx \sum_i \sigma_i(\lambda)\, S_i(\Omega) + \sum_j^N b_j \lambda^j + k_R R(\lambda). \tag{4.5}$$

at least over a limited wavelength range (width of $\approx 50\,\mathrm{nm}$) and for thin molecular absorbers (with OTs on the order of few percent). The first term on the right hand

side accounts for absorption by different trace gases i, with absorption cross-section $\sigma_i(\lambda)$ and slant column density (SCD)

$$S_i(\Omega) = \int_0^L c_i(s)ds, \tag{4.6}$$

which is the trace gas concentration $c_i(s)$ integrated along the effective light path L through the atmosphere. Since the effective light path changes with λ, S_i also depends on λ. It is, however, typically assumed to be constant over the modelled wavelength range of the DOAS analysis. The second term in Eq. 4.5 is a polynomial ($N \approx 2$ to 5) that accounts for spectral broadband features caused by scattering and aerosol absorption. Particularly, it accounts for the effects introduced by the integral term of the RTE (Equation 3.36), which would normally be very complex to consider. The term $k_R R(\lambda)$ accounts for narrowband features caused by the "filling-in" of Fraunhofer lines (Grainger and Ring, 1962; Solomon et al., 1987; Bussemer, 1993; Wagner, 1999) due to inelastic Raman scattering. $R(\lambda)$ is the "Ring spectrum" that describes the expected shape of the Raman introduced narrow-band features while k_R specifies their magnitude. There are multiple approaches to infer $R(\lambda)$ (Wagner et al., 2001) either from measurements, modelling or combined approaches. In this study we use the approach implemented in the DOASIS software (Kraus, 2006) where

$$R(\lambda) = \frac{I_{inel}}{I_z(\lambda) - I_{inel}(\lambda)}. \tag{4.7}$$

$I_z(\lambda)$ is a zenith spectrum recorded at low SZA with the applied instrument. $I_{inel}(\lambda)$ is the modelled Raman single scattering radiance (considering Stokes- and Anti-Stokes scattering on nitrogen and oxygen), assuming $I_z(\lambda)$ as the incident radiance. A complete derivation of Equation 4.7 can for instance be found in Wagner et al. (2001).

For the detection of most trace gases, differences in optical depth smaller than 10^{-3} have to be resolved. Amongst others, due to imperfect knowledge of I_{TOA} and the instrumental slit function, this is typically not possible if literature spectra of $I_{TOA}(\lambda)$ are used in Eq. 4.4. Instead, SOTs are evaluated against spectra from the same instrument but from another viewing direction Ω_0. This yields the so called *differential slant optical thickness* (dSOT)

$$\Delta\tau(\lambda, \Omega, \Omega_0) = \ln\left(\frac{I(\lambda, \Omega_0)}{I(\lambda, \Omega)}\right) \tag{4.8}$$

$$= \sum_i \sigma_i(\lambda)\, \Delta S_i(\Omega, \Omega_0) + \sum_j b_j \lambda^j + k_R R(\lambda) \tag{4.9}$$

in equivalence to Eq. 4.5, however, with the SCD S_i being replaced by the *differential slant column density* (dSCD)

$$\Delta S_i = S_i(\Omega) - S_i(\Omega_0). \tag{4.10}$$

As we shall see later, both dSCDs and dSOTs play a crucial role throughout this thesis as they constitute the input for the RAPSODI inversion algorithm.

4.2.3 Instrument spectral resolution

So far we have ignored the fact that, in practical applications, instruments have limited spectral resolution. The instrument's response to a spectral delta-peak is called the "instrumental slit function" (ISF) $H(\lambda)$. Its width indicates the instrument's resolution, which is, for typical DOAS instruments, about two orders of magnitude larger than the natural line widths. Instead of the real spectrum $I(\lambda)$ (we omit Ω here for readability), the instrument detects a smoothed spectrum

$$I^*(\lambda) = I(\lambda) \circ H(\lambda) = [I_{\mathrm{TOA}}(\lambda) \exp(-\tau(\lambda))] \circ H(\lambda) \tag{4.11}$$

with $(\circ)$ indicating a convolution. Assuming that the real spectra have constant radiance over typical spectral widths of $H(\lambda)$ and that narrow-band absorbers have small OTs, the convolution and the exponent in Equation 4.11 commute. In this case the limited resolution can be accounted for by replacing $\sigma_i(\lambda)$ in Eq. 4.9 by the convoluted cross-section

$$\sigma_i^*(\lambda) = \sigma_i(\lambda) \circ H(\lambda) \tag{4.12}$$

(Platt and Stutz, 2008). Equations 4.8 and 4.9 can then be rewritten as

$$\begin{aligned} \ln I^*(\lambda, \Omega) \approx \ln I^*(\lambda, \Omega_0) &- \sum_i \sigma_i^*(\lambda)\, \Delta S_i(\Omega, \Omega_0) \\ &- \sum_j b_j \lambda^j - k_R R(\lambda) + C(\lambda). \end{aligned} \tag{4.13}$$

Without going into further mathematical detail, it shall be noted that the approximations taken in this step are not ideal and can have different consequences for the DOAS analysis results, such as the "I_0-effect" (Platt et al., 1997) or the "tilt-effect" (Lampel et al., 2017). The term $C(\lambda)$ in Eq. 4.13 represents diverse correction terms that are used to account for such effects.

The I_0-effect originates from strong spectral structures in the solar spectrum and/or the absorption cross-section that cannot be resolved by the instrument. The interaction of these unresolved spectral features has the consequence that, particularly for strong absorbers, the instrument perceives absorption structures that slightly differ from the ISF convoluted literature cross-sections assumed in Eq. 4.13. A first order correction can be achieved by applying altered cross-sections: following (Johnston, 1996), these are calculated according to

$$\sigma_i^{(I_0)} = \frac{1}{S_i^{(I_0)}} \cdot \frac{H(\lambda) \circ \hat{I}(\lambda)}{H(\lambda) \circ \left[\hat{I}(\lambda) \exp(-\sigma_i(\lambda) S_i^{(I_0)})\right]}, \tag{4.14}$$

with $\hat{I}(\lambda)$ being a high resolution TOA literature spectrum and $S_i^{(I_0)}$ being a typical expected SCD of the respective trace gas. Applying both the corrected and the uncorrected cross-section in Eq. 4.13, allows the DOAS fit (see Section 4.2.4) to

approximately reproduce the absorption structures for any S_i by linearly combining σ_i and $\sigma_i^{(I_0)}$. Within this thesis, the I_0 correction will be applied for water vapour absorption in the Vis range (see Section 13.3) using the TOA literature spectrum by Chance and Kurucz (2010).

4.2.4 The DOAS fit

On the basis of the Eq. 4.13, a fit (in the following referred to as "DOAS fit") can be performed, bringing the observed optical thickness on the left hand side into agreement with the model on the right hand side by minimizing the cost function:

$$\chi^2 = \int_{\lambda_1}^{\lambda_2} \Bigg[\ln I^*(\lambda,\Omega) - \ln I^*(\lambda,\Omega_0) + \sum_i \sigma_i^*(\lambda)\,\Delta S_i(\Omega,\Omega_0) + \sum_j b_j \lambda^j + k_R R(\lambda) - C(\lambda) \Bigg]^2 d\lambda. \tag{4.15}$$

λ_1 and λ_2 indicate the spectral fitting range. Taking literature values for $\sigma_i(\lambda)$, the parameters to be varied are ΔS_i, b_j and k_R. Note that $R(\lambda)$, $\sigma_i(\lambda)$ and the polynomial have to be linearly independent, or in other words, $R(\lambda)$ and $\sigma_i(\lambda)$ must contain characteristic narrowband spectral features that particularly cannot be reproduced by the polynomial. As discussed in Section 3.3.2, this is fulfilled for a large number of trace gases if the DOAS fit is performed over sufficiently large spectral windows. During the fit it is typically required to allow small spectral shifts and squeezes of $I^*(\lambda,\Omega)$, σ_i and $R(\lambda)$ with respect to $I^*(\lambda,\Omega_0)$ to account for instrumental drifts or the tilt-effect (Lampel et al., 2017). It is further common to include an "offset-polynomial" in the fitting procedure: it is added to $I^*(\lambda,\Omega_0)$ (prior to the calculation of $\ln I^*(\lambda,\Omega_0)$) to account e.g. for straylight in the spectrometer.

For the DOAS fit we used the HeiDOAS python library (Frieß, 2020). Explicit examples of DOAS fit results are shown in Section 13.3.

The resulting dSCDs ΔS_i are the primary output of the DOAS analysis and the only input for typical conventional MAX-DOAS inversion algorithms. In most applications the broadband information contained in b_j is discarded. Also in this study we will not further consider b_j and instead reincorporate the broadband information into the inversion in terms of dSOTs at distinct wavelengths (see Section 7.2). The information contained in k_R will be ignored in this thesis, even though Wagner et al. (2009) showed it to contain further information on aerosols. This might be subject to future investigations.

4.3 Inversion procedure

The conventional MAX-DOAS retrieval of the atmospheric state requires a set of dSCDs recorded under different viewing directions. As qualitatively indicated in

Fig. 4.1, measurements become increasingly sensitive to trace gas abundances at low altitudes with decreasing elevation angle (Hönninger and Platt, 2002). *Elevation scans* have therefore established as the geometry of choice for the retrieval of aerosol and trace gas vertical distributions. They include a set of spectra recorded at three to ten different EAs (with increasing resolution at low EAs) at a fixed RAA, with integration times of about 1 min each. The number of viewing directions is a trade-off between temporal resolution and information content of the measurements. Note that recent developments (including this thesis) gradually extend the focus of MAX-DOAS measurements from sole trace gas observations to aerosol profile and property retrievals. Depending on the purpose, other geometries (e.g. sampling the solar aureole region) might be advantageous and should be considered in the future. Investigations in these directions are presented in Section 9.3.

For the inversion, an RTM is used to reproduce the observed dSCDs in an artificial atmosphere. The model parameters are iteratively adapted to bring modelled and measured dSCDs into closure, thereby approaching the real atmospheric state.

In conventional MAX-DOAS retrieval algorithms, separate inversions are performed for each species. As described in Section 2.4, O_4 dSCDs are typically used as the only source of information on aerosols. In a first inversion procedure, therefore only O_4 dSCDs are simulated and the aerosol vertical distribution is optimised to reproduce the measured O_4 dSCDs. With the knowledge on the aerosol vertical distribution, further inversions are performed to retrieve vertical distributions of different trace gases from the corresponding dSCDs. As we shall see later, this is has been improved in our newly developed RAPSODI retrieval algorithm, which is capable to retrieve all species simultaneously in a shared model atmosphere.

In the recent years, a multitude of MAX-DOAS inversion algorithms have been implemented that apply different approaches in terms of parametrisation, prior constraints and optimisation procedure (Irie et al., 2008; Clémer et al., 2010; Wang et al., 2013; Yilmaz, 2012; Bösch et al., 2018; Chan et al., 2019; Vlemmix et al., 2011; Beirle et al., 2019). The RAPSODI retrieval is based on the optimal estimation (OEM) formalism. The concept of OEM is crucial to understand some of the approaches taken in this thesis. The formalism is therefore discussed in a dedicated section (5).

4.4 The airmass factor

In astronomy, the "airmass" describes the "amount of air that one is looking through" (Green, 1992) and is defined as the integral over the air density along a distinct LOS. The "airmass factor" (AMF) is often defined as the ratio between the air mass along some slant LOS and the airmass along the zenith viewing direction. In the MAX-DOAS community, the term is used in a slightly different way, as it does not refer to the amount of air but the amount of a certain trace gas that one is looking through.

As introduced in Equation 4.6, the concentration c_i of a trace gas i integrated along a slant path yields the "slant column density" or SCD. Integration of the

concentration along the vertical z yields the so-called "vertical column density" (VCD)

$$V_i = \int_0^{TOA} c_i(z)dz. \tag{4.16}$$

A related and often used quantity is the *aerosol optical thickness* (AOT) similarly defined as

$$\text{AOT} = \int_0^{TOA} K_{\text{aer}}^{(e)}(z)dz \tag{4.17}$$

but with the aerosol extinction coefficient $K_{\text{aer}}^{(e)}(z)$ being integrated. The AMF is defined as the ratio of SCD and VCD:

$$A_i(\lambda, \Omega) = \frac{S_i(\lambda, \Omega)}{V_i} \tag{4.18}$$

Often, AMFs and VCDs of single atmospheric layers l are regarded: they are then referred to as *box airmass factors* (BAMFs) A_l and *box vertical columns* (BVCDs) $V_{i,l}$. For optically homogeneous layers (as assumed in a model atmosphere) the BAMF is independent of the considered trace gas as it simply describes the ratio of slant and vertical light path. It is related to the AMF according to

$$A_i = 1/V_i \sum_l A_l V_{i,l}. \tag{4.19}$$

In the context of radiative transport simulations, BAMFs are a very useful concept to describe complex path geometries, as they basically boil down any ensemble of light paths to ratios between the effective slant and the vertical light path through each layer. For small OTs the BAMFs can be calculated according to

$$A_l(\lambda, \Omega) = -\frac{1}{I(\lambda, \Omega)} \frac{dI}{d\tau_l^{(a)}}, \tag{4.20}$$

with $\tau_l^{(a)}$ being the layer's vertical absorption optical thickness (see Appendix C).

4.5 From conventional to polarimetric MAX-DOAS

The easiest way to make use of polarimetric information on the instrumental side is to install a motorised linear polarising filter within the telescope of the MAX-DOAS instrument. As described in 11, this approach was pursued for the PMAX-DOAS instrument. The polariser allows to record spectra of skylight of different polarisation orientations, or "polariser angles" (PA) δ. The so recorded spectra will

in the following be referred to as "polarimetric spectra". The viewing geometry $\Omega = \{\theta, \phi, \alpha\}$, as introduced above for non-polarimetric observations, will in the following be extended by the PA, hence $\Omega = \{\theta, \phi, \alpha, \delta\}$. Throughout this thesis, δ describes the orientation of the polariser's transmitting axis with respect to the horizontal and increases clockwise when looking towards the instrument. The DOAS spectral analysis can be readily applied to polarimetric spectra just in the same way as described above, but we will refer to the resulting dSCDs by "polarimetric dSCDs". Also the other concepts introduced above (e.g. the calculation of dSOTs and AMFs) are readily applicable to polarimetric data, just by considering the PA as an additional parameter in Ω.

For the inversion algorithm, the major requirement is a forward model based on a vectorised RTM, which can reproduce the polarimetric observations. Another important aspect is that information on the SOP of skylight needs to be incorporated in the inversion to exploit the full potential of polarimetry. This information is not contained in polarimetric dSCDs. Therefore, also polarimetric dSOTs at discrete wavelengths will be fed to the RAPSODI algorithm. This is described in further detail in Section 7.2 in the course of the RAPSODI algorithm description.

5 Optimal estimation formalism

Simply speaking, an "inversion" can be regarded as fitting some model $\mathbf{F}(\mathbf{x})$ that depends on a set of n parameters we are interested in (summarised in the *state vector* $\mathbf{x}$, living in the *state space*) to a set of m observations (summarised in the *measurement vector* $\mathbf{y}$, living in the *measurement space*). Throughout this thesis we refer to the elements of $\mathbf{x}$ and $\mathbf{y}$ as *parameters* and *measurements*, respectively. The aim is to find the state vector $\hat{\mathbf{x}}$ that brings the model results $\mathbf{F}(\hat{\mathbf{x}})$ into best agreement with given measurements $\hat{\mathbf{y}}$, according to some definition of "best agreement", typically given in terms of a cost function.

For a first introduction let's consider the trivial case of a well-posed problem with an ideal model and error-free measurements. The problem can then be formulated according to

$$\hat{\mathbf{y}} \stackrel{!}{=} \mathbf{F}(\hat{\mathbf{x}}). \tag{5.1}$$

To find the solution $\hat{\mathbf{x}}$, the model $\mathbf{F}$ needs to be inverted. For further simplification let's assume that $\mathbf{F}$ is linear, meaning that each measured quantity y_i depends linearly on the model parameters according to

$$y_i = K_{i1}x_1 + K_{i2}x_2 + \cdots + K_{i,n}x_n + c, \tag{5.2}$$

with c being some offset that needs to be eliminated by subtracting it from y_i prior to the inversion. In this case, $\mathbf{F}$ can be expressed as an $m \times n$ matrix $\mathbf{K}$ containing the derivatives of $\mathbf{F}(\mathbf{x})$,

$$K_{ij} = \frac{\partial F_i(\mathbf{x})}{\partial x_j} = \frac{\partial y_i}{\partial x_j}. \tag{5.3}$$

In inversion theory and within this study, $\mathbf{K}$ is referred to as the *weighting function matrix* or the *weighting functions* (WF). Equation 5.1 then becomes $\mathbf{y} \stackrel{!}{=} \mathbf{Kx}$ (with K being a quadratic matrix of full rank here, since we assume a well posed problem), hence, a set of $m = n$ linear equations and unknowns, which can be solved by multiplying both sides with the inverse of the model $\mathbf{K}^{-1}$ to obtain the solution $\hat{\mathbf{x}} = \mathbf{K^{-1}y}$. However, in general things are more complicated:

1. $\hat{\mathbf{y}}$ is typically prone to measurement errors, which should be appropriately considered and propagated into the results.

2. The problem might be ill-posed in the sense that $\mathbf{K}$ is not invertible. While overconstrained problems are very common (consider a linear fit with two

unknowns to a large set of datapoints), it might on the other hand be underconstrained: an obvious case is, if there are less measurements than unknown parameters ($m < n$). But even with $m \geq n$, the measurements might be insensitive with respect to to distinct parameters x_i (lying in the nullspace of $\mathbf{K}$) or several x_i might be linearly dependent, such that $\text{rank}(\mathbf{K}) < n$. Note also that problems might be over- and underconstrained at the same time, depending on which x_i is regarded.

3. $\mathbf{F}(\mathbf{x})$ might be some complicated non-linear model (in the MAX-DOAS case it is a radiative transport model) and solutions need to be found iteratively.

It is common practice to apply least-squares methods to solve overconstrained problems. They can easily be implemented to also consider measurement errors and combining them with iterative approaches like the Gauss-Newton or the Levenberg-Marquardt method allows for solving non-linear problems.

One might argue that underconstrained problems can be avoided by choosing a suitable parametrisation. However, the amount of information on the individual parameters x_i in typical MAX-DOAS retrievals strongly depends on the atmospheric conditions. Therefore, it is not clear which x_i will actually be retrievable prior to the inversion. In such cases approaches like the optimal estimation inversion formalism (OEM) are desirable: its most notable strength is that it can handle potentially underconstrained problems, while simultaneously keeping track of the actual information on the individual x_i that are inferred from the measurements. A comprehensive description can be found in the book by Rodgers (2000).

5.1 Uncertainties

For our purposes, any uncertainties (in the measurement as well as in the state space) are assumed to be adequately described by a Gaussian probability density function (PDF). This is typically not ideal but is well justified as a trade-off between an accurate description of the problem and computational performance. The uncertainty of a scalar quantity z is then simply characterised by the variance σ^2. Equivalently, the uncertainty of a vector $\mathbf{z}$ in a multidimensional space is characterised by its covariance matrix $\mathbf{S}$, generally defined as

$$S_{ij} = \langle (z_i - \bar{z}_i)(z_j - \bar{z}_j) \rangle, \tag{5.4}$$

with $\langle\rangle$ being the expected value operator and $\bar{z} = \langle z \rangle$. Its diagonal elemnts contain the variances of each z_i; the off-diagonal elements describe potential correlations between them. The Gaussian PDF for the scalar case is

$$P(z) = \frac{1}{\sqrt{2\pi}\sigma} \exp\left[-\frac{(z - \bar{z})^2}{2\sigma^2} \right], \tag{5.5}$$

where $\bar{z}$ indicates the mean value, while for the multivariate case it is

$$P(\mathbf{z}) = \frac{1}{(2\pi)^{n/2}|\mathbf{S}|} \exp\left[-\frac{1}{2}(\mathbf{z} - \bar{\mathbf{z}})^T \mathbf{S^{-1}} (\mathbf{z} - \bar{\mathbf{z}}) \right] \tag{5.6}$$

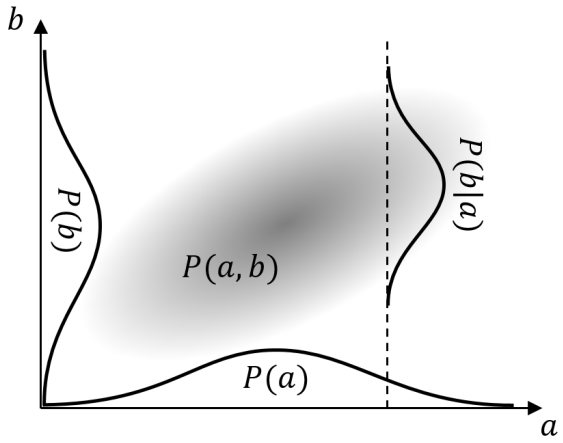

Figure 5.1: Illustration of Bayes' theorem assuming Gaussian PDFs (adapted from Rodgers (2000)).

Just as $\mathbf{S}$ and σ^2 describe uncertainties, their inverses $\mathbf{S}^{-1}$ and $1/\sigma^2$ can be regarded as measures for the knowledge about a quantity. The inverses play a crucial role in OEM and will in the following be referred to as *knowledge* or *precision* matrices.

5.2 A priori knowledge

It is often ignored that, even before performing any measurement, the space of possible solutions can mostly be confined on the basis of experience (former measurements, climatologies, models and other sources of information). In the OEM formalism, such knowledge is referred to as *a priori* and its assimilation into the inversion is the game changer regarding underconstrained problems. It is described by a PDF in state space, in the Gaussian case characterised by the *a priori state vector* $\mathbf{x_a}$ and associated covariance $\mathbf{S_a}$. As we shall see below, $\mathbf{x_a}$ might be considered as a set of "backup values" for each parameter that the retrieval resorts to if too little information is contained in the measurements.

5.3 Bayes' theorem

Bayes' theorem is an important prerequisite in OEM for the correct propagation of uncertainties into the final result. It allows to identify the class of possible states and their PDFs, considering all available information. Note that Bayes' theorem is generally valid for arbitrary PDFs even though in this study it is only applied to Gaussian PDFs. Let's consider a two-dimensional PDF $P(a, b)$ describing the uncertainty of a vector (a, b) as illustrated in Figure 5.1. Let $P(a)$ be the PDF of a, i.e. $P(a, b)$ integrated over all values of b, and let $P(b)$ be its equivalent for b. It

can be shown that the conditional PDF of a for a given value of b is

$$P(a|b) = P(a,b)/P(a), \tag{5.7}$$

and likewise for $P(b|a)$. Bayes' theorem brings the two conditional PDFs into relation according to

$$\boxed{P(a|b) = \frac{P(b|a)P(a)}{P(b)}.} \tag{5.8}$$

Note that $P(a)$ in Eq. 5.7 and $P(b)$ in Eq. 5.8 are only normalising factors and can be omitted for our purposes. In general, a and b might be vectors, making Eq. 5.8 applicable also to problems of higher dimensions as they are discussed in the following.

5.4 Solution of linear problems

As introduced above, the basic quantities to start from are:

- The measurements, represented by a Gaussian PDF $P_y(\mathbf{y})$ in measurement space, with the observed values $\hat{\mathbf{y}}$ as mean value and the measurement uncertainties $\mathbf{S_y}$ as covariance.
- A priori knowledge, represented by a Gaussian PDF $P_a(\mathbf{x})$ in state space with mean value $\mathbf{x_a}$ and covariance $\mathbf{S_a}$.
- A forward model $\mathbf{F}(\mathbf{x})$, mapping an arbitrary point in state space into measurement space. In the linear case, $\mathbf{F}$ can be expressed in terms of the weighting function matrix $\mathbf{K}$.

The first step is to find the PDF $P(\mathbf{x}|\hat{\mathbf{y}})$ of solution states, evolving from $P_a(\mathbf{x})$, given the measurements $\hat{\mathbf{y}}$. Following Eq. 5.6 for the multivariate Gaussian distribution, the a priori PDF is given by

$$-2\ln P_a(\mathbf{x}) = (\mathbf{x}-\mathbf{x_a})^T\mathbf{S_a^{-1}}(\mathbf{x}-\mathbf{x_a}), \tag{5.9}$$

and likewise

$$-2\ln P_y(\mathbf{y}) = (\mathbf{y}-\hat{\mathbf{y}})^T\mathbf{S_y^{-1}}(\mathbf{y}-\hat{\mathbf{y}}). \tag{5.10}$$

We omitted the normalising factor $(2\pi)^{n/2}|\mathbf{S}|$, as it is not of relevance for the actual optimisation. In the case of a given value for $\mathbf{x}$, the corresponding PDF $P_y(\mathbf{y}|\mathbf{x})$ in measurement space is given by

$$-2\ln P_y(\mathbf{y}|\mathbf{x}) = (\mathbf{y}-\mathbf{K}\mathbf{x})^T\mathbf{S_y^{-1}}(\mathbf{y}-\mathbf{K}\mathbf{x}). \tag{5.11}$$

Inserting these into Bayes theorem (Eq. 5.8) and setting $\mathbf{y} = \hat{\mathbf{y}}$ yields the desired PDF

$$-2\ln P(\mathbf{x}|\hat{\mathbf{y}}) = (\hat{\mathbf{y}} - \mathbf{K}\mathbf{x})^T \mathbf{S}_y^{-1} (\hat{\mathbf{y}} - \mathbf{K}\mathbf{x}) + (\mathbf{x} - \mathbf{x_a})^T \mathbf{S}_a^{-1} (\mathbf{x} - \mathbf{x_a}) =: \chi^2, \quad (5.12)$$

which is again a Gaussian distribution. The r.h.s. is simultaneously the cost function of the problem, with the first term punishing deviations between modelled and actual measurements and the second term punishing deviations of the state from the a priori. Minimising χ^2 w.r.t $\mathbf{x}$ yields the most probable state $\hat{\mathbf{x}}$ that we define to be the solution of the inversion (generally for non-Gaussian PDFs, the solution may be defined differently, e.g. as the median or the expected value of $P(\mathbf{x}|\hat{\mathbf{y}})$). $\hat{\mathbf{x}}$ is easy to find here, since Eq. 5.12 can be rewritten as

$$-2\ln P(\mathbf{x}|\hat{\mathbf{y}}) = (\mathbf{x} - \hat{\mathbf{x}})^T \hat{\mathbf{S}}^{-1} (\mathbf{x} - \hat{\mathbf{x}}), \quad (5.13)$$

with the mean

$$\boxed{\hat{\mathbf{x}} = (\mathbf{K}^T \mathbf{S}_y^{-1} \mathbf{K} + \mathbf{S}_a^{-1})^{-1} (\mathbf{K}^T \mathbf{S}_y^{-1} \hat{\mathbf{y}} + \mathbf{S_a}^{-1} \mathbf{x_a})} \quad (5.14)$$

being the solution and the covariance

$$\boxed{\hat{\mathbf{S}} = (\mathbf{K}^T \mathbf{S_y}^{-1} \mathbf{K} + \mathbf{S_a}^{-1})^{-1}} \quad (5.15)$$

describing its uncertainty. At first glance, Eq. 5.14 looks bulky, but it can be interpreted in a simple manner: recalling that $\mathbf{K}$ is only required to transform measurement space quantities into state space, Eq. 5.14 turns out to be a knowledge-weighted arithmetic mean of a priori and measurements. The second bracket represents a weighted sum of $\mathbf{x_a}$ and $\hat{\mathbf{y}}$ while the first bracket is the corresponding normalisation factor. Figure 5.2 illustrates all important quantities and their interaction for an explicit example with $m = n = 2$, i.e. two parameters being retrieved from two measurements. Using the forward model, the measurement PDF (blue) can be transformed from measurement space into state space, to derive the solution PDF (orange) considering the a priori knowledge (green) according to Eq. 5.14. In this particular example, the measurements are very sensitive to x_1, but not to x_2 (see second column of $\mathbf{K}$). Consequently, $\hat{x}_1$ is dominated by the measurement and $\hat{x}_2$ by the a priori term. Note that $\mathbf{K}^{-1}\mathbf{y}$ and $(\mathbf{K}^T \mathbf{S_y}^{-1} \mathbf{K})^{-1}$ are shown here for explanatory reasons. In fact $\mathbf{K}$ is not necessarily invertible for arbitrary problems and this is also not required for the calculation of the final result $\hat{\mathbf{x}}$ (see Eq. 5.14 and Eq. 5.15).

It is further instructive to consider the scalar case ($m = n = 1$): then, $\hat{\mathbf{y}}$ becomes a single measurement $\hat{y}$ whose uncertainty is described by its variance σ_y^2 instead of $\mathbf{S_y}$. Likewise, $\mathbf{x_a}$ becomes a single parameter a priori value x_a with variance σ_a^2 and $\mathbf{K}$ becomes a single derivative $\partial y / \partial x$. We can further define

$$\hat{y}' = \frac{\partial x}{\partial y} \hat{y} \quad \text{and} \quad \sigma_y' = \frac{\partial x}{\partial y} \sigma_y \quad (5.16)$$

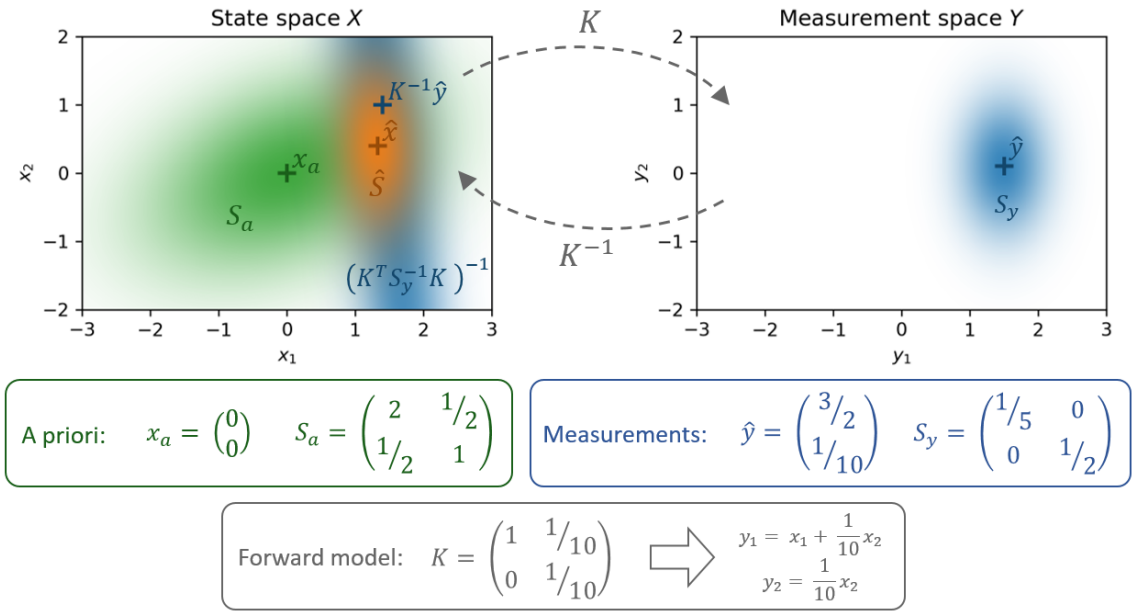

Figure 5.2: Example of a linear problem with two parameters (in a 2D state space on the left) being retrieved from two measurements (in the 2D measurement space on the right), assuming Gaussian PDFs. The PDFs are depicted here as blurred ellipses with their mean values indicated by cross markers. The a priori, measurement and solution PDFs are depicted in green, blue and orange, respectively. For the detailed description and interpretation, see main text.

being the measurement and its error, each transformed into state space. Eq. 5.14 then becomes the familiar weighted arithmetic mean between two quantities with associated uncertainties:

$$\hat{x} = \frac{\sigma_y'^{-2}\hat{y}' + \sigma_a^{-2}x_a}{\sigma_y'^{-2} + \sigma_a^{-2}}, \tag{5.17}$$

and Eq. 5.15 becomes

$$\frac{1}{\hat{\sigma}^2} = \frac{1}{\sigma_y'^2} + \frac{1}{\sigma_a^2}. \tag{5.18}$$

Equation 5.17 well reflects the boon and bane of the OEM formalism: even if lots of information on x is contained in the measurements ($\sigma_y' \ll \sigma_a$), the result $\hat{x}$ will approach $\hat{y}'$ but always remain biased towards the a priori. On the other hand, if either measurement errors are large ($\sigma_y \to \infty$) or the measurement is insensitive towards the desired parameter ($\partial y/\partial x \to 0$), $\hat{x}$ approaches x_a. Hence, in the case of an ill-posed problem, with little information on x contained in the measurements, the retrieval resorts back to a reasonable a priori value and remains stable, whereas in the case of algorithms not using any a priori information, $\hat{x}$ would be dominated by measurement noise and diverge. It is therefore important to inspect the amount of information that the measurements provide for each parameter as discussed in the following.

5.5 Quantification of information content

Once we have calculated the solution $\hat{\mathbf{x}}$, it is not yet clear to what extent each parameter $\hat{x}_i$ is either dominated by a priori or measurement information. $\hat{\mathbf{x}}$ should therefore only be regarded in conjunction with a measure for the amount of information on each $\hat{x}_i$ that could be inferred from the measurement. In OEM, such a measure is the *averaging kernel matrix* (AVK), defined as

$$\boxed{\mathbf{A} = \frac{\partial \hat{\mathbf{x}}}{\partial \mathbf{x}} = (\mathbf{K}^T \mathbf{S_y}^{-1} \mathbf{K} + \mathbf{S_a}^{-1})^{-1} \mathbf{K}^T \mathbf{S_y}^{-1} \mathbf{K}} \tag{5.19}$$

The first representation of $\mathbf{A}$, in terms of a partial derivative, provides immediate insight into the general concept. On the diagonal $A_{ii} = \partial \hat{x}_i / \partial x_i$ we obtain the sensitivity of each retrieved parameter value $\hat{x}_i$ to changes in its real value x_i. If little information was retrieved from the measurements, $\hat{x}_i$ is dominated by the constant a priori term in Eq. 5.14 and A_{ii} will be close to zero. On the other hand, if $\hat{x}_i$ strongly depends on the measurements, it will follow any change of x_i and A_{ii} will be close to one. In fact, A_{ii} are values between zero and one indicating the relative amount of information gained from the measurements in relation to the a priori knowledge. The trace of A is often referred to as the *degrees of freedom of signal* (DOFS), which play a crucial role throughout this thesis. The off-diagonal entries

A_{ij} $(i \neq j)$ contain information on the cross-sensitivity of x_i to all other parameters x_j. They are particularly useful if discretised quantities are retrieved (e.g. vertical concentration profiles, represented in the state vector as a finite number of concentrations at different altitudes), as they provide information on the achieved vertical resolution. The second representation of $\mathbf{A}$ in Eq. 5.19 allows for another perception of $\mathbf{A}$. It is easy to see here that $\mathbf{A}$ is a sort of ratio of the measurement knowledge transformed into state space $\mathbf{K}^T{\mathbf{S_y}}^{-1}\mathbf{K}$, over the total knowledge $\mathbf{K}^T{\mathbf{S_y}}^{-1}\mathbf{K}+{\mathbf{S_a}}^{-1}$. This can again be well illustrated by the scalar case, with the same conventions as introduced in Section 5.4. The averaging kernel for our lonely parameter x is then given by

$$A = \frac{\sigma_y'^{-2}}{\sigma_y'^{-2} + \sigma_a^{-2}}. \tag{5.20}$$

In the ideal case of a retrieval achieving full sensitivity with respect to all parameters and no remaining correlations it is $\mathbf{A} = \mathbf{1}$. Related relevant quantities in this context are the sensitivity of $\hat{\mathbf{x}}$ to the a priori

$$\mathbf{A}_a = \frac{\partial \hat{\mathbf{x}}}{\partial \mathbf{x}_a} = \mathbf{1} - \mathbf{A} \tag{5.21}$$

and the *gain matrix*

$$\mathbf{G} = \frac{\partial \hat{\mathbf{x}}}{\partial \mathbf{y}} = (\mathbf{K}^T\mathbf{S}_y^{-1}\mathbf{K} + \mathbf{S}_a^{-1})^{-1}\mathbf{K}^T\mathbf{S}_y^{-1} \tag{5.22}$$

providing the sensitivity of $\hat{\mathbf{x}}$ to the measurements.

AVKs can also be considered as the *glasses* of a retrieval. They contain all required information to predict how a retrieval will perceive a given true state $\mathbf{x}_t$, considering its limited sensitivity and resolving capabilities. The perceived state is given by

$$\tilde{\mathbf{x}} = \mathbf{A}\mathbf{x}_t + \mathbf{A}_a\mathbf{x}_a = \mathbf{x}_a + \mathbf{A}(\mathbf{x}_t - \mathbf{x}_a) \tag{5.23}$$

This process plays an important role for the direct comparison of measurement techniques with different AVKs (see e.g. Section 16) and is in OEM terminology referred to as "smoothing", even though Equation 5.23 provokes much more than a simple smoothing of $\mathbf{x}_t$. We therefore instead use the term "convolution", which we think is conceptionally closer to the actual nature of the process.

5.6 Error components

The retrieval covariance $\hat{\mathbf{S}}$ can be subdivided into a *noise error* $\mathbf{S}_m$ and a *smoothing error* $\mathbf{S}_s$ contribution. The noise error covariance is obtained using the gain matrix to propagate the measurement noise into state space:

$$\mathbf{S}_m = \mathbf{G}\mathbf{S}_y\mathbf{G}^T \tag{5.24}$$

Smoothing errors are those deviations that arise because $\hat{\mathbf{x}}$ will always be a *smoothed* version of the true state $\mathbf{x}_t$ (see Eq. 5.23). Typically, they cannot be calculated since $\mathbf{x}_t$ is not known. However, they can be estimated according to

$$\mathbf{S}_s = \mathbf{A}_a \mathbf{S}_a \mathbf{A}_a^T \tag{5.25}$$

under the assumption that the retrieved state is close to the true state.

5.7 Solution of non-linear problems

The typical MAX-DOAS inversion belongs to the class of *moderately non-linear* problems: the forward radiative transport model is non-linear but a smooth function of the atmospheric state parameters, and it is adequate to linearise $\mathbf{F}$ around $\hat{\mathbf{x}}$ for the error analysis once the solution $\hat{\mathbf{x}}$ has been found.

As in the linear case, $\hat{\mathbf{x}}$ can be found by minimising the cost function χ^2 (Eq. 5.12), this time however for a general forward model $\mathbf{F}$ instead of $\mathbf{K}$. We need to find the state that satisfies

$$\nabla_{\mathbf{x}}(-2 \ln P(\mathbf{x}|\hat{\mathbf{y}})) = -\mathbf{K}^T(\mathbf{x})\mathbf{S}_y^{-1}(\hat{\mathbf{y}} - \mathbf{F}(\mathbf{x})) + \mathbf{S}_a^{-1}(\mathbf{x} - \mathbf{x}_a) \stackrel{!}{=} 0. \tag{5.26}$$

A common approach for problems of this kind is to apply *Newtonian iteration*: the zero point of a vector-valued function $\mathbf{g}(\mathbf{x})$ can be found by iterating over $\mathbf{x}$ according to

$$\mathbf{x}_{i+1} = \mathbf{x}_i - (\nabla_{\mathbf{x}}\mathbf{g}(\mathbf{x}_i))^{-1}\ \mathbf{g}(\mathbf{x}_i). \tag{5.27}$$

Inserting Eq. 5.26 as $\mathbf{g}(\mathbf{x})$ yields

$$\nabla_{\mathbf{x}}\mathbf{g}(\mathbf{x}_i) = \mathbf{K}^T\mathbf{S}_y^{-1}\mathbf{K} + \mathbf{S}_a^{-1} - (\nabla_{\mathbf{x}}\mathbf{K}^T)\mathbf{S}_y^{-1}(\hat{\mathbf{y}} - \mathbf{F}(\mathbf{x})). \tag{5.28}$$

It contains the second derivative $\nabla_{\mathbf{x}}\mathbf{K}^T$ of the forward model, which is expensive to compute. Fortunately, it is small in the case of moderately linear problems and can be omitted to obtain the *Gauss-Newton* method. Inserting it into Eq. 5.27 yields the iteration scheme:

$$\mathbf{x}_{i+1} = \mathbf{x}_i + (\mathbf{K}_i^T\mathbf{S}_y^{-1}\mathbf{K}_i + \mathbf{S}_a^{-1})^{-1}\left[\mathbf{K}_i^T\mathbf{S}_y^{-1}(\hat{\mathbf{y}} - \mathbf{F}(\mathbf{x}_i)) - \mathbf{S}_a^{-1}(\mathbf{x}_i - \mathbf{x}_a)\right] \tag{5.29}$$

Levenberg (1944) and Marquardt (1963) found that the convergence can be improved if a factor $(1+\gamma)$ is introduced in the first bracket, effectively reducing the iteration step size. This yields the iteration scheme applied for our purposes:

$$\boxed{\mathbf{x}_{i+1} = \mathbf{x}_i + (\mathbf{K}_i^T\mathbf{S}_y^{-1}\mathbf{K}_i + (1+\gamma)\mathbf{S}_a^{-1})^{-1}\left[\mathbf{K}_i^T\mathbf{S}_y^{-1}(\hat{\mathbf{y}} - \mathbf{F}(\mathbf{x}_i)) - \mathbf{S}_a^{-1}(\mathbf{x}_i - \mathbf{x}_a)\right]} \tag{5.30}$$

One has to provide a *first guess* $\mathbf{x}_0$: for our purposes we choose $\mathbf{x}_0 = \mathbf{x}_a$, but generally $\mathbf{x}_0$ might be chosen differently. In fact, it is a common mistake by less

experienced users to confuse *a priori* (as a crucial part of the cost function) and *first guess* (the starting point for the iteration).

There are several methods to test for convergence of the iteration. For our purposes we consider the retrieval to have converged if either the relative decrease in the cost function

$$D^2 = \frac{|\chi^2_{i+1} - \chi^2_i|}{\chi^2_i} \tag{5.31}$$

or the normalised step size in $\mathbf{x}$

$$d^2 = \frac{1}{n}(\mathbf{x}_i - \mathbf{x}_{i+1})^T \hat{\mathbf{S}}^{-1}(\mathbf{x}_i - \mathbf{x}_{i+1}) \tag{5.32}$$

fall below a given threshold.

For the error and information content analysis, the same equations as for the linearised problem can be applied.

6 Polarisation of skylight

The polarisation of skylight has been investigated for over 200 years, starting with its discovery 1811 by Francois Arago. However, its usefulness for remote sensing of atmospheric constituents was very limited until accurate mathematical descriptions and solutions of the atmospheric radiative transport problem were developed, among others by Ambartsumian (1942) and Chandrasekhar (1947). In fact, particularly the modelling of skylight polarisation and its dependence on the atmospheric state is still an active field of research. This chapter provides a qualitative overview on the main features of skylight polarisation.

6.1 Useful equations

For qualitative considerations of skylight polarisation we introduce a few useful equations. Consider a ground-based narrow FOV optical instrument observing the sky at viewing elevation angle α, relative azimuth angle ϕ and solar zenith angle θ, as sketched in Figure 6.1. Then, the single scattering angle Θ_{ss}, which is the angle between the direct solar beam and the instrument line of sight (LOS), is given by

$$\cos\Theta_{ss} = \sin\theta\cos\alpha\,(\cos\phi + \sin\phi) + \cos\theta\sin\alpha. \tag{6.1}$$

Further, for a prediction of the approximate angle of maximum polarisation χ (see Eq. 3.25), it is useful to introduce an equation for the angle θ', under which the Sun illuminates the FOV-plane (see Figure 6.1). It is given counterclockwise in the instrument viewing direction and with respect to the horizontal. The FOV-plane is perpendicular to the instrument LOS. It is

$$\tan\theta' = \frac{\sin\alpha\cos\phi\sin\theta - \cos\alpha\cos\theta}{\sin\phi\sin\theta}. \tag{6.2}$$

Assuming a pure Rayleigh atmosphere and single scattering only, the expected orientation of the polarisation can be directly inferred according to

$$\chi = \theta' + 90°. \tag{6.3}$$

In many cases this is very close to reality (see Section 6.2).

As we will see later, the information content in polarisation can be enhanced for a given set of elevation angles, by choosing RAAs such that the DOLP in the resulting direction will be large. It is therefore useful, e.g. for the real-time optimisation of measurement geometries in the field, to have an equation for the RAA ϕ_{90} that

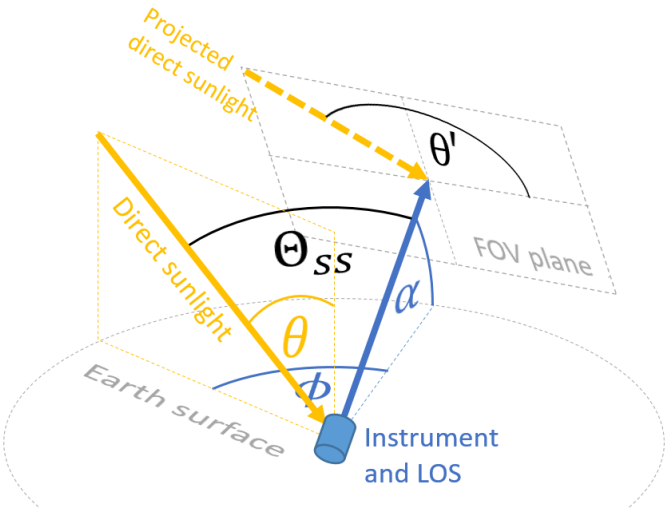

Figure 6.1: Illustration of the angles that define the viewing geometry. Further, the *FOV-plane* (perpendicular to the instrument LOS), θ' and the single scattering angle Θ_{ss} are indicated.

enforces a single scattering angle as close to 90° as possible. For given SZA and EA, it is

$$\phi_{90} = \begin{cases} \arccos\left(-\frac{\tan\alpha}{\tan\theta}\right), & \text{if } \alpha < \theta \\ 180°, & \text{if } \alpha \geq \theta \end{cases} \tag{6.4}$$

6.2 Angular dependence of skylight polarisation

The angular dependence of skylight polarisation on clear sky days is mostly driven by Rayleigh scattering on molecules. According to the scattering properties introduced in Section 3.3.2, in a pure Rayleigh atmosphere considering single scattering only, one would expect a DOLP of unity at scattering angles of 90° and an orientation of polarisation χ perpendicular to the incident angle of the Sun into the observer's FOV according to Eq. 6.3. In the real atmosphere this approximation holds quiet well at least regarding the position of the DOLP maximum and χ. However, multiple scattering and reflections from the ground induce deviations from this simplified model even in the absence of aerosols.

Comprehensive investigations on the polarisation patterns of skylight have been conducted by Emde et al. (2010). Figure 6.2 shows - among others - full radiative transport simulation results for a Rayleigh atmosphere. The first thing to note is that the maximum DOLP significantly differs from unity. The impact of multiple scattering on the polarisation orientation χ and the angular position of the maximum DOLP are not visible in Figure 6.2. We investigated both using the RAPSODI forward model (see Section 7). The shift in the position of the DOLP-maximum due to multiple scattering is investigated in Figure 6.3: it shows that for full RT-simulations

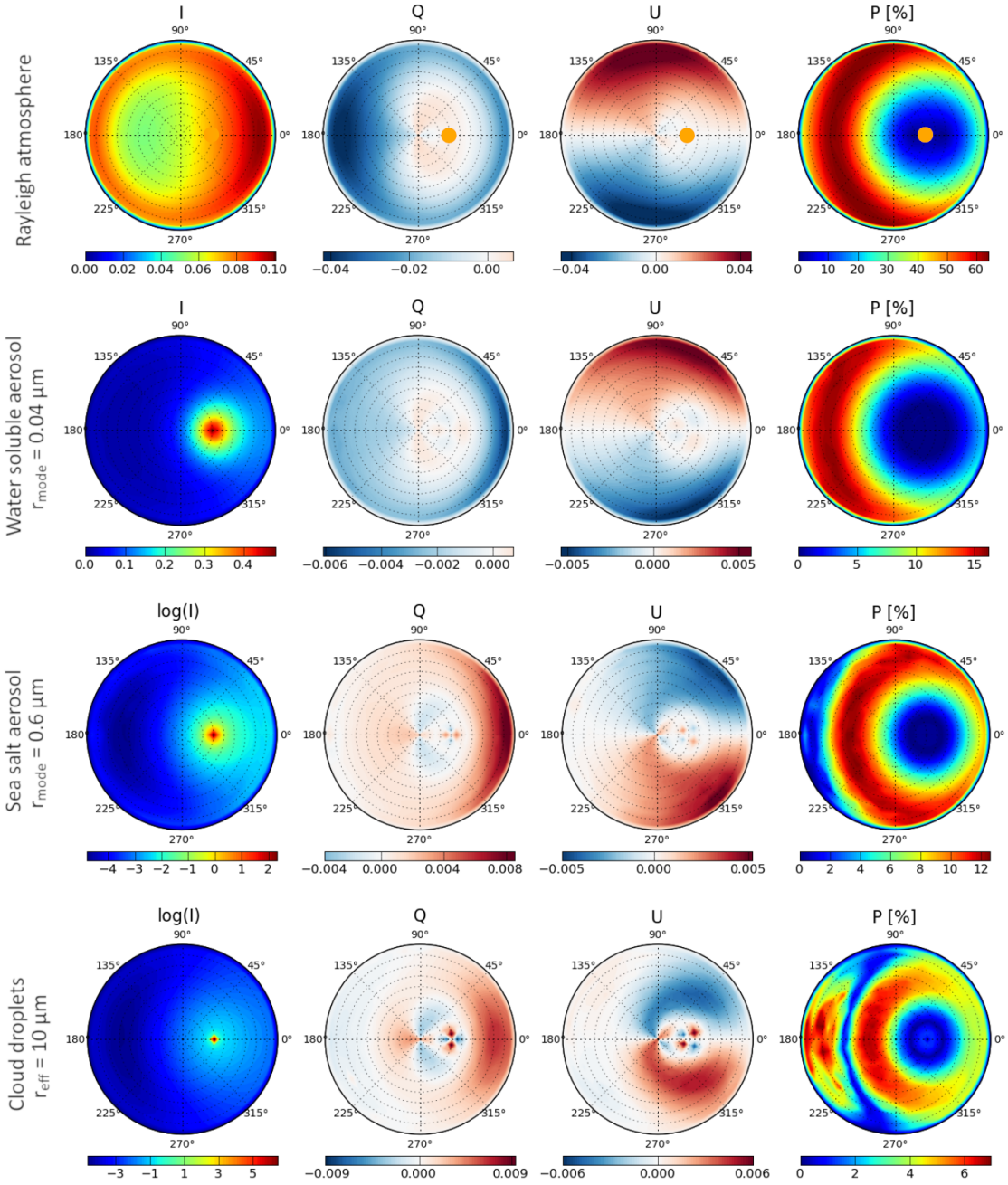

Figure 6.2: Skylight polarisation patterns (Stokes parameters, normalised to extraterrestrial irradiance and DOLP) produced by four different atmospheric constituents at 350 nm and SZA = 30°. Top row shows a pure Rayleigh atmosphere, remaining rows include aerosol only. The figure was adapted from Emde et al. (2010), the reader is referred to the original publication for further details.

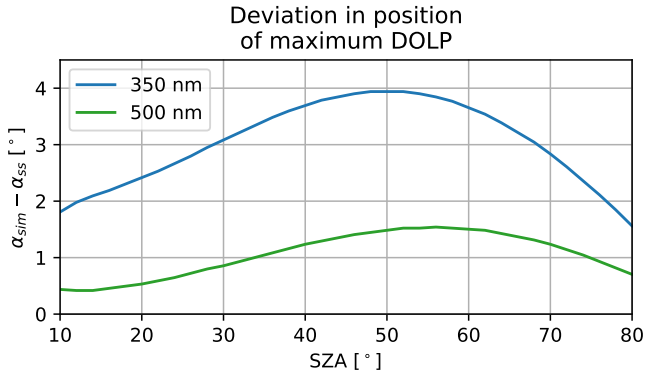

Figure 6.3: Angular position of the DOLP-amximum in the sky, described in terms EAs α in the solar principle plane (RAA of $\phi = 180°$). Compared are the position α_{ss}, expected from single scattering considerations and the "real" position α_{sim}, derived from RT-simulations.

(Rayleigh atmosphere with surface albedo of zero), the position of maximum DOLP in the solar principle plane can differ from the single-scattering approximation by several degrees in viewing elevation. The impact of multiple scattering on the polarisation orientation χ is illustrated in Figure 6.4. The simulated χ values strongly differ from what one would expect from single scattering considerations, particularly at small single scattering and viewing elevation angles. Qualitatively speaking, the Earth surface "cuts away" parts of the multiple scattering field. For low elevations and large SZAs at RAA $\phi = 0°$ for instance, the consequence is that predominantly vertically polarised multiple scattered light reaches the observer, outweighing the horizontally polarised single scattered light and ultimately leading to a rotation in χ by 90°. Among others, this effect leads to the phenomenon of unpolarised spots in the sky radiance, the so-called "neutral points" (Horváth and Varjú, 2004). In general, multiple scattering gains impact towards shorter wavelengths, where the atmospheric OT increases. In the real atmosphere, also aerosol has to be taken into account. As expected from the aerosol scattering properties in Section 3.3.3 and as shown in Figure 6.2, the polarisation patterns caused by different aerosol types can be very different, but they are also considerably weaker in magnitude (regarding the DOLP) than the Rayleigh scattering pattern. In very first approximation, the presence of aerosol therefore can be considered to decrease the overall DOLP of skylight. However, in scenarios with high aerosol load the DOLP pattern can also be significantly distorted (see e.g. Boesche et al., 2006).

For completeness we simulated the skylight polarisation patterns for the standard mixed aerosol case introduced in Section 3.3.3, which is assumed for several investigations performed in this thesis. The simulations were performed using the RAPSODI forward model, the results are shown in Figure 6.5.

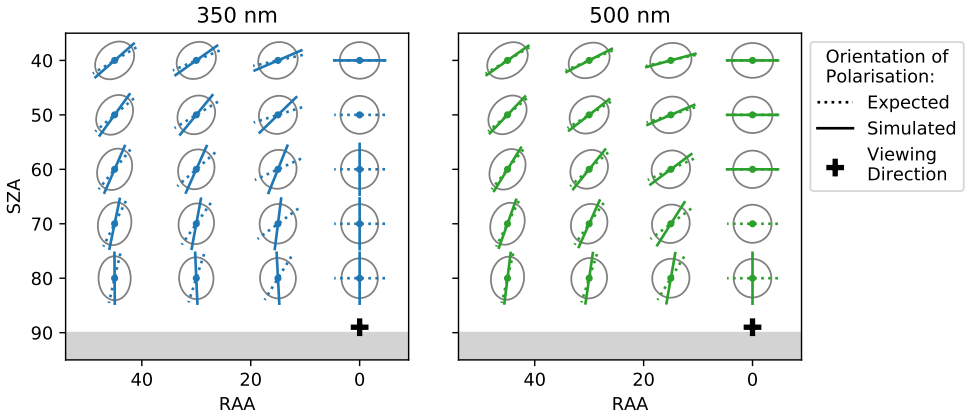

Figure 6.4: The polarisation orientation χ in a Rayleigh atmosphere for a viewing elevation angle of 1°. Each symbol represents a solar geometry and indicates χ as expected from single scattering considerations (dotted) and χ as obtained from RT-simulations (solid).

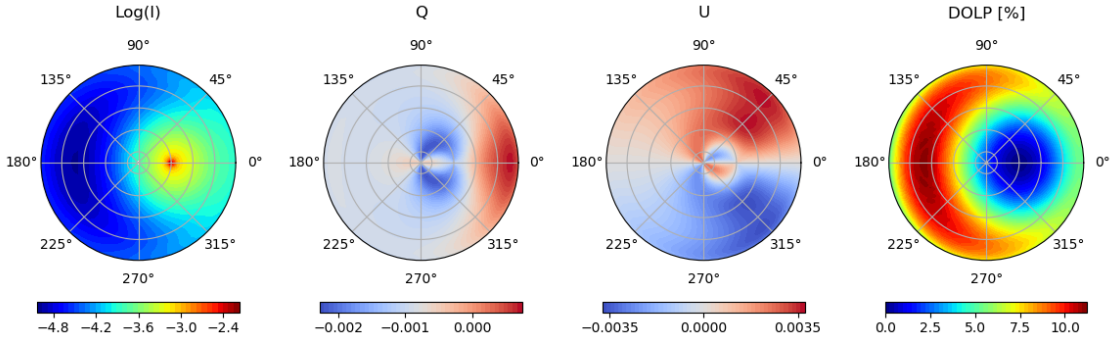

Figure 6.5: Skylight polarisation patterns, produced by the bi-modal Mie-aerosol introduced in Section 3.3.3. Rayleigh scattering was not considered here. An exponential profile with 1 km scale height and AOT of 0.4 was assumed. The figure is similar to Figure 6.2

6.3 Spectral dependence of skylight polarisation

A good overview on the spectral dependence of skylight polarisation including the fine-structure (variations on the nm-scale) is provided by Aben et al. (1999) and references therein. For a qualitative discussion of the relevant mechanisms, we consult two DOLP spectra here, recorded with the PMAX-DOAS instrument (see Section 11) under nearly the same geometries but on two clear sky days with different aerosol conditions. The spectra are shown in Figure 6.6. A typical broadband spectral feature is the decrease in DOLP towards the UV due to the increasing impact of Rayleigh multiple scattering. when going to larger wavelengths (exceeding the wavelength range covered by Figure 6.6) the DOLP typically reaches a maximum, before decreasing again since less polarising aerosol scattering prevails over strongly polarising Rayleigh single scattering. However, as indicated in the figure, the exact shape and magnitude of broadband DOLP strongly depends on aerosol properties and also on the viewing geometry (see e.g. Xu and Wang, 2015, for detailed investigations).

The spectral fine-structure is dominated by two effects, namely inelastic Raman scattering and strong trace gas absorption. Raman scattering is strongly depolarising (see Section 3.3.2) and the spectral shift therefore causes a "filling-in" of Fraunhofer lines with nearly unpolarised light, ultimately resulting in DOLP variations coinciding with the peaks and dips in the solar spectrum (Aben et al., 1999). This is best visible in Figure 6.6 in the case of the strong calcium lines around 390 nm. At wavelengths of strong trace gas absorption, short light paths through the atmosphere are favoured. Whether this increases or decreases the DOLP depends on the viewing geometry and the vertical distribution of the absorber. In Figure 6.6, this effect is best visible close to 300 nm where the stratospheric ozone layer's optical thickness increases quickly towards the UV. During side studies we found that this effect makes polarimetric UV observations in a single viewing direction sensitive to the stratospheric ozone concentration. Further investigations in theis direction might be performed in the future. Another prominent example for strong trace gas absorption altering the spectral DOLP pattern is the oxygen A-band at about 760 nm (Preusker et al., 1995), which is however not shown in Figure 6.6.

6.4 Polarisation and effective light paths

While the Stokes parameter's and the DOLP's angular and spectral patterns and their dependencies on the atmospheric state have been extensively studied in former publications, very little attention has been paid to the fact that light of different SOPs arriving at the Earth's surface has taken different effective paths through the atmosphere. Polarimetric measurements therefore allow to access new light path geometries, which is an important aspect when aiming at the retrieval of spatial distributions of atmospheric constituents. A convenient concept for the description of effective light paths are airmass-factors (AMFs) A, as introduced in Section 4.4.

In the following, we present model simulations (performed with the RAPSODI

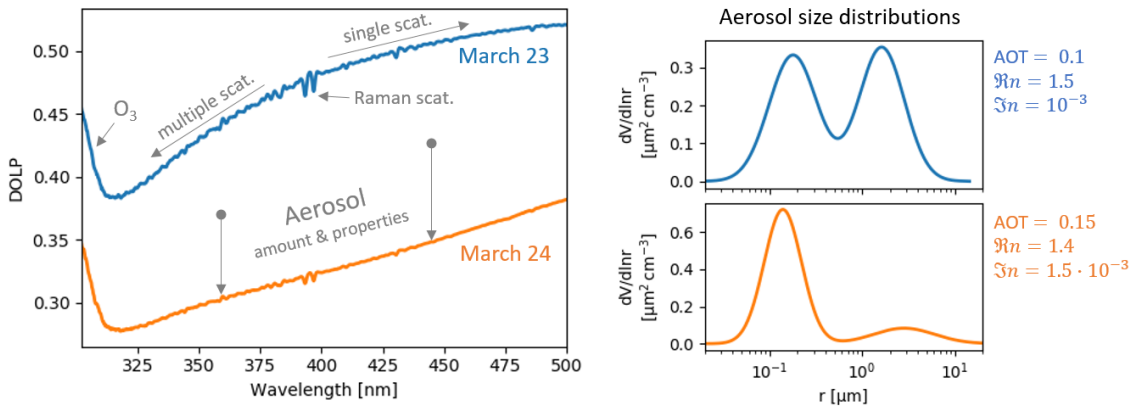

Figure 6.6: Left: Two DOLP spectra recorded by the PMAX-DOAS instrument (see Section 11) under similar geometries (SZA $\approx 60°$, RAA $\approx 90°$, EA $= 3°$) but on two clear sky days with different aerosol conditions. Right: coincident aerosol amount and properties as observed by the nearby Sun photometer (see Section 12.4.3).

forward model, see Section 7.4) providing some insight into the dependence of O_4 AMFs and BAMFs on the skylight polarisation. For convenience, we define the "AMF excentricity"

$$\epsilon = 2\frac{\max_\delta(A) - \min_\delta(A)}{\max_\delta(A) + \min_\delta(A)}, \tag{6.5}$$

quantifying the relative change in AMF that can be achieved with a polariser in a distinct viewing direction. δ is the polariser orientation and A are either AMFs or BAMFs. Figure 6.7 shows the AMF excentricities ϵ over the sky hemisphere. The sky patterns are similar to the DOLP, i.e. largest excentricities are primarily expected in directions of strong polarisation. However, in contrast to the DOLP, ϵ_{O_4} decreases significantly when leaving the solar principal plane and going to lower EAs, even if $\theta_{ss} \approx 90°$ (e.g. RAA $= 100°$, EA $= 10°$). ϵ is smaller for gases that are confined to low altitudes. Figure 6.8 shows the BAMFs in a viewing direction of particularly large O_4 AMF excentricity. It reveals that measurements at different polariser angles in first instance lead to a scaling of BAMF profiles but not to a significant change in their vertical shape. Accordingly, the effect of AMF excentricity is expected to improve sensitivity to trace gas and aerosol VCDs, but is to have minor impact on the vertical resolution of retrievals. On the other hand, the excentricity particularly in the Vis is strikingly large up to altitudes of ≈ 10 km. The retrieval of aerosol and trace gas VCDs from measurements in a single viewing direction might therefore be feasible. The dependence of the O_4 AMF on the polariser angle of the observing instrument is illustrated in the right panel of Figure 6.9 and exhibits a few remarkable features in comparison to the radiance angular pattern (shown in the left panel): (1) the O_4 AMF significantly differs from the sinusoidal radiance pattern, rather resembling a lemon than the familiar peanut. (2) The extrema of radiance and O_4 AMF patterns

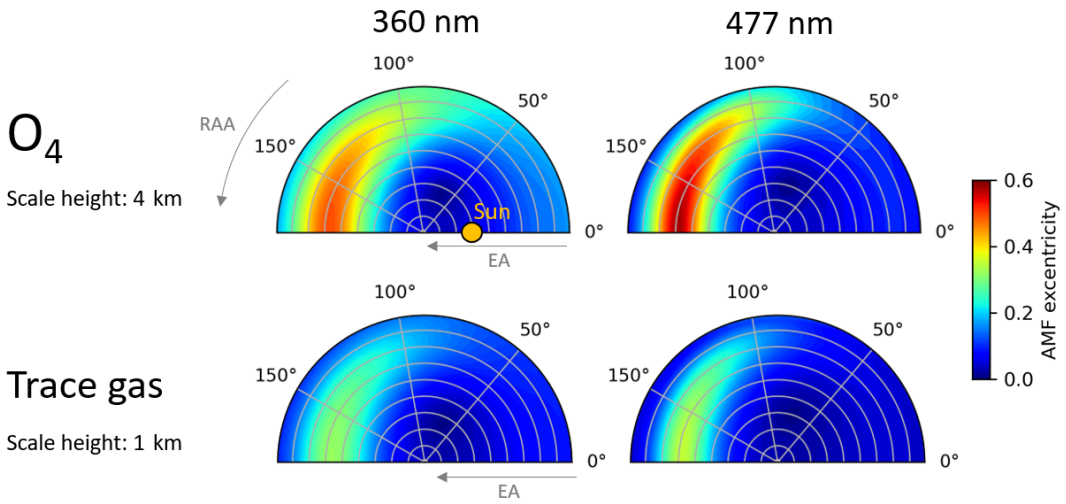

Figure 6.7: Excentricity of the AMF modeled over the sky hemisphere in a Rayleigh atmosphere in the two O_4 absorption wavelengths at 360 and 477 nm, respectively. Upper row show AMFs for O_4, bottom row shows AMFs for an arbitrary trace gas confined to lower altitudes (exponential profile with scale height of 1 km).

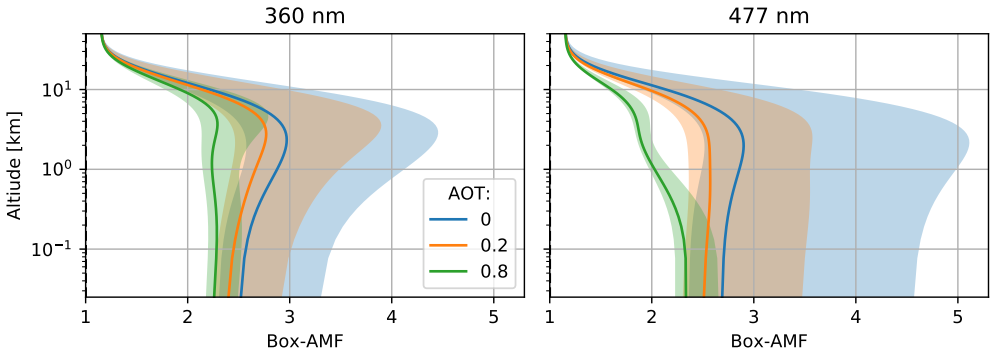

Figure 6.8: Box-AMFs at 360 and 477 nm, respectively, for different AOTs. We assume the Mie standard mixed aerosol introduced in Section 3.3.3. Lines show conventional "non-polarimetric" bAMFs, while shaded areas indicate the variation with polariser angle. The assumed geometry is RAA = 180°, SZA = 30° and EA = 30°, where these variations are particularly large (compare Figure 6.7).

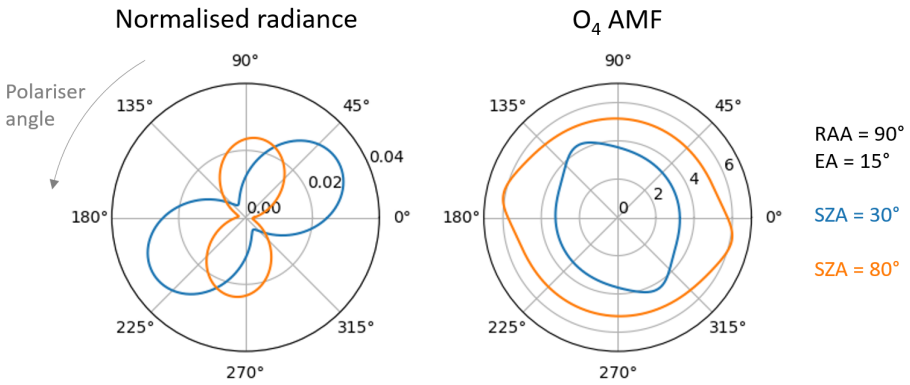

Figure 6.9: Dependence of radiance (left) and O_4 AMF (right) on the polariser angle of the observing instrument, simulated in a Rayleigh atmosphere at 477 nm.

appear at similar polariser angles but do not necessarily coincide. Depending on the surface albedo, viewing geometries and atmospheric state, deviations on the order of 10° are possible. Unfortunately, this effect is hardly visible in Figure 6.9. Finally, the dependence of the O_4 AMF on the AOT is investigated in Figure 6.10. Similar to the DOLP, the excentricity decreases with increasing AOT but the detailed shape of the decrease is quiet different. This indicates that DOLPs and ϵ_{O_4} carry similar but not equivalent information on the atmosphere's aerosol content.

The findings from the simulations are also well apparent in the field measurements presented in Section 15.1. Particularly the O_4 dSCDs recorded at different polarisation angles split up as predicted here.

6.5 Concluding remarks

From the precedent sections and the RT effects described Section 3, we obtain a first idea on the advantages of polarimetric MAX-DOAS measurements, which can be qualitatively summarised into two major aspects:

1. The SOP strongly depends on aerosol content and aerosol properties of the atmosphere. This is particularly the case regarding the magnitude and spectral dependence of the DOLP.

2. Light of different SOP has taken different effective light paths from TOA to the instrument. This allows to realise new light path geometries that are normally not "accessible" with conventional non-polarimetric MAX-DOAS observations.

Sensitivity studies and a thorough quantification of the increase in information are performed in Section 8.4 and 9.2, respectively.

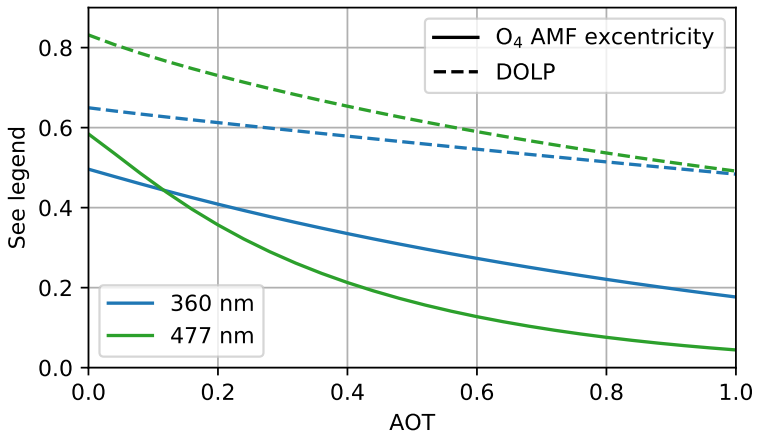

Figure 6.10: Dependence of the O_4 AMF excentricity (and DOLP, for comparison) on the aerosol optical thickness. The applied aerosol properties are defined in Table 3.2. The underlying geometry is SZA= 30°, RAA=180°, EA=30°.

7 The RAPSODI retrieval algorithm

7.1 Overview

A multitude of MAX-DOAS profile algorithms exist within the community (Irie et al., 2008; Clémer et al., 2010; Wang et al., 2013; Yilmaz, 2012; Bösch et al., 2018; Chan et al., 2019; Vlemmix et al., 2011; Beirle et al., 2019). Recently, efforts have been taken to compare and validate the results of the existing algorithms based on synthetic data (Frieß et al., 2019) and real measurements (Frieß et al., 2016; Tirpitz et al., 2020). The algorithms are based on different RTMs and inversion approaches (OEM, parametrised and others). They differ in the exact implementation but share the same simplifying assumptions in multiple aspects. To overcome some of the current limitations of MAX-DOAS retrieval algorithms, we developed the RAPSODI (Retrieval of Atmospheric Parameters from Spectroscopic Observations using DOAS Instruments) algorithm. Its notable features are:

1. It is the first MAX-DOAS retrieval algorithm capable of considering information from the polarisation state of skylight.

2. It is the first algorithm to simultaneously retrieve all species of interest in a shared model atmosphere, thereby considering and exploiting synergetic effects. In former algorithms, different species were retrieved in separate retrieval runs.

3. It is the first algorithm to retrieve information on aerosol microphysical properties (size distribution and complex refractive index) by making use of a Mie model that we coupled to the RTM. In former algorithms, information on aerosol properties were either prescribed or retrieved in terms of simplified optical parameters (Henyey-Greenstein approximation with single scattering albedo and asymmetry parameter as parameters).

4. It digests measurements from multiple wavelengths simultaneously. This allows to directly use information from the spectral dependence of dSCDs and spectral broadband features in terms of dSOTs. Only few of the former algorithms (e.g. HeiPRO Yilmaz, 2012) have similar functionalities implemented.

RAPSODI is fully backward compatible. Hence non-polarimetric monochromatic retrievals performed separately for aerosol and trace gases at a single wavelength are possible and the Mie model can be replaced by a Henyey-Greenstein approximation by setting corresponding flags in the retrieval configuration. The RAPSODI user

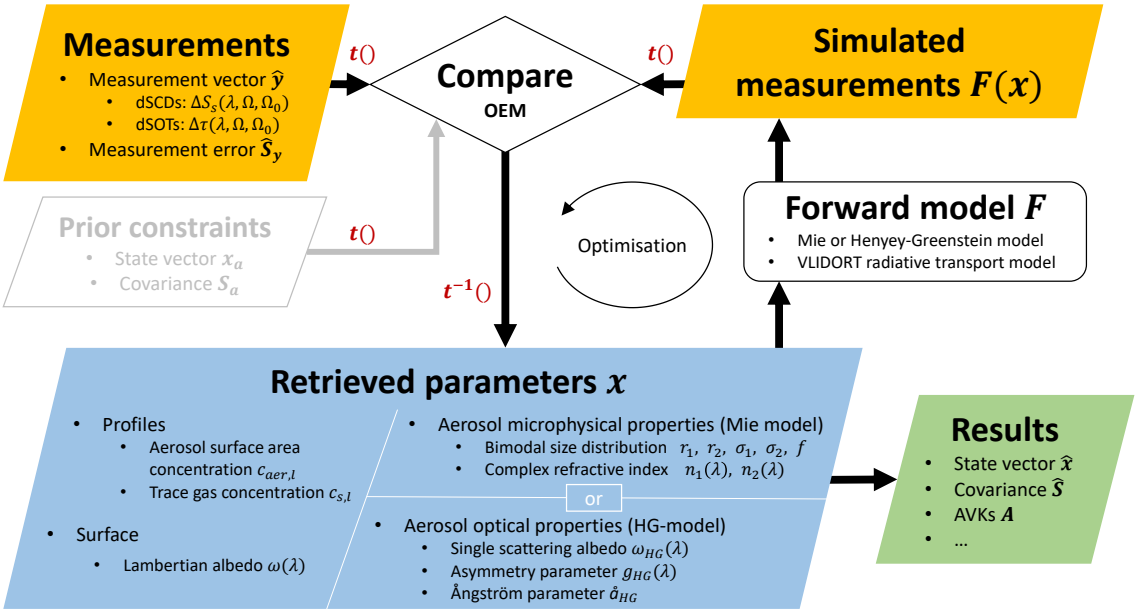

Figure 7.1: Schematic overview of the RAPSODI retrieval algorithm. OEM is used to iteratively optimise the parameters $\mathbf{x}$ to bring real and simulated measurements into closure. The individual components are discussed in detail in the following subsections. Red labels next to arrows indicate transformations to/from optimised units, as described in Section 7.5.

interface and main framework are implemented in Python and are planned to be published including a comprehensive documentation in the near future. The inversion scheme uses the optimal estimation formalism (OEM) described in Section 5. The forward model $\mathbf{F}$ is based on VLIDORT (details in Section 7.4). Figure 7.1 shows a schematic overview, with the individual components being discussed in detail in the following subsections.

7.2 The Measurement vector

The RAPSODI measurement vector $\mathbf{y}$ contains dSCDs $\Delta S_s(\lambda, \Omega, \Omega_0)$ and dSOTs $\Delta\tau(\lambda, \Omega, \Omega_0)$ for different trace gas species s (including O_4), viewing geometries $\Omega = \{\theta, \phi, \alpha, \delta\}$ (with θ, ϕ, α, δ being solar zenith angle (SZA), relative viewing azimuth angle (RAA), viewing elevation angle (EA) and the instrument's polariser angle (PA)), reference geometries Ω_0 and radiation wavelengths λ. SZA, RAA and EA define what in the following will be referred to as the "viewing direction". PAs describe the orientation of the polariser's transmitting axis with respect to the horizontal and increase clockwise when looking towards the instrument. The derivation of dSCDs and dSOTs from the raw spectra using the DOAS spectral analysis was already described in Section 4.2. DSCDs carry the information on the trace gas abundances, whereas dSOTs carry information on the SOP of skylight and broad

band spectral features. Note that, in contrast to former algorithms, Ω_0 is not necessarily the zenith direction, depending on what information is supposed to go into the retrieval. This is discussed in detail in Section 7.2.2. Both dSCDs and dSOTs can be "polarimetric" or "non-polarimetric". The latter case corresponds to conventional measurements performed without polarising filter in the instrument telescope. Then the viewing geometry is fully described by the viewing direction, hence $\Omega = \{\theta, \phi, \alpha\}$.

During inversion, radiative transport simulations are performed at each λ, at which measurements are provided by the user. For computational reasons, it is advantageous if multiple measurements share the same wavelength, where possible.

7.2.1 Wavelengths of dSCDs

RAPSODI treats dSCDs as if inferred at a single effective wavelength λ. It is up to the user to chose λ for each provided dSCD, such that it is representative for the applied DOAS fitting range.

In this thesis we will apply the fitting ranges and corresponding representative wavelengths λ proposed in Kreher et al. (2019). For arbitrary fitting ranges $[\lambda_1, \lambda_2]$ and species s with absorption cross-section $\sigma_s(\lambda)$ as proposed by subtract a polynomial of same order as the polynomial applied in the DOAS fit to obtain $\sigma'_s(\lambda)$ and then calculate the weighted average wavelength

$$\lambda = \frac{\int_{\lambda_1}^{\lambda_2} \lambda' |\sigma'_s(\lambda')| d\lambda'}{\int_{\lambda_1}^{\lambda_2} |\sigma'_s(\lambda')| d\lambda'} \tag{7.1}$$

7.2.2 Incorporating different kinds of information

It is crucial to consider that, depending on how dSOTs are calculated and incorporated into $\hat{\mathbf{y}}$, the information they carry can be somewhat different. Recall that dSOTs are differential quantities basically quantifying the intensity ratio between two spectra. For this thesis, it is useful to distinguish between two basic kinds of dSOTs:

1. DSOTs between spectra recorded in the same viewing direction (SZA, RAA, EA) but at different polariser orientations contain information on the light's SOP and - if dSOTs are provided at multiple wavelengths - the SOP's spectral dependence.

2. In contrast, dSOTs between spectra of different viewing directions contain information on the spectral broadband variation of radiance over the sky hemisphere.

Within this thesis (for the evaluation of synthetic as well as real data) we will stick to the concept illustrated in Figure 7.2. When polarimetric information shall be exploited, the first kind of dSOTs (red arrows) is incorporated into $\hat{\mathbf{y}}$. If the change of sky radiance with viewing direction shall be used as a further source of

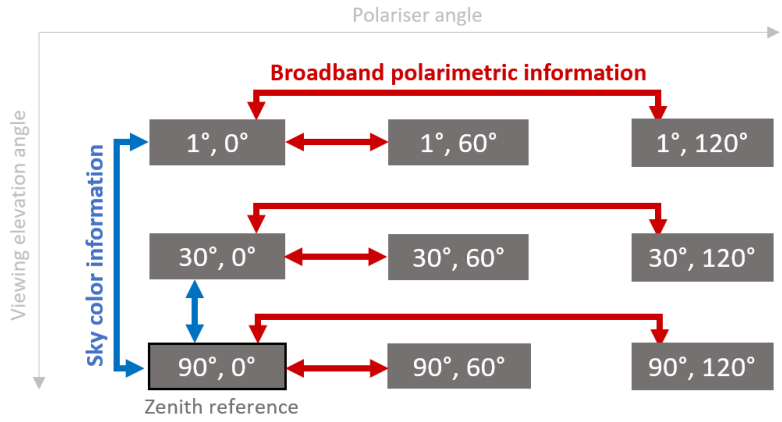

Figure 7.2: Illustration of how dSOTs carry different kinds of information and how they will be incorporated into the retrieval in this thesis. Each box represents a spectrum, recorded at a distinct elevation and polariser angle (first and second number, respectively). Arrows represent dSOTs between them. Arrow colours indicate the kind of information they carry (see text).

information, we incorporate dSOTs between spectra of different viewing direction and a distinct polariser angle (blue arrows) to effectively establish the connection between all spectra without incorporating redundant information.

As described in Section 4, broadband features in the differential optical depth over wavelength ranges of $\approx 100\,\text{nm}$ can be described by low order polynomials. Hence, broad band information can be fully captured by providing dSOTs at a few wavelengths only. Given the exponential wavelength dependence of Rayleigh and aerosol extinction cross-sections (see Section 3), they are ideally given in equidistant steps in $\log(\lambda)$. However, for the computational reasons given above, in this study we provide dSOTs at wavelengths where also dSCDs need to be simulated anyway and "fill" spectral gaps reasonably, avoiding strong Fraunhofer lines.

7.2.3 Example measurement vector

A typical set of input measurements for the RAPSODI retrieval is illustrated in Figure 7.3. For explanatory reasons, three raw spectra from the PMAX-DOAS instrument are shown in the background, each recorded at another PA but at a single viewing direction. From these spectra, dSCDs of O_4, HCHO and NO_2 (with respect to some reference spectrum which is not shown) are derived here at four effective wavelengths using the DOAS spectral analysis technique. DSOTs are calculated at six wavelengths. Considering further viewing directions, typical total numbers of input measurements m for the RAPSODI retrieval are on the order of a few hundred.

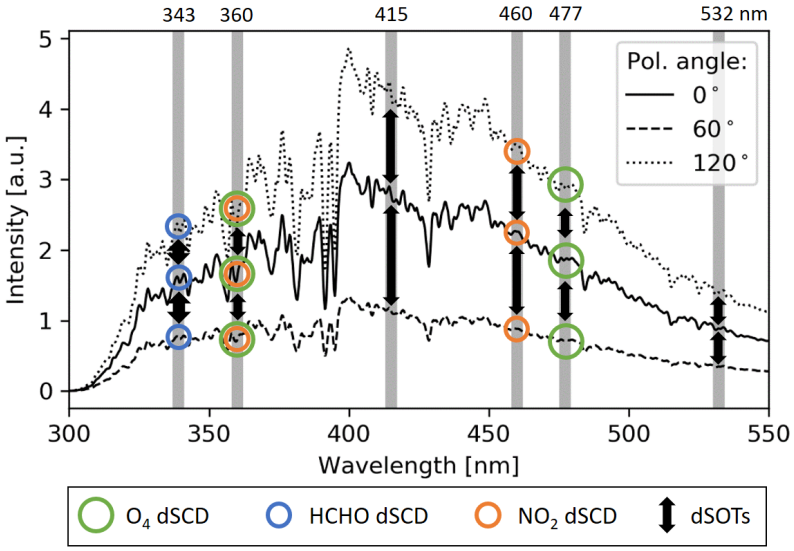

Figure 7.3: Typical set of input measurements $\hat{\mathbf{y}}$, depicted with the help of three skylight example spectra, recorded with the PMAX instrument at different PAs at a single viewing direction. For a detailed descriptions please refer to the main text.

7.3 State vector

The state vector $\mathbf{x}$ contains the parameters to be retrieved. Retrievable quantities are the concentrations $c_{s,l}$ of aerosol and trace gases (O_4 excluded) in each layer l, the Lambertian surface albedos $\omega_{\text{surf}}(\lambda)$ at multiple wavelengths, and optical or microphysical aerosol parameters, depending on the aerosol model used. If the Henyey-Greenstein approximation is applied (see Section 3.3.3), the asymmetry parameters $g_{\text{hg},l}(\lambda)$, the single scattering albedos $\omega_{\text{hg},l}(\lambda)$ and the Ångström exponent $\mathring{a}_{\text{hg},l}$ appear in the state vector. These parameters can be linked over λ and/or l, allowing to determine average values of g_{hg}, ω_{hg} and $\mathring{a}_{\text{hg}}$ over the full altitude and/or wavelength range.
The state vector will contain microphysical aerosol properties if the Mie aerosol model is applied: the mode median radii $r_{l,m}$ of each of the two modes m of the assumed bi-modal size distribution (according to Eq. 3.51), the modal widths $\sigma_{l,m}$, the complex refractive indices $n_{l,m}(\lambda)$, and the modal fraction f_l. Again, RAPSODI allows to link quantities over l, λ and also m. Throughout this thesis, we will assume the same aerosol properties for all layers and therefore in the following drop the l-index for aerosol properties. Regarding the different atmospheric constituents, this thesis focusses on aerosol, HCHO and NO_2, with their profiles represented by $c_{\text{aer},l}$, $c_{\text{HCHO},l}$ and $c_{\text{NO2},l}$, respectively.

A complete overview of the retrievable parameters relevant for this thesis is given in Table 7.1. Spectrally dependent retrieved parameters ($\omega_{surf}(\lambda)$, $g_{\text{hg}}(\lambda)$, $\omega_{\text{hg}}(\lambda)$, $n_1(\lambda)$ and $n_2(\lambda)$) are retrieved at each simulated wavelength, but kept dependent via

Table 7.1: Retrievable parameters, i.e. potential elements of the state vector $\mathbf{x}$. Concentrations are retrieved for each model layer l. A dependence on λ indicates that the corresponding parameter is retrieved at each simulated wavelength.

Kind	Parameter	Symbol	Units	Transf.[a]
Profile	Aerosol surface area concentration	$c_{aer,l}$	$\mu m^2\,cm^{-3}$	log
	HCHO concentration	$c_{HCHO,l}$	molec cm^{-3}	log
	NO_2 concentration	$c_{NO_2,l}$	molec cm^{-3}	log
Surface	Lambertian albedo	$\omega_{surf}(\lambda)$	-	frac
HG model	Ångsgtröm exponent	$\mathring{a}_{\mathrm{hg}}$	-	lin
	Asymmetry parameter	$g_{\mathrm{hg}}(\lambda)$	-	frac
	Single scattering albedo	$\omega_{\mathrm{hg}}(\lambda)$	-	frac
Mie model	Fine mode median radius	r_1	µm	log
	Coarse mode median radius	r_2	µm	log
	Fine mode width	σ_1	-	log
	Coarse mode width	σ_2	-	log
	Fine mode real refractive index	$\Re\, n_1(\lambda)$	-	lin
	Coarse mode real refractive index	$\Re\, n_2(\lambda)$	-	lin
	Fine mode imag. refractive index	$\Im\, n_1(\lambda)$	-	log
	Coarse mode imag. refractive index	$\Im\, n_2(\lambda)$	-	log
	Modal fraction	f	-	frac

[a] Applied transformation in the OEM scheme. See Section 7.5 for details.

an a priori correlation (see Section 7.6). For future implementations, however, other approaches should be considered, for instance using regularisation or polynomial wavelength dependencies. In the following we will often omit indices l, dependencies on λ and viewing directions for convenience, when they can be inferred from the context. In the case of multispectral polarimetric retrievals, typical lengths n of $\mathbf{x}$ are of the order of one hundred (see e.g. Section 9.2).

7.3.1 Parametrisation of aerosol

Conventional algorithms typically retrieve aerosol abundances in terms of the extinction coefficient profiles $K_{\mathrm{aer}}^{(e)}$. However, since $K_{\mathrm{aer}}^{(e)}$ depends on λ, this is not convenient for a multispectral retrieval where the information from observations at multiple wavelengths shall be canalised into a single vertical profile for each species. RAPSODI therefore quantifies aerosol concentrations in terms of the (wavelength-independent) surface area concentration in units of $[\mu m^2\,cm^{-3}]$. It has the advantage over number or volume concentrations to be proportional to the extinction cross-section and minimises cross-correlations between aerosol concentration and microphysical properties during the inversion.

The use of aerosol surface area concentrations has a few consequences. First, it

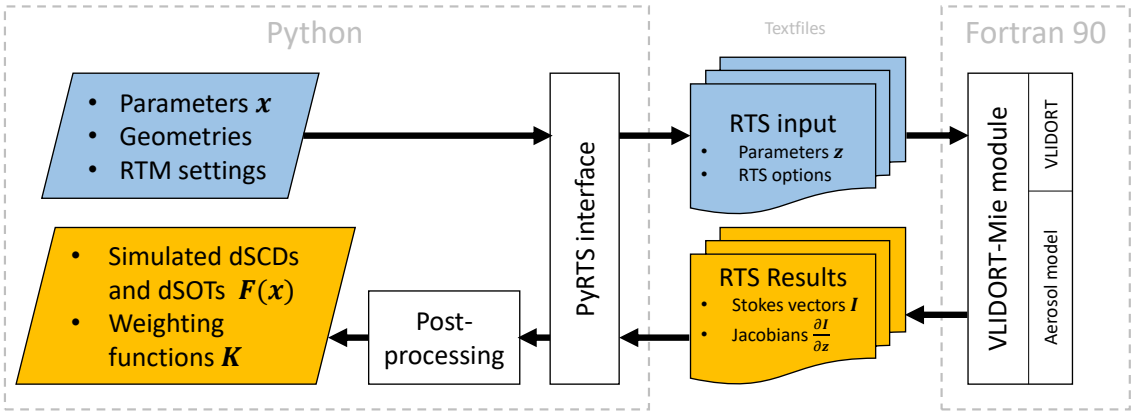

Figure 7.4: Schematic overview of the RAPSODI forward model. It makes use of the PyRTS library, which in turn calls and communicates with the VLIDORT-Mie module using textfiles.

shall be noted that the aerosol vertical columns are in the following quantified in terms of aerosol VCDs V_{aer} in units of $[\mu\mathrm{m}^2\,\mathrm{cm}^{-2}]$ instead of the more familiar AOTs (see Section 4.4). AOTs and VCDs are related according to

$$\mathrm{AOT}(\lambda) = \frac{1}{4} V_{\mathrm{aer}} E(\lambda), \tag{7.2}$$

with E being the aerosol bulk extinction efficiency. For typical values of $E \approx 2$ and considering the units it is

$$\mathrm{AOT} \approx \frac{1}{2} V_{\mathrm{aer}} \times 10^{-8} \frac{\mathrm{cm}^2}{\mu\mathrm{m}^2}, \tag{7.3}$$

which is a useful relation to put the aerosol VCDs reported throughout this study into context. A second consequence concerns the application of the HG aerosol model: Here, the user has to provide a scattering efficiency E_{hg} at a reference wavelength λ_E to establish the link between the layers' aerosol surface concentration $c_{aer,l}$ and the vertical optical thickness $\tau_{aer,l}(\lambda)$ according to

$$\tau_{\mathrm{aer},l}(\lambda) = \frac{1}{4}\, h_l\, E_{\mathrm{hg}} \left(\frac{\lambda_E}{\lambda}\right)^{\mathring{a}_{\mathrm{hg}}} c_{\mathrm{aer},l}, \tag{7.4}$$

for arbitrary simulation wavelengths λ. h_l is the vertical extent of layer l here.

7.4 The RAPSODI forward model

The full forward model of the RAPSODI algorithm consists of multiple components. A schematic overview is provided by Figure 7.4. For the radiative transport simulations, we use VLIDORT 2.8.3 Beta (Spurr, 2021, 2006, 2008), which is implemented

in Fortran 90. We coupled it with an also readily available Fortran 90 Mie model code based on De Rooij and Van der Stap (1984) and Spurr et al. (2012). It derives the aerosol optical properties that VLIDORT requires (bulk scattering phase matrix elements, single scattering albedo and extinction cross-section) as well as their derivatives with respect to the input parameters, from the aerosol microphysical properties given in Table 7.1. The Mie model can be replaced by a HG model (Henyey and Greenstein, 1941) by setting a corresponding flag in the RAPSODI settings. The basic concepts and assumptions behind both, Mie and HG aerosol model, have already been introduced in Section 3.3.3.

7.4.1 The VLIDORT-Mie module

We combined aerosol model and VLIDORT Fortran codes and compiled it into a single executable, in the following referred to as "VLIDORT-Mie module". It requires input settings and provides simulation results in the form of text files. Its output are simulated Stokes parameters $\mathbf{I}$ and their derivatives $\partial\mathbf{I}/\partial\mathbf{z}$ with respect to the VLIDORT-Mie module input parameters $\mathbf{z}$ for a given set of viewing directions. The VLIDORT-Mie module simulates results for a single wavelength at a time Hence, the module will be called multiple times during a multispectral RAPSODI forward model run. The configuration of VLIDORT and the VLIDORT-Mie code to provide the derivatives $\partial\mathbf{I}/\partial\mathbf{z}$ is non-trivial and is therefore described in detail in Appendix A. For technical reasons, $\mathbf{z}$ contains parameters different to the RAPSODI state vector $\mathbf{x}$: it does not include the Ångstrom parameter $\mathring{a}_{\mathrm{hg}}$ and instead of the trace gas concentrations it contains the combined vertical molecular absorption optical depth $\tau_{gas,l}$. The calculation of the actually required quantities $\mathbf{F}(\mathbf{x})$ (dSCDs and dSOTs) as well as weighting functions $\mathbf{K} = \partial\mathbf{F}(\mathbf{x})/\partial\mathbf{x}$ from the VLIDORT-Mie module output occurs in a post-processing step as described below.

Simulations can be performed either considering the full stokes vector with scattering processes described by Mueller matrices (often referred to as "vectorised RTS") or considering only the scalar radiance I with scattering described by scalar phase functions (referred to as "scalar RTS"). The latter is useful to improve the computational performance of the retrieval in cases where the SOP is not of interest. This is discussed in more detail in Section 8.3.

7.4.2 The PyRTS library

For convenient use of VLIDORT-Mie module, we further implemented a python library (in the following referred to as "PyRTS") that automatically creates the required input setting text files, calls the VLIDORT-Mie module, and afterwards reads in the results. PyRTS features a user-friendly interface to simplify its assimilation into the RAPSODI inversion algorithm but also for its stand-alone use in further applications.

7.4.3 Post-processing of the RTM results

The RAPSODI forward model makes use of the PyRTS library and post-processes its results to the actually required quantities, namely $\mathbf{F}(\mathbf{x})$ (dSCDs and dSOTs) as well as weighting functions $\mathbf{K} = \partial\mathbf{F}(\mathbf{x})/\partial\mathbf{x}$. The post processing comprises multiple steps. First, the radiances $I(\lambda, \Omega)$ and corresponding derivatives $\partial I(\lambda, \Omega)/\partial\mathbf{z}$ for all viewing geometries Ω (including the PA) are derived from the simulated Stokes vectors and their derivatives using Eq. 3.26. Second, derivatives of the radiances with respect to those retrieved parameters x in $\mathbf{x}$ that are not included in $\mathbf{z}$ have to be calculated applying the chain rule

$$\frac{\partial I}{\partial x} = \sum_j \frac{\partial I}{\partial z_j}\frac{\partial z_j}{\partial x} \tag{7.5}$$

For trace gas concentrations it is

$$\frac{\partial I}{\partial c_{s,l}} = \frac{\partial I}{\partial \tau_{gas,l}}\sigma_s h_l \tag{7.6}$$

with σ_s being the respective trace gas absorption cross-section and h_l being the respective layer's vertical extent. To improve readability, we refer to $I(\lambda, \Omega)$ and $I(\lambda, \Omega_0)$ by I and I_0, respectively. The derivatives with respect to the Ångström parameter are

$$\frac{\partial I}{\partial \mathring{a}_{\mathrm{hg},l}} = c_{aer,l} \ln\left(\frac{\lambda_E}{\lambda}\right)\frac{\partial I}{\partial c_{aer,l}} \tag{7.7}$$

with λ being the simulation wavelength and with λ_E being the wavelength, for which the user provided the HG extinction efficiency E_{hg}. With these two equations one obtains the complete set of layerwise derivatives $\partial I/\partial\mathbf{x}_l$. Summing those over respective subgroups according to the linking options defined by the user yield the derivatives $\partial I/\partial\mathbf{x}$. Next, the simulated dSOTs are derived according to

$$\Delta\tau(\lambda, \Omega, \Omega_0) = \ln\left(\frac{I_0}{I}\right) \tag{7.8}$$

while their weighting functions are given by

$$\frac{\partial\Delta\tau(\lambda, \Omega, \Omega_0)}{\partial\mathbf{x}} = \frac{1}{I_0}\frac{\partial I_0}{\partial\mathbf{x}} - \frac{1}{I}\frac{\partial I}{\partial\mathbf{x}} \tag{7.9}$$

There are several ways to calculate dSCDs. One way is to infer the BAMFs A_l using Equation 4.20 and derive the SCDs S for each species i according to

$$S_i = \sum_l A_l V_{i,l} \tag{7.10}$$

with $V_{i,l}$ being the BVCDs. However, for the derivatives of SCDs (and therefore the dSCDs) with respect aerosol concentrations, surface albedo and aerosol properties,

this approach requires derivatives of the AMFs, hence, second order derivatives of I. We therefore follow the approach proposed by Spurr (2018). It is based on additional RT simulations with each trace gas i (including O_4) removed from the model atmosphere. These yield 'gas free' radiances $I^{(i)}(\lambda, \Omega)$, with the superscript (i) indicating the removed species. DSCDs can then be calculated according to

$$\Delta S_i(\lambda, \Omega, \Omega_0) = \frac{1}{\sigma_i(\lambda)} \ln\left(\frac{I_0}{I}\frac{I^{(i)}}{I_0^{(i)}}\right). \tag{7.11}$$

The dSCD weighting functions with respect to trace gas concentrations is given by

$$\frac{\partial \Delta S_i(\lambda, \Omega, \Omega_0)}{\partial \mathbf{x}} = \frac{1}{\sigma_s(\lambda)}\left(\frac{1}{I_0}\frac{\partial I_0}{\partial \mathbf{x}} - \frac{1}{I}\frac{\partial I}{\partial \mathbf{x}}\right) \tag{7.12}$$

and with respect to aerosol surface concentrations, surface albedo and aerosol properties they are

$$\frac{\partial \Delta S_i(\lambda, \Omega, \Omega_0)}{\partial \mathbf{x}} = \frac{1}{\sigma_s(\lambda)}\left(\frac{1}{I_0}\frac{\partial I_0}{\partial \mathbf{x}} - \frac{1}{I}\frac{\partial I}{\partial \mathbf{x}} + \frac{1}{I^{(i)}}\frac{\partial I^{(i)}}{\partial \mathbf{x}} - \frac{1}{I_0^{(i)}}\frac{\partial I_0^{(i)}}{\partial \mathbf{x}}\right) \tag{7.13}$$

7.4.4 Treatment of Raman-Scattering

A single VLIDORT run performs an RT-simulation at a single wavelength only. Coupling between different wavelengths, as occurring in reality due to inelastic Raman scattering, is therefore complex and computationally expensive. As an approximation, the RAPSODI forward model accounts for molecular scattering by using the full Rayleigh cross-section and scattering matrix according to Section 3.3.2 (including both Cabannes and Raman scattering) but assumes Raman scattering to be elastic. Any spectral patterns arising from Raman induced wavelength shifts will therefore not be reproduced by the model. This needs to be considered in the data evaluation (see Section 13.4). Advanced approximations to account for inelastic scattering have been proposed e.g. by Landgraf et al. (2004) and their implementation into the RAPSODI algorithm might be subject of future efforts.

7.4.5 Forward model validation

Regarding the simulation of radiances, the VLIDORT RTM has been thoroughly validated by its authors against benchmark results from Coulson et al. (1960), Garcia and Siewert (1989) and Siewert (2000). We further validated the radiances provided by the VLIDORT-Mie module to results by Boesche et al. (2006), who also use a Mie parametrisations in terms of a bi-modal size distribution for the evaluation of polarimeter observations. The dSCDs provided by the full RAPSODI forward model were validated against data from Frieß et al. (2019) as outlined in Section 8.2.1. The analytically derived weighting functions were validated against finite difference estimates. The latter are obtained by calculating the ratio $\Delta y/\Delta x$, with Δy being the change in each observation induced by a small change Δx in each retrieved parameter.

7.5 Transformation functions and scaling

The RAPSODI algorithm allows to transform parameters $\mathbf{x}$ to numerically more favourable quantities $\mathbf{x}'$ before the OEM formalism is applied. By default, the RAPSODI retrieval allows for two different transformation functions $x' = t(x)$ applicable to the individual parameters:

1. The *log*-transformation allows to retrieve parameters in logarithmic space:

$$x' = \ln(x) \tag{7.14}$$

   In this way, negative values in x are avoided and larger values of x are allowed. This is convenient for most parameters, e.g. vertical profiles, aerosol median radii, and modal widths.

2. The *frac*-transformation maps fractional quantities between zero and one - like albedos, asymmetry parameters and modal fractions - into the $(-\infty, \infty)$ space by applying the transformation

$$x' = -\ln\left(\frac{1}{x} - 1\right) \tag{7.15}$$

In this study, we only make use of these two transformations but generally, RAPSODI allows arbitrary transformation functions to be defined by the user. Main motivations for the transformations are: (1) numerical failure due to discrete boundaries in the parameter values and unphysical results are avoided. (2) The inversion formalism by Rodgers (2000) assumes typical variations and uncertainties of the parameters to be normally distributed, which is often better fulfilled for suitably transformed quantities. The applied transformations for each parameter are listed in Table 7.1.

Besides these transformations, it is crucial for numerical reasons that all parameters and measurements are of similar orders of magnitude within the OEM formalism. This is for instance not ensured if measurements are processed in their standard units: $\hat{\mathbf{y}}$ for instance simultaneously contains dSCDs of the order of 10^{16} molec cm^{-2} and dSOTs of the order of 10^{-2}. The RAPSODI algorithm therefore internally scales all quantities in state and measurement space by corresponding diagonal matrices $\mathbf{D}_x$ and $\mathbf{D}_y$, with

$$D_{x,ii} = \sqrt{\frac{1}{S_{a,ii}}} \quad \text{and} \quad D_{y,ii} = \sqrt{\frac{1}{S_{y,ii}}} \tag{7.16}$$

Considering both transformations and scaling, the quantities internally used within

the OEM formalism are therefore

$$
\begin{aligned}
\mathbf{x}'_a &= \mathbf{D_x t}(\mathbf{x}_a) && \Longleftrightarrow && \mathbf{x}_a &= \mathbf{D_y t}^{-1}(\mathbf{x}'_a) \\
\mathbf{y}' &= \mathbf{D_y y} && \Longleftrightarrow && \mathbf{y} &= \mathbf{D_y}^{-1}\mathbf{y}' \\
\mathbf{S}'_a &= \left.\frac{\partial \mathbf{x}'}{\partial \mathbf{x}}\right|_{\mathbf{x}_a} \mathbf{D}_x\, \mathbf{S}_a\, \mathbf{D}_x \left.\frac{\partial \mathbf{x}'}{\partial \mathbf{x}}\right|_{\mathbf{x}_a} && \Longleftrightarrow && \mathbf{S}_a &= \mathbf{D}_x^{-1} \left.\frac{\partial \mathbf{x}}{\partial \mathbf{x}'}\right|_{\mathbf{x}_a} \mathbf{S}'_a \left.\frac{\partial \mathbf{x}}{\partial \mathbf{x}'}\right|_{\mathbf{x}_a} \mathbf{D}_x^{-1} \\
\mathbf{S}'_y &= \mathbf{D}_y\, \mathbf{S}_y\, \mathbf{D}_y && \Longleftrightarrow && \mathbf{S}_y &= \mathbf{D}_y^{-1}\, \mathbf{S}'_y\, \mathbf{D}_y^{-1} \\
\mathbf{K}'_i &= \mathbf{D}_y\, \mathbf{K}_i\, \mathbf{D}_x^{-1} \left.\frac{\partial \mathbf{x}}{\partial \mathbf{x}'}\right|_{\mathbf{x}_i} && \Longleftrightarrow && \mathbf{K}_i &= \mathbf{D}_y^{-1}\, \mathbf{K}_i \left.\frac{\partial \mathbf{x}'}{\partial \mathbf{x}}\right|_{\mathbf{x}_i} \mathbf{D}_x
\end{aligned}
$$

with the index i indicating the current retrieval iteration here. As indicated in Figure 7.1 by red symbols, these transformations are applied on the transitions between user interface and OEM formalism, as well as between the forward model and the OEM formalism.

Note that, linearisations of $\mathbf{S}'_a$ and $\mathbf{K}'$ are performed around different states ($\mathbf{x}_a$ and $\mathbf{x}_i$, respectively). The different linearisation points have to be considered during back-transformation of relevant output quantities, like the covariance of the retrieved state $\hat{\mathbf{S}}_i$ or the AVKs $\mathbf{A}_i$. They cannot be transformed as a whole, but need to be calculated according to:

$$
\hat{\mathbf{S}}_\mathbf{i} = \mathbf{D}_x^{-1} \left(\left.\frac{\partial \mathbf{x}'}{\partial \mathbf{x}}\right|_{\mathbf{x}_a} \mathbf{S}_a'^{-1} \left.\frac{\partial \mathbf{x}'}{\partial \mathbf{x}}\right|_{\mathbf{x}_a} + \left.\frac{\partial \mathbf{x}'}{\partial \mathbf{x}}\right|_{\mathbf{x}_i} \mathbf{K}_i'^{T} \mathbf{S}_y'^{-1} \mathbf{K}'_i \left.\frac{\partial \mathbf{x}'}{\partial \mathbf{x}}\right|_{\mathbf{x}_i} \right)^{-1} \mathbf{D}_x^{-1} \tag{7.17}
$$

$$
\mathbf{A}_i = \hat{\mathbf{S}}_\mathbf{i}\, \mathbf{D}_x \left.\frac{\partial \mathbf{x}'}{\partial \mathbf{x}}\right|_{\mathbf{x}_i} \mathbf{K}_i'^{T} \mathbf{S}_y'^{-1} \mathbf{K}'_i \left.\frac{\partial \mathbf{x}'}{\partial \mathbf{x}}\right|_{\mathbf{x}_i} \mathbf{D}_x \tag{7.18}
$$

7.5.1 Delta-M scaling

The order of phase function expansion coefficients applied in discrete ordinate RTMs (see Section 3.4) is typically limited for computational reasons: RAPSODI uses 200 for the single scattering radiance field but only $2n_{hss}$ for the multiple scattering field, with n_{hss} indicating the number of half-space streams, i.e. the number of discrete ordinates per half-space applied in the RT-simulation (see Section 3.4 and 8.1). The representation particularly of strong forward scattering peaks in the phase function $P(\mu)$ (with $\mu = \cos(\theta)$) is therefore inaccurate. For the multiple scattering field we make use of the *Delta-M* scaling method, which significantly improves the accuracy of RTM results under negligible additional computational efforts (Wiscombe, 1977). It truncates the forward scattering peak ($P(\mu) = P(\mu')$) for values of μ above a threshold μ' and assumes the truncated radiation fraction

$$
E' = 2\pi \int_{\mu'}^{1} P(\mu) d\mu + 2\pi(\mu' - 1)\, P(\mu') \tag{7.19}
$$

to remain unscattered. In accordance with Wiscombe (1977), in VLIDORT μ' is chosen to satisfy $E' = \beta_{2n_{hss}}/(2n_{hss}+1)$. The individual phase matrix elements are scaled according to Chami et al. (2001).

7.6 A priori covariance

In the cost function (Eq. 5.12), the a priori covariance matrix $\mathbf{S}_a$ defines how and to which extent a deviation of $\hat{\mathbf{x}}$ from $\mathbf{x_a}$ is 'punished'. In the real atmosphere, vertical gradients in the profiles will not be arbitrarily large. It is therefore reasonable to assume an a priori correlation (i.e. non-zero off-diagonal elements in $\mathbf{S}_a$) between concentrations in different layers. It is also reasonable to assume an increase in correlation with altitude, as the size of atmospheric turbulence patterns increases and profiles are expected to be smoother at higher altitudes than at the surface.

The RAPSODI algorithm uses a standard approach to create a priori matrices for vertical profiles. It requires the standard deviation σ_l of the species' concentration in each layer l, a correlation length L_0 to be assumed at the surface and a parameter δ that describes the increase of L_0 with altitude. The a priori covariance matrix for a single vertical profile is then calculated according to

$$S_{ij} = \sigma_i \, \sigma_j \, \exp\left[-\frac{|h_i - h_j|}{L_{ij}}\right], \tag{7.20}$$

with h_l being the center altitude of layer l and with

$$L_{ij} = L_0 \left[1 + \frac{\delta}{2}\,(h_i + h_j)\right]. \tag{7.21}$$

This definition of the covariance matrix differs from the definition in (Clémer et al., 2010) that has often been used in MAX-DOAS studies. Clémer et al. (2010) use a gaussian instead of an exponential decay:

$$S_{ij} = \sigma_i \, \sigma_j \, \exp\left[-\frac{\ln 2}{2}\left(\frac{h_i - h_j}{L_c}\right)^2\right] \tag{7.22}$$

We found that both definitions - Eq. 7.20 and 7.22 - lastly yield similar profiling results and DOFs if $L_0 \approx 5L_c$ (and $\delta = 0$). This is why correlation lengths in this work might appear large compared to distinct former MAX-DOAS profiling publications. Even though the user is able to provide custom a priori covariance matrices, for this thesis we will stick to the approach described above with δ being set to zero, if not stated otherwise. A similar approach is taken for spectrally resolved quantities ($\omega_{surf}(\lambda)$, $g_{\mathrm{hg}}(\lambda)$, $\omega_{\mathrm{hg}}(\lambda)$, $n_1(\lambda)$ and $n_2(\lambda)$): here a spectral correlation length can be defined and, equivalently to Eq. 7.20, the corresponding a priori covariance matrix is calculated assuming a correlation exponentially decaying with the spectral distance between the retrieved wavelength nodes.

It shall be noted that RAPSODI also allows to replace $\mathbf{S}_a^{-1}$ by a regularisation matrix R according to the concepts described in Tikhonov (1963) and Twomey (1963). This approach, however, will not be applied or investigated within this thesis.

Part II

Studies with synthetic data

8 Miscellaneous

In this chapter we present different first investigations based on synthetic data. It is structured as follows: Section 8.1 discusses the impact of crucial settings of the RAPSODI forward model on the simulation results. In Section 8.2 we perform a validation of the RAPSODI algorithm by retrieving profiles from an independent set of synthetic non-polarimetric dSCDs. Section 8.3 investigates the impact of the scalar approximation in RT-simulations (instead of performing the full vectorised RT-simulation) on the forward model results. In Section 8.4, we simulate and investigate weighting functions to approximately assess the actual sensitivity of (polarimetric) MAX-DOAS observations to different atmospheric parameters.

It shall be noted that many of the settings, assumptions and approaches taken in the following sections are inspired by Frieß et al. (2019), who performed a comprehensive comparison between eight existing MAX-DOAS profiling algorithms on the basis of synthetic data for typical atmospheric conditions. Further details are discussed in the corresponding sections.

8.1 Computational considerations

In discrete-ordinate RTMs, some settings are a tradeoff between simulation accuracy and computational performance. Most critical are the number of considered discrete ordinates (in VLIDORT described by the number of discrete ordinates per half-space, or "half-space streams" n_{hss}, see also Section 3.4) and the number of atmospheric layers. Figure 8.1 shows the impact of both on the computation time. It is obvious that particularly the choice of n_{hss} can significantly accelerate the RT-simulation and thus the retrieval.

The absolute computation times vary strongly, depending on the number of considered measurements and retrieved parameters as well as the detailed settings. Conventional non-polarimetric monochromatic retrievals of a single species' vertical profile from elevation scan data (dSCDs at ten EAs) take 3 to 6 seconds on a standard personal Laptop (manufactured in 2018). Hereby, we assumed 40 atmospheric layers, the HG aerosol model and $n_{hss} = 6$. In contrast, a polarimetric multispectral retrieval of aerosol, HCHO and NO_2, surface albedo and aerosol microphysical properties (Mie-model), from elevation scan data at multiple wavelengths (dSCDs and dSOTs, as applied in Section 9.5 for the Multi-S-P mode) takes five to ten minutes.

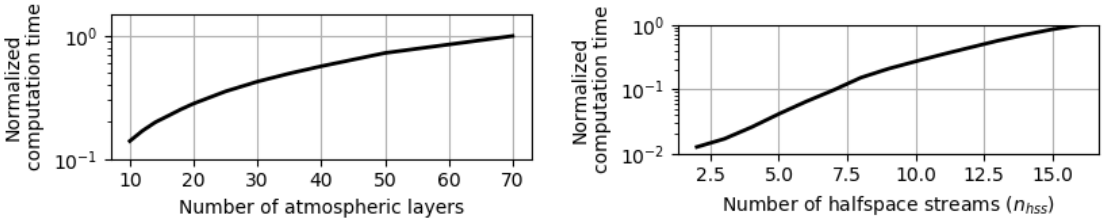

Figure 8.1: Dependence of the RAPSODI forward model computation time on the number of simulated atmospheric layers (left) and the number of applied half-space streams (right).

8.1.1 Number of atmospheric layers

Since the atmospheric pressure profile is exponential while also the vertical resolution of MAX-DOAS observations decreases with altitude, it is reasonable to introduce an exponential vertical grid with increasing layer thickness according to

$$h_l = a(b^l - 1) \tag{8.1}$$

with h_l being the altitude of the layer boundaries and $l = [0, l_{max}]$. The constants a and b can be chosen to meet distinct constraints. The RAPSODI retrieval has a built-in function with the arguments being the number of layers l_{max}, the TOA altitude $h_{l_{max}}$ and the surface layer height h_1. It derives corresponding values for a and b and returns the grid according to Eq. 8.1.

To investigate the impact of the choice of the grid, forward simulations with different l_{max}, $h_{l_{max}}$ and h_1 were performed. We assumed exponential profiles for aerosol and trace gases (scale height of 1 km, AOT of 0.25 and VCD of 2×10^{16} molec cm^{-2} for HCHO and NO_2). The HG aerosol model ($\mathring{a}_{\mathrm{hg}} = 0$, $\omega_{\mathrm{hg}} = 0.92$, $g = 0.68$) and $n_{hss} = 10$ were applied. Simulations with $l_{max} = 100$, $h_{l_{max}} = 80$ km and $h_1 = 25$ m were assumed as ground truth. Simulations were further performed for each combination of viewing geometries according to Table 8.1 and polariser angles $\delta \in [0, 90, 120°]$. The simulated observations are dSOTs, O_4 dSCDs (at 360 and 477 nm), HCHO dSCDs (at 343 nm) and NO_2 dSCDs (at 360 and 460 nm). Figure 8.2 shows the results. The values plotted are the maximum deviation from the ground truth observed for each set of simulated geometries and wavelengths. Black lines indicate typical measurement uncertainties: for dSCDs we adapt the values proposed by Frieß et al. (2019) (2×10^{41} molec^2 cm^{-5} for O_4, 2×10^{15} molec cm^{-3} for HCHO and 5×10^{14} molec cm^{-3}), the dSOT uncertainty (0.02) is inspired by our findings in Section 13.1.

Already for 30 model layers the deviations are well below the typical measurement uncertainties at least by more than a factor of four. When regarding different viewing geometries and simulation wavelengths individually, there is no simple systematic behaviour pointing to particularly problematic settings. We conclude that an exponential grid of 30 to 40 layers, spanning an altitude range of ≈ 60 km with a

surface layer height of $\approx 50\,\mathrm{m}$ provides sufficiently accurate simulations results for our purposes, given that profile features that the user aims to retrieve can still be resolved.

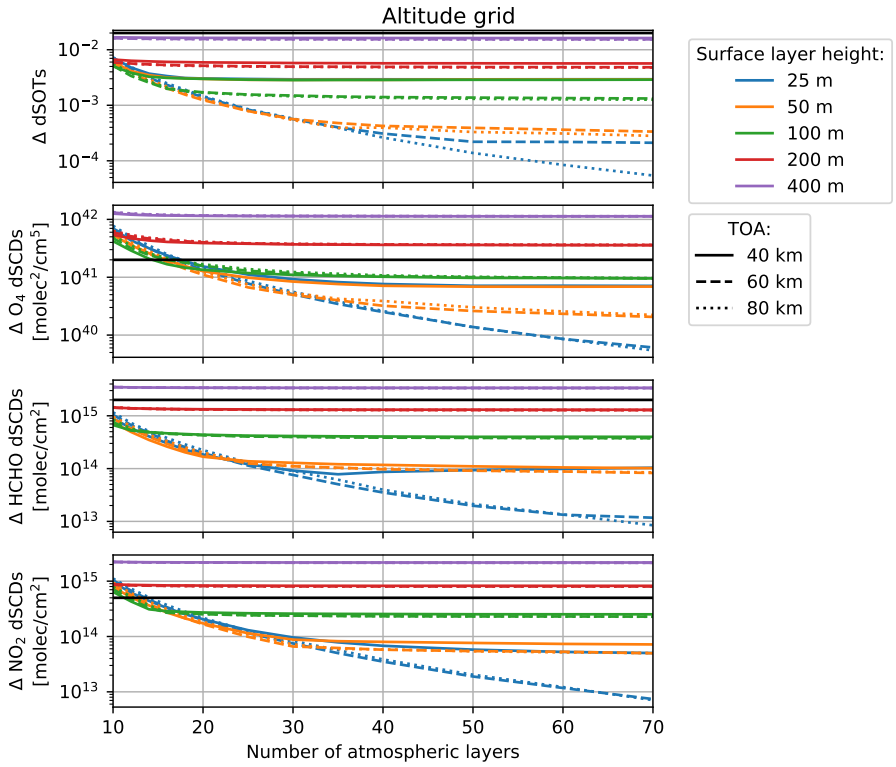

Figure 8.2: Observed deviations of different simulated quantities (different subplots) from the ground truth for different model vertical grids. Data points represent the maximum deviation observed over a set of observations at different viewing geometries and wavelengths. Thin horizontal black lines indicate typical measurement uncertainties.

8.1.2 Number of discrete ordinates

Similar investigation as for the altitude grid were performed for the number of discrete ordinates assumed in the VLIDORT simulation (see Section 3.4). The user must provide VLIDORT with the "number of half-space streams" (n_{hss}), i.e. the number of discrete ordinates in the upper and lower half-space. We performed simulations at different n_{hss} and compared the results with a "ground truth" simulation with $n_{hss} = 32$. The deviations are shown in Figure 8.3. We assumed almost the same atmospheric scenario and viewing geometries as in Section 8.1.1 before. However, we performed simulations for two cases (left and right panel of Figure 8.3) with different AOTs and asymmetry parameters g_{hg}.

Most critical are simulations at high AOTs, large g_{hg}, large SZAs and RAA = 0°, i.e. when looking towards the sun. However, for most scenarios, $n_{hss} \geq 4$ yields sufficiently accurate simulation results. We also varied the vertical profile of aerosol and applied the Mie model instead of the HG-approximation (with settings resulting in similar aerosol optical properties). This, however, only changed details in the graphs, while the major conclusion remained the same. Throughout this study we apply $n_{hss} = 6$, if not stated otherwise.

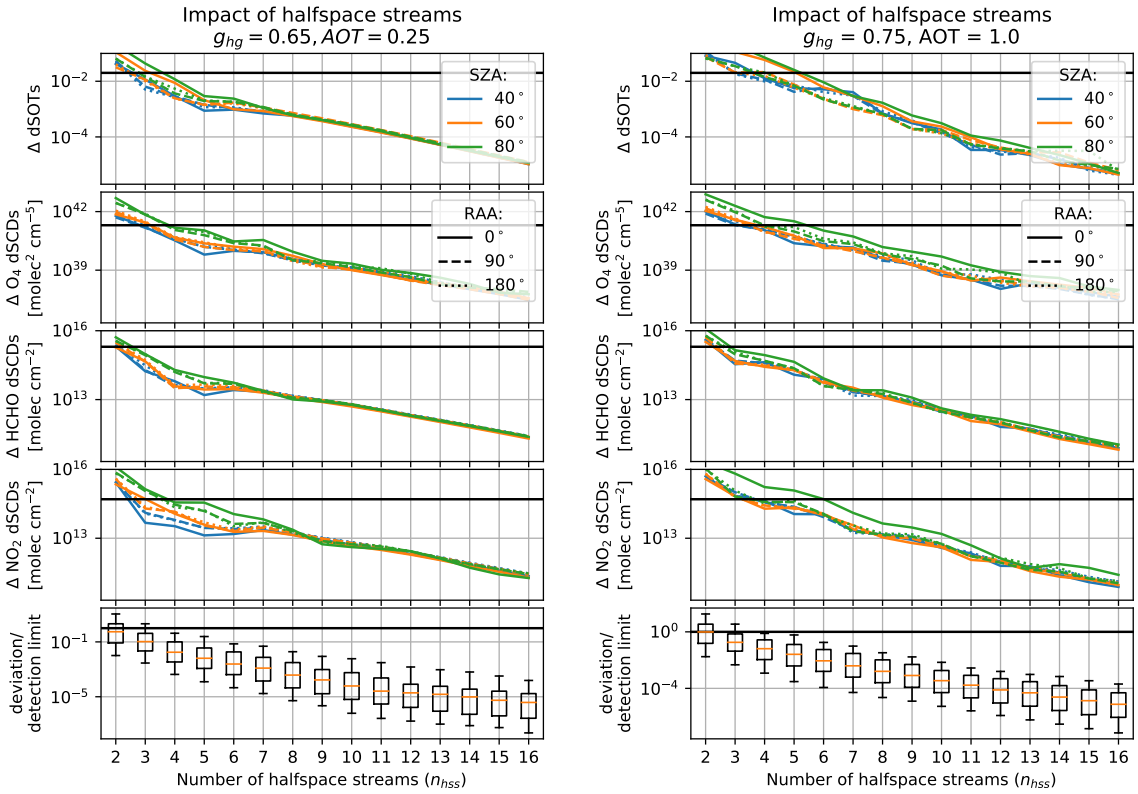

Figure 8.3: Observed deviations of different simulated quantities (different panel rows) from the ground truth for different n_{hss} values. The left panel shows results for $g_{\mathrm{hg}} = 0.65$ and low aerosol load (AOT = 0.25). The right panel shows results for an asymmetry parameter of $g = 0.75$ and higher aerosol load (AOT = 1.0). Data points represent the maximum deviation observed over a set of observations at different viewing elevation angles and wavelengths. Horizontal black lines indicate typical measurement uncertainties. The lowest row shows the distribution of the deviations of all observations relative to the typical measurement uncertainties as box-whisker plots, with boxes (whiskers) indicating the 25th to 75th (5th to 95th) percentiles.

8.2 Retrievals from an independent dataset

In a study by Frieß et al. (2019), a comprehensive comparison between eight existing MAX-DOAS profiling algorithms on the basis of synthetic data was performed. The study can be subdivided into two major parts: in a first step Frieß et al. simulated and compared synthetic dSCDs for a comprehensive set of different atmospheric conditions and viewing geometries, using the forward models of the different algorithms. Furthermore, they created a set of "median dSCDs", calculated as the median over the results from all participating forward models. In a second step, inversions were performed on the basis of the median dSCDs to investigate to what extent the algorithms "reconstruct" the original underlying atmospheric states.

As one of the validation exercises, we repeated parts of the study applying the RAPSODI algorithm. Even though the study is limited to non-polarimetric dSCDs, this exercise is useful for the validation of the RAPSODI forward model and its optimal estimation retrieval scheme. The results are outlined in the following.

The simulated synthetic observations by Frieß et al. (2019) comprise dSCDs of O_4 (at 360 and 477 nm), NO_2 (460 nm) and HCHO (343 nm). The different assumed profiles for aerosol and trace gases (NO_2 and HCHO) are illustrated in Figure 8.4. The different solar and viewing geometries are summarised in Table 8.1. Simulations were performed for each combination of aerosol profiles, trace gas profiles, EAs, SZAs and RAAs. A surface albedo of 0.06 and HG-aerosol with an asymmetry parameter of 0.68 and a single scattering albedo of 0.92 was assumed. For further details on the setup, the reader is referred to the original publication.

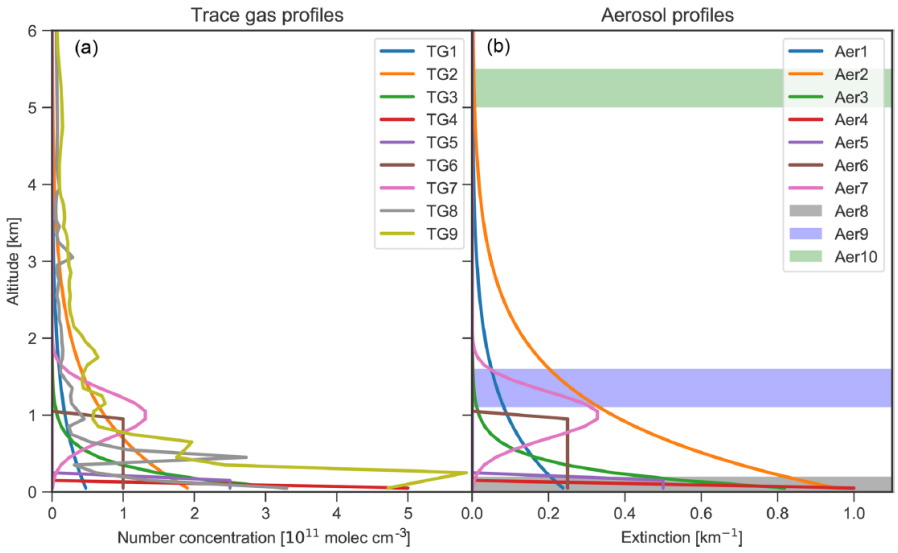

Figure 8.4: Different trace gas number concentration (a) and aerosol extinction profiles (b) assumed for the simulation of the synthetic dSCDs. The shaded areas in (b) indicate the location of fog and cloud layers with an extinction coefficient of 10 km^{-1}. Figure is taken from Frieß et al. (2019).

Table 8.1: Viewing geometries, for which dSCDs were simulated

Parameter	Values [°]
EA (α)	1, 2, 3, 4, 5, 6, 8, 15, 30
SZA (θ)	50, 60, 80
RAA (ϕ)	0, 90, 180

8.2.1 Forward simulations

First, the different atmospheric scenarios and viewing geometries according to Figure 8.4 and Table 8.1 were implemented in RAPSODI and the forward model was executed to simulate the required dSCDs. Figure 8.5 compares the results to the median dSCDs by Frieß et al..

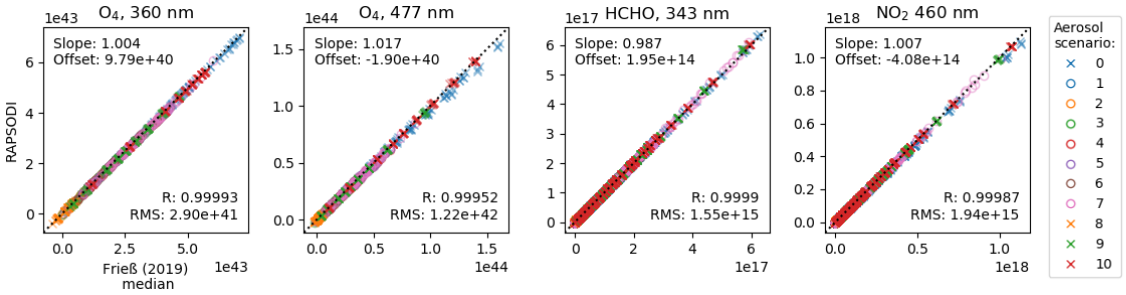

Figure 8.5: Comparison of dSCDs from the RAPSODI forward model (vertical axis) and the median dSCD dataset provided by Frieß et al. (2019).

The overall agreement is satisfactory. Even though the deviations (RMSD) are larger than typical dSCD uncertainties proposed by Frieß et al. (2×10^{41} molec^2 cm^{-5} for O_4, 2×10^{15} molec cm^{-3} for HCHO and 5×10^{14} molec cm^{-3}), they are of the order or smaller than typical deviations between the forward models compared in Frieß et al. and thus also on the order of potential errors in the median dSCDs. Particularly large deviations are observed for the aerosol free atmosphere (Aerosol profile 0), at SZA = 80°, for the O_4 dSCDs in the visible and NO_2 dSCDs. Similar deviations were observed for other algorithms compared by Frieß et al. (2019), who propose the different treatment of Earth's sphericity as the main reason.

8.2.2 Retrieval results

The median dSCDs from Frieß et al. (2019) were fed to the RAPSODI algorithm and profiles were retrieved. The approach of separate retrievals for aerosol and trace gases (as applied in conventional retrievals) was taken: first, aerosol profiles were retrieved from O_4 dSCDs only. Then, for the trace gas retrievals in the UV (HCHO at 343 nm) and the Vis (NO_2 at 460 nm) the corresponding aerosol profiles retrieved

from O_4 at 360 nm and 477 nm, respectively, were assumed. Figure 8.6 and 8.7 show the retrieval results for aerosol and trace gas profiles.

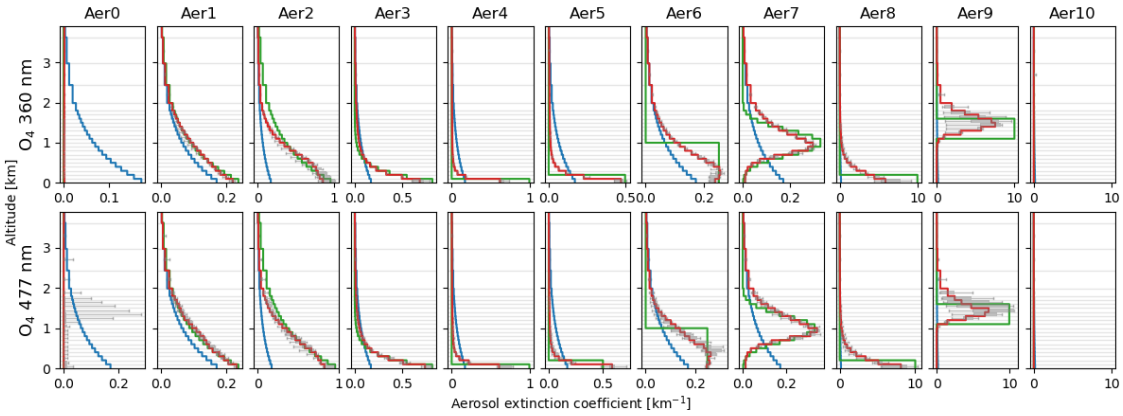

Figure 8.6: Comparison of retrieved (red lines) and true (green lines) vertical profiles of aerosol extinction for each aerosol scenario (columns). Red lines indicate the median of retrieved profiles for all SZA - RAA combinations. The (25 - 75 %) and (5 %–95 %) percentiles are shown as grey boxes and whiskers, respectively. The blue line indicates the a priori profile.

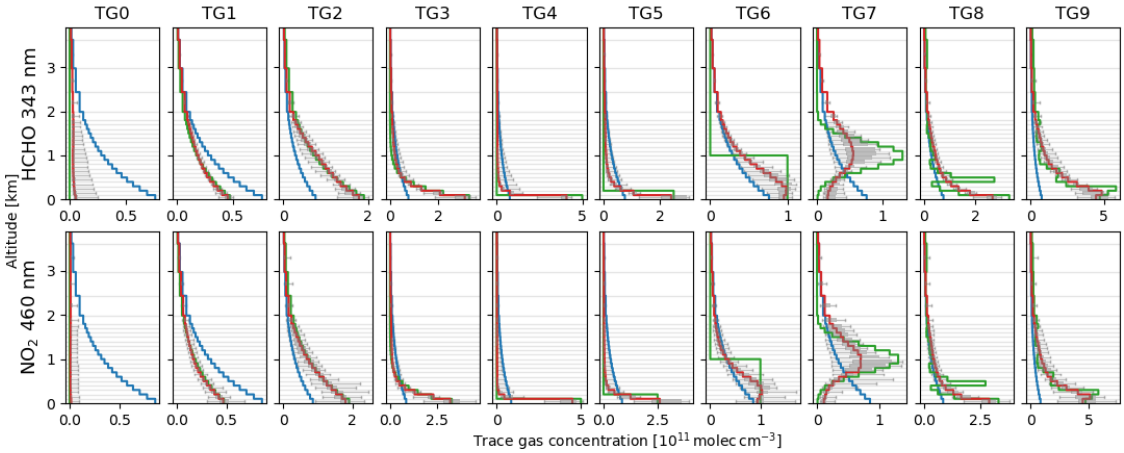

Figure 8.7: Same as Figure 8.6, but for trace gas concentration profiles for HCHO and NO_2. Here, the box-whisker plots represent the statistic over all RAA-SZA combinations and aerosol scenarios.

The profiles are mostly reliably retrieved within the capabilities of typical MAX-DOAS inversion algorithms and considering the limited information content in the measurements (compare results from other algorithms in Frieß et al. (2019)). Aerosol profile 10 is the cloud layer at 5 km altitude, located outside the plotting range. It is not detected at all due to the limited sensitivity of the measurements to such altitudes: the retrieved aerosol profile remains close to zero over the entire altitude

range. To avoid confusion, it shall be noted that Frieß et al. (2019) discuss retrieval results for two sets of dSCDs. One with a 5 % noise added to the median dSCDs ("v1n") to simulate atmospheric inhomogeneities and temporal variations and one without noise ("v1"). The profiles in Figure 8.6 and 8.7 were retrieved from the "v1" - hence the noiseless - median dSCDs.

8.3 Scalar versus vectorised simulations

In the ideal case, RT-simulations are performed considering the full stokes vector ("vectorised" RT-simulations) even in cases where lastly only the unpolarised radiance is of interest and not the SOP. However, for computational reasons, it is common practise for unpolarised MAX-DOAS inversions (and many other applications) to not run full stokes but "scalar" RTMs. The latter keep track only of the radiance I instead of all stokes parameters and describe scattering events by scalar phase functions instead of full Müller-matrices.

For the single scattering radiance field, there is no difference expected between scalar and vectorised simulated radiances I, given that sunlight arriving at the TOA is unpolarised. However, this changes for the multiply scattered radiance field: the scalar simulation assumes the light to remain unpolarised all along it's way through the atmosphere. But as described in Section 3, light that has undergone scattering is potentially polarised and the angular dependence of subsequent scattering processes can only be correctly considered by vectorised RTMs.

Of course, for most parts of this thesis, we perform vectorised simulations, as we are interested in the full SOP. However, regarding former algorithms and the application of RAPSODI for non-polarimetric retrievals it is of interest to estimate the impact of the scalar approximation on the simulation results. There are several studies investigating its impact on radiances (e.g. Lacis et al., 1998; Mishchenko et al., 1994; Hasekamp et al., 2002). Corresponding investigations for dSCDs are mentioned in Clémer et al. (2010) or Wagner et al. (2019), but only in the form of side studies.

To obtain a comprehensive picture, we used the RAPSODI forward model to simulate two sets of non-polarimetric dSCDs, with the scalar and the vectorised approach, respectively, on the basis of the scenarios by Frieß et al. (2019), as already introduced in Section 8.2. Figure 8.8 compares the results in form of scatter plots. Figure 8.9 shows the same data as box-whiskers, aggregated by the underlying aerosol scenarios.

The deviations are not large but on the order of those observed between different forward models (see Section 8.2) and exceed typical dSCD measurement uncertainties. There is a clear tendency towards negative deviations, hence an underestimation of dSCDs when the scalar approximation is used. It is largest for scenarios with no or low aerosol load (compare Figure 8.4), which is expected, as in these cases, strongly polarising molecular scattering dominates the RT. Regarding different species, largest deviations relative to the typical dSCD uncertainties occur for O_4.

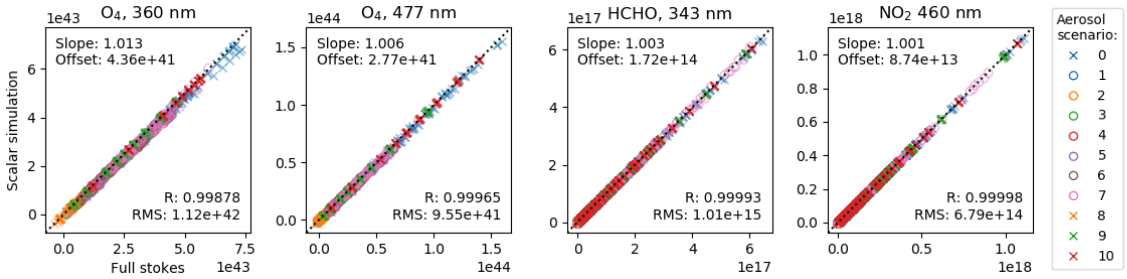

Figure 8.8: Comparison of dSCDs for different species from the RAPSODI forward model using full stokes RT simulations and the scalar approximation respectively.

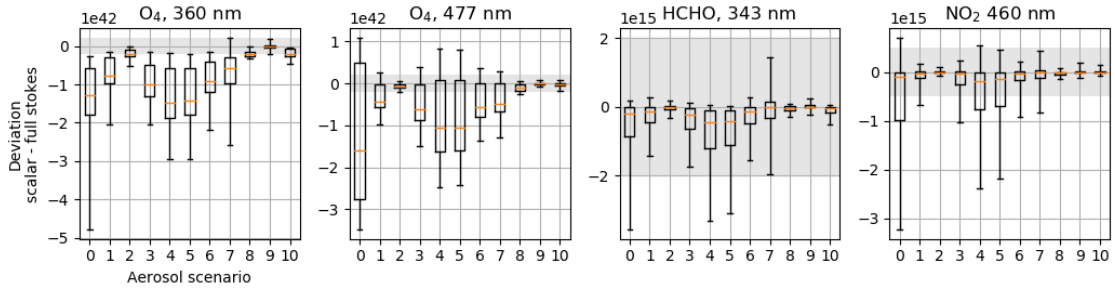

Figure 8.9: Same data as in Figure 8.8 but depicted in the form of box-whisker plots aggregated by the underlying aerosol scenarios. Grey shaded areas indicate the typical detection limits from the DOAS spectral analysis as proposed by Frieß et al. (2019).

Further, deviations increase with decreasing wavelengths, where the contribution of multiple scattered light to the total radiance increases. Figure 8.10 aggregates the same data by different solar and viewing geometries. Deviations seem to increase with SZA. Regarding RAAs, smallest deviations appear at 0°, where the average DOLP is expected to be smaller than at RAAs of 90° or 180° (compare Section 6.2). For the elevation angles, the patterns are different depending on the species and the retrieval wavelength. In summary, the scalar approximation seems most critical for large SZAs, small wavelengths and scenarios as well as viewing directions under which large DOLPs are expected. The magnitude of the deviations is not critical for typical MAX-DOAS profile retrievals, however, for cases where very accurate simulation results are essential, our findings should be kept in mind.

8.4 Weighting function analysis

To obtain a first idea on the potential of polarimetric MAX-DOAS observations, it is useful to investigate their sensitivity to different atmospheric parameters. For this purpose we simulated weighting functions in a model atmosphere with an

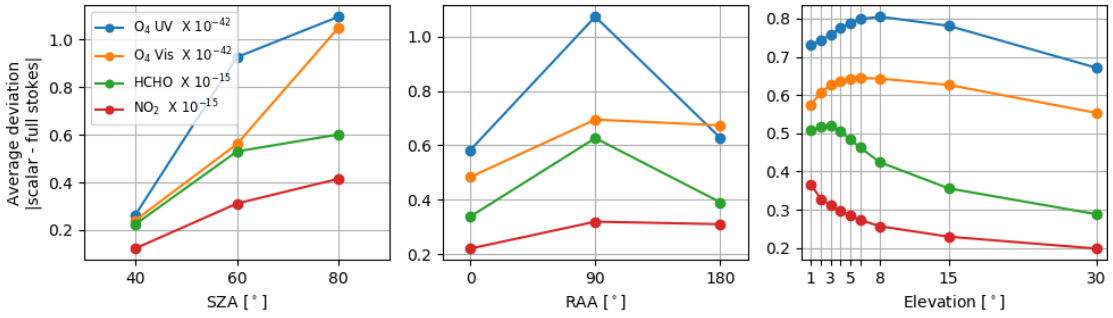

Figure 8.10: Same data as in Figure 8.8, this time aggregated by different solar and viewing geometries. Values for O_4 are given in molec^2 cm^{-5}, values for HCHO and NO_2 are given in molec cm^{-2}.

exponential aerosol profile of 1 km scale height and an aerosol vertical column of $V_{aer} = 10^8\,\mu m^2\,cm^2$. We assume standard mixed aerosol with properties according to Table 3.2.

To keep things as concise as possible we focus on four observable quantities: non-polarimetric SOTs $\tau = \ln(I_{TOA}/I)$, DOLPs D_L, non-polarmetric O_4 SCDs S_{o4} and the polarimetric O_4 SCD excentricity (ϵ_{O_4}). The latter is defined as,

$$\epsilon_{O_4} = 2\frac{\max_\delta(S_{O_4}) - \min_\delta(S_{O_4})}{\max_\delta(S_{O_4}) + \min_\delta(S_{O_4})}, \tag{8.2}$$

(in analogy to Eq. 6.5) with δ being the instrument PA. For the four observables (in this section represented by Y), we calculated normalised weighting functions $\bar{K}$ with respect to multiple atmospheric parameters $X \in [V_{aer}, r_1, r_2, \sigma_1, \sigma_2, \Re n, \Im n, f]$ according to

$$\bar{K} = \frac{\sigma_X}{\sigma_Y}\frac{\partial Y}{\partial X}. \tag{8.3}$$

The normalising factor includes a typical a priori uncertainty σ_X and a typical measurement error σ_Y. This normalisation is convenient since values of $|\bar{K}| \ll 1$ indicate that there is not much to learn from the measurement, whereas values of $|\bar{K}| \gtrsim 1$ indicate "useful" sensitivity. For the a priori uncertainties σ_X we assumed the values given in Table 9.4. For the measurement uncertainties of SOTs (σ_τ) and O_4 SCDs (σ_{S_o4}) we assumed 0.02 and 2 %, respectively. Uncertainties of DOLPs and O_4 excentricity were approximated by $\sigma_{D_L} = \sqrt{2}\cdot\sigma_\tau/\tau$ and $\sigma_{\epsilon_{o4}} = \sqrt{2}\cdot\sigma_{S_{o4}}/S_{O_4}$, respectively.

The SZA was set to 30°. Simulations were performed for multiple EAs α in the solar principal plane. They range from 1° (just above the horizon at RAA $\phi = 0°$) to 179° (just above the horizon at RAA $\phi = 180°$). Wavelengths λ between 300 and 600 nm were considered. The results are shown in Figure 8.11.

It shall be noted that the sensitivities of τ and D_L have already been extensively investigated within the aerosol community (e.g. Dubovik and King, 2000b;

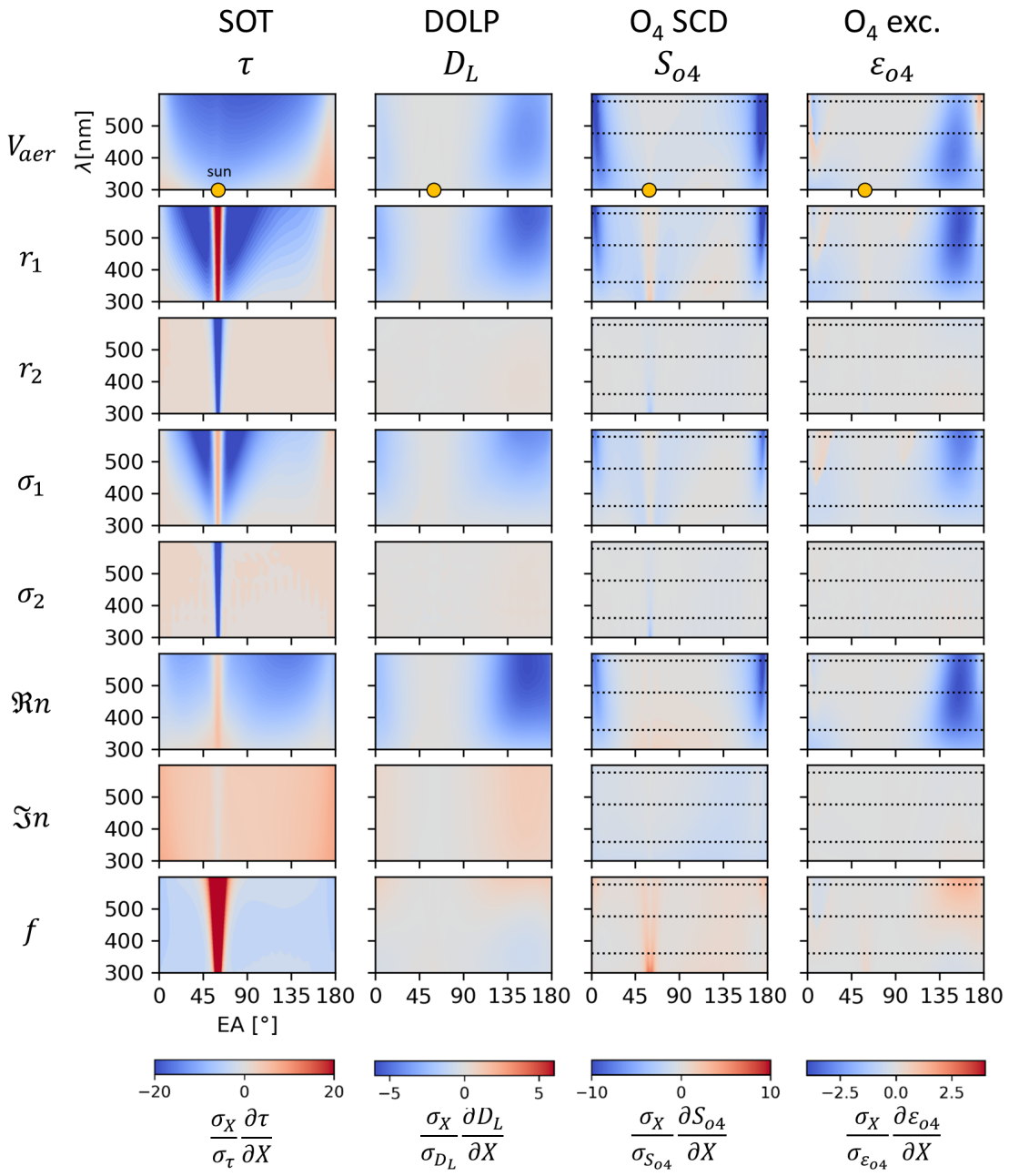

Figure 8.11: Normalised weighting functions of four key observables (columns) to different parameters (rows) for multiple wavelengths (vertical axes) and EAs in the solar principal plane (horizontal axes). See main text for further details. Black dotted lines indicate wavelengths were O_4 actually exhibits absorption bands (360, 477 and 577 nm, compare also Figure 3.3).

Boesche et al., 2006; Li et al., 2009) and the sensitivity of S_{O_4} to the aerosol abundance is exploited in conventional MAX-DOAS retrievals (e.g. Frieß et al., 2006). The fundamentally new aspects in Figure 8.11 are the sensitivity of S_{O_4} to aerosol microphysical properties and the consideration of ϵ_{O_4}.

The weighting functions provide first interesting insights. It is well known that observations of SOTs in the solar aureole region are very sensitive to aerosol properties (e.g. Dubovik and King, 2000b) but also S_{O_4} exhibits significant sensitivities here (e.g. to the modal fraction f), particulalry at short wavelengths. In Section 6.4, we already found that DOLP and ϵ_{O_4} behave similar to some extent. However, in Figure 8.11 the weighting function patterns for the two quantities differ, indicating that polarimetric SCDs of O_4 provide a "new kind" of information on aerosols, that, to our knowledge, has not yet been used by any other remote sensing approach. In general, the weighting functions with respect to different parameters exhibit very similar patterns, even though of different sign and magnitude. Therefore, rather strong (anti-)correlations might be expected during the retrieval. The sensitivity to the coarse mode parameters r_2 and σ_2 is generally very low. Significant information can only be inferred from SOTs in the solar aureole region. In contrast, typical MAX-DOAS elevation scans at RAAs larger than a few degrees are unlikely to allow a meaningful retrieval of coarse mode aerosol properties even if polarimetric information is incorporated.

9 Multispectral polarimetric retrievals with RAPSODI

In this chapter, the potential of the novel features of the RAPSODI algorithm are investigated on the basis of synthetic data. The focus is on polarimetric observations and how they improve our knowledge on the atmospheric state compared to conventional non-polarimetric measurements. Furthermore, the effect of simultaneous retrievals of aerosol and trace gases, the feasibility of aerosol microphysical property retrievals, the potential of unconventional viewing geometries and the incorporation of spectral broad band information are discussed. Regarding the polarimetric observations, we assume an instrument similar to the PMAX-DOAS as described in Section 11. Hence, a MAX-DOAS instrument with a motorised linear polariser inside the telescope, allowing to record spectra of skylight at different polarisation orientations, from which polarimetric dSOTs and dSCDs are inferred.

9.1 Synthetic dataset

The basis for our studies are synthetic measurements (dSCDs and dSOTs), simulated with the RAPSODI forward model for a multitude of atmospheric conditions and viewing geometries. Where possible, the underlying scenarios were once again adapted from Frieß et al. (2019) as already introduced in Section 8.2.1.

Table 9.1 provides an overview on the simulated observations. Simulations are performed at six different wavelengths $\lambda \in [343, 360, 415, 460, 477, 532\,\mathrm{nm}]$. DSCDs are simulated for O_4, HCHO and NO_2. As shown in Table 9.1, dSOTs are simulated at all six wavelengths, whereas trace gas dSCDs are limited to wavelengths where the corresponding gases achieve significant OTs to be detected by DOAS in reality. The wavelengths for dSCD simulation are representative for typically applied DOAS spectral fitting ranges and were adapted from the settings used in Tirpitz et al. (2020).

The different vertical profiles for aerosol and trace gases assumed for the simulation calculations are shown in Figure 9.1, and their key properties are listed in Table 9.2. Compared to Section 8.2.1, the number of different aerosol profiles was reduced here: the extreme cases with optically thick fog and cloud layers were not considered. Synthetic observations were calculated for all 63 combinations of aerosol and trace gas profiles, always applying a common trace gas profile for both, NO_2 and HCHO. The aerosol extinction coefficient profiles (in units of km^{-1}) defined in Frieß et al. (2019) were converted to aerosol area concentration profiles in $\mu\mathrm{m}^2\,\mathrm{cm}^{-3}$ (as required by RAPSODI) assuming an extinction efficiency of $E_{aer} = 2$. For pressure,

Table 9.1: Overview on the simulated observations.

Observations	λ [nm]	Absorption cross-section	Assumed error
dSOTs	343, 360, 415 460, 477, 532	N.A.	0.02
O_4 dSCDs	360, 477	293 K, Thalman and Volkamer (2013)	$2 \cdot 10^{41}$ molec^2 cm^{-5}
HCHO dSCDs	343	297 K, Meller and Moortgat (2000)	$2 \cdot 10^{15}$ molec cm^{-2}
NO_2 dSCDs	360, 460	294 K, Vandaele et al. (1998)	$5 \cdot 10^{14}$ molec cm^{-2}

temperature and humidity profiles, we assumed a US standard atmosphere. Ozone was not included.

In contrast to Frieß et al. and Section 8.2.1, we use an exponential altitude grid according to Equation 8.1 here, with 40 layers spanning an altitude range from 0 to 60 km and with a surface layer height of 50 m, resulting in values of $a = 0.3676$ and $b = 1.13602$ to be inserted into Eq. 8.1. As described in Section 8.1, these settings were found to be appropriate for our purposes. The original profiles by Frieß et al. were adapted to the new grid and thus occasionally changed in shape, while the profiles' total vertical columns were preserved. Even though 40 layers are considered within the forward model, only the lowest 25 layers between 0 and ≈ 8.5 km are actually retrieved, since the sensitivity of the measurements for trace gas and aerosol abundances above are negligible (see for instance right panel of Figure 9.3).

We further performed simulation calculations for different solar and instrument viewing geometries according to Table 9.3. SZA (θ), RAA (ϕ) and EA (α) define what in the following will be referred to as the *viewing direction*. PAs (δ) describe the orientation of the polariser's transmitting axis with respect to the horizontal and increase counter-clockwise when looking into the viewing direction of the instrument. Measurements without polariser are indicated by a dash ($\delta = -$). Observations are simulated for each combination of EA, SZA, RAA and PA. We assume the instrument to be located on the ground at sea level. In the following we will refer to each set of an aerosol profile, a trace gas profile, distinct SZA and elevation scan RAA as *atmospheric scenario*.

We calculate observations for two aerosol cases: in the first case we apply the Mie aerosol model and in the second case the HG aerosol model (both described in Section 7.3.1). The applied aerosol parameters for both cases are given in Table 9.4 and are the same in all simulations. The effect of different aerosol sizes is investigated separately in Section 9.2. The Mie parameters are those for the "standard mixed aerosol" that was already introduced in Section 3.3.3 including illustrations of the size distribution (Figure 3.6), the bulk optical properties (Figure 3.7) and the scattering matrix (Figure 3.8). For the HG-model, we assume a scattering efficiency of $E_{\mathrm{hg}} = 2$ at $\lambda_{E_{\mathrm{hg}}} = 400$ nm.

The resulting synthetic dataset consists of over one million dSOTs and dSCDs and one hundred million associated weighting functions, simulated for all possible

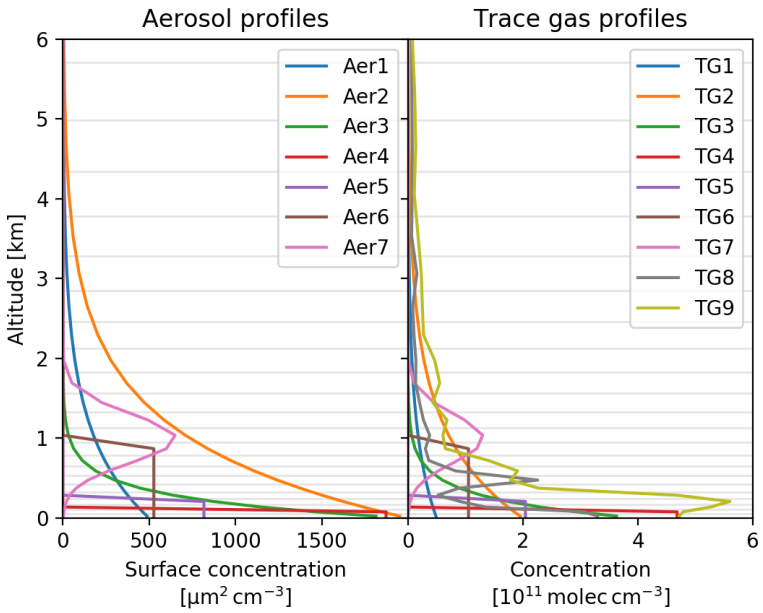

Figure 9.1: Aerosol area concentration (left) and trace gas concentration (right, same profiles for HCHO and NO_2) vertical profiles used as input for the forward modelling of the synthetic data. Key properties of each profile are also described in Table 9.2.

combinations of aerosol profiles, trace gas profiles, viewing geometries and aerosol models introduced before. Any subset of the simulated observations can be summarised into a synthetic measurement vector $\hat{\mathbf{y}}$ to be fed to the RAPSODI retrieval algorithm. Particularly, observations can be added or removed and the effect on the inversion results can be assessed. We investigate different sets of measurements, in the following referred to as *measurement modes*. $\hat{\mathbf{y}}$ always includes a full elevation scan including all ten EAs given in Table 9.3. Depending on the measurement mode, the corresponding almucantar scan is included or not. For a convenient representation, each measurement mode is described by a code, consisting of several flags as defined in Table 9.5, indicating which observations are incorporated. A few examples shall be given here for illustration: The mode labels 'UV' and 'Vis' indicate conventional retrievals from non-polarimetric dSCDs for each species at a single wavelength in the UV and Vis spectral range, respectively, and assume that all species are retrieved separately. In contrast, the mode label 'Multi-S-P-A' indicates that the measurement set was extended to all wavelengths, that all species are retrieved simultaneously, and that polarimetric observations as well as an almucantar scan have been included.

Apart from different measurement modes, we also modify the set of retrieved state vector elements $\mathbf{x}$ by applying either the Mie or the HG aerosol model and thereby retrieving either the aerosol microphysical or optical properties. We further consider a *fixed aerosol* case: here, the retrieval is performed using the HG-model, however,

Table 9.2: Description of aerosol and trace gas profiles as depicted in Figure 9.1. Aerosol VCDs are in 10^8 µm^{2}cm^{-2} and trace gas VCDs in 10^{15} moleccm^{-2}

Profile	Description	VCD
Aer0	No aerosol	0.0
Aer1	Exponential, 1 km scale height	0.5
Aer2	Exponential, 1 km scale height	2.0
Aer3	Exponential, 250 m scale height	0.5
Aer4	Box profile, 107 m height	0.2
Aer5	Box profile, 245 m height	0.2
Aer6	Box profile, 948 m height	0.5
Aer7	Gaussian at 1 km, 300 m FWHM	0.5
TG0	No trace gas	0.0
TG1	Exponential, 1 km scale height	5.0
TG2	Exponential, 1 km scale height	20.0
TG3	Exponential, 250 m scale height	10.0
TG4	Box profile, 107 m height	5.0
TG5	Box profile, 245 m height	5.0
TG6	Box profile, 948 m height	10.0
TG7	Box profile, 948 m height	10.0
TG8	NO_2 balloon sonde profile[a] (2016-09-14)	17.73
TG9	NO_2 balloon sonde profile[a] (2016-09-21)	40.88

[a] Balloon sonde flights were performed during the CINDI-2 campaign in the Netherlands in 2016 (Kreher et al., 2019)

with the concentration profiles as the only state vector elements being retrieved. The underlying HG parameters and surface albedo are set to the true values as given in Table 9.4.

9.2 General information content analysis

A major aim of this thesis is to investigate how the information on the state vector elements $\mathbf{x}$ changes for different measurement modes, particularly by adding polarimetric observations. For the quantification of information we will follow the concept of degrees of freedom of signal (DOFS) as introduced in Section 5.5. Note that, for the calculation of DOFS, we do not need to perform any inversion, since Eq. 5.19 only requires the a priori covariance $\mathbf{S}_a$, the measurement covariance $\mathbf{S}_y$ as well as the weighting functions $\mathbf{K}$, calculated for a distinct atmospheric state $\hat{\mathbf{x}}$. The weighting functions were already derived for the scenarios described above during creation of the synthetic observation dataset. It is now straightforward to derive DOFS for any atmospheric scenario, measurement mode and aerosol case, by including the respective elements in $\mathbf{K}$, $\mathbf{S}_y$ and $\mathbf{S}_a$. Table 9.6, 9.7 and 9.8 show the average DOFS

Table 9.3: Solar and instrument viewing geometries applied for the simulation of synthetic observations. Simulations were performed for each combination of EA, SZA, RAA and PA. A dash in the PA indicates non-polarimetric observations.

Parameter	Values [°]
SZA (θ)	40, 60, 90
RAA (ϕ)	Elevation scans: 0, 90, 180° Almucantar scan: 2, 2.5, 3, 3.5, 4, 5, 6, 10, 12, 14, 16, 18, 20, 25, 30, 35, 40, 45, 50, 60, 70, 80, 90, 100, 120, 140, 160, 180
EA (α)	1, 2, 3, 4, 5, 6, 8, 15, 30, 90
PA (δ)	-, 0, 60, 120

Table 9.4: Settings for the state vector elements $\mathbf{x}$ applied in this study. The *true values* were used for the forward simulation of synthetic observations. Typically observed values for surface albedo and aerosols were adapted from Dubovik et al. (2002). Typically observed values for trace gas concentrations were derived from data presented in (Tirpitz et al., 2020). Remaining table columns describe the a priori settings applied for the inversion procedure.

Parameter	True value	Apriori value	Apriori uncertainty	Correlation length	Typically observed values
c_{aer}	see Fig. 9.1	Exp. profile[a]	50 %	1 km	$(6.6 \pm 5.6) \cdot 10^2$ µm^2/cm^3
c_{HCHO}	see Fig. 9.1	Exp. profile[b]	50 %	1 km	$(5.0 \pm 3.4) \cdot 10^{10}$ molec/cm^3
c_{NO_2}	see Fig. 9.1	Exp. profile[c]	50 %	1 km	$(18 \pm 10) \cdot 10^{10}$ molec/cm^3
ω_{surf}	0.043	0.054	0.03	400 nm	0.043 ± 0.011 [f]
g_{hg}	0.74	0.69	0.1	400 nm	0.74 ± 0.05 [f]
ω_{hg}	0.91	0.94	0.1	400 nm	0.91 ± 0.03 [f]
$\mathring{a}_{\mathrm{hg}}$	1.2	0.8	0.4	-	$0.4 < \mathring{a}_{\mathrm{hg}} < 2.0$
r_1	0.095 µm	0.111 µm	30 %	-	(0.095 ± 0.016) µm
r_2	0.49 µm	0.43 µm	30 %	-	(0.49 ± 0.06) µm
σ_1	0.46	0.5	20 %	-	0.46 ± 0.04
σ_2	0.76	0.71	20 %	-	0.76 ± 0.05
$\Re\, n_m$	1.44	1.46	0.1	400 nm	1.44 ± 0.02 [f]
$\Im\, n_m$	0.011	0.018	100 %	400 nm	0.011 ± 0.007 [f]
f	0.9983	0.996	0.003	-	0.9983 ± 0.0023

[a] 1 km scale height, VCD of $0.5 \cdot 10^8$ µm^2 cm^2
[b] 1 km scale height, VCD of $8 \cdot 10^{15}$ molec/cm^2
[c] 1 km scale height, VCD of $9 \cdot 10^{15}$ molec/cm^2
[f] Value at 440 nm

obtained on each parameter for the Mie model, the HG model and the fixed aerosol case, respectively. Remember that concentrations c_s are retrieved at 25 altitudes to

Table 9.5: Overview on the flags that describe different measurement modes.

Flag	Description
	Spectral band of the observations.
UV	UV indicates that only observations at 343 and 360 nm go into the retrieval.
Vis	Vis includes only observations at 415, 460, 477 and 532 nm.
Multi	Multi includes observations at all available wavelengths (see Table 9.1).
S	Indicates a simultaneous retrieval of all species in a common model atmosphere. In contrast to the other flags, this is a retrieval setting and therefore does not change the composition of the measurement vector. If 'S' is not contained in the mode description, species are retrieved separately: first, aerosol concentrations and properties as well as surface albedo are inferred from O_4 dSCDs and dSOTs, then each trace gas profile is retrieved in the resulting atmosphere with all other parameters being fixed.
P	Indicates the incorporation of polarimetric information. No 'P' in the mode code indicates that only observations with no polariser ($\delta = -$) are considered. Otherwise, DSCDs at all PAs except $\delta = -$ are incorporated, each evaluated against the reference SCD at $\alpha = 90°$ and $\delta = 0°$. Further, to capture broadband polarisation features, dSOTs at $\delta \in [60, 120°]$ are incorporated, each evaluated against the SOT at the same viewing direction and $\delta = 0°$ (see Section 7.2.2 for further explanations).
I	Indicates that spectral broadband features between different viewing directions serve as additional source of information. In this case, dSOTs at $\delta = 0°$ are incorporated, each evaluated against the SOT at $\alpha = 90°$ and $\delta = 0°$ (see Section 7.2.2 for further explanation).
A	Indicates the incorporation of an almucantar scan, performed under the same solar geometries and atmospheric conditions as the elevation scan. The effects of 'S' and 'P' described above also apply for the almucantar dSCDs and dSOTs.

Table 9.6: The DOFS achieved by different measurement modes (table rows) for the individual state vector elements (table columns) averaged over the simulated atmospheric scenarios scenarios, namely all combinations of aerosol profiles, trace gas profiles, SZAs and RAAs. Here, for the case that surface albedo and Mie model input parameters are retrieved. The lowest row shows the number of summarised parameters, hence, the maximum possible number of DOFS.

Measurement mode					Total	Profiles			Surface	Aerosol properties								
Band	S	P	A	I		c_{aer}	c_{HCHO}	c_{NO_2}	ω_{surf}	r_1	r_2	σ_1	σ_2	$\Re n_1$	$\Re n_2$	$\Im n_1$	$\Im n_2$	f
UV	✗	✗	✗	✗	8.6	1.21	1.93	2.97	0.17	0.65	0.04	0.21	0.09	0.81	0.0	0.33	0.02	0.21
UV	✓	✗	✗	✗	8.9	1.51	1.76	2.59	0.24	0.68	0.05	0.24	0.11	1.01	0.0	0.43	0.03	0.24
UV	✓	✓	✗	✗	12.5	2.5	2.14	3.11	0.72	0.77	0.08	0.43	0.19	1.23	0.01	0.77	0.06	0.42
Vis	✗	✗	✗	✗	7.2	1.3	0.0	2.89	0.18	0.65	0.05	0.36	0.09	0.82	0.0	0.47	0.06	0.31
Vis	✓	✗	✗	✗	7.5	1.52	0.0	2.31	0.26	0.66	0.05	0.37	0.1	1.26	0.0	0.57	0.08	0.33
Vis	✓	✓	✗	✗	11.1	2.65	0.0	2.79	0.83	0.75	0.08	0.57	0.15	1.57	0.04	0.86	0.22	0.59
Multi	✓	✗	✗	✗	13.5	1.99	1.77	2.89	0.67	0.73	0.07	0.51	0.16	2.77	0.01	1.32	0.15	0.44
Multi	✗	✓	✗	✗	20.8	2.89	2.34	3.77	1.62	0.85	0.1	0.72	0.23	4.95	0.13	2.12	0.42	0.63
Multi	✓	✓	✗	✗	21.9	3.24	2.21	3.43	1.95	0.87	0.11	0.75	0.26	5.22	0.15	2.54	0.5	0.65
Multi	✓	✗	✓	✗	18.2	2.66	1.99	3.2	1.57	0.86	0.24	0.82	0.69	2.96	0.05	1.95	0.29	0.92
Multi	✓	✓	✓	✗	27.4	3.91	2.5	3.77	2.95	0.97	0.31	0.95	0.78	5.62	0.5	3.21	0.99	0.96
Multi	✓	✗	✗	✓	20.8	2.46	1.83	2.99	1.62	0.81	0.11	0.69	0.24	5.15	0.04	3.86	0.45	0.55
Multi	✓	✓	✓	✓	32.6	4.12	2.55	3.83	3.93	0.99	0.71	0.98	0.93	5.93	0.97	5.12	1.52	0.98
					110	25	25	25	6	1	1	1	1	6	6	6	6	1

obtain profiles and that ω_{surf}, g_{hg}, ω_{hg}, n_1 and n_2 are retrieved at six wavelengths. For these state vector elements the DOFS are summed up, therefore yielding values > 1. The number of summed state vector elements, hence, the maximum possible number of DOFS, is indicated in the lowest table row. The results for Mie aerosol are also visualised in Figure 9.2. In the following discussions and investigations we will focus on the Mie aerosol case, as it provides the most complete parametrisation of the atmospheric state.

The effect of polarimetric information (flag P) for different cases can be inferred by comparing UV-S and UV-S-P, Vis-S and Vis-S-P, Multi-S and Multi-S-P and so on. A significant increase in information is observed for all these modes when adding polarimetric information, particularly on aerosol optical and fine mode microphysical properties, aerosol profiles and surface albedo. For the Multi-S-P mode, the increase is about 1.2 DOFS (60 %) for the aerosol profile, 0.5 DOFS (20 %) for trace gas profiles, 1.3 DOFS (190 %) in the surface albedo and 4.7 DOFS (80 %) for aerosol properties. For the HG-model, these figures slightly reduce for profiles and surface albedo. Regarding the fixed aerosol case (Table 9.8), the increases in DOFS are significantly smaller (by about 50 % compared to the Mie model case), indicating that a large fraction of the increase in information on the profiles in the Mie model case is an indirect effect of the improved knowledge on aerosol properties and surface albedo.

In addition to the information shown in the DOFS tables, it is worth discussing the individual effects of polarimetric dSCDs and polarimetric dSOTs. While po-

Table 9.7: Same as Table 9.6 but for the case that surface albedo and HG aerosol parameters are retrieved.

Measurement mode					Total	Profiles			Surface	Aerosol properties		
Band	S	P	A	I		c_{aer}	c_{HCHO}	c_{NO_2}	ω_{surf}	g_{hg}	ω_{hg}	$\mathring{a}_{\mathrm{hg}}$
UV	✗	✗	✗	✗	8.2	1.7	1.91	2.95	0.2	0.93	0.55	0.0
UV	✓	✗	✗	✗	8.4	1.98	1.78	2.63	0.26	1.01	0.66	0.09
UV	✓	✓	✗	✗	10.9	2.79	2.16	3.12	0.7	1.11	0.94	0.13
Vis	✗	✗	✗	✗	6.8	1.91	0.0	2.89	0.29	0.95	0.75	0.0
Vis	✓	✗	✗	✗	7.1	2.09	0.0	2.47	0.36	1.1	0.87	0.17
Vis	✓	✓	✗	✗	9.4	2.92	0.0	2.9	0.84	1.35	1.11	0.28
Multi	✓	✗	✗	✗	13.0	2.51	1.8	2.91	0.72	2.5	1.77	0.81
Multi	✗	✓	✗	✗	18.6	3.14	2.31	3.75	1.48	4.55	2.45	0.88
Multi	✓	✓	✗	✗	19.6	3.5	2.21	3.42	1.79	4.84	2.87	0.93
Multi	✓	✗	✓	✗	16.0	3.08	2.05	3.21	1.61	2.83	2.26	0.92
Multi	✓	✓	✓	✗	22.9	3.99	2.49	3.77	2.61	5.5	3.56	0.98
Multi	✓	✗	✗	✓	20.1	2.98	1.84	3.0	1.79	4.95	4.63	0.92
Multi	✓	✓	✓	✓	27.0	4.23	2.54	3.85	3.83	5.99	5.59	1.0
					93	25	25	25	6	6	6	1

larimetric dSCDs predominantly increase the information on the vertical profiles, polarimetric dSOTs increase information mainly on aerosol properties. However, polarimetric dSCDs and dSOTs also carry significant amounts of equivalent information: starting from the Multi-S mode in the Mie aerosol case, the incorporation of polarimetric dSCDs increases the total DOFS from 13.5 to 17.8, whereas including only polarimetric dSOTs yields 18.8 DOFS. Including both yields the Multi-S-P mode with 21.9 DOFS.

The left panel of Figure 9.3 shows the increase in DOFS between the Multi-S and the Multi-S-P measurement mode (referred to by "ΔDOFS"), grouped by the different aerosol scenarios. As expected ΔDOFS mostly depends on the aerosol scenario, as the effective light paths are predominantly determined by the atmosphere's aerosol content. The dependence on the trace gas profiles is not shown here, but was found to have minor effect on ΔDOFS, at least for optically thin trace gases. The figure indicates that the information content on aerosol properties in polarimetric observations is not only dependent on the aerosol optical thicknesses but further, an aerosol vertical distribution over a large altitude range, preferably from the surface to altitudes of several hundred metres, is advantageous. The right panel of Figure 9.3 shows DOFS profiles, namely the DOFS obtained for the concentrations of different species in each retrieved layer. The DOFS profiles indicate a large relative increase in information on aerosol concentrations at higher altitudes between 1 and 4 km. However, the absolute values are still rather small (< 0.2), such that aerosol abundances at these altitudes remain hardly retrievable even with polarimetric MAX-DOAS observations.

The effect of the simultaneous retrieval of aerosol and trace gases (flag S) can be inferred by comparing the measurement modes UV and UV-S as well as Vis and Vis-S. As expected, the information content in aerosol profiles and properties is slightly enhanced (by about 0.3 and 0.4 DOFS, respectively) since besides the O_4 dSCDs also

Table 9.8: Same as Table 9.6 but for the case that only profiles are retrieved while surface and aerosol properties are fixed to the true values as given in Table 9.4.

Measurement mode					Total	Profiles		
Band	S	P	A	I		c_{aer}	c_{HCHO}	c_{NO_2}
UV	✗	✗	✗	✗	7.2	2.3	1.91	2.95
UV	✓	✗	✗	✗	7.2	2.55	1.86	2.75
UV	✓	✓	✗	✗	8.7	3.22	2.26	3.2
Vis	✗	✗	✗	✗	5.4	2.56	0.0	2.89
Vis	✓	✗	✗	✗	5.4	2.78	0.0	2.67
Vis	✓	✓	✗	✗	6.6	3.53	0.0	3.1
Multi	✓	✗	✗	✗	8.2	3.22	1.88	3.08
Multi	✗	✓	✗	✗	9.7	3.66	2.31	3.75
Multi	✓	✓	✗	✗	9.8	3.99	2.28	3.57
Multi	✓	✗	✓	✗	9.2	3.69	2.11	3.41
Multi	✓	✓	✓	✗	10.8	4.35	2.56	3.92
Multi	✓	✗	✗	✓	8.6	3.57	1.88	3.1
Multi	✓	✓	✓	✓	10.9	4.41	2.56	3.92
					75	25	25	25

trace gas dSCDs are sensitive to aerosols (as they affect the slant light path). On the other hand, the information on trace gas concentrations is reduced (≈ -0.4 DOFS), since the retrieval "becomes aware" of their cross-sensitivity to aerosol parameters and propagates the corresponding errors. Both effects have been omitted in former MAX-DOAS retrieval algorithms. The gain in information slightly prevails, resulting into an increase of about 0.3 DOFS in the total information content.

The information content in the measurements can further be enhanced by including almucantar scans (A) and the spectral broad band features (I). Our investigations indicate that, compared to conventional monochromatic retrievals, the total information content of MAX-DOAS observations can be more than doubled by applying multispectral, polarimetric dSOT and dSCD observations under optimised viewing geometries.

In general, the information obtained on the coarse mode aerosol properties remains low (less than 5 of 14 possible DOFS) for all measurement modes even for the Multi-S-P-A-I mode. The impact of the aerosol size distribution on the DOFS is discussed in more detail below.

We further investigated to what extent the DOFS depends on the AOT. Simulations for the Mie aerosol case at $\theta = 60$, $\phi = 90$ for different aerosol VCDs were performed, assuming an exponential c_{aer} profile with a scale height of 1 km. The TG1 scenario was chosen for the trace gas profiles. The obtained DOFS for three measurement modes and three parameter subgroups are illustrated in the left panel of Figure 9.4. For small AOTs (< 0.2) the DOFS for profiles remain constant. For higher values, the horizontal visibility range in the atmosphere and thus the sensitivity decreases. The DOFS for the surface albedo are generally low for non-polarimetric measurements. For multispectral measurements, highest values (DOFS of ≈ 5 for albedos at six different wavelengths) are obtained for low aerosol loads.

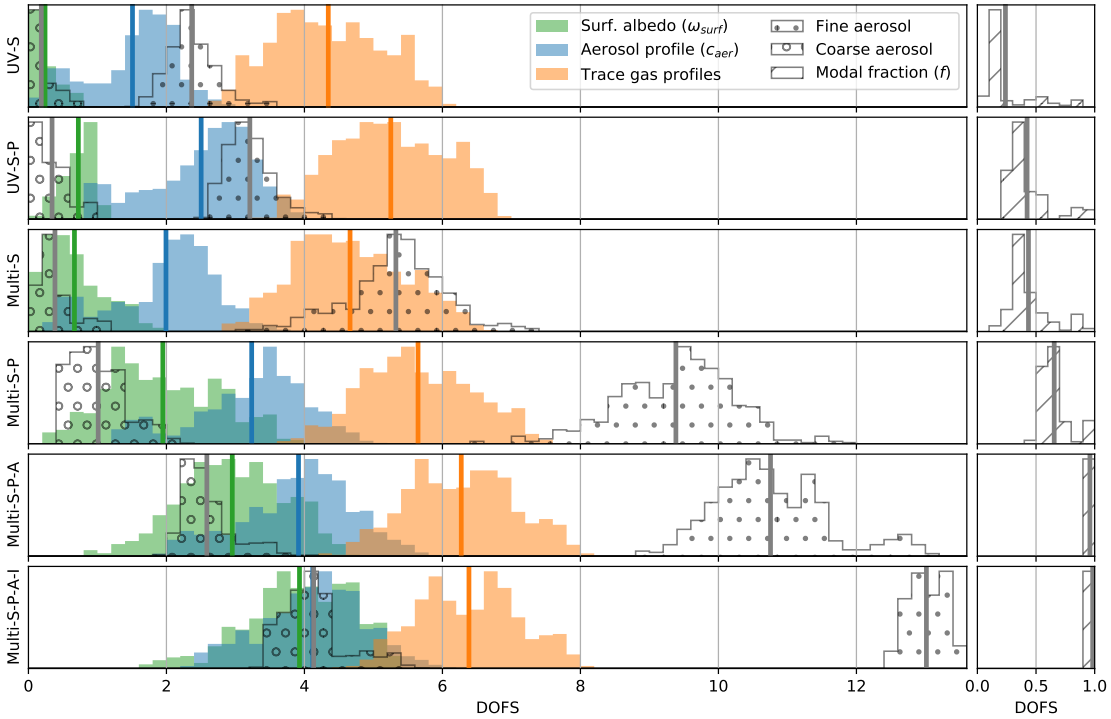

Figure 9.2: Visualisation of Table 9.6. Shown are histograms of the DOFS obtained for different parameter subgroups (see legend). Each occurence corresponds to one atmospheric scenario. Trace gas profile DOFS for NO_2 and HCHO have been summed up. Subplot rows show different measurement modes according to the labels on the left axes. The histograms are peak normalised, the vertical axis therefore indicates the number of occurences in arbitrary units. Histograms for the modal fraction f are shown in separate panels on the right to maintain readability of the figure. The aerosol scenario Aer0 (no aerosol) was excluded here.

For aerosol properties, there are two limiting factors: with decreasing aerosol abundance, of course the sensitivity towards aerosol properties decreases. On the other hand, the DOFS also decrease with high AOTs, again due to the limited visibility range. Maximum DOFS are achieved at AOTs around unity.

The right panel of Figure 9.4 shows the dependence of DOFS on the aerosol size for a monomodal Mie aerosol with properties as defined for the fine mode in Table 9.4, but with different mode radii r_1. We assume profile scenarios Aer1-TG1, $\theta = 60°$ and $\phi = 90°$. Note that the aerosol surface area is kept constant, whereas the AOT changes with r_1, due to the associated changes in aerosol scattering efficiency. For the UV-S and the Multi-S-P mode, there are only limited size ranges in which all aerosol parameters can be reasonably retrieved. This is expected, since the shape of the major aerosol scattering efficiency flank (see Figure 3.4) at size parameters close to unity strongly depends on the aerosol microphysical properties.

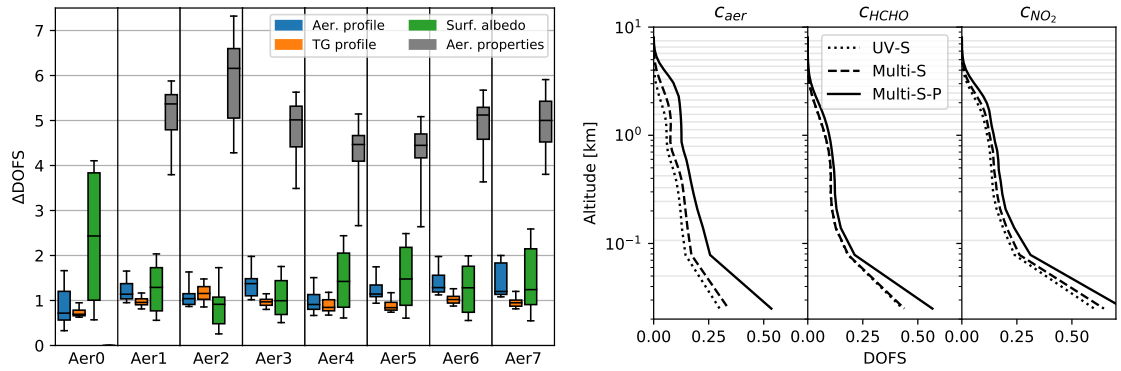

Figure 9.3: Left panel: box-whisker plots of DOFS increase grouped by different aerosol profile scenarios (different subplots) and parameter sub-groups (box colors) for the Mie model case. Δ DOFS is the difference in DOFS between the polarimetric (Multi-S-P) and non-polarimetric (Multi-S) measurement mode. Right panel: average DOFS profiles grouped by species (different subplots) for different measurement modes as indicated in the legend. Horizontal grey lines indicate model layer boundaries.

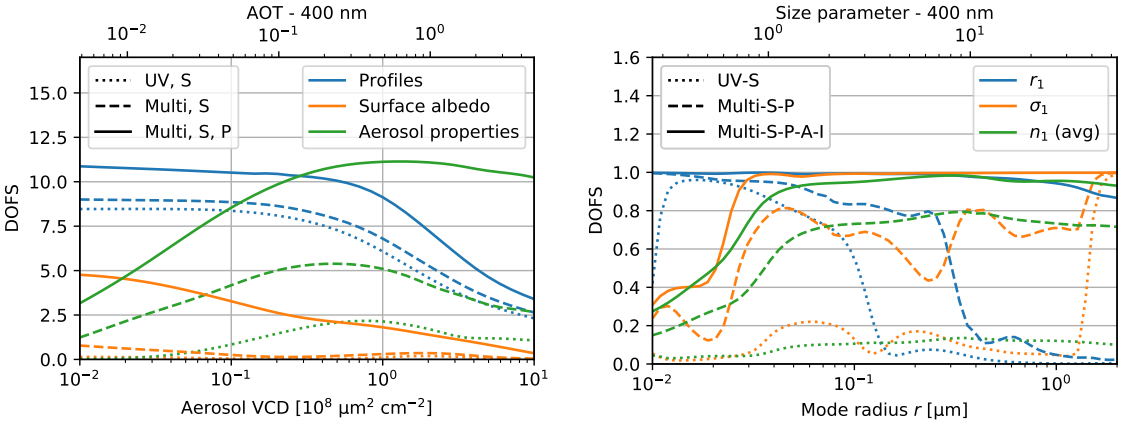

Figure 9.4: Dependence of DOFS on AOT (left panel) and aerosol size (right panel) for three different measurement modes and three state vector element subgroups. Simulations were performed with Mie aerosol, $\theta = 60°$, $\phi = 90°$ and trace gas scenario TG1. In the right panel, a monomodal size distribution is assumed. n_1 are average DOFS obtained for the real and imaginary refractive indices at multiple wavelengths. The size parameter on the top axis was calculated from the effective radius $r_{eff,1}$ according to Eq. 3.54.

Observations at corresponding wavelengths are therefore expected to yield most information. Consequently, for the Multi-S-P mode (also incorporating the larger

Vis wavelengths), the upper limit of the "useful" r_1-range is extended compared to UV-S. By adding an almucantar scan (A), the range cannot be further extended (not shown in the figure). In contrast, including (P), (A) and (I) simultaneously yields DOFS close to unity for all aerosol parameters and sizes up to $r_1 = 2\,\mu m$. Recall, however, that we consider monomodal aerosol here. The general lack of information on coarse aerosol indicated in Figure 9.2 suggests that in the bi-modal case, the modes remain hardly distinguishable. The "useful" size range might also be enhanced by extending the spectral range of observations to larger wavelengths. In fact, O_4 features absorption bands also at 577 and 630 nm. In the future, our investigations might therefore be extended to larger wavelengths. Interestingly, all measurement modes shown in Figure 9.4 yield very good information on r_1 for small r_1, while the information on the modal width increases with r_1.

9.3 Considerations on viewing geometries

The information content of polarimetric MAX-DOAS observations is expected to depend on the set of viewing geometries, at which measurements are provided. The left panel of Figure 9.5 shows the dependence of DOFS on the viewing geometry, namely different SZAs and elevation scan RAAs. For non-polarimetric observations, the dependence is generally weak, whereas for polarimetric observations there is a significant dependence with peak-to-peak changes of approximately 4 DOFS. The information content is lowest for elevation scans close to the sun, where the single scattering angles realised over the elevation scan are smaller than at larger RAAs. The thought arises, if polarimetric information is maximised at viewing directions with single scattering angles close to 90° (were large DOLPs are expected). This is well fulfilled for all EAs for instance if SZAs are large and elevation scan RAAs are close to 90°. In fact, for SZA $\theta = 80°$, a maximum in DOFS can be observed around RAAs $\phi = 90°$, exclusively for the Multi-S-P measurement mode.

To investigate this further, we also tested what in the following will be referred to as "tilted elevation scans": we assume the same set of EAs as before, but calculate RAAs for each EA according to Eq. 6.4 to ensure single scattering angles as close to 90° as possible. The resulting geometry for $\theta = 40°$ is illustrated in the right panel of Figure 9.5. The total DOFS obtained for such a tilted elevation scan with Mie aerosol, Aer1-TG1 profiles and measurement mode Multi-S-P yields 23.8. This is slightly smaller than the total DOFS of 24.4, achieved with a conventional vertical elevation scan at $\phi = 140°$ under equal atmospheric conditions (see Figure 9.5).

So far, we assumed measurements at three fixed PAs to always capture the full information on the light's polarisation state. However, for most viewing directions, the approximate orientation of the skylight polarisation χ can be reasonably predicted from Equation 6.2. As discussed in Section 3.1, two spectra, recorded with the polariser's transmitting axis parallel and perpendicular to the predicted χ, yield nearly the same information as the approach with three PAs. In fact, simulations for $\theta = 60°$, $\phi = 90°$, Mie aerosol and Aer1-TG1 profiles yields the nearly the same

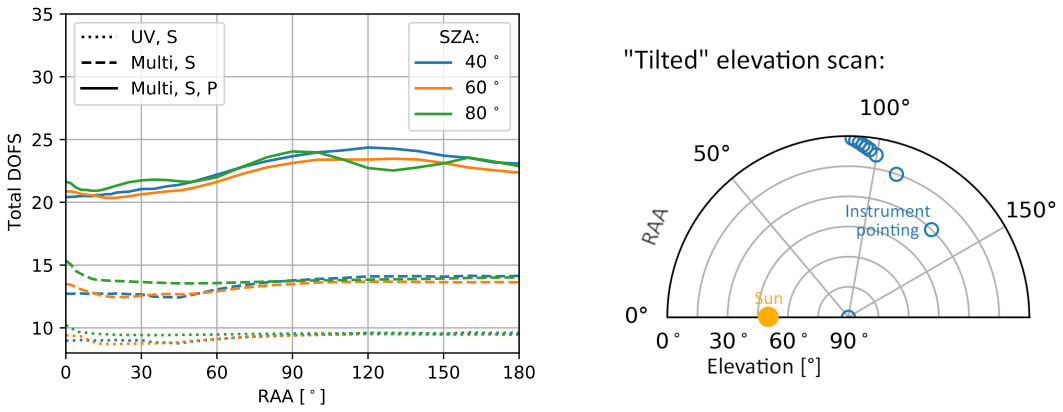

Figure 9.5: Left panel: dependence of the total DOFS on the viewing geometry, namely different SZAs (line colors) and elevation scan RAAs (x-axis). Simulations were performed with Mie aerosol and for the profile scenario Aer1-TG1. Right panel: illustration of the *tilted elevation scan* discussed in the main text.

number of total DOFS for both approaches: with two PAs one achieves 22.7 DOFS, with three PAs it is 23.0 DOFS. The approach with two angles improves the temporal resolution by a factor 2/3. Alternatively, the exposure times might be enhanced by a factor 3/2, yielding a corresponding gain in light (resulting in reduced dSCD uncertainties by a factor $\sqrt{2/3}$, see Section 9.6 for the reasoning), leading to an increase in total DOFS to 23.5. In the future also hybrid approaches incorporating measurements with and without polariser might be considered.

To further improve temporal resolution of MAX-DOAS measurements, it is also of interest, to what extent the number of viewing directions might be reduced without significant loss of information. For a test, we used measurement mode Multi-S-P-A, Mie aerosol, $\theta = 60°$, $\phi = 90°$, Aer1-TG1 and calculated the total DOFS for two cases: with the full elevation and almucantar scans according to Table 9.3 and with reduced elevation (EA $\in$ [1, 2, 5, 10, 30, 90°]) and almucantar scans ($\phi \in$ [2, 2.5, 3., 3.5, 4, 5, 7, 10, 15°]). The two cases yield total DOFS of 28.2 and 27.6, respectively. This is a surprisingly small decrease in information, considering the strong reduction in the number of viewing directions (from 38 to 15).

We conclude that there is a high potential for the optimisation of measurement geometries. In the future, the ideal geometries for different numbers of viewing directions might be investigated by performing more comprehensive studies in this direction.

9.4 Correlation coefficient matrix

In Section 8.4, it was shown that changes in different aerosol related parameters affect the observations in similar ways. Therefore, the retrieval results of the corresponding parameters are expected to exhibit significant correlations. It is therefore useful to have a glimpse either on the off-diagonal elements of $\mathbf{A}$ or on the correlation coefficient matrix $\mathbf{C}$, calculated from the retrieval covariance $\hat{\mathbf{S}}$ (see Equation 5.15) according to:

$$\mathbf{C} = (\mathrm{diag}(\hat{\mathbf{S}}))^{-\frac{1}{2}} \hat{\mathbf{S}} (\mathrm{diag}(\hat{\mathbf{S}}))^{-\frac{1}{2}} \tag{9.1}$$

We discuss $\mathbf{C}$ here, since it is unitless by definition and since we expect it to be more familiar to the reader. Figure 9.6 and 9.7 show sub-matrices of $\mathbf{C}$ (only including the correlation between surface albedo and aerosol related quantities for the Mie model case) for the Multi-S-P and the Multi-S-P-A-I mode, respectively.

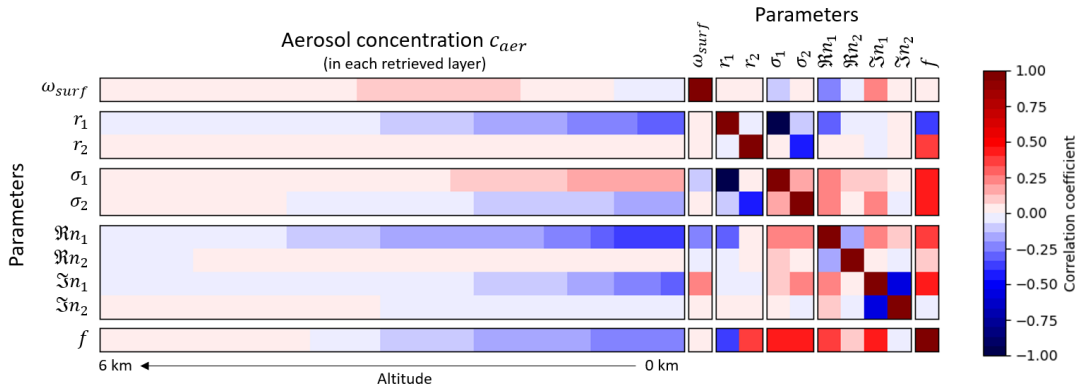

Figure 9.6: Correlation coefficient (sub-)matrix for the Mie aerosol case and the Multi-S-P mode, averaged over all atmospheric scenarios and viewing geometries.

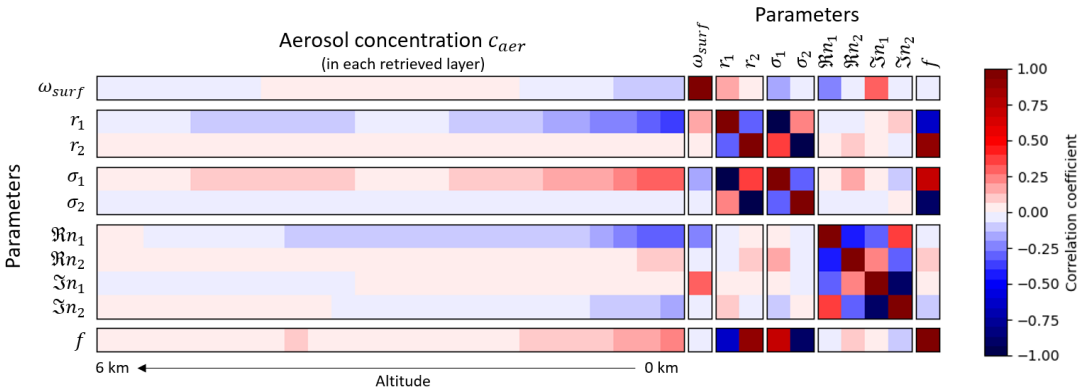

Figure 9.7: Same as Figure 9.7 but for the Multi-S-P-A-I mode.

On the first glance, it is counterintuitive that the correlation strength between many parameters increases for the Multi-S-P-A-I mode (compared to the Multi-S-P mode) despite it incorporates more observations and thus information. This effect is related to the OEM approach. In the Multi-S-P case, less information is available on the parameters. As a consequence, the latter are drawn closer to their fixed a priori values (compare Equation 5.12). Therefore they exhibit only small dependencies on the measurements and the correlation with other parameters is reduced. Accordingly, the additional information in the Multi-S-P-A-I case (from the almucantar scan as well as the dSOTs between different viewing directions) has two counteracting effects: on the one hand, it helps to disentangle the parameters, on the other hand, it reduces the a priori biases, thereby favouring correlations.

Both figures indicate large anticorrelations (up to ≈ -0.9) between median radius r_m and modal width σ_m for both modes m. Also the modal fraction f shows strong (anti)correlation to r_m and σ_m. Furthermore, the imaginary parts of the refractive indices of the two modes are strongly anticorrelated. Regarding refractive indices it might be generally reasonable to assume common values for both modes. AERONET retrievals make this assumption (see Section 12.4.3) and we also do so for the evaluation of field measurements in Section 16. There are further smaller (absolute values < 0.5) but significant correlations between multiple other parameters. For instance r_1, σ_1 and $\Re n_1$ show notable correlation with aerosol concentrations in distinct altitude ranges. As we shall see in Section 9.5, for the retrievals from synthetic observations under ideal conditions such correlations appear to not be very critical, at least for the (P)-modes. However, particularly in retrievals from field data recorded under atmospheric conditions that cannot be well represented by the model atmosphere (e.g. spatio-temporal inhomogeneities, complex Earth surface properties, aerosol size distributions deviating from the bi-modal approximation), they might destabilise the retrieval.

9.5 Retrieval results

The synthetic observations simulated before can also be used as input $\hat{\mathbf{y}}$ for RAPSODI to perform actual inversions. This was done for a reduced dataset of seven combinations of aerosol and trace gas profiles (Aer1-TG6, Aer2-TG5, Aer3-TG4, Aer4-TG1, Aer5-TG2, Aer6-TG7 and Aer7-TG3), for $\theta = 60°$, $\phi = 90°$ and for both the Mie and HG aerosol case. As before, different measurement modes are realised by feeding different sets of observations $\hat{\mathbf{y}}$ to RAPSODI. Each inversion was performed eleven times here: ten times (to obtain some statistics) with a random noise component added to $\hat{\mathbf{y}}$ with standard deviations according to the assumed uncertainties in Table 9.1 and once with $\hat{\mathbf{y}}$ without noise, hence with $\hat{\mathbf{y}}$ being the exact simulated observations. Figure 9.8 to 9.11 show the retrieval results for a few selected cases, comparing the ground truth, a priori and retrieved state vector elements. Figure 9.12 illustrates the quality of the convergence by comparing the input observations with the modelled observations for the retrieved atmospheric

states. Figure 9.13 shows a statistical representation of all retrieval results. Furthermore, Table 9.9 indicates the accuracies achieved by the different measurement modes, expressed in RMSDs between retrieved and true values.

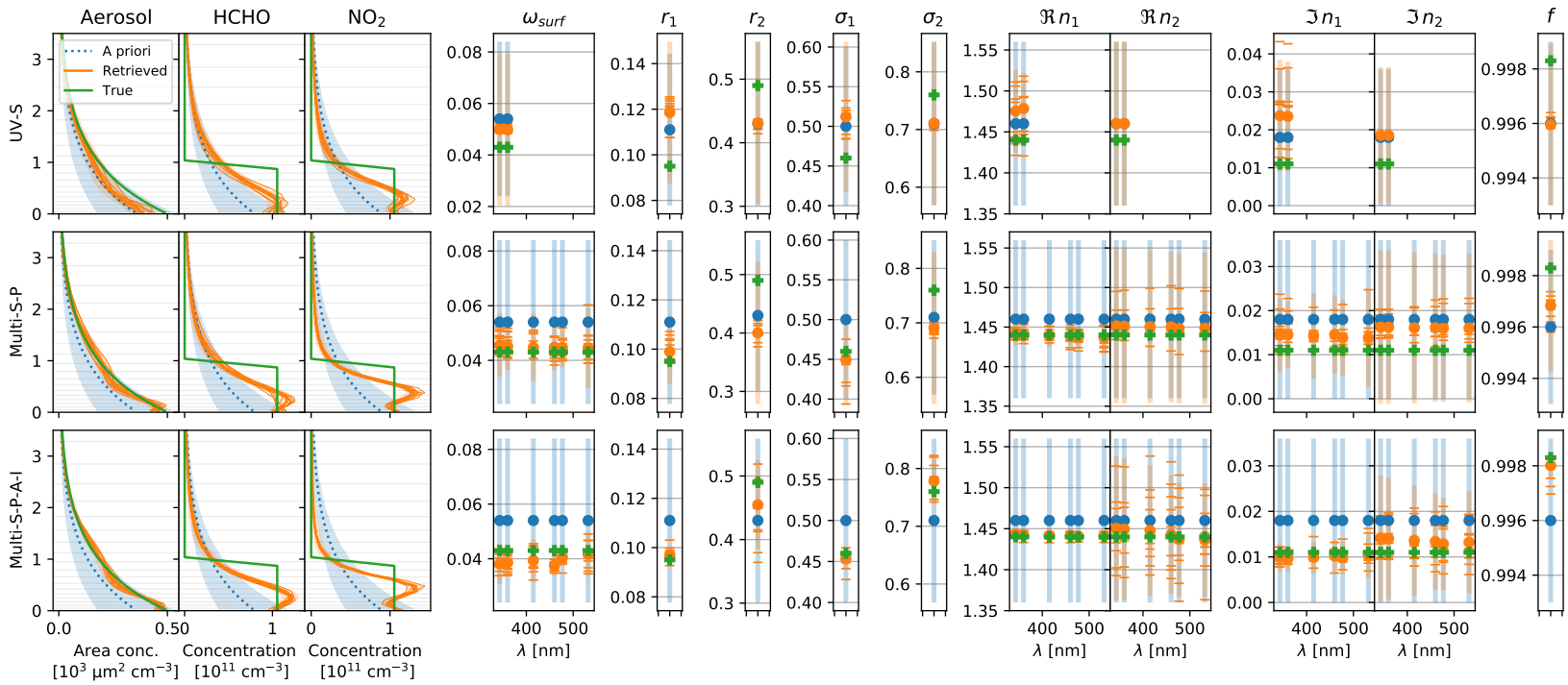

Figure 9.8: Retrieval results for the Aer1-TG6 scenario and Mie aerosol. Different subplot rows show different measurement modes (see captions on the left). The first three subplot columns show profiles with altitude in km on the y-axis. Remaining columns show values (y-axis) of other state vector elements (see captions at the top), eventually for different wavelengths (x-axis). Blue lines and symbols show a priori values, green lines and crosses show true values. Orange thick lines and circles show results for a noiseless retrieval while thin lines and dashes indicate the results of the five retrievals with random noise added to the observations. Transparent areas and bars indicate uncertainties.

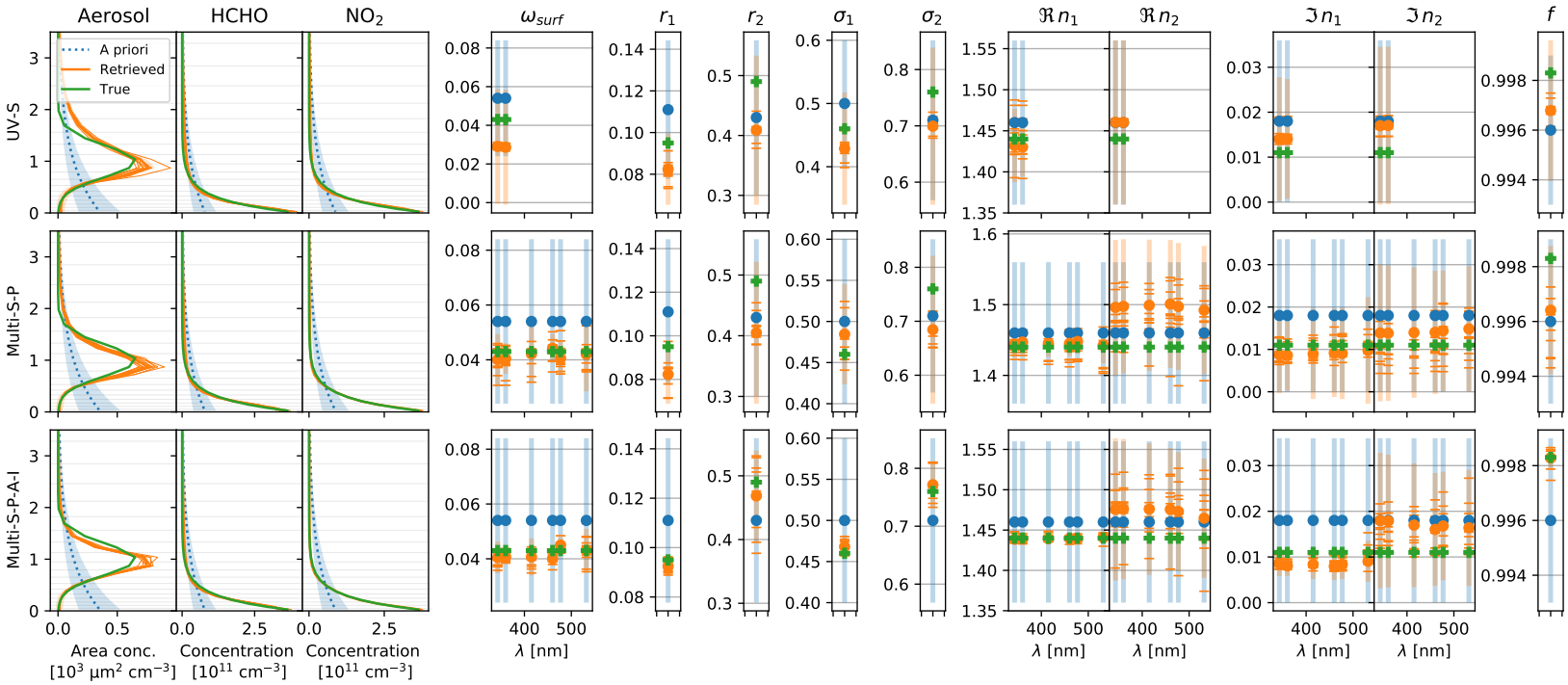

Figure 9.9: Retrieval results for the Aer7-TG3 scenario and Mie aerosol. Description of Figure 9.8 applies.

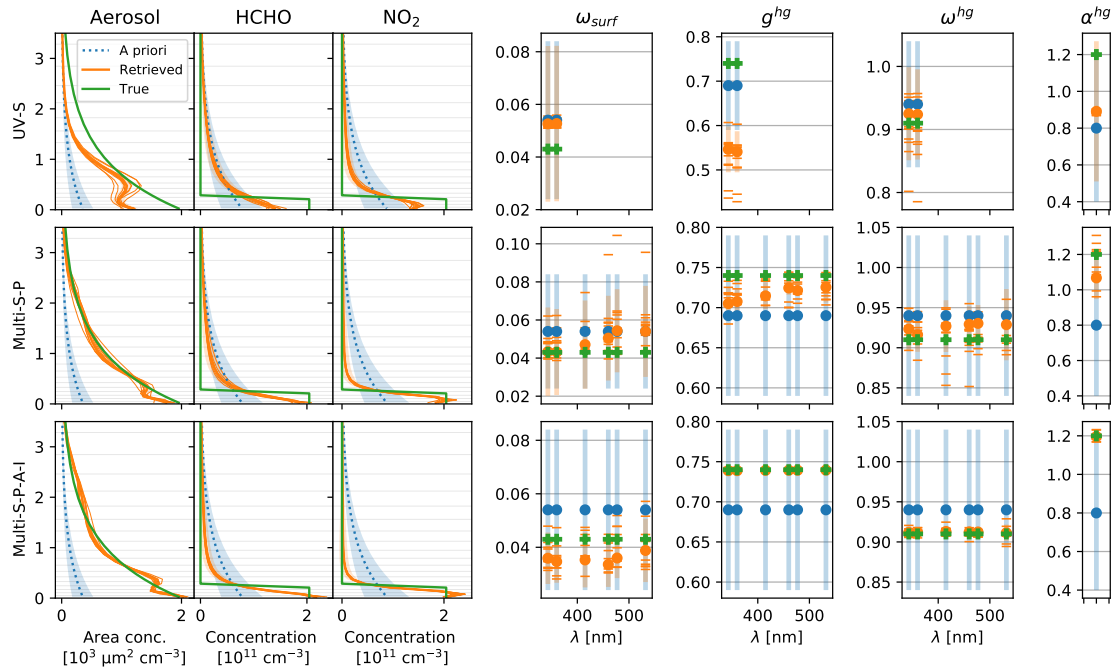

Figure 9.10: Retrieval results for the Aer2-TG5 scenario and HG aerosol. Description of Figure 9.8 applies.

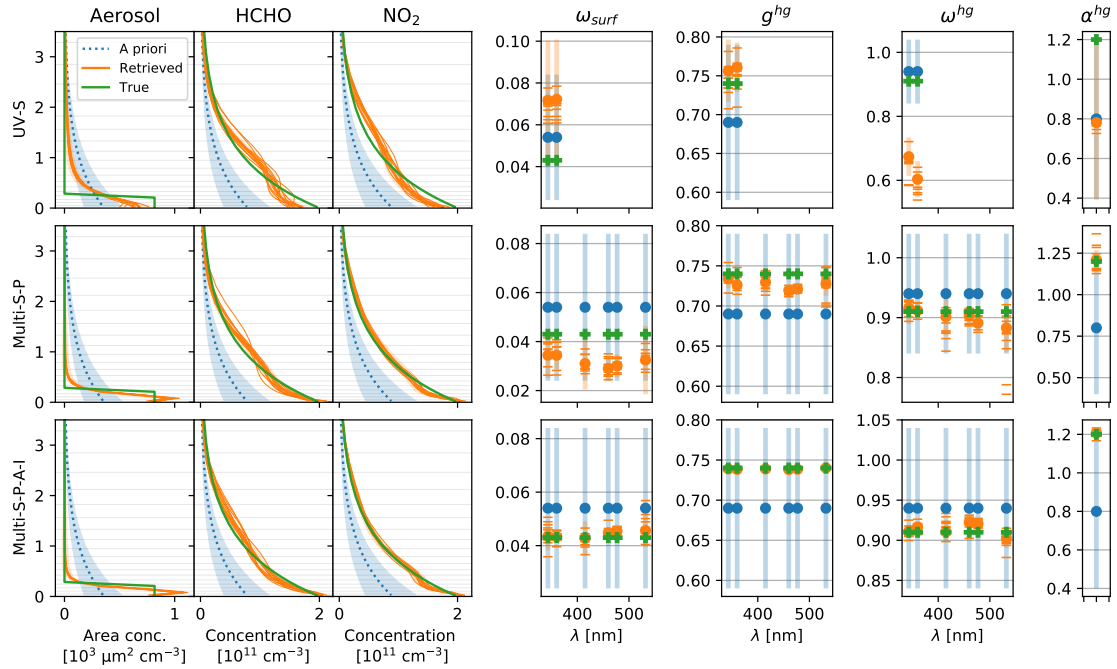

Figure 9.11: Retrieval results for the Aer5-TG2 scenario and HG aerosol. Description of Figure 9.8 applies.

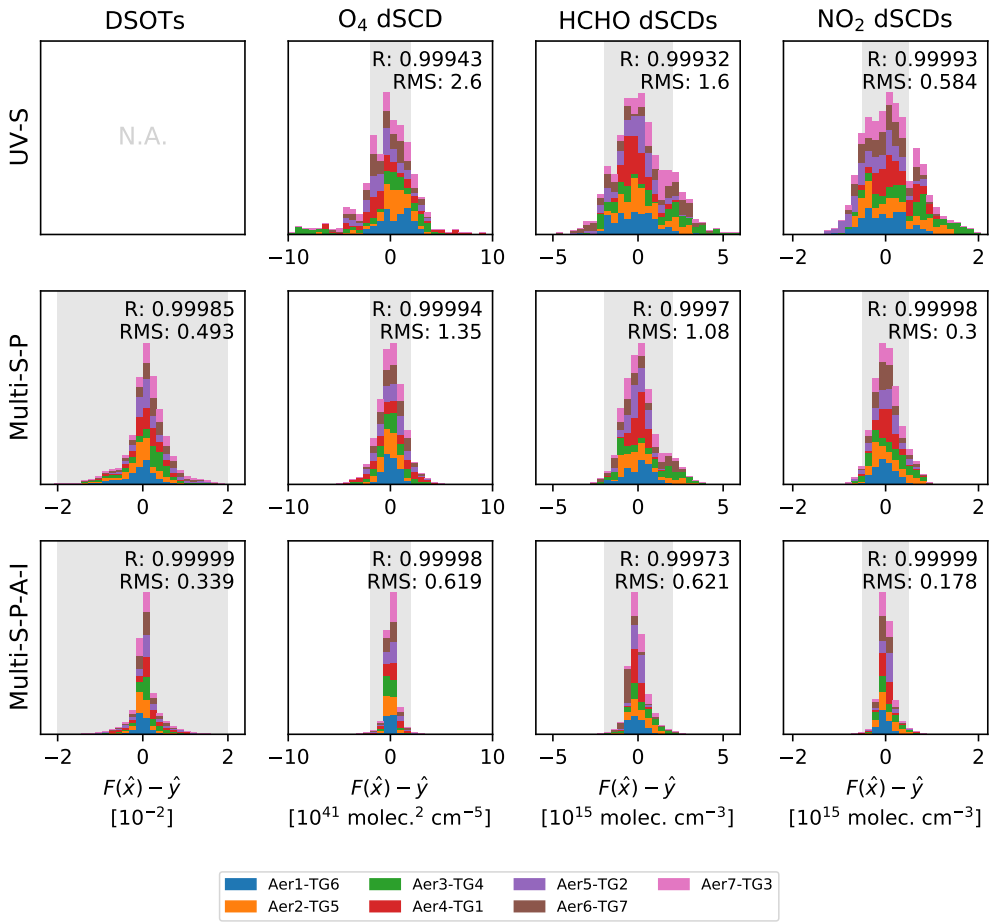

Figure 9.12: Deviations between the input observations $\hat{\mathbf{y}}$ and the modelled observations $\mathbf{F}(\hat{\mathbf{x}})$ for the retrieved states $\hat{\mathbf{x}}$ to investigate the quality of the convergence. Subplot columns show different kinds of observations. Subplot rows represent different measurement modes. Y-axes are occurrences in arbitrary units. Grey shaded areas indicate the assumed measurement uncertainties according to Table 9.1. RMS values are given in the horizontal axes' units.

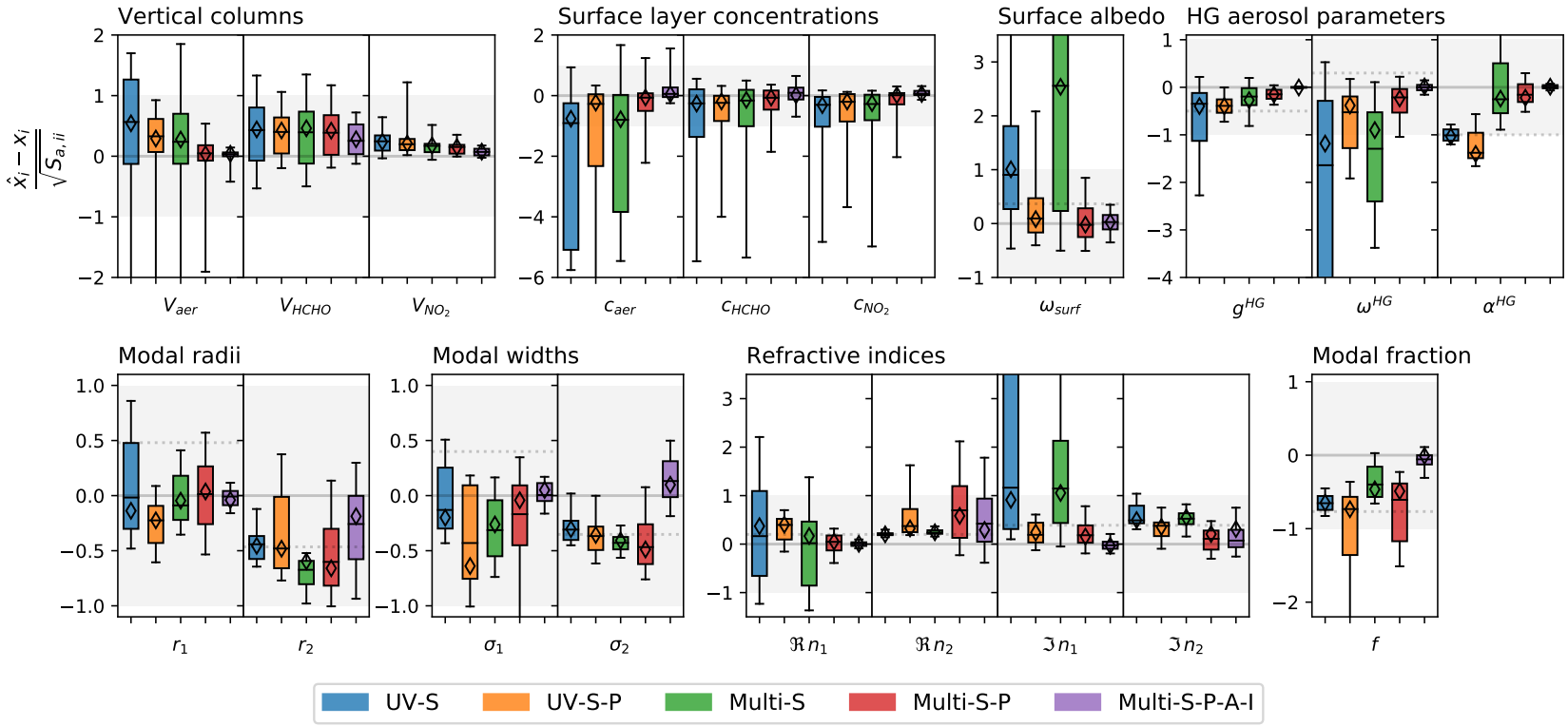

Figure 9.13: Statistical representation of all retrieval results, grouped by parameter (different subplots) and different measurement modes (box colours according to legend). The y-axis represents the difference to the true value, normalised by the a priori uncertainty. Then latter is indicated by the grey shaded areas. Where possible, dotted grey lines indicate the a priori value. Deviations $\ll 1$ with little bias towards the a priori indicate a successful retrieval. Boxes span the 25th to 75th, whiskers the 5th to 95th percentile. Dashes indicate the median, diamonds the median of the retrievals with noiseless observations.

Figure 9.12 generally shows good agreement between $\hat{\mathbf{y}}$ and $\mathbf{F}(\hat{\mathbf{x}})$ mostly within the measurement uncertainties that also define the magnitude of the synthetic random noise added to $\hat{\mathbf{y}}$. Interestingly, the deviations are largest for the UV-S case even though compared to the other modes, much fewer measurements need to be reproduced by optimising the same set of state vector elements. The same is true if comparing Multi-S-P and Multi-S-P-A-I. This indicates that fewer observations increase the risk for the inversion to end up in a local minimum of the OEM cost-function. This is supported by the retrieval results in Figure 9.13: particularly for the UV-S mode, the retrieval sometimes diverges (e.g. for ω_{surf}, ω_{hg} and $\Im n_1$) instead of resorting to the a priori values (e.g. in the case of n_2 or f). This might be related to the non-linearity of the problem, but also technical issues cannot be fully excluded as the reason. Nevertheless, the results mostly behave as one would expect from the information content analysis in Section 9.2. The example retrieval results shown in Figure 9.8 to 9.11 demonstrate, that the major features of the profiles are well reconstructed by the retrieval, particular in the case of the Multi-S-P and the Multi-S-P-A-I modes. The incorporation of polarisation (comparison between Multi-S and Multi-S-P mode) significantly improves the results for aerosol columns and surface concentrations. Further it strongly stabilises the retrieval with respect to surface albedo and fine mode refractive indices. For some microphysical properties (e.g. r_1, σ_1, f) the results degrade. This can partly be attributed to stronger biases towards the a priori for the Multi-S mode that lead to "more stable" results. Nevertheless, the overall RMSD for aerosol microphysical properties is reduced by about 40 %, mainly due to the strong improvement in the refractive indices (note that they are retrieved at multiple wavelengths). Multi-S-P and particularly Multi-S-P-A-I allow to very reliably retrieve the full set of state vector elements for the HG-case. The retrieval of microphysical properties is feasible, but reliable results (in particular for coarse mode properties) are only achieved when the Multi-S-P-A-I mode is applied.

9.6 Increased noise for polarimetric observations

So far we assumed equal uncertainties for non-polarimetric and polarimetric observations. This is rather unrealistic if the same temporal resolution is supposed to be achieved in both cases. For non-polarimetric dSCDs, a single spectrum has to be recorded at each viewing direction. For polarimetric observations as assumed above, three spectra need to be recorded in the same time period (neglecting the time losses due to repositioning of the polariser). Further, at least for setups similar to the PMAX-DOAS (see Section 11), in average half of the light entering the telescope will be rejected by the linear polariser. Hence, regarding a single polarimetric observation only a sixth of the light will be available compared to its non-polarimetric counterpart. The precision of MAX-DOAS dSCDs is typically limited by photon shot noise, the uncertainty of polarimetric dSCDs is therefore expected to increase by a factor $\sqrt{6}$. The situation is different for dSOTs. Their initially assumed uncer-

Table 9.9: Accuracy of the retrieval results (expressed in RMSDs between retrieved and true values) achieved by theMulti-S, Multi-S-P and Multi-S-P-A-I modes. "Absolute" columns are in units as indicated on the left. "[%]" columns show RMSDs relative to the a priori uncertainty in percent. c_i values refer to the concentrations in the surface layer.

Parameter	Multi-S Absolute	[%]	Multi-S-P Absolute	[%]	Multi-S-P-A-I Absolute	[%]
V_{aer} [10^8 µm^2 cm^{-2}]	0.29	225	0.093	73	0.027	21
V_{HCHO} [10^{16} molec cm^{-2}]	0.19	68	0.16	58	0.11	38
V_{NO_2} [10^{16} molec cm^{-2}]	0.076	24	0.057	18	0.03	9
c_{aer} [µm^2 cm^{-3}]	500.0	286	170.0	95	110.0	63
c_{HCHO} [10^{10} molec cm^{-3}]	8.1	207	2.9	74	1.4	35
c_{NO_2} [10^{10} molec cm^{-3}]	8.2	186	3.1	70	0.69	16
ω_{surf}	0.14	456	0.012	41	0.0061	20
g_{hg}	0.037	37	0.02	20	0.0013	1
ω_{hg}	0.18	185	0.048	48	0.0087	9
$\mathring{a}_{hg}$	0.27	68	0.12	30	0.019	5
r_1 [µm]	0.0085	25	0.012	37	0.003	9
r_2 [µm]	0.093	72	0.084	65	0.062	48
σ_1	0.043	43	0.058	58	0.011	11
σ_2	0.061	43	0.07	49	0.036	25
$\Re n_1$	0.085	85	0.021	21	0.0059	6
$\Re n_2$	0.026	26	0.1	100	0.087	87
$\Im n_1$	0.035	193	0.0068	38	0.0021	11
$\Im n_2$	0.01	56	0.0047	26	0.0063	35
f	0.0013	44	0.0027	88	0.00042	14

tainty of 2% was chosen considering systematic effects (see Section 13.1 and 13.4) and is much larger than typical photon shot noise contributions in DOAS applications ($\approx 10^{-4}$). Hence, for dSOTs the loss of light is expected to have negligible impact on the total accuracy.

In reality, there are several arguable aspects:

1. As discussed in Section 9.3, the polariser positions δ might be optimised during the measurement to enhance the information content per spectrum compared to the approach with three fix polariser positions taken here.

2. Also MAX-DOAS dSCDs are prone to systematic errors, for instance due to uncertainties in the literature cross-sections, instrumental effects or simplifying assumptions in the DOAS spectral analysis. Further, deviations between measured and modelled dSCDs much larger than the actual measurement accuracy might occur due to horizontal and temporal variability in the atmosphere (see also Section 9.7).

3. Instrumental setups detecting two polarisation directions simultaneously, using polarising beam splitters and multiple spectrometers, are conceivable. On the

Table 9.10: Obtained DOFS for the Mie aerosol case. Table is similar to Table 9.6, but with the noise of polarimetric dSCDs increased by a factor of $\sqrt{6}$.

Measurement mode					Total	Profiles			Surface	Aerosol properties								
Band	S	P	A	I		c_{aer}	c_{HCHO}	c_{NO_2}	ω_{surf}	r_1	r_2	σ_1	σ_2	$\Re n_1$	$\Re n_2$	$\Im n_1$	$\Im n_2$	f
UV	✗	✗	✗	✗	8.6	1.21	1.93	2.97	0.17	0.65	0.04	0.21	0.09	0.81	0.0	0.33	0.02	0.21
UV	✓	✗	✗	✗	8.9	1.51	1.76	2.59	0.24	0.68	0.05	0.24	0.11	1.01	0.0	0.43	0.03	0.24
UV	✓	✓	✗	✗	9.9	1.93	1.6	2.49	0.52	0.71	0.06	0.35	0.11	1.06	0.0	0.65	0.05	0.34
Vis	✗	✗	✗	✗	7.2	1.3	0.0	2.89	0.18	0.65	0.05	0.36	0.09	0.82	0.0	0.47	0.06	0.31
Vis	✓	✗	✗	✗	7.5	1.52	0.0	2.31	0.26	0.66	0.05	0.37	0.1	1.26	0.0	0.57	0.08	0.33
Vis	✓	✓	✗	✗	9.1	2.11	0.0	2.31	0.59	0.7	0.06	0.5	0.11	1.38	0.03	0.69	0.17	0.48
Multi	✓	✗	✗	✗	13.5	1.99	1.77	2.89	0.67	0.73	0.07	0.51	0.16	2.77	0.01	1.32	0.15	0.44
Multi	✗	✓	✗	✗	17.7	2.28	1.72	3.1	1.25	0.79	0.08	0.62	0.15	4.87	0.1	1.89	0.36	0.53
Multi	✓	✓	✗	✗	18.5	2.56	1.65	2.81	1.46	0.81	0.08	0.64	0.16	5.09	0.11	2.18	0.41	0.55
Multi	✓	✗	✓	✗	16.4	2.39	1.86	3.05	1.19	0.8	0.18	0.69	0.51	2.89	0.02	1.74	0.22	0.87
Multi	✓	✓	✓	✗	22.7	2.98	1.75	2.97	2.24	0.9	0.2	0.86	0.52	5.53	0.28	2.78	0.76	0.9
Multi	✓	✗	✗	✓	20.8	2.46	1.83	2.99	1.62	0.81	0.11	0.69	0.24	5.15	0.04	3.86	0.45	0.55
Multi	✓	✓	✓	✓	29.2	3.27	1.78	3.02	3.45	0.98	0.69	0.97	0.93	5.91	0.8	5.02	1.35	0.98
					110	25	25	25	6	1	1	1	1	6	6	6	6	1

other hand, such setups quickly become complex: it would for instance be required for the DOAS analysis to switch the beams of different polarisation between the spectrometers inorder to assure that they are virtually recorded with a common ISF (see also Section 4.2).

For the following investigations we assume an increased uncertainty (factor $\sqrt{6}$) for all polarimetric dSCDs, even though for the reasons given above, the truth might lie somewhere between the idealised case discussed in Section 9.2 and the 'worst' case discussed here. Tables 9.10 to 9.12 again show the DOFS for the Mie, the HG and the fixed aerosol case while Figure 9.14 illustrates the results for the Mie model case. Figure 9.15 shows a statistic over the retrievals as performed in Section 9.5 but with increased uncertainty and random noise on the polarimetric dSCDs.

Table 9.11: DOFS for the HG aerosol case. Table is similar to Table 9.7, but with the noise of polarimetric dSCDs increased by a factor of $\sqrt{6}$.

Measurement mode					Total	Profiles			Surface	Aerosol properties		
Band	S	P	A	I		c_{aer}	c_{HCHO}	c_{NO_2}	ω_{surf}	g_{hg}	ω_{hg}	$\mathring{a}_{\mathrm{hg}}$
UV	✗	✗	✗	✗	8.2	1.7	1.91	2.95	0.2	0.93	0.55	0.0
UV	✓	✗	✗	✗	8.4	1.98	1.78	2.63	0.26	1.01	0.66	0.09
UV	✓	✓	✗	✗	8.7	2.18	1.61	2.51	0.45	1.02	0.82	0.09
Vis	✗	✗	✗	✗	6.8	1.91	0.0	2.89	0.29	0.95	0.75	0.0
Vis	✓	✗	✗	✗	7.1	2.09	0.0	2.47	0.36	1.1	0.87	0.17
Vis	✓	✓	✗	✗	7.7	2.37	0.0	2.42	0.57	1.16	0.93	0.2
Multi	✓	✗	✗	✗	13.0	2.51	1.8	2.91	0.72	2.5	1.77	0.81
Multi	✗	✓	✗	✗	15.8	2.53	1.69	3.08	1.04	4.43	2.23	0.76
Multi	✓	✓	✗	✗	16.5	2.84	1.64	2.82	1.24	4.65	2.5	0.84
Multi	✓	✗	✓	✗	14.7	2.86	1.9	3.07	1.26	2.67	2.05	0.88
Multi	✓	✓	✓	✗	19.0	3.14	1.74	2.96	1.84	5.35	3.09	0.92
Multi	✓	✗	✗	✓	20.1	2.98	1.84	3.0	1.79	4.95	4.63	0.92
Multi	✓	✓	✓	✓	24.0	3.45	1.76	3.03	3.33	5.98	5.51	0.99
					93	25	25	25	6	6	6	1

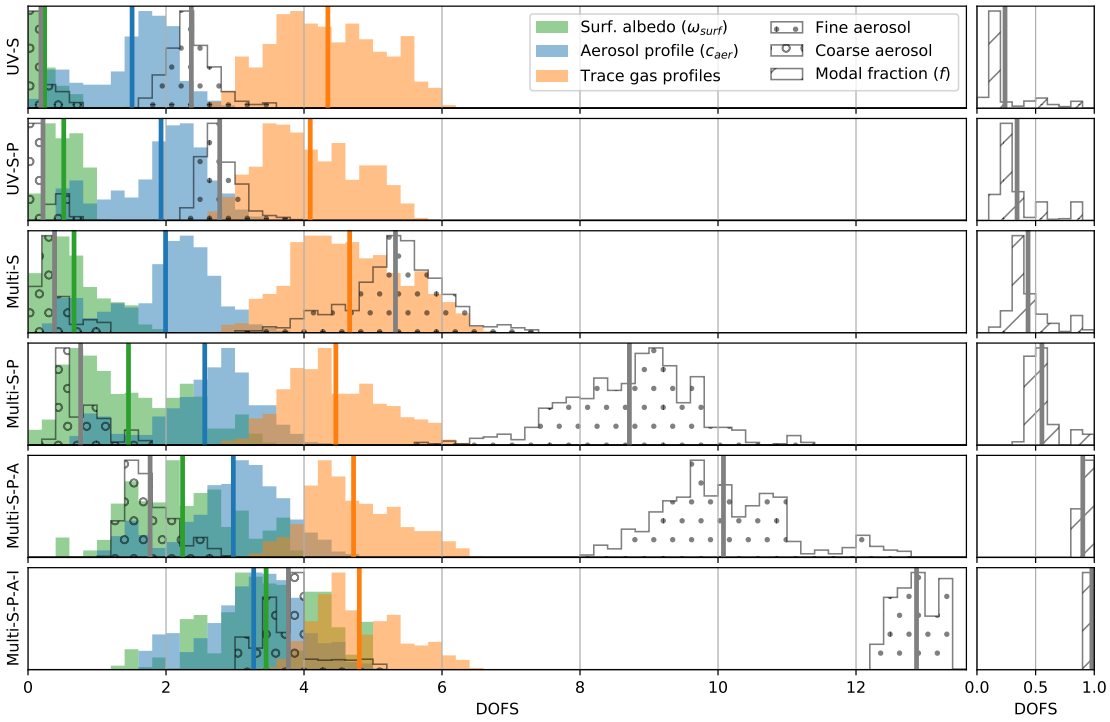

Figure 9.14: Visualisation of Table 9.10. Figure is similar to Figure 9.2.

Table 9.12: Obtained DOFS for the fixed aerosol case. Table is similar to Table 9.8, but with the noise of polarimetric dSCDs increased by a factor of $\sqrt{6}$.

Measurement mode					Total	Profiles		
Band	S	P	A	I		c_{aer}	c_{HCHO}	c_{NO_2}
UV	✗	✗	✗	✗	7.2	2.3	1.91	2.95
UV	✓	✗	✗	✗	7.2	2.55	1.86	2.75
UV	✓	✓	✗	✗	6.8	2.6	1.66	2.58
Vis	✗	✗	✗	✗	5.4	2.56	0.0	2.89
Vis	✓	✗	✗	✗	5.4	2.78	0.0	2.67
Vis	✓	✓	✗	✗	5.4	2.88	0.0	2.56
Multi	✓	✗	✗	✗	8.2	3.22	1.88	3.08
Multi	✗	✓	✗	✗	7.8	3.01	1.69	3.08
Multi	✓	✓	✗	✗	7.9	3.28	1.67	2.91
Multi	✓	✗	✓	✗	8.6	3.42	1.97	3.23
Multi	✓	✓	✓	✗	8.3	3.47	1.76	3.04
Multi	✓	✗	✗	✓	8.6	3.57	1.88	3.1
Multi	✓	✓	✓	✓	8.4	3.56	1.77	3.05
					75	25	25	25

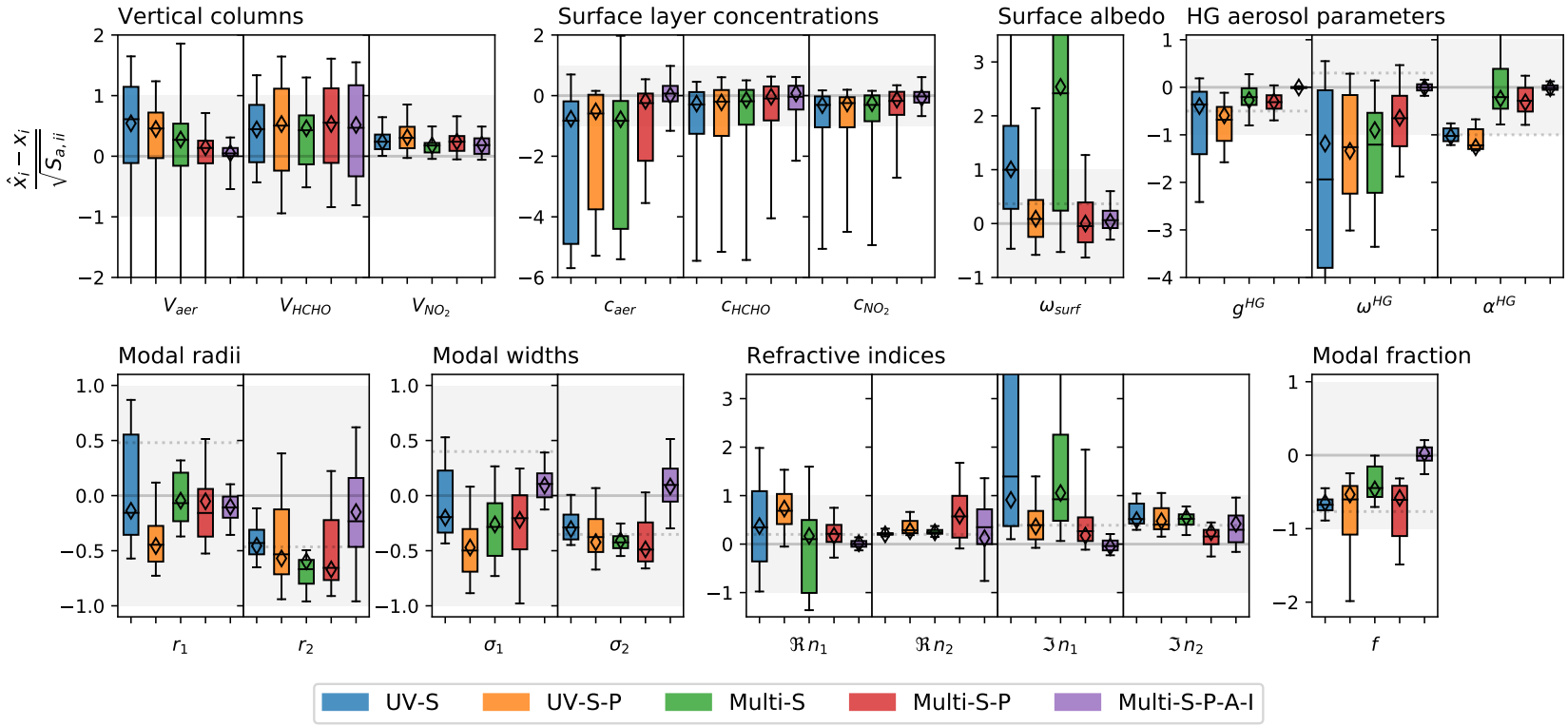

Figure 9.15: Statistical representation of all retrieval results, with increased noise for polarimetric dSCDs. Figure is similar to Figure 9.13.

As expected, the information gain obtained from polarimetric observations is generally lower (when using a single instrument and when the same time resolution is desired), however, by different amounts for different parameter subgroups. The gain in information on aerosol properties is not much affected, since a large part of the information here is inferred from the polarimetric dSOTs, rather than from the dSCDs. In contrast, the information gain for the vertical profiles is significantly reduced. For all aerosol cases, the use of polarimetric observations even reduces the information on trace gas profiles, indicating that the loss of light due to the polariser compensates the advantage of additionally available light paths (see Section 6.4). The increase in information for aerosol profiles reduces by 50 %, compared to the idealised assumption of equal uncertainties for polarimetric and non-polarimetric observations. For instance in the Mie aerosol case, the increase in DOFS between the Multi-S and the Multi-S-P measurement mode is $\Delta\text{DOFS} = 0.6$, instead of $\Delta\text{DOFS} = 1.2$ as obtained for the idealised case in Section 9.2. In the case of the fixed aerosol model, incorporation of polarimetric obervations decreases the DOFS by 0.2 for trace gas, while the DOFS for aerosol profiles remain similar ($\Delta\text{DOF} < 0.1$). The retrieval results in Figure 9.15 show a degradation for the polarisation incorporating measurement modes, however, the major conclusions drawn in Section 9.5 remain qualitatively valid.

9.7 Effect of spatio-temporal variability in atmospheric composition

The forward models in MAX-DOAS retrievals assume horizontally homogeneous atmospheres over typical MAX-DOAS horizontal sensitivity ranges of several kilometres. Furthermore, a single atmospheric state is retrieved from observations acquired over time periods of several minutes. Spatio-temporal variability therefore can in principle cause deviations between the modelled and the measured observations much larger than actual measurement uncertainties. Ideally, the retrieved atmospheric state in such cases corresponds to a kind of spatio-temporal average. However, large variability is expected to induce significant biases in the results or even prevent the inversion to achieve reasonable convergence.

In order to investigate the impact of spatio-temporal variability on the retrieval results, we simulated inhomogeneity by adding random noises of different relative magnitude (0, 2, 4, 6, 8 and 10 %) to the observations $\hat{\mathbf{y}}$ (in addition to the noise that is expected from the measurement uncertainties) before performing the same retrievals as discussed in Section 9.5, but this time limited to the Aer1-TG1 case. This inhomogeneity noise was assumed to act equally on observations in the same viewing direction. For each inhomogeneity magnitude, ten retrievals were performed, each time recalculating the random noise pattern. To put the noise magnitudes into perspective: Frieß et al. (2019) for instance assumes an inhomogeneity noise of 5 %, motivated by observations performed during the CINDI-2 campaign (Kreher et al.,

2019). Figure 9.16 shows a statistical representation of the results for the Multi-S-P and Multi-S-P-A-I measurement modes.

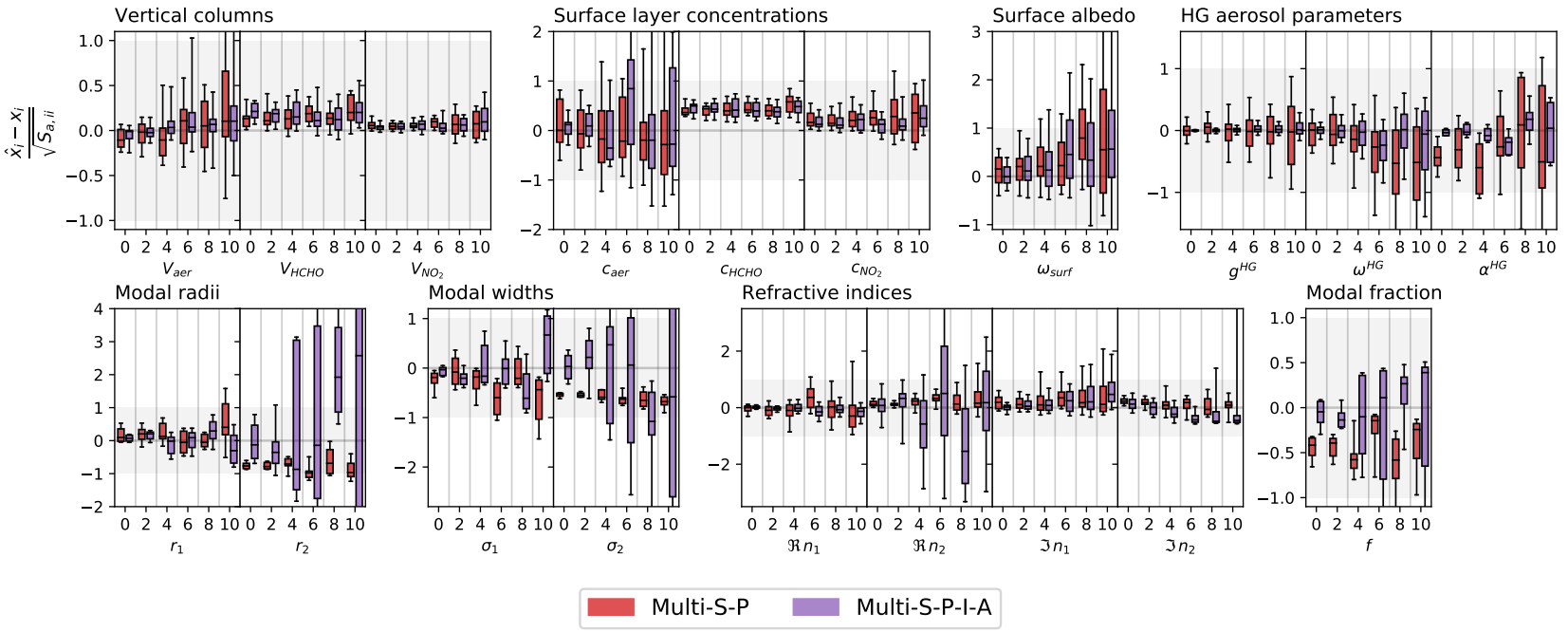

Figure 9.16: Statistical representation of the retrieval results for the Multi-S-P and the Multi-S-P-A-I modes, with inhomogeneity noises of different magnitude (x-axis indicates noise magnitudes in percent). The figure is organised similar to Figure 9.13. For some parameters, statistics is only performed over five available values and therefore, the whiskers overlap with the box limits.

Ten retrievals per noise magnitude are probably not sufficient to obtain a reasonable statistics, however, regarding the development over the full noise magnitude range still provides a first estimate of the sensitivity of the parameters to spatio-temporal variations. In the most problematic cases - for instance coarse mode aerosol properties and surface albedo - the results exceed the a priori uncertainty (grey shaded area) already at noise levels of a few percent. In contrast, the effect on trace gas VCDs and surface concentrations is low. Also the retrieval of HG aerosol properties seems to be feasible in the presence of inhomogeneities, at least for the Multi-S-P-A-I mode.

9.8 Impact of a priori covariance

The DOFS presented in this chapter are a measure for the information gain compared to the a priori knowledge and therefore depend on the assumed a priori covariance $\mathbf{S}_a$ (see Equation 5.19). Also, the retrieval results will be differently biased towards the a priori. In the ideal case, $\mathbf{S}_a$ is calculated by inferring expected variability as well as cross-correlations between the state vector elements of interest from climatologies. These are obviously space- and time dependent and so is $\mathbf{S}_a$. Furthermore, $\mathbf{S}_a$ often contains some arbitrary component, since in practice it is common to make simplifying assumptions (also in this thesis) and sometimes $\mathbf{S}_a$ is tweaked to prevent divergence of the inversion. Unfortunately, not only the actual DOFS but also the absolute and relative differences (e.g. between different measurement modes) are affected by changes in $\mathbf{S}_a$.

To investigate the impact of the choice of $\mathbf{S}_a$, we calculated DOFS for different scalings k_a of $\mathbf{S}_a$ for a standard atmospheric scenario. The results are depicted in Figure 9.17 for different measurement modes and parameter subgroups. These dependencies on the choice of $\mathbf{S}_a$ should be kept in mind when regarding the quantitative results in this chapter. However, the major qualitative findings are generally valid.

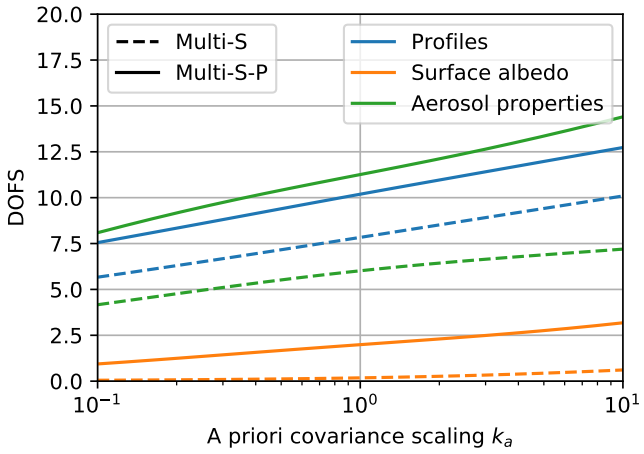

Figure 9.17: The change of DOFS obtained for different measurement modes and parameter subgroups, if $\mathbf{S_a}$ is scaled by a factor k_a. Calculations were performed for $\theta = 60°$, $\phi = 90°$, Mie aerosol and Aer1-TG1 profiles.

9.9 Concluding remarks

The results in the former sections suggest, that polarimetric information significantly increases the total information content of MAX-DOAS observations, in particular for aerosol related quantities. Table 9.13 is intended to provide a succinct summary: it shows the approximate improvement in information (in terms of DOFS) and retrieval results accuracy (in terms of RMSD) for crucial parameter subgroups when going from non-polarimetric (Multi-S mode) to polarimetric (Multi-S-P) retrievals. It assumes that the Mie-aerosol model is applied and that all atmospheric parameters are retrieved (comprising aerosol profiles, trace gas profiles and aerosol properties). The values represent averages over all atmospheric scenarios and viewing geometries as described and applied in Section 9.1 and 9.5. In the table we distinguish between an "idealised" case, which assumes the same measurement error for non-polarimetric and polarimetric observations (compare Section 9.2) and the "increased noise" case, where an increased noise is assumed for the polarimetric observations (compare Section 9.6). The increase in total DOFS (sum over DOFS from all parameters) ranges between 40 % (increased noise) and 60 % (idealised case). The increase in information is largest for aerosol related quantities, whereas, for trace gas profiles, it is rather small and even degrades for the increased noise case. Similar patterns can be observed regarding the accuracy of the results: the RMSD decrease is largest for aerosol related quantities. Interestingly, for concentrations in the surface layer, the accuracy improves similarly for all species by about 70 %, at least in the idealised case.

In the Multi-S-P mode, fine and coarse mode parameters can be retrieved to accuracies of 30 % and 70 % of the a priori uncertainty, respectively. Note also that some coarse mode parameters (r_2, $\Im n$ and also f) are still strongly biased towards

Table 9.13: Approximate relative changes in information (DOFS) and accuracy (RMSD between retreival results and true values) when going from non-polarimetric (Multi-S mode) to polarimetric (Multi-S-P) retrievals from elevation scan observations, applying the Mie aerosol model. Positive numbers indicate an improvement, hence an increase in DOFS or a decrease in RMSD, respectively.

		Idealised[a] [%]	Increased noise[b] [%]
Information	Aerosol profiles	60	30
	TG profiles	20	-5
	Aerosol properties	80	70
Accuracy	Aerosol VCD	70	60
	TG VCD	20	-40
	Aerosol conc.[c]	70	50
	TG conc.[c]	70	-40
	Aerosol properties	40	40

[a] Assuming same measurement noise for non-polarimetric and polarimetric observations (see Section 9.2)
[b] Assuming increased noise for polarimetric observations (see Section 9.6)
[c] Values refer to the concentrations in the surface layer

the a priori due to the limited available information in the measurements. However, if also optimised viewing geometries and broad band spectral information is incorporated (Multi-S-P-A-I mode), the information can be further increased by about 50 % (increase in DOFS compared to the Multi-S-P mode) with the largest increase for aerosol microphysical properties (70 %). Fine and coarse mode parameters can then be retrieved to accuracies of 10 % and 30 % of the a priori uncertainty and the a priori biases for the coarse mode are strongly reduced.

Things change again if potential inhomogeneities in the atmosphere are taken into account (simulated by adding an additional noise of up to 10 % to the measurements, see Section 9.7). Particularly the retrieval of surface albedo and coarse mode microphysical properties becomes extremely unstable or even impossible if measurement conditions are not ideal. For other parameters, the results degrade but remain useful in the sense that the deviations to the true values mostly remain smaller than the a priori uncertainties. In the future, the situation might be improved by extending the spectral range and by reasonable linking of parameters of different aerosol size modes (e.g. assuming a common refractive index for both modes).

The novel feature of the RAPSODI retrieval to retrieve all atmospheric species simultaneously in a single model atmosphere has advantages, however, the effect is small. First, it exploits additional information on aerosol contained in the trace gas dSCDs (increasing the DOFS of aerosol profiles by about 20 %). Second, it for the first time considers the sensitivity of trace gas profiles to the light path

constraining aerosol abundances. As a consequence, the information on trace gas profiles is reduced by about 15 %.

Part III

Evaluation of field measurements

10 Introductory remarks

For the application of the RAPSODI retrieval algorithm to real data we developed a polarisation sensitive 2D-MAX-DOAS instrument (PMAX-DOAS) that has been deployed at the Meteorological Observatory Hohenpeissenberg (MOHP) in Bavaria since autumn 2019. The MOHP is operated by the German weather service and accommodates different instruments for the long-term monitoring of atmospheric aerosol and trace gases for comparison and validation of the PMAX-DOAS data. They are in the following referred to as "supporting observations".

The following part of the thesis is structured as follows: Section 11 introduces the PMAX-DOAS instrument and discusses challenging aspects regarding the design of polarimetric MAX-DOAS instruments. Section 12 describes measurement setup and location, including the available supporting observations at the MOHP. Section 13 outlines the spectral analysis, i.e. it describes how dSOTs and dSCDs are inferred from the raw PMAX-DOAS spectra. Section 14 describes the retrieval setup. Section 15 compares the measured dSOTs and dSCDs with forward model simulations. Section 16 shows actual retrieval results and compares them with data from the supporting observations.

11 The PMAX-DOAS instrument

11.1 Instrument overview

The principal setup of the PMAX-DOAS instrument is illustrated in Figure 11.1 and is in many aspects similar to typical former MAX-DOAS instruments (see Section 4). It consists of a spectrometer unit that is located indoors and an outdoor telescope unit, both connected via a quartz fibre bundle. In order to be able to collect skylight from any viewing direction, the telescope unit is mounted on a commercial motorised pan-tilt head (model Eneo VPT-501/HZ RAL7035, 0 to 360° range in viewing azimuth, −90 to 90° range in viewing elevation, 0.02° angular resolution).

The telescope housing accommodates two separate telescope channels: one for diffuse skylight and one for direct sun observations. A motorized mirror enables to switch between them. Within this thesis we limit our investigations to skylight data, nevertheless the direct-sun telescope will shortly be described for completeness below. Beside the telescope channels, an industrial camera was added to the telescope unit for sun tracking and assessment of cloud conditions. Depending on the investigated spectral range and the measurement geometry (elevation scan, direct sun observations or almucantar scans, see Section 12.2), different colour filter combinations can be applied to the telescope channels and the camera over a motorised filter wheel just behind the telescope windows.

For this thesis, the skylight telescope channel including the polarising filter is of most relevance: the light enters the housing through a quartz window, passes the filter wheel and encounters a α-BBO Glan-Thompson (GT) linear polarising filter on a motorized rotary stage. These kind of polarising filters feature a broad spectral transmission range from 200 nm to 1100 nm, large acceptance angles of $\approx 15\,^{\circ}$ and very high extinction ratios (specified by the supplier to $< 5 \times 10^{-6}$ (Artifex-Engineering, 2021) and validated during instrument characterisation to $< 10^{-4}$). The linearly polarised light is coupled into a bundle of 19 optical quarz fibres of 100 µm diameter each, using a lens of focal length $f = 75$ mm and a clear aperture of 15 mm. The ideal clear aperture for the applied spectrograph (f-number of $f/4$) is about 19 mm, but could not be realised here for opto-mechanical reasons. The fibres are arranged in a horizontally extended rectangular shape, as illustrated in Figure 11.2. This arrangement widens the horizontal FOV, thereby enhancing the light throughput, while the vertical FOV, which is critical for the information content in MAX-DOAS observations, remains small. The theoretically expected telescope FOV is approximately $0.7° \times 0.25°$ and was validated in the lab to $0.75° \times 0.26°$ (FWHM, average intensity over instrument spectral range) by scanning over a small white lightsource. To localize the telescope pointing in the camera FOV (e.g. for sun

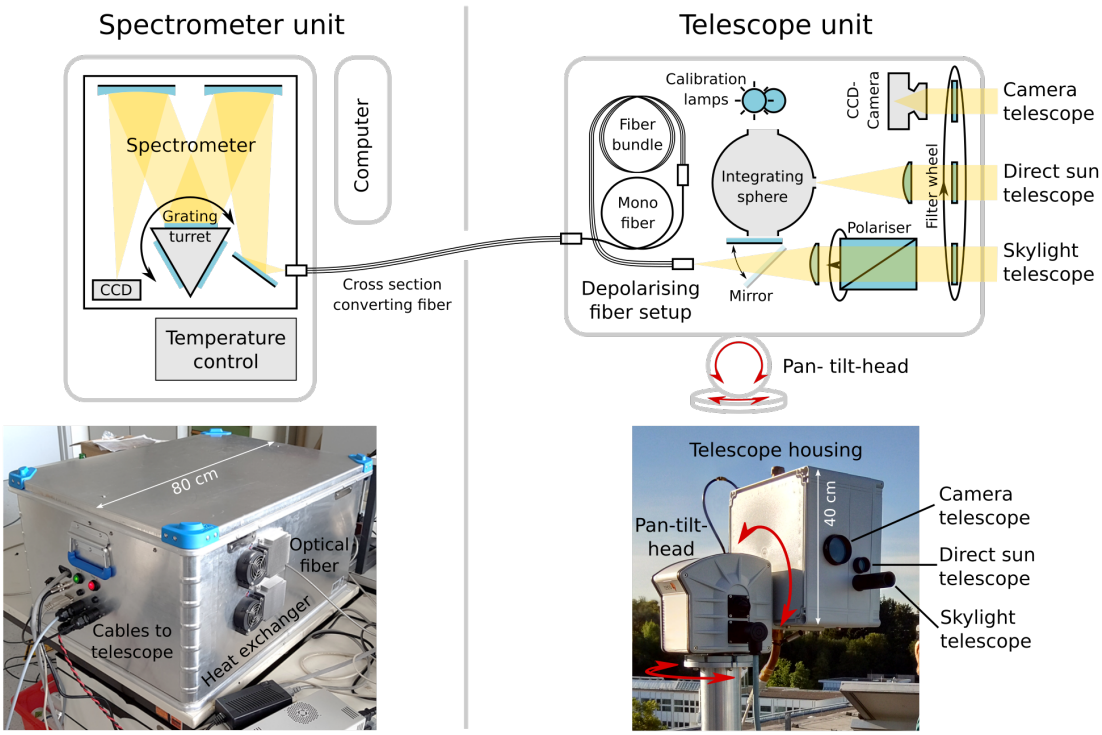

Figure 11.1: Schematics and images of the PMAX-DOAS spectrometer and telescope unit.

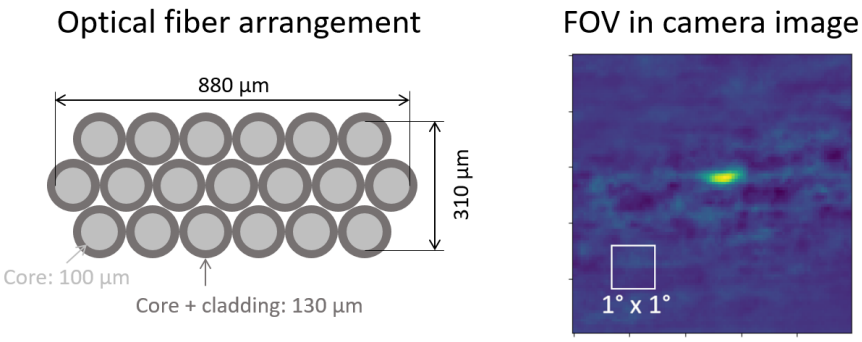

Figure 11.2: Optical fibre arrangement and FOV of the skylight telescope. The image on the right shows the correlation between camera image pixels and coincident spectrometer radiances. Blue and yellow indicate weak and strong correlation, respectively.

tracking purposes), we applied the approach described in Sihler et al. (2017): time series of radiances (field data) detected by the spectrometer are correlated against coincident camera images. Image pixels in the FOV of the telescope are expected to yield the strongest correlation. For the implementation of this approach, we used the corresponding python routines implemented by Gliß et al. (2017). The result for the correlation between the PMAX-camera and the skylight telescope are shown in the right panel of Figure 11.2.

In the direct sun telescope, a lens of $f = 100\,\mathrm{mm}$ and $\mathrm{CA} = 10\,\mathrm{mm}$ focusses the incoming light onto a 5 mm aperture of an integrating sphere, resulting in a telescope FOV full aperture angle of approximately 3°. The large FOV assures the solar disc (0.5°) to be fully covered by the FOV even under imperfect instrument pointing. Similar to (Herman et al., 2009), the integrating sphere is used here to assure optical illumination uniformity, thereby avoiding undesired spectral features caused by Fraunhofer line OT variation over the solar disk (Scheffler and Elsässer, 1974). A mirror mounted to a servo-motor allows to couple the light from the integrating sphere into the skylight telescope fibre bundle while simultaneously blocking light from the skylight telescope itself. For calibration purposes, the integrating sphere features a third port with two calibration lamps: a halogen lamp and a mercury gas lamp, the latter with distinct emission peaks to determine and track wavelength calibration and ISF of the spectrometer.

The design of the spectrometer unit was in large parts adapted from Nasse (2019). It features a two-stage temperature stabilisation. The spectrometer itself (Acton 300i) is equipped with temperature controlled resistive heating foils on each face and is enclosed in Styrodur foam. This setup is placed within the aluminium box shown in Figure 11.1 that features the second stage: air circulates within the box and is temperature controlled using Peltier elements in one of the box faces with heat exchangers on the in- and outside. At the MOHP, where the unit was placed inside an air-conditioned lab, the temperature of the spectrometer could be stabilised to a precision better than $\pm 0.05\,\mathrm{K}$. The CCD detector (Andor DV420-BU) features

an independent temperature control and was cooled to −28 °C to minimise its dark current. The Acton 300i spectrometer features a turret with three different gratings with triangular grooves. For most of the measurements presented in this thesis, we applied a grating with 300 grooves per mm and a blaze wavelength of 420 nm. With the fibre setup described below and the applied CCD-detector this yields a spectral coverage from 285 to 565 nm at a resolution of 1.3 nm (FWHM). The CCD detector is two dimensional (1024x256) but full binning over the 256 px in the vertical was applied during readout.

A peculiarity of the PMAX-DOAS is the rather unconventional fibre setup. In (MAX-)DOAS instruments, the use of fibres has several mechanical and optical advantages:

1. Freedom in the placement of the instrument components, since telescope and spectrometer do not have to be physically attached.

2. Light bundle cross-section can easily be changed e.g. from roundish shapes in the telescope to slit like configurations as desired on the spectrometer side.

3. Particularly in combination with "mode mixing" (Stutz and Platt, 1997), they assure a uniformly illuminated spectrometer FOV even if inhomogeneous scenes (e. g. clouds, Earth surface, artificial light sources) are regarded.

4. Fibres scramble the polarisation state of the transmitted radiation (Platt and Stutz, 2008), which is important to avoid undesired polarisation sensitivity of the fibre-spectrometer setup.

The PMAX-DOAS fibre setup is sketched in Figure 11.3. It makes use of all of these advantages but was particularly optimised to depolarise the gathered light before entering the spectrometer. We found that even long (several metres) multi-mode optical fibres can be poor polarisation scramblers, rather changing the polarisation state due to birefringent effects than efficiently reducing the DOP. This is discussed in more detail in Section 11.3. The full fibre thread consists of three parts. Starting from the telescope side, light passes a cross-section converter first that transforms the linearly polarised light from the polarising filter into light of 19 largely independent states of partial elliptical polarisation. These are mixed together in a thick mono-fibre that ensures a uniform illumination of another cross-section converter connected to the spectrograph. The telescope-side fibre bundle and the mixing fibre are coiled up and installed within the telescope box, whereas the last cross-sectional converter establishes the actual connection between telescope and spectrometer (see also Figure 11.1)

The entire PMAX-DOAS setup is controlled by a computer. Measurement routines and corresponding hardware control were implemented using the MS-DOAS software by Frieß (2018). The key properties of the PMAX-DOAS are summarised in Table 11.1.

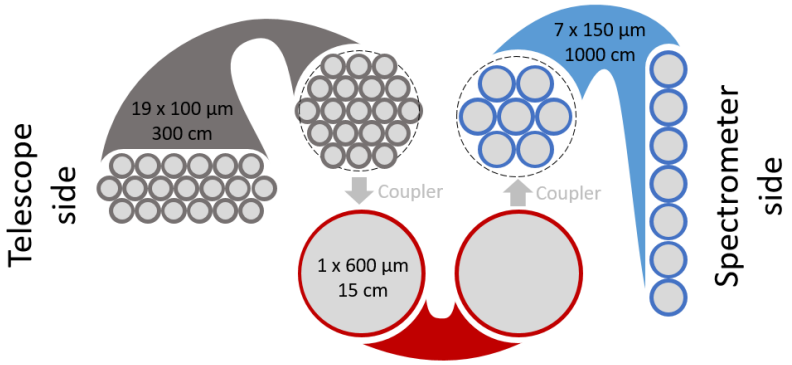

Figure 11.3: Optical fibre setup of the PMAX-DOAS instrument.

Table 11.1: Key properties of the PMAX-DOAS instrument.

Telescope	FOV: $0.7° \times 0.25°$
	Focal length: 75 mm
	Clear aperture: 15 mm
	Etendue: 0.03 mm^2sr
Spectrometer	Acton 300i Czerny-Turner
	Focal length: 300 mm
	f-number: $f/4$
Detector	Andor DV420 BU
	Resolution: 1024 px (full vertical binning)
	Max. counts: $2^{16} = 65536$
Spectral coverage	285 to 565 nm
Spectral resolution	1.3 nm (FWHM of ISF)

11.2 Undesired polarisation sensitivities

This chapter intends to draw attention to different polarisation related aspects of the instrumental design. To obtain meaningful polarimetric observations with the PMAX-DOAS, polarisation dependent properties of any optical components other than the GT-polariser need to be considered. Ideally, the instrument is designed to meet two major requirements:

1. Components before the GT-polariser (window, colour filter) neither feature polarisation dependent transmission nor alter the SOP of the incoming sky-light.

2. The entire setup behind the GT-polariser (lense, fibre, spectrometer) is equally sensitive to linearly polarised light at any orientation χ.

If these requirements are not fulfilled, the instrument features what we will in the following refer to as "undesired polarisation sensitivity" (UPS), which can lead to

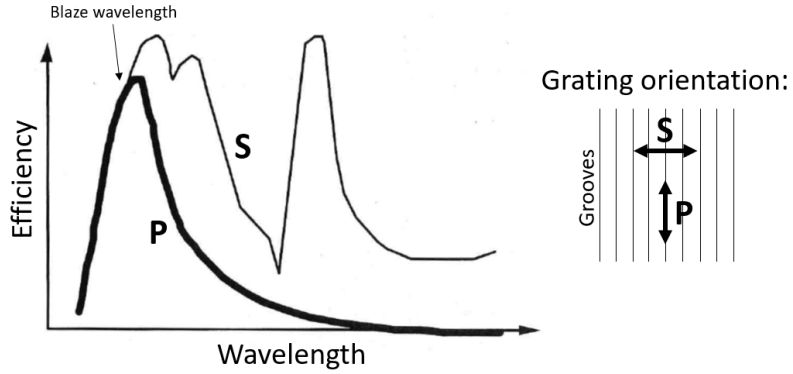

Figure 11.4: Typical efficiency curves for gratings with triangular grooves. Curves are given for polarisations parallel (P) and perpendicular (S) to the grooves. The figure was adapted from Palmer (2002).

systematic errors in the measured dSOTs and dSCDs, unless the UPS is well characterised and accounted for. In the following we will discuss the UPS of different optical components of the instrument.

The PMAX-DOAS skylight telescope channel is symmetric around its optical axis and therefore not expected to cause UPS. An exception is its asymmetric fibre configuration (see Figure 11.2). However, assuming that the Fresnel equations hold for the surfaces of all involved optical components (window, colour filter, polariser surfaces and lens), the impact of this asymmetry is estimated to be negligible: the ratio of the transmittances for light polarised along the fibre configuration's long and short principal axis is expected to deviate from unity by less than 10^{-3}.

More critical is the UPS of the instrument components behind the polariser. Grating spectrometers are well known to be polarisation sensitive. The spectrometer's mirrors and the CCD detector window obey the Fresnel equations, thereby inducing spectral broadband UPS. This is particularly the case for spectrometers that contain not only a collimating and a focussing mirror, but also deflecting mirrors (like the applied Acton 300i as sketched in Figure 11.1). Even more critical is the polarisation dependence of the diffraction grating efficiency. Typical efficiency curves for gratings with triangular grooves are shown in Fig. 11.4. For light polarised perpendicular to the grooves (S), the efficiency is typically significantly larger than for parallelly polarised light (P) and features multiple discontinuities. The latter are often referred to as "Wood's anomalies" (first discovered by Wood, 1902) and are related to the complex phenomenon of "Surface Plasmon Polaritons" (Maystre, 2012). These anomalies are particularly critical for MAX-DOAS observations, since they potentially introduce residual structures in the DOAS fit.

In the lab, we determined the total polarisation sensitivity of the Acton 300i applied in the PMAX-DOAS. The measurement results are shown in Figure 11.5. Linearly polarised light at different orientations was directly fed to the spectrometer. A 150 µm pinhole was used as entrance aperture of the spectrometer and a halogen lamp in conjunction with a 1200 µm monofibre served as light source. Different

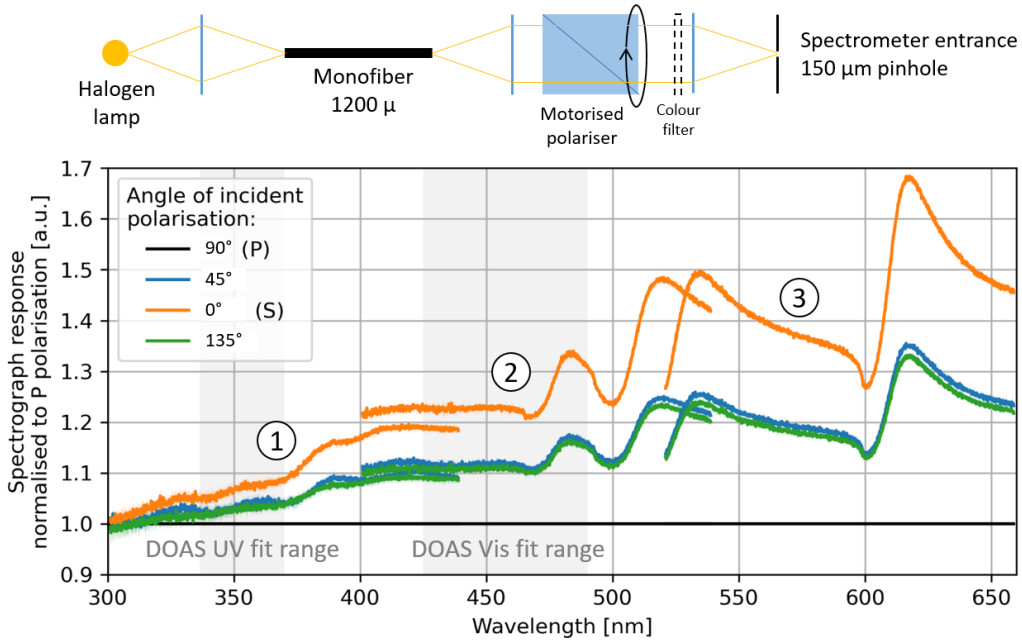

Figure 11.5: Polarisation sensitivity of the Acton 300i spectrometer. The sketch at the top illustrates the experimental setup. The measurements were performed at three different grating positions (circled numbers) to achieve broad spectral coverage. Grey areas indicate the fitting ranges later used for the DOAS spectral analysis (see Section 13.3).

polarisation states were realised with a motorised GT-polariser. A grating with 600 grooves per mm and a blaze wavelength of 300 nm was applied at three different turret positions, to realise different spectral ranges.

The results show a strong dependence of the spectrometer response with respect to the orientation of polarisation (up to 70 %, increasing with spectral distance from the blaze wavelength). The positions of the Wood's anomalies depend on the light's incidence angle on the grating, therefore spectrally overlapping measurements at different turret positions do not show the same features at the same wavelengths. The measurements at 45° and 135° are expected to yield equal results. The slight deviations between them indicate that the polariser was not perfectly aligned with respect to the grooves of the grating. Even though for the PMAX-DOAS measurements presented in Section it was decided to use another grating (see Table 11.1), the major conclusion remains: when performing PMAX-DOAS observations, the light should ideally get depolarised behind the linear polariser, before being fed to the spectrometer, to ensure equal response to light of any SOP coming from the telescope.

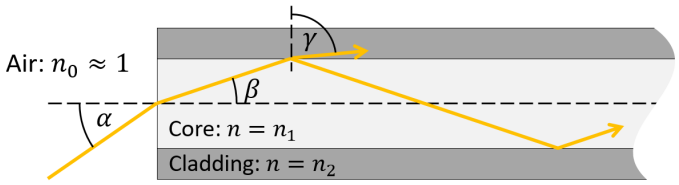

Figure 11.6: Guiding principle of a step index fibre. For incident angles $\alpha < \alpha_{max}$, γ exceeds 90°, resulting in total internal reflection at the core-cladding interface and thus guiding of the ray within the core. The cladding is typically surrounded by a strongly absorbing mantle (not shown in the figure). Light leaving the core can therefore be assumed to be lost.

11.3 Scrambling polarisation with optical fibres

In the past, multimode optical fibres of few metres length have been considered to be efficient polarisation scramblers in the DOAS community (Platt et al., 1997; Platt and Stutz, 2008). In the initial design phase of the PMAX-DOAS, we therefore expected a simple fibre setup (a single cross-section converter of 10 m length, at best in conjunction with a preconnected monofibre) to achieve suitable depolarisation. However, as described in the following, results from our characterisation of the PMAX-DOAS setup suggest that particularly in modern fibres, polarisation (at least the DOP) can be largely maintained over considerable fibre lengths.

11.3.1 General remarks on optical fibres

Depending on the application (communications, spectroscopy, power transmission, sensor technology and others) fibres of very different properties exist. We will limit our considerations to those typically applied in DOAS applications: step index multimode quartz glass fibres. In the following paragraphs we will shortly explain the meaning of this term. Details can be found in any textbook on optical fibres, e.g. Mitschke (2016).

"Step index" indicates that the fibre consists of a core with refractive index n_1 surrounded by a cladding of refractive index $n_2 < n_1$. Hence, in contrast to "gradient index fibres", the refractive index changes stepwise at the core-cladding interface. As illustrated in Figure 11.6, total reflection at this interface - i.e. guiding of light inside the core - is ensured only for incident angles

$$\alpha < \alpha_{max} = \arcsin(\mathrm{NA}), \qquad \text{with} \qquad \mathrm{NA} = \sqrt{n_1^2 - n_2^2} \tag{11.1}$$

being the numerical aperture of the fibre. The refractive index n_0 of the air outside the fibre is assumed to be unity here. The quartz fibres investigated applied in this study have NA = 0.22, corresponding to a full aperture angle of $2 * \alpha_{max} \approx 25°$ or an f-number of $f/2.2$.

For an accurate description of the behaviour of light in fibres and to understand the term "mode", one has to resort to wave-optics. Solving the Maxwell equations

for radiation in optical fibres yields that only discrete spatial E-field oscillation patterns and their superpositions can exist within the fibre. These are referred to as "modes". Each mode can be excited by incident light of appropriate wavelength and discrete incidence angle α. Some textbooks also treat "modes" and "rays entering the fibre at different angles" as equivalent (Mitschke, 2016). The "V-number" or "normalised frequency" has established as a measure for the number of excitable modes. It is given by

$$V = \frac{2\pi}{\lambda_0} d\mathrm{NA}, \tag{11.2}$$

with λ_0 being the vacuum radiation wavelength and d being the fibre diameter. Fibers with $V < 2.405$ (corresponding to $\lambda_0/d \approx 0.6$ for NA $= 0.22$) are considered "monomodal" fibres, since only the fundamental mode (the E-field pattern over the fibre cross-section approximately follows a 2D gaussian distribution) can be excited. "Multimode" fibres satisfy $V > 2.405$, often $V \gg 2.405$. The actual number of excitable modes can be asymptotically approximated by

$$m = \frac{V^2}{2} \qquad \text{for} \qquad V \to \infty. \tag{11.3}$$

In the PMAX-DOAS fibre setup, the smallest V values are around 230 ($d = 100\,\mu\mathrm{m}$, $\lambda = 600\,\mathrm{nm}$), hence, $m \approx 2.5 \times 10^4$ if the fibre's FOV is fully illuminated. We qualitatively summarise: "multimode" in our context means that the fibre has a diameter much larger than typical radiation wavelengths, thereby allowing a large number of modes and thus accepting radiation nearly at any incidence angle between 0° and α_{max}. It shall be noted that, for such fibres, the behaviour of radiation can in good approximation be described by ray optics instead of wave optics.

"Quartz glass" of course refers to the material. It is typically used for DOAS instruments, since in contrast to other materials, it exhibits high transmission over a broad wavelength range from the UV to the near infrared.

11.3.2 Mode mixing

In an ideal optical fibre - in the sense that the fibre cross-section is circularly symmetric, the materials are homogeneous and the fibre is not bent - the distribution of radiation power over the different modes is maintained. However, any motion or bending of the fibre and even temperature fluctuations lead to coupling between the modes or "mode mixing" (Mitschke, 2016). In DOAS applications, enforced mode mixing by static bending or steady motion of the fibre helps to obtain a uniform power distribution in the emerging beam that is fed to the spectrometer, thereby significantly improving the DOAS detection limit (Stutz and Platt, 1997).

11.3.3 Polarisation in fibres

Due to its importance for communication purposes the behaviour of polarisation in single and few mode fibres has been studied extensively and can meanwhile be

theoretically described (Rogers, 2008). In contrast, literature on the polarisation characteristics of multimode fibres is rather scarce and even contradictory: while some researchers claimed that multimode fibres cannot maintain the SOP, others demonstrated that it might be possible (Kiesewetter, 2010).

In an ideal optical fibre the incident SOP is preserved at least for light at small incidence angles (Mitschke, 2016). It is suggested that the main driver for changes of the SOP in real fibres are imperfections (Agrawal, 2012). Most of them are introduced during manufacturing, e.g. imperfect symmetry of the fibre core, inhomogeneous material refractive index or birefringence due to built-in strain arising from the cooling process when the fibre is drawn. But also bending of the fibre during use slightly changes the quartz crystal structure thereby inducing birefringence. Further, at larger incident angles, the process of total internal reflection induces phase-shifts between the parallel and perpendicular polarised components (with respect to the reflecting surface) of a ray, thereby affecting its polarisation state (Azzam, 2004). The predominant scattering process in fibres in the UV-Vis is Rayleigh scattering with typical extinction coefficients of $5 \times 10^{-3}\,\mathrm{m}^{-1}$ (Grattan and Meggitt, 2000). Considering that only forward scattered radiation will remain in the fibre core (scattering angles smaller $2\alpha_{max}$), for which the SOP is basically maintained (see Section 3.3.5), scattering is expected to have negligible impact.

It is important to understand that the effects listed above in first instance change the SOP of individual rays but not necessarily reduce their DOP. Fibres with sufficiently homogeneous birefringence for instance behave like long wave plates (in fact, fibres are sometimes modelled as a single or a series of waveplates, e.g. by Gölz, 2012)): as illustrated in Figure 11.7, the SOP of initially linearly polarised light, oriented at 45° with respect to the slow and fast axis of a birefringent optical fibre, oscillates between linear and circular polarisation along the fibre at typical spatial periods of several metres (Mitschke, 2016). Hence, the DOLP oscillates between zero and unity while the DOP is maintained. Therefore, a fibre that yields an emergent DOLP of zero under distinct incident polarisation orientations and position on the lab bench, might yield arbitrary DOLPs in other situations, depending on how it is bent and how the birefringence principal axes are oriented. In monomode fibres, effective depolarisation - in the sense that the DOP is reduced - was suggested to be mainly be caused by anisotropies in the fibre (Marcuse, 1975), e.g. changes in the birefringence over the fibre cross-section, leading to a superposition of rays of different SOPs.

After all, it seems that a profound understanding of the behaviour of polarisation in step index multimode fibres has not yet been established. During characterisation of the PMAX-DOAS, we therefore performed own measurements to investigate their depolarisation capabilities. In the following some of the results are presented and discussed.

The experimental setup and the results of a first experiment are shown in Figure 11.8. Vertically linearly polarised light ($\chi_0 = 90°$) was fed to a short fibre (diameter $d = 600\,\mu\mathrm{m}$ and length of $L = 0.5\,\mathrm{m}$) at an f-number of $f/4$, which corresponds to the

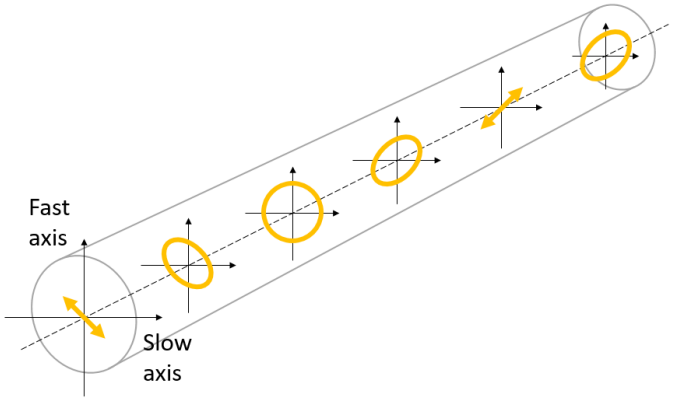

Figure 11.7: A homogeneously birefringent fibre behaves like a waveplate. At small incident angles α, the SOP of incident linearly polarised light at 45° orientation with respect to the birefringence principal axes oscillates between linear and circular SOPs over the fibre length.

FOV of most Czerny-Turner spectrometers. The emerging light was analysed using a another motorised polariser ("analyser"), an integrating sphere and a spectrometer. The integrating sphere was found to strongly depolarise incoming light (remaining DOP $< 5 \times 10^{-3}$ when incident light is fully polarised) and is necessary here to avoid biases due to the spectrometer's polarisation sensitivity (see Figure 11.5). The plots in Figure 11.8 show the measured intensities over the analyser orientation for different wavelengths. Shown are the results for two cases: once the fibre is straight, once it is bent (bending radius of $\approx$ 12 cm in the plane 45° to the horizontal). It is remarkable that in both cases the resulting intensity patterns can well be described by a simple linear retarder model according to Equation 3.35, fitting only the difference in refractive index Δn between slow and fast axis (independent of wavelength) and the orientation of the polariser δ with respect to the fast axis. This indicates that the DOLP is reduced mostly due to birefringence in the fibre, while the DOP is largely maintained. Bending of the fibre introduces significant additional birefringence (Δn increase by 30 %). Also, the order of magnitude of Δn is in agreement with values reported e.g. by (Mitschke, 2016). Further experiments on the basis of the same setup showed:

- By stronger bending of the fibre, birefringence could be further increased. If multiple bends are applied (S-shaped, as applied in typical static mode mixers) the single linear retarder model breaks down. However, we found no indication for a significant reduction in the DOP.

- Roughening of the fibre entrance (thereby creating a quasi built-in diffusing disc to enforce mode mixing, inspired by Nasse et al., 2019)) had no significant impact on the emerging polarisation state. This might be expected, since forward scattering largely maintains the SOP and light scattered at larger angles will not be guided by the fibre.

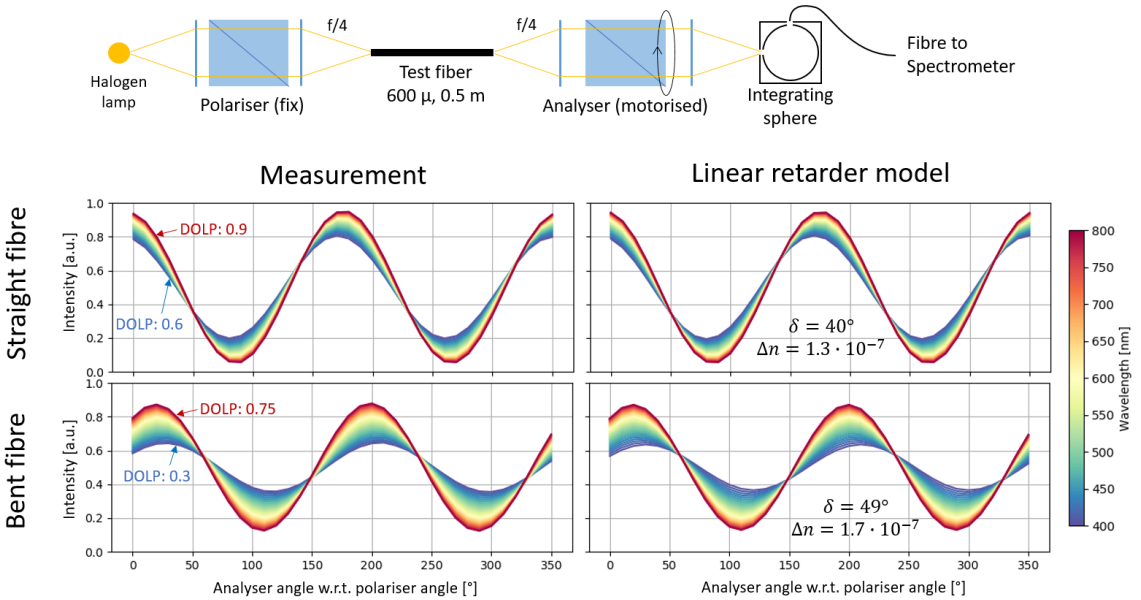

Figure 11.8: Observed behaviour of vertically linearly polarised light in a short fibre (diameter of 600 µm and length of 0.5 m). Top panel illustrates the measurement setup. Left plots show normalised intensities detected with the spectrograph for a straight (top) and a bent fibre (bottom, bending radius of $\approx$ 12 cm in the plane 45° to the horizontal). Right plots show the results of a simple linear retarder model according to Equation 3.35, fitted to the data. Fitted parameters are the difference in refractive index Δn between the fast and slow axis, and the orientation δ of the polariser with respect to the fast axis.

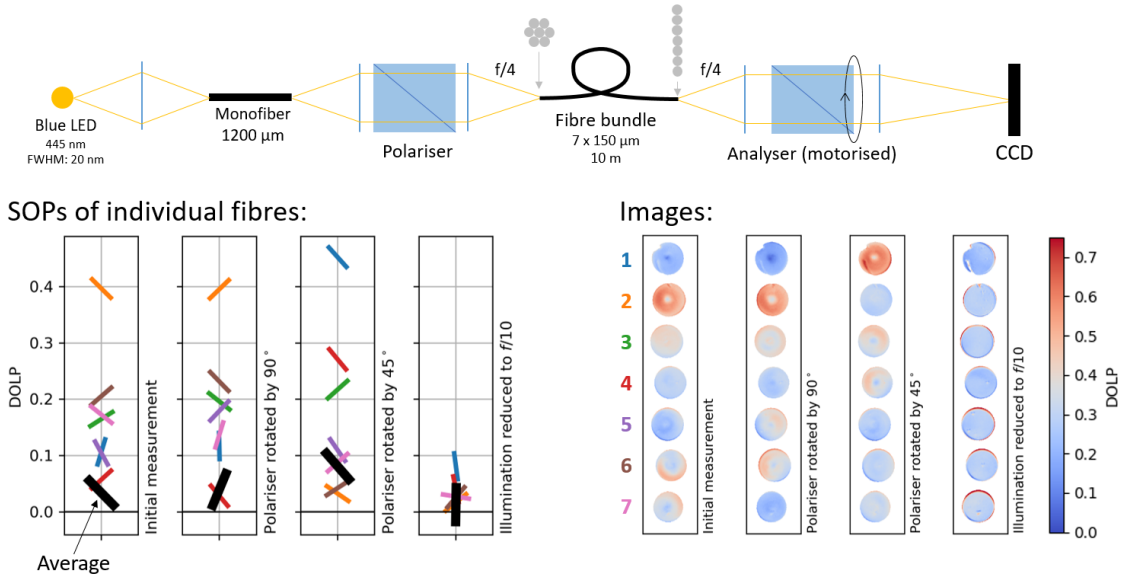

Figure 11.9: Observed behaviour of initially linearly polarised light in a long fibre bundle (seven fibres of 150 µm diameter and length of 10 m). The measurement setup is illustrated at the top. Four configurations were investigated (see subplot labels and main text for explanations). Left panel: DOLP and polarisation orientation (indicated by the marker's orientations) emerging from the individual fibres for each of the four configurations. Right panel: "Images" of the DOLP, as observed with the CCD through the analyser.

- For longer fibres ($d = 200\,\mu\text{m}$, $L = 3\,\text{m}$), the linear retarder model could still describe the general pattern, but scaling of the modelled intensity variations by 0.7 was necessary to bring measurements and model into agreement. This indicates that in longer fibres, the DOP is indeed reduced.

In another measurement, we investigated the different polarisation states emerging from a fibre bundle, using a blue LED as light source (Peak wavelength of 445 nm and spectral FWHM of 20 nm) and a camera CCD as detector. The experimental setup and results are illustrated in Figure 11.9. Four configurations were realised: an initial measurement with incident vertical linear polarisation ($\chi_0 = 90°$), two measurements with the incident polarisation rotated to $\chi_0 = 0°$ and 45°, respectively, and a measurement with the illumination angle reduced from $f/4$ to $f/10$. The variation of χ_0 in the second and third measurement is useful here to investigate birefringent effects, since the orientation of the incident polarisation is changed with respect to the fast and slow axis (if existent) of the individual fibres. A rotation by $\Delta\chi_0 = 90°$ (second measurement) effectively switches the roles of fast and slow axis but would be expected to lastly yield similar DOLPs behind the fibre bundle, in case that the latter can be approximated as a series of waveplates. In fact, this can be observed in the data. In contrast, a rotation by $\Delta\chi_0 = 45°$ is expected to "switch

the roles" of the individual fibres: for those, with the principal axes oriented close to 0° and 90°, birefringent effects should gain impact, while for those with principal axes oriented closer to 45° and 135°, the opposite is expected. In fact, also this can to some extent be observed in the data. All this indicates that in the first three measurements, the DOP (unfortunately not directly measured here) is on the order of 0.5 for all fibres, while the DOLP is modulated due to birefringence. Remarkable are the strong spatial patterns in DOLP over the cross-sections of individual fibres (see bottom right of Figure 11.9), which appear to be strongly smoothed out if the illumination angle is reduced. Extreme values observed at the fibre edges are most likely measurement artefacts. It is further interesting that a reduction of the illumination angle in the fourth measurement seems to generally reduce the DOLP and very likely also the DOP. The average emerging DOLP over the entire bundle remains below 10 % for all four configurations. The application of fibre bundles with subsequent mixing of the emerging light (e.g. by a thick monofibre) is therefore a promising approach to achieve good depolarisation.

We performed further investigations in these directions in the course of a bachelor's project (Öhmke, 2019), in which a large set of different fibres was characterised, measuring the full SOP (including the circular component). Major findings of Öhmke (2019) were:

- To reduce an initial DOP of unity to $1/e$, an average fibre length L_e of one to two metres is required.

- Some fibres appeared to well maintain the DOP ($L_e \approx 10m$). This was the case only for "modern" fibres, produced by 2015 or later. It is not clear whether this is related to improvements in the manufacturing process (less defects) or to ageing effects.

- A systematic dependence of L_e on the fibre thickness could not be found, indicating that an increasing number of internal reflections does not significantly improve polarisation scrambling.

- Changing the angular illumination (reducing the f-number or applying ring apertures) turned out to have significant but very different impact on L_e for different fibres. A general conclusion on whether large or small incidence angles favour polarisation scrambling in the fibre could not be drawn.

- Classical "gentle" mode mixing approaches like static bending or steady vibration of the fibre did not significantly improve depolarisation. Only very strong shaking (amplitude of 10 cm, frequency of 5 Hz) over a considerable fibre length (6 m coiled up to 7 winds) was successful. Under such conditions, the mechanically induced birefringence seems strong enough to cause significant variation in the SOP such that the temporally averaged DOP approaches zero.

11.3.4 Alternative polarisation scrambling approaches

There are numerous other approaches to scramble polarisation. Typically, they induce a high frequency spatial, temporal or spectral variation in the SOP, such that the averaged emerging polarisation state appears effectively randomized. However, many of the approaches are restricted regarding the wavelength range or the state of incident polarisation. A promising solution are spatial polarisation scramblers that rely on "wedged waveplates", i.e. birefringent crystals of varying thickness (as described e.g. in McGuire Jr. and Chipman, 1990) that transform any incoming SOP into a spatially varying pattern of SOPs over their aperture. The emerging beam averaged over the entire aperture therefore appears depolarized. Such polarisation scramblers are amongst others applied in satellite instruments like OMI or TROPOMI (Levelt et al., 2006; Veefkind et al., 2012). We performed experiments with a commercially available wedged waveplate (DPU-25 by Thorlabs). However, installing it behind the polariser in the PMAX-DOAS skylight telescope channel could not be accomplished without obtaining significant and variable residual structures (magnitude of several 10^{-3}) in the DOAS fit, arising from the wavelength dependence of the spatial SOP pattern over the waveplates aperture in conjunction with transmission characteristics of other components of the setup. This approach was therefore not further pursued but, if optimised, might be a solution for future PMAX-DOAS instrument designs.

11.3.5 Concluding remarks

Avoiding UPS in typical MAX-DOAS setups (telescope → optical fibre setup → grating spectrometer) is not trivial. The former assumption of fibres being efficient polarisation scramblers seems arguable. The behaviour of polarisation, particularly in multimode fibres with large acceptance angles, appeared to be complex and a profound understanding could not be developed in the course of our literature research and investigations. However, our results indicate that birefringence (induced during manufacturing and mechanical strain during use) is the main driver for the behaviour of polarisation in modern step index multimode quartz fibres. Single fibres of few metres length were found to reliably change the SOP, whereas an actual depolarisation sufficient for our purposes (emerging DOP on the order of 1 % at incident DOP of unity) could not be ensured. In contrast, the application of fibre bundles with subsequent mixing of the emerging light from all fibres achieves good depolarisation. This approach was lastly implemented in the PMAX-DOAS (see Figure 11.3). The characterisation of the final fibre setup was not possible before deployment in the field, but the total UPS of the instrument is estimated in Section 13.1.1 to be less than 1 %.

Note that these findings not only have implications for the PMAX-DOAS but also for conventional MAX-DOAS instruments: when evaluating skylight spectra of different viewing directions (and thus different SOPs) against each other in the DOAS analysis, the Wood's anomalies potentially introduce residual structures in

the DOAS fit and affect the quality of the dSCD results. Furthermore, as discussed in Section 6.4, AMFs vary with the SOP of the detected light. Consequently, UPS in MAX-DOAS instruments potentially biases the radiative transport and therefore the retrieved quantities.

12 Measurement location and setup

12.1 Location overview

The PMAX-DOAS has been measuring at the Meteorological Observatory Hohenpeissenberg (MOHP, 47.801° N, 11.009° E, ground altitude of 977 m above sea level) in Bavaria, southern Germany, since autumn, 2019. The MOHP is operated by the German Weather Service (Deutscher Wetterdienst, DWD). An overview on the observatory and its surroundings are illustrated in Figure 12.1 and 12.2. As indicated in the figures, the PMAX-DOAS was installed on the balcony of the MOHP main observation tower with the telescope at an altitude of 1000 m above sea level. Figure 12.3 shows the view from the balcony (DWD webcam) in the approximate PMAX-DOAS elevation scan direction (see Section 12.2 for details on the measurement procedure). The DWD operates a large suite of instruments for atmospheric monitoring at the MOHP. Those instruments of relevance for our retrieval setup, comparison, and validation purposes, are indicated in Figure 12.1 and 12.2. In the following they will be referred to as "supporting observations". They comprise in-situ measurements, radiosonde data, Sun photometer observations, and diverse meteorological observations. These are discussed in detail in Section 12.4.

12.2 PMAX-DOAS measurement procedure

The daily measurement routine performed by the PMAX-DOAS is illustrated in Figure 12.4. It includes different kinds of observations: during twilight (dawn as well as dusk), spectra are only recorded in the zenith viewing direction. During daylight, the PMAX performs elevation scans in an azimuthal viewing direction of 295° with respect to North, followed by direct sun observation. Every fourth elevation-direct-sun cycle (about every 70 min), an almucantar scan is performed. At night, spectra for correction and calibration purposes are recorded. These comprise dark spectra to determine CCD offset and dark-current as well as mercury lamp spectra for the spectrometers wavelength calibration and determination of the ISF.

The exposure times were dynamically adapted to the lighting conditions to ensure a saturation level of the spectrometer's CCD of about 50 %. The azimuthal direction of the elevation scans was chosen according to three major criteria: (1) to ensure an unobstructed view with a low and flat horizon, (2) to have a uniform ground (forest) for the negative EAs and (3) to cover most of the RAA range between 0 and 180° over the day. In the case of elevation and almucantar scans, the PA sequence performed in each viewing direction includes redundant measurements (at same PA) and follows an oscillating pattern. This has two advantages: (1) averaging over the

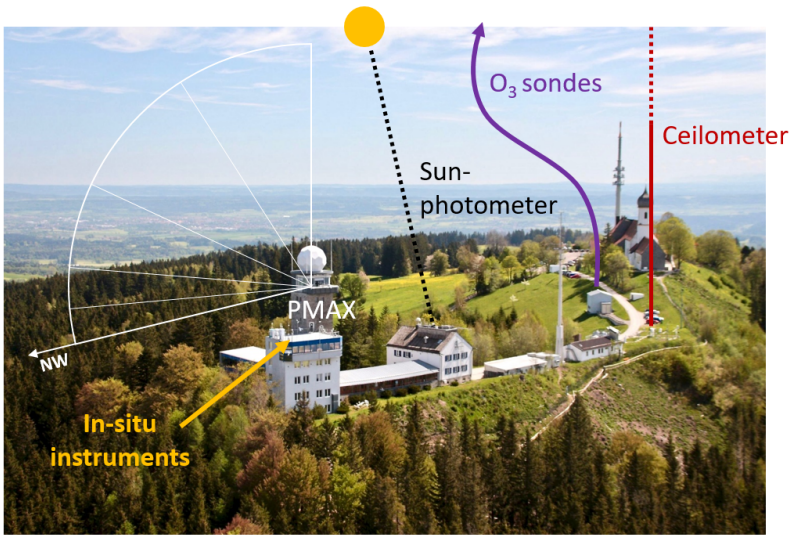

Figure 12.1: Image of the MOHP. The positions and approximate viewing geometries of the relevant instruments, including the PMAX-DOAS, are indicated. Image provided by Koehler (2021)

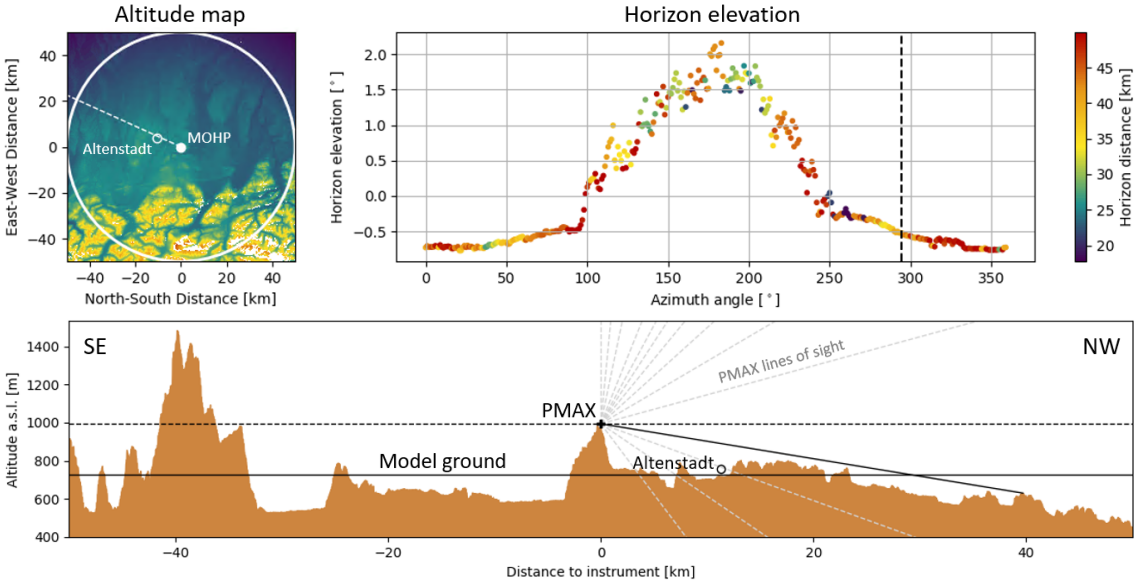

Figure 12.2: Topography around the MOHP within a radius of 50 km. Earth's curvature is taken into account. Top: topographic map (laeft) and horizon elevation as seen from the PMAX-DOAS on the tower balcony (right). The dashed line indicates the elevation scan azimuth direction. Bottom: cross-section of the MOHP topography along the elevation scan direction. Altitude data originates from NASA's Shuttle Radar Topography Mission (van Zyl, 2001), parsed using the Python-SRTM library (Charnock, 2020).

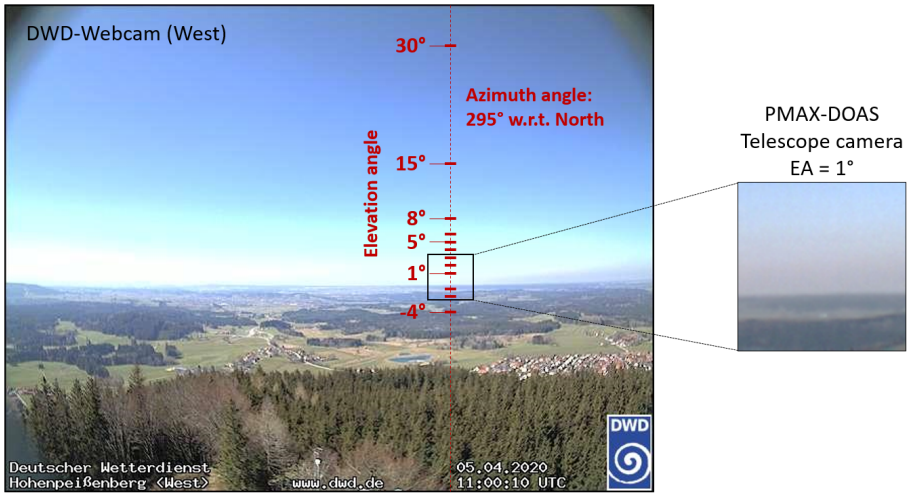

Figure 12.3: West view from the tower balcony. Left: DWD-Webcam image with the approximate PMAX-DOAS elevation scan geometry indicated in red. Right: Image from the PMAX-DOAS telescope camera.

redundant observations yields three spectra at different polariser angle, virtually recorded simultaneously and (2) comparison of the redundant spectra allows to assess uncertainties introduced by temporal variations in the skylight radiance.

12.3 Investigated time period

Over the operation time at MOHP a considerable dataset could be recorded. For this thesis, however, we focus on three clear sky days with different aerosol conditions and nearly complete data coverage regarding the PMAX-DOAS as well as the supporting observations: the 5th, the 8th and the 10th of April, 2020. Furthermore, we limit our investigations to elevation scans only. The investigation of the full dataset was out of the scope for this thesis and might be subject to future activities.

12.4 Supporting observations

12.4.1 In-situ instruments

The DWD operates different in-situ instruments on the rooftop on one of the MOHP buildings (see Figure 12.1), 7 m below the PMAX-DOAS. Nearly continuous measurements are available for O_3 (ThermoFisher Model 49i based on UV absorption) and NO_2 (ThermoFisher Model 42i-TL based on chemoluminescence) at temporal resolutions of 1 min and 2 min, respectively. Within this thesis, O_3 data is used to constrain the retrieval atmosphere (see Section 14.4) while the NO_2 measurements are used to validate the PMAX-DOAS retrieved NO_2 concentration in the corresponding atmospheric layer.

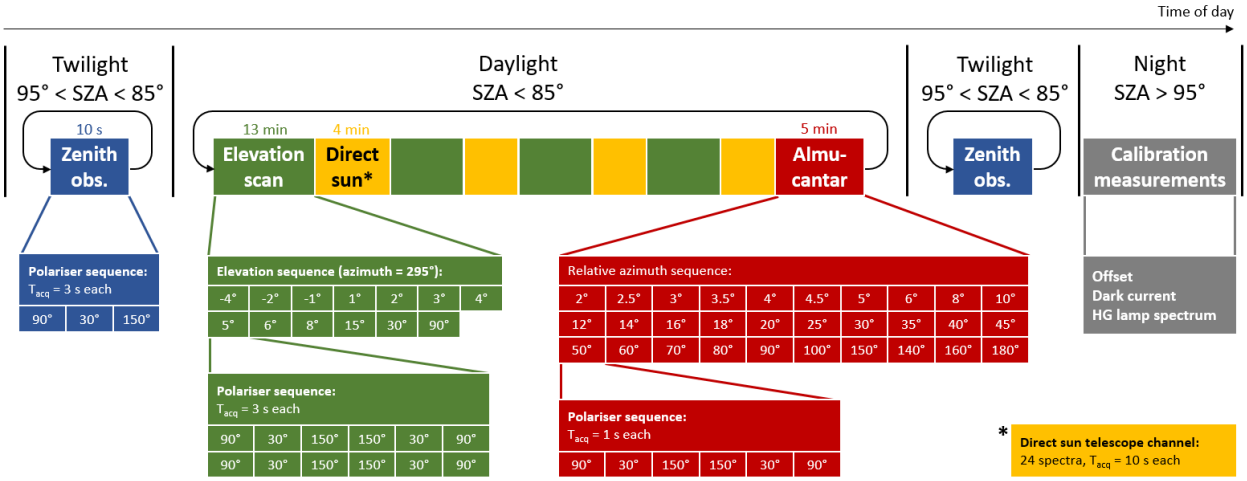

Figure 12.4: Illustration of the PMAX measurement procedure over the day. Depending on the SZA, different measurement patterns are performed and repeated.

12.4.2 Ozone sondes

In few day intervals, the DWD launches radiosondes from the MOHP, providing vertical profiles of temperature, pressure, relative humidity and O_3 at a vertical resolution of approximately 50 m up to altitudes of 35 km. Example profiles are shown in Figure 14.3. For the time period investigated in this thesis, the sonde launches on 2020-04-01 at 5:50h and on 2020-04-10 at 4:39h are of relevance. Their data is used to constrain the retrieval atmosphere.

12.4.3 Sun photometer

The DWD operates a Sun photometer (CE318-T) on the rooftop on one of the MOHP buildings (see Figure 12.1) 10 m below the PMAX-DOAS). The photometer is part of the Aerosol Robotic Network (AERONET, see Holben et al., 1998). Its primary data are direct-sun and sky radiances at 1020, 870, 675 and 440 nm wavelength. AOTs are directly inferred by determining the attenuating effect of aerosol on direct sunlight. Surface albedo and column integrated aerosol optical as well as microphysical properties are deduced by applying inversion methods (Dubovik and King, 2000b; Dubovik et al., 2000; Sinyuk et al., 2020). We use the AERONET Version 3 inversion products, with a temporal resolution of approximately 1 h. Wavelength dependent quantities are provided at the measurement wavelengths listed above. Where necessary, they were spectrally inter- or extrapolated to the required wavelengths in the UV and Vis assuming a logarithmic dependence (in analogy to the definition of the Ångström exponent in Equation 3.50) of each parameter X to wavelength λ according to

$$\ln(X_\lambda) = a \cdot \ln(\lambda) + b, \tag{12.1}$$

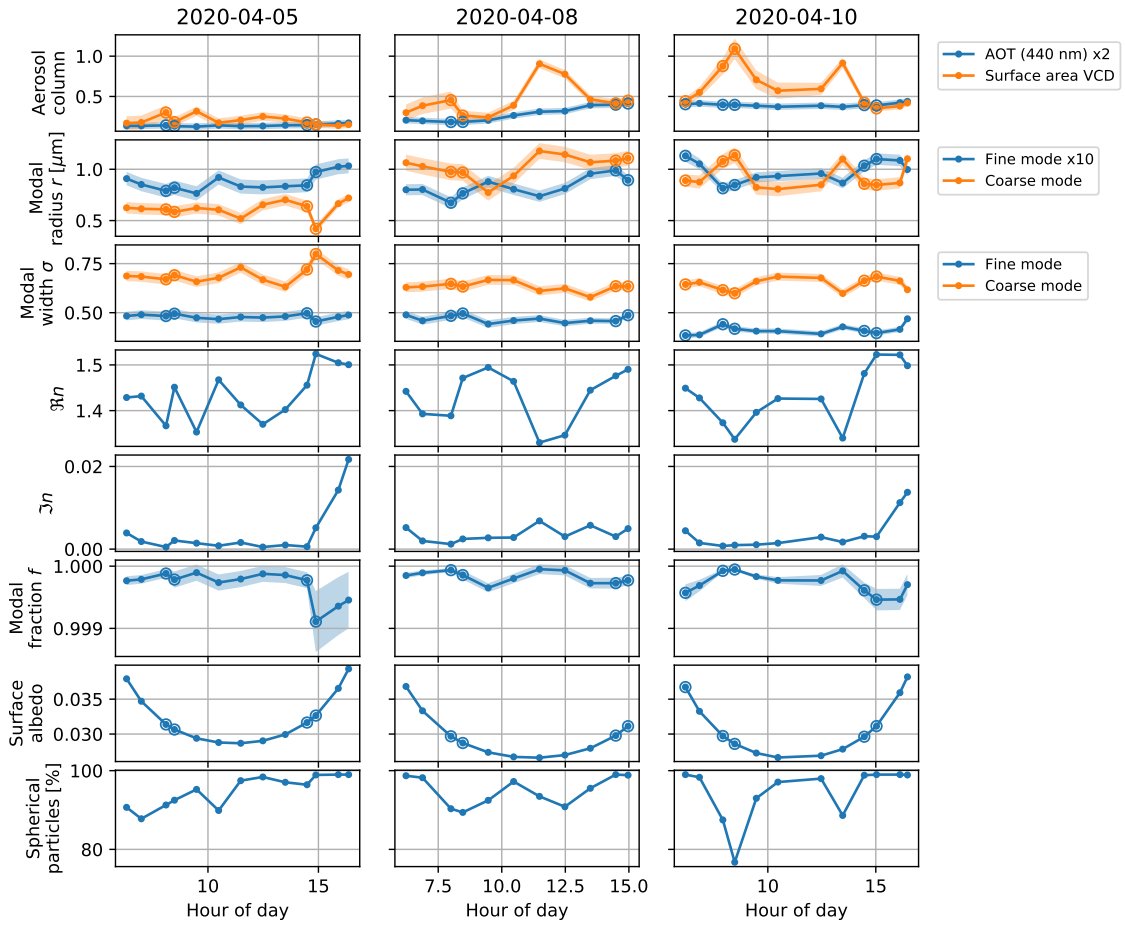

Figure 12.5: Data from the Sun photometer over three investigated days. Shaded areas indicate uncertainties, where available. Lines with small dot markers indicate Level 1.5 data. Those that "survived" the Level 2.0 quality filters are circled.

with the parameters a and b inferred from the Sun photometer observations of X at 440 and 675 nm. Where necessary, temporal gaps were interpolated linearly. AERONET provides aerosol microphysical properties assuming a bi-modal size distribution described in terms of volume concentration column, mode volume median radii, mode standard deviations as well as a common aerosol refractive index for both modes. From these, the RAPSODI native parameters (aerosol area VCD, number median radii, bi-modal fraction) were deduced applying Equations 3.55 to 3.58. The Sun photometer observations of relevance for this thesis over the three investigated days are illustrated in Figure 12.5. For AERONET inversion V3 data, there are different quality levels available. With increasing level, data has undergone increasingly strict quality assurance criteria, which are described in detail in Holben et al. (2006). Highest quality is provided with the level 2.0 data, however, its data coverage is very scarce ($< 25\,\%$ of Level 1.5 data) and for some quantities there is no

Level 2.0 data provided at all. We therefore use level 1.5 data, even though they are expected to be less reliable and need to be interpreted with care. In fact, Figure 12.5 already raises some concerns: while the AOT changes very smoothly over the day, aerosol properties, and thus the surface area VCD, show much stronger variability. At the same time, the variations in surface area VCD and different aerosol properties appear strongly correlated, indicating that the quantities compensate for each others deviations from the truth.

In contrast to level 1.5, level 2.0 data also provides error estimates for some of the aerosol properties. To obtain approximate uncertainties also for level 1.5 data, the level 2.0 uncertainties were linearly interpolated to the level 1.5 timestamps.

Recall that the RAPSODI algorithm assumes all particles to be spherical. The AERONET Version 3 inversion results also provide an estimate for the fraction of spherical particles, contributing to the total aerosol amount. It is shown in the lowest row of Figure 12.5. Most values are above 80 %, we therefore consider the spherical approximation in the RAPSODI retrieval to be justified for the investigated days.

12.4.4 Ceilometer

Information on the aerosol vertical profiles was obtained by combining the Sun photometer aerosol columns with data from a ceilometer (Lufft CHM15k Nimbus, at 975 m above sea level). The latter continuously provided vertically resolved information on the atmospheric aerosol content by measuring the intensity of elastically backscattered light from a pulsed laser beam (1064 nm) propagating in zenith direction (see e.g. Wiegner and Geiß, 2012). The raw data are attenuated backscatter coefficient profiles over an altitude range from 200 m to 15 km above the ceilometer (175 m to 15.0 km above the PMAX-DOAS), with a temporal and vertical resolution of one hour and 15 metres, respectively. These were converted to aerosol area concentration and aerosol extinction profiles by scaling with coincident Sun photometer aerosol area VCDs and AOTs, respectively. The resulting aerosol profiles over the three investigated days are shown in Figure 12.6.

12.4.5 Meteorology

The DWD also provided in-situ measurements of pressure, temperature and relative humidity from two locations, the MOHP and a weather station in Altenstadt. The position of the latter is also indicated in Figure 12.2 and will be used to constrain the atmospheric conditions at altitudes below the MOHP.

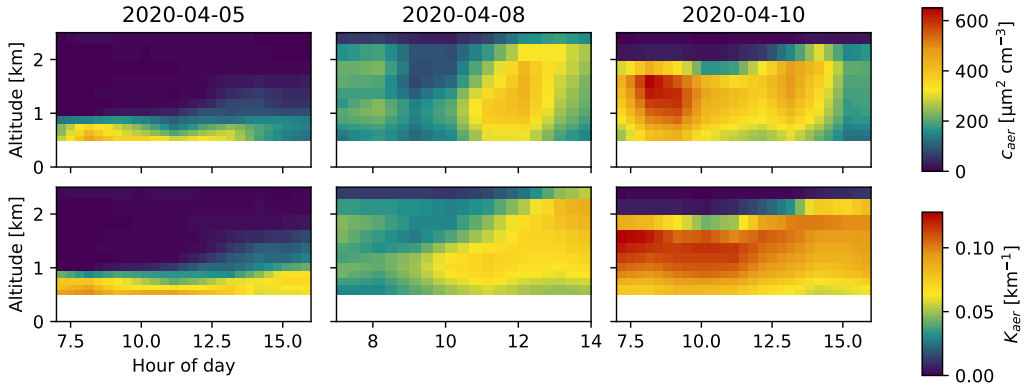

Figure 12.6: Scaled ceilometer backscatter profiles for the three investigated days. Top row shows aerosol surface area concentrations, bottom row shows extinction coefficient profiles at 477 nm. For better comparability, the zero altitude and the vertical grid correspond to the settings later applied in the retrieval (see Section 14.3).

13 Spectral analysis

The first step in the PMAX-DOAS data evaluation is to infer dSOTs and dSCDs (as required by the RAPSODI retrieval) from the raw PMAX-DOAS spectra. The corresponding procedures are outlined in this chapter.

13.1 Sources of errors

Prior to the actual spectral analysis, it is useful to discuss a few potential error sources and their impact on the inferred dSOTs and dSCDs. In conventional MAX-DOAS retrievals, the DOAS fit error is often assumed as the measurement error for dSCDs (sometimes it is multiplied by a factor of ≈ 2, inspired by Stutz and Platt (1996), who performed comprehensive investigations on the relation between DOAS fit error and actual dSCD uncertainty). For gases with SOTs in the few percent range, however, this is a very optimistic approach. Typical DOAS fit errors for O_4 in the Vis for instance are on the order of few $10^{41}\,\mathrm{molec}^2\,\mathrm{cm}^{-5}$ that compare to O_4 dSCDs up to $10^{44}\,\mathrm{molec}^2\,\mathrm{cm}^{-5}$, hence, the assumed relative errors turn out to be extremely small ($< 1\,\%$). In this regime, other error sources need to be considered, first of all the limited accuracy of the instrument to realise a distinct viewing geometry (including the RAA ϕ, EA α and, in the case of the PMAX-DOAS, the PA δ). Also for dSOTs, the major sources of uncertainty are systematic effects like imperfect realisation of the viewing geometry, instrumental UPS but also natural variations in the skylight radiance between subsequently recorded spectra (at least in the presence of clouds). In the following, we will estimate the impact of some of these effects on the observed quantities.

13.1.1 Viewing geometry and undesired polarisation sensitivity

Regarding the instrument pointing accuracy in conventional MAX-DOAS observations, most attention is paid to the EA, since - particularly at low EAs - already slight deviations on the order of few tenths of degrees induce significant biases in the measured dSCDs (see e.g. Donner et al. (2019) and Figure 13.3). In contrast, deviations in the RAA are considered less critical (see e.g. Zielcke, 2015), at least for RAAs $\gtrsim 10°$. For PMAX-DOAS, things are more critical due to the additional rotation axis of the polariser and its "interaction" with the other axes. In fact, high accuracy in all three axis (EA, RAA and PA) is important to obtain meaningful measurements here. This can be illustrated by a simple example: consider an instrument with ideal EA and PA calibration but a bias in the azimuth angle. When

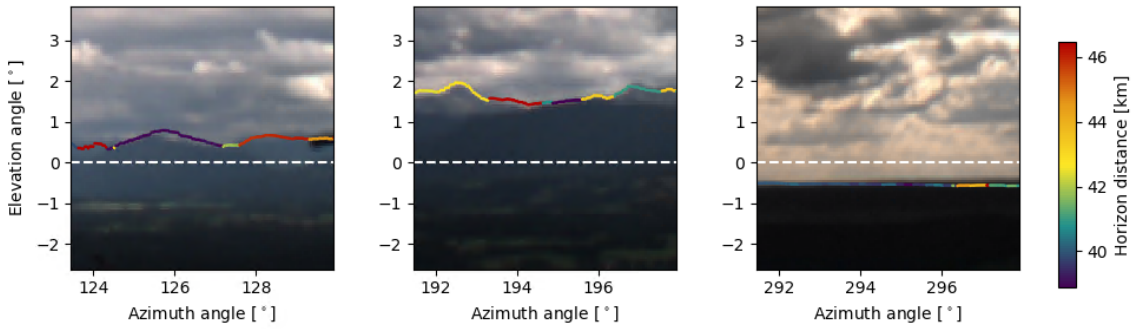

Figure 13.1: Validation of the PMAX-DOAS azimuthal pointing by comparing camera images of the horizon in different directions with the horizon elevation calculated from NASA SRTM data (coloured lines). The camera in the telescope is not perfectly horizontally aligned, which causes some of the deviations at the image borders.

the instrument points to the zenith, the bias in the azimuth directly propagates into the PA (while the impact decreases with $\sin(\alpha)$ towards lower EAs).

The pedestal of the PMAX-DOAS telescope is equipped with a 2D water level. This water level and the elevation motor offset were calibrated in the lab as illustrated in Appendix B. The water level allowed to reproduce an upright position of the telescope azimuth axis in the field to tilting angles $< 0.2°$. At MOHP, the tilt in the elevation scan plane was furthermore optimised to an uncertainty of $\approx 0.1°$ by scanning over a small lamp at several metres distance that was vertically adjusted in using a laser level (see Appendix B for details).

The primary adjustment and validation of the azimuthal pointing was achieved by comparing telescope camera images with expected horizon elevations, calculated from SRTM ground elevation data (van Zyl, 2001). Such a comparison (for the adjusted setup) is shown in Figure 13.1. In this way an azimuthal pointing accuracy better than a few tens of degree could be achieved, at least at low EAs.

Another useful reference to assess the instrument's pointing accuracy is the position of the Sun in the sky. The latter can be accurately predicted from astronomical calculations (also considering atmospheric refraction). Throughout this study we used the Pysolar library (Zebner et al., 2017) for this purpose. During direct-sun observations performed at MOHP, the position of the sun within the camera FOV was compared to the expected position according to the Pysolar calculations and the instrument's nominal pointing. The instrument's elevation pointing turned out to be systematically too low (0 to 0.5° below the sun), while the azimuthal miss-pointing varied between -0.5 and $0.5°$ over the day. Reasons for these deviations might be imperfect calibration of the pan-tilt head regarding the angular span or non-orthogonality between the rotation and optical axes of the telescope. For the direct-sun observations, a real-time fine adjustment of the instrument pointing on the basis of the sun position in the camera FOV was performed, thereby achieving a pointing accuracy better than 0.1° in both, elevation and azimuth pointing. Sub-

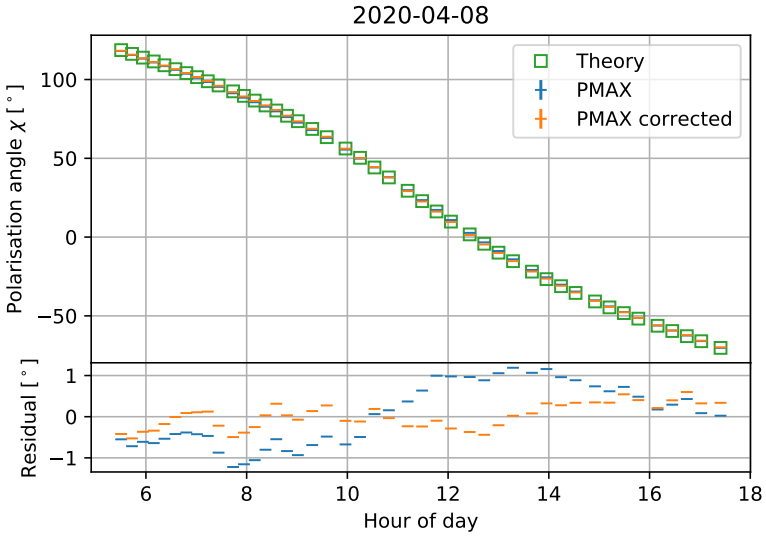

Figure 13.2: Comparison of the theoretical and observed orientation of skylight polarisation in the zenith viewing direction over one day (2020-04-08) between 350 and 450 nm. See text for further details.

sequent almucantar scans were performed with RAAs relative to the fine adjusted pointing to achieve maximum accuracy in the RAA.

The orientation of the polariser was only approximately calibrated (to about 0.5° accuracy) in the lab. The fine adjustment and validation was performed in the field by evaluating zenith observations on clear sky days. For symmetry reasons, the orientation of polarisation χ of zenith skylight is determined by the solar geometry according to Equation 6.3, at least in a homogeneous atmosphere. Figure 13.2 compares expected and observed χ for the adjusted setup. In average, there is good agreement, indicating that the polariser's orientation is accurate to a few tenths of degrees. Some short term variation is expected due to atmospheric inhomogeneity, the variation of the skylight intensity between subsequently recorded spectra at different PAs and the limited precision of the applied rotary stage (OWIS DRTM 40, repeatability $< 0.2°$). However, the residual also features a systematic S-pattern of $\approx 1°$ amplitude, which is also apparent for other clear sky days than 2020-04-08. This might again be partly explained by non-orthogonality between the telescope rotation axes but also by remaining UPS of the instrument. In fact, slight scaling of the observed radiances $I_{30°}$ and $I_{150°}$ by factors of 1.01 and 0.995, respectively, largely removes the pattern (orange markers in Figure 13.2 show the corrected data).

Generally, the effect of different misalignments and their impact on the actual observations is not trivial to assess. In the future, advanced approaches might be applied to improve and simplify the instrument pointing calibration: Riesing et al. (2018) for instance proposes a quaternion-based approach to infer relevant setup parameters (including non-orthogonalities between the rotation axes) from the instrumental miss-pointing during direct-sun observations.

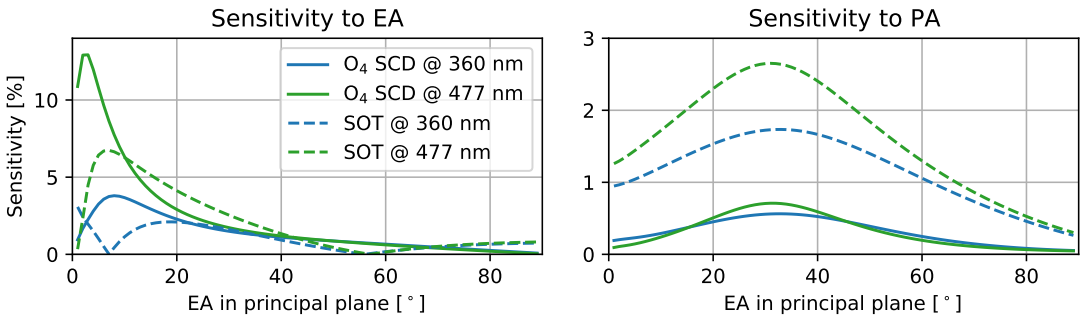

Figure 13.3: Sensitivity of O_4 SCDs and SOTs in the principal plane (RAA $\phi = 180°$, SZA $\theta = 30°$) to changes in the EA α and PA δ. O_4 SCD (S_{O_4}) sensitivities are given in $\left|\frac{1}{S_{O_4}}\frac{\partial S_{O_4}}{\partial \alpha}\right|$ and $\left|\frac{1}{S_{O_4}}\frac{\partial S_{O_4}}{\partial \delta}\right|$, respectively. SOT ($\tau$) sensitivities are given in $\left|\frac{\partial \tau}{\partial \alpha}\right|$ and $\left|\frac{\partial \tau}{\partial \delta}\right|$.

For now, we stick to rough estimates based on the measurements above: the accuracy for all three axes (EA, RAA and PA) over the full hemisphere is approximately 0.5°. The accuracy in EA at low EAs in the elevation scan direction is about 0.1°. The UPS of the instrument will be assumed to introduce an error of 1 % on the observed radiances.

To estimate the impact of pointing and PA uncertainties on the actually measured quantities, we simulated the sensitivity of O_4 SCDs and SOTs in a Rayleigh atmosphere in Figure 13.3. As discussed before, the EA is most critical at low elevations, where O_4 SCDs change by more than 10 % per degree in EA. Misalignment of the polariser has significant impact (≈ 0.025 per degree) on SOTs at larger wavelengths and in directions of large DOLP. We will refer to these findings for the error estimation of dSCDs and dSOTs in Section 13.3 and 13.4, respectively.

Lastly, we would like to propose a simple method for an accurate polariser angle calibration that might be applied for future setups: almost perfectly horizontally polarised light can easily be realised through specular reflection on a water surface close to the Brewster angle (see Appendix B). Using the light's polarisation orientation as reference, it should be feasible to determine the instrument's polariser orientation with respect to the horizon to better than $\lesssim 0.1°$.

13.1.2 Skylight variability

The variability of the detected skylight radiance in time can introduce significant uncertainties when deriving dSOTs between subsequently recorded spectra. Such changes might not only be caused by real variation in the skylight radiance but also by instrumental effects or sporadic obstruction of the LOS for any reason (e.g. human beings working on the MOHP balcony or insects in the telescope). As indicated in Figure 12.4, the polariser sequence performed at each viewing direction follows a cyclic pattern: within about 1 min, four spectra per PA are recorded and their

comparison allows to assess the magnitude of skylight variability over the sequence. Figure 13.4 shows histograms of the standard deviations between spectra of equal PA recorded in a single viewing direction on a clear sky and a cloudy day. Only data with SZAs $\theta < 75°$ was considered to avoid large radiance drifts due to changes in the solar geometry over the PA sequence. Apart from few outliers, the variation is well below 1 % for clear sky days. Interestingly, also on the cloudy day, the average variation remains relatively small (few percent) most of the time. The maximum variation observed over the entire day is 22 %. Note, however, that in extreme situations (e.g. single clouds passing the instrument FOV) skylight radiance changes can become extremely large.

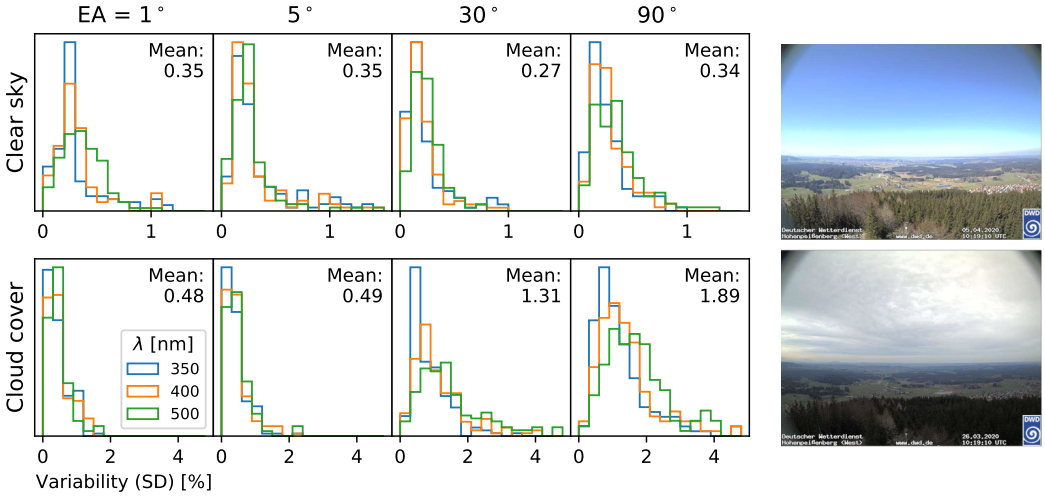

Figure 13.4: Relative variability in skylight radiance, observed between spectra of equal PA, for a clear sky day (2020-04-05, top row) and a day with nearly continuous cloud cover (2020-03-26, bottom row). Corresponding DWD-webcam images on the right illustrate the conditions.

13.1.3 Variability in fibre transmission

A last interesting aspect, is the changes in transmission of optical fibres if they are bent. In the PMAX-DOAS, the fibre-bundle connecting the moving telescope with the spectrometer unit is bent in different directions depending on the telescope pointing. This affects dSOTs between spectra recorded in different viewing direction. To estimate the magnitude of this effect, spectra of the halogen lamp inside the telescope were recorded in quick succession, while driving the telescope to different elevation and azimuthal positions. The resulting bending of the fibre introduced changes in the detected radiance with a standard deviation of $> 2\,\%$ (and $\approx 10\,\%$ peak-to-peak). As described later on, for the retrievals from field data presented in this thesis we will not include dSOTs between spectra of different viewing directions.

Therefore, these findings are not of relevance. However, for future evaluations they should be kept in mind.

13.2 Spectral Pre-processing

The raw spectra from the PMAX-DOAS were corrected for CCD offset and dark current. The pixel-to-wavelength calibration was achieved using spectra with well-known emission lines from the mercury gas lamp installed inside the PMAX-DOAS telescope. Typical offset spectrum, dark current spectrum and wavelength calibration results are shown in Figure 13.5. Furthermore, the spectra were corrected for non-linearity of the CCD readout amplifier (determined to about 1 %), following the approach described in Horbanski (2015). Spectra of same PA and viewing direc-

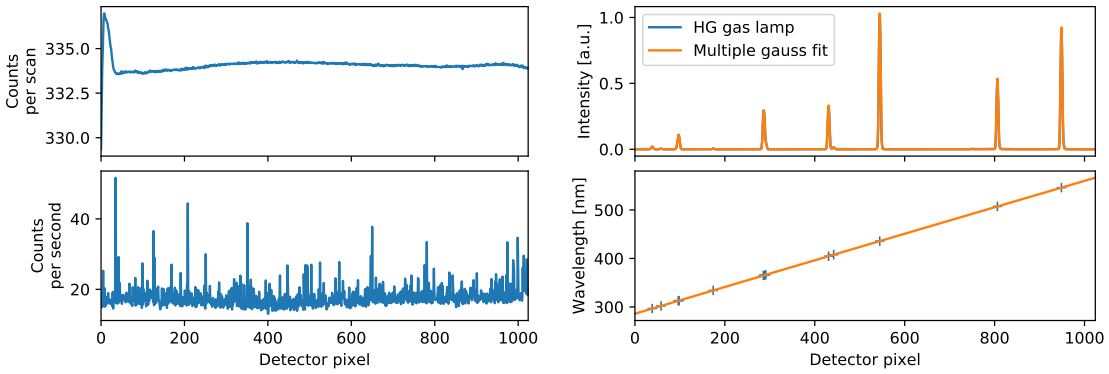

Figure 13.5: Left panel: typical CCD offset and dark current spectra. Right panel: pixel to wavelength calibration using a mercury gas lamp spectrum.

tion (according to the polariser angle sequences in Figure 12.4) were averaged. The standard deviation between them was used to infer the skylight variability over the sequence.

VLIDORT is computationally most efficient if dSCDs and dSOTs for a single solar geometry (SZA, RAA) are provided, i.e. if all observations belonging to an elevation scan are recorded simultaneously. This was virtually achieved by linear temporal interpolation of the spectra between subsequent elevation scans.

We also created a set of non-polarimetric data by summarising the spectra of different PAs according to Equation 3.27. The resulting set of spectra is equivalent to conventional MAX-DOAS observations and is useful to later assess the improvements achieved through the incorporation of polarimetric information.

13.3 Differential slant columns

DSCDs were inferred using the DOAS spectral analysis based on HEIDOAS (Frieß, 2020) outlined in Section 4.2. DOAS fits were performed in two spectral ranges in the

Table 13.1: List of literature absorption cross-sections applied for the DOAS fits

Species	Temperature	Reference
O_4	293 K	Thalman and Volkamer (2013)
HCHO	294 K	Meller and Moortgat (2000)
NO_2	294 K	Vandaele et al. (1998)
O_3	223 K	Serdyuchenko et al. (2014)
H_2O	296 K	HITEMP (Rothman et al., 2010)
$H_2O^{(I_0)}$ [a]	296 K	HITEMP (Rothman et al., 2010)

[a] I_0-corrected with $S^{(I_0)} = 5 \times 10^{23}$ molec cm^{-2} (see Equation 4.14)

Table 13.2: Applied DOAS fit settings (adapted from Kreher et al., 2019)

	UV	Vis
Spectral fit ranges	336.5 - 370 nm	425 - 490 nm
Included species	O_4, HCHO, NO_2	O_4, NO_2, O_3
	O_3, H_2O	H_2O, $H_2O^{(I_0)}$
Fit polynomial order	4	4
Offset polynomial order	2	2

UV and Vis, respectively. Table 13.1 lists the applied trace gas literature absorption cross-sections. The instrumental slit function for convolution of the cross-sections was inferred from the mercury lamp emission peak at 334 nm. Table 13.2 summarises the important fit settings. These were adapted from Kreher et al. (2019). The Ring spectrum was inferred according to Equation 4.7 from a noon zenith spectrum on 2020-04-05. The DOAS fit was applied to both non-polarimetric and polarimetric spectra, yielding a non-polarimetric and a polarimetric set of dSCDs, respectively. All spectra were evaluated against the zenith reference of the respective scan (with PA = 0° in the case of polarimetric spectra).

Figure 13.6 shows example fits in the UV and Vis spectral range for a spectrum recorded at EA = 5° evaluated against the zenith reference. Particularly in the Vis fit, the residual exhibits systematic structures around the rather strong O_4 absorption band, indicating that the DOAS fit setup is not ideal and might be optimised in the future. Nevertheless, the residual magnitude is sufficiently small to achieve reasonable detection limits for the gases of interest and the purpose of a first proof of concept. For the dSCD uncertainty we assume twice the DOAS fit error. Based on the investigations in Section 13.1.1, we further (quadratically) add a 2 % uncertainty due to the instrument's limited pointing and PA accuracy.

Figure 13.7 shows the non-polarimetric dSCDs inferred in the UV spectral range for all three species and over the three investigated days. Polarimetric dSCDs are shown and discussed separately in Section 15.1.

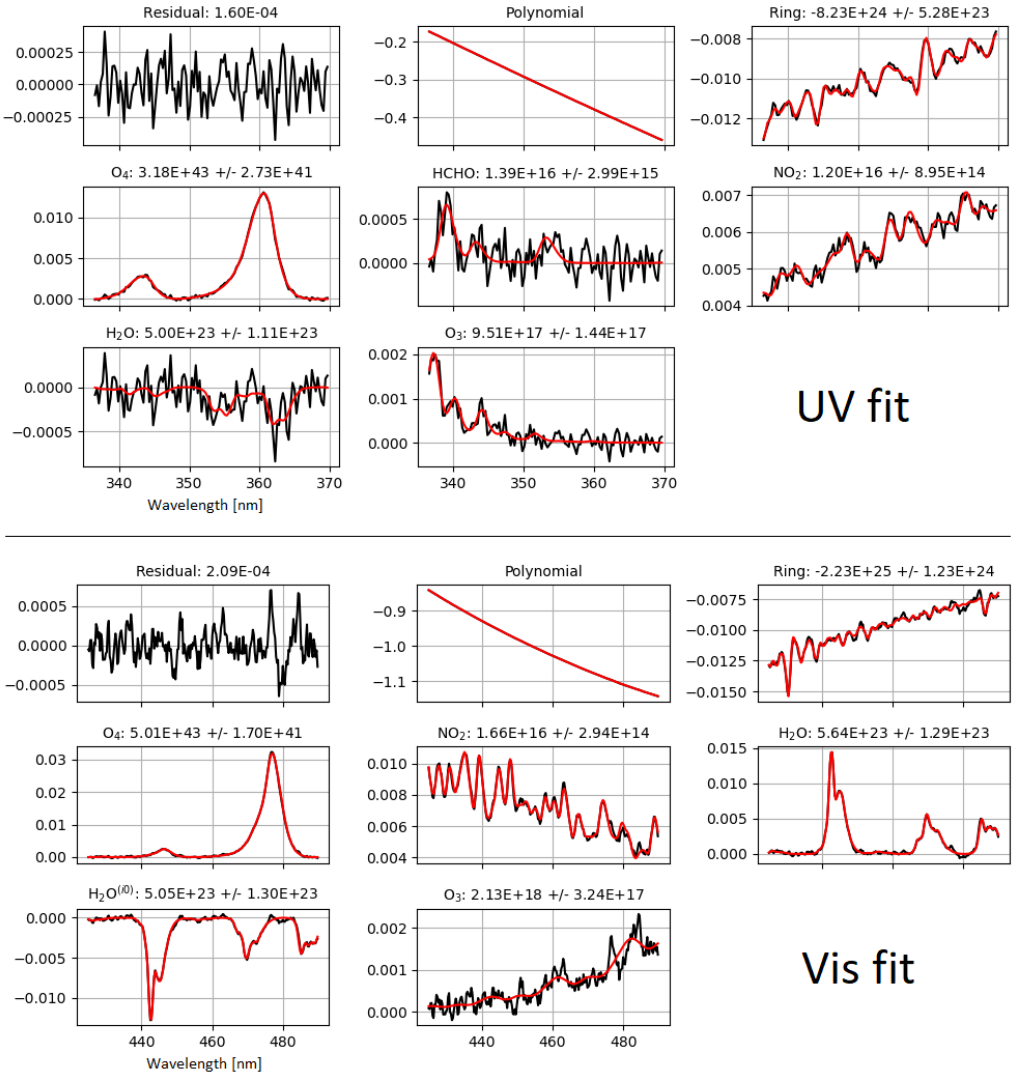

Figure 13.6: Results of two example DOAS fits in the UV (top) and Vis (bottom) spectral range. Black lines show the observed SOT, red lines indicate the fitted DOAS model (see Equation 4.13). The vertical axis indicates optical thicknesses. Numbers above the subplots represent the fit results (standard deviation for the residual, dSCDs for trace gases and Ring coefficient k_R in the case of the Ring spectrum

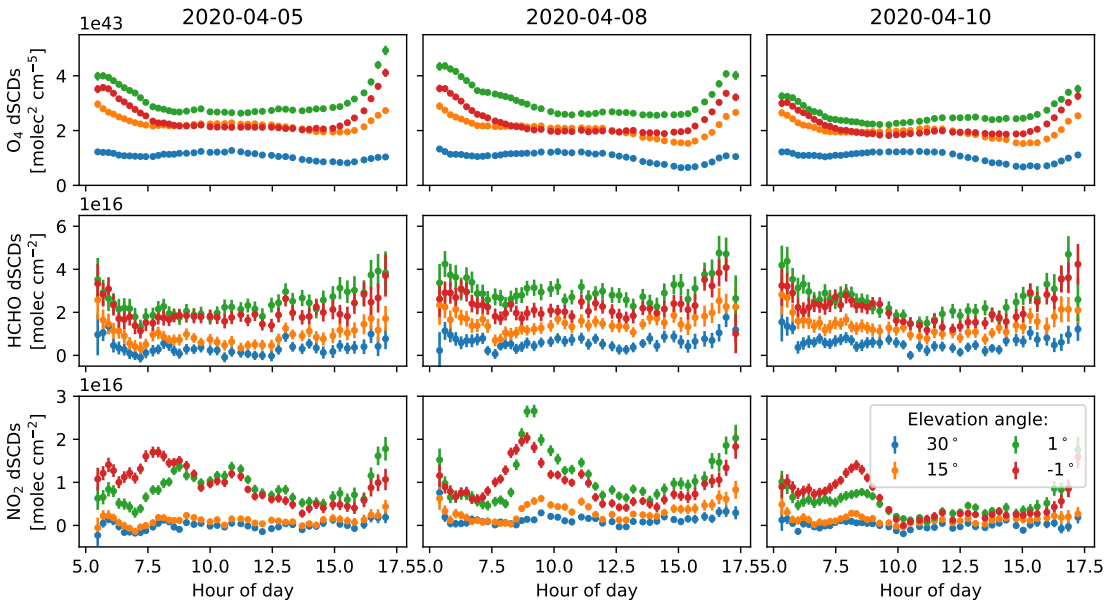

Figure 13.7: Time-series of UV DSCDs of all three species over the investigated days at selected elevation angles.

13.4 Differential slant optical thicknesses

DSOTs were derived from the PMAX-DOAS polarimetric spectra according to Equation 4.8, at wavelengths of 343, 360, 415, 460, 477 and 532 nm. In the evaluation of real data, we focus on the incorporation of polarimetric information. According to the considerations in Section 7.2.2, we therefore only include dSOTs between spectra recorded in the same viewing direction: spectra at PAs $\delta \in [30, 150°]$ are evaluated against $\delta = 90°$ as reference. No dSOTs are derived from the non-polarimetric spectra.

For polarised radiances we assume a measurement precision of 2 %, motivated by the investigations performed in Section 13.1 regarding the uncertainty in polariser orientation and potential remaining UPS of the instrument. Further, the temporal variation in skylight radiance observed over the corresponding PA sequence (see Section 13.1.2) is quadratically added but with typical contributions of 0.3 % only of minor relevance, most of the time. Consequently, typical dSOT uncertainties are of the order of $\sqrt{2} \cdot 0.02 \approx 0.028$.

13.4.1 Correction for inelastic Raman scattering

Recall that the RAPSODI forward model assumes Raman scattering to be an elastic scattering process (see Section 7.4.4), whereas in reality photons undergo wavelength shifts (3.3.2). The resulting filling-in of Fraunhofer-lines causes spectral narrowband features in the real OTs and will therefore lead to deviations between measured and

modelled dSOTs. Recall that the DOAS fit provides information on the OT changes due to inelastic scattering in the form of the Ring-spectrum $R(\lambda)$ and its magnitude k_R (see Section 4.2.4). This information can be used to virtually "shift" the Raman scattered photons in the dSOT observations back to their TOA wavelengths, to improve agreement with the model. We partly achieve this by the following approach: for each pair of spectra, Raman fit coefficients k_R are obtained using the DOAS analysis. A wavelength dependent $k_R(\lambda)$ is derived by linearly interpolating between the two $\ln(k_R)$ values obtained in the UV and Vis DOAS fit range. Then the spectral Raman dSOT $\Delta\tau_R(\lambda) = k_R(\lambda) \cdot R(\lambda)$ can be calculated. By subtracting a polynomial, the narrowband features of $\Delta\tau_R$ are extracted, which approximately describe the OT changes due to wavelength shifts. The resulting $\Delta\tau R'(\lambda)$ are then subtracted from the observed dSOTs $\Delta\tau(\lambda)$, to obtain what might be considered as "Raman shift compensated" dSOTs. Maximum magnitudes of $\Delta\tau R'(\lambda)$ at the wavelengths of interest are of the order of few 10^{-3}. Even though the approach is not ideal, it should sufficiently reduce the impact of Raman scattering on dSOTs to negligible amounts compared to other sources of uncertainties.

14 Retrieval setup

14.1 Measurement vector

In the following, retrievals are performed for each elevation scan (see the PMAX-DOAS measurement routine in Figure 12.4). The observations of an entire scan are summarised in $\hat{\mathbf{y}}$ and fed to the RAPSODI algorithm. The results therefore have a temporal resolution of approximately 17 min (compare Figure 12.4). An overview on the measurement vector elements is given in Table 14.1 together with typical uncertainties. Note that the uncertainties for dSCDs (particularly O_4) are considerably larger than those assumed by Frieß et al. (2019) and in the synthetic data analysis in Section 9.1. This is mostly a consequence of the additional 2 % error that we introduced to account for the instrument miss-pointing.

14.2 Treatment of negative elevations

Observations at negative EAs are particularly critical, since the instrument looks directly towards the Earth's surface. A first aspect is that the light path length between instrument and observed spot on the ground depends on topography. In the forward model, which assumes a flat ground, we account for this following the approach by Zhang (2014). It is illustrated in Figure 14.1: the elevation angles assumed in the model are adapted such that the distance between instrument and observed ground spot in the model correspond to the real distance.

A second critical aspect is the increased sensitivity of negative EA observations to the very local surface's optical properties. As shown in Figure 14.2, the PMAX-DOAS detected radiances reflected by the ground exhibit a strong directionality. Largest albedos are perceived for Vis wavelengths, when the Sun is located behind the instrument (RAA = 180°). This is in line with independent observations of typical forest BRDFs (Nag et al., 2017) and indicates that the assumption of a

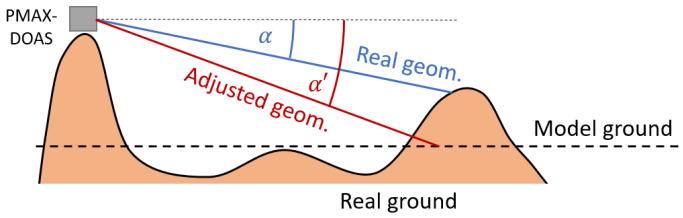

Figure 14.1: Illustration of the EA adaption for the RAPSODI forward model. α and α' indicate the real and the model elevation angle, respectively.

Table 14.1: Overview on the different kinds of observations included in the measurement vector $\hat{\mathbf{y}}$. Last column shows typical measurement uncertainties for the non-polarimetric and the polarimetric data (in brackets). Uncertainties of dSCDs are given in molec^2 cm^{-5} (O_4) and molec cm^{-2} (HCHO, NO_2).

Observations	Simulation wavelength [nm]	Typical uncertainties
dSOTs[a]	343, 360, 415 460, 477, 532	N.A. (0.028)
O_4 UV dSCDs	360	$10 \cdot 10^{41}$ ($12 \cdot 10^{41}$)
O_4 Vis dSCDs	477	$8 \cdot 10^{41}$ ($9 \cdot 10^{41}$)
HCHO dSCDs	343	$6 \cdot 10^{15}$ ($10 \cdot 10^{15}$)
NO_2 UV dSCDs	360	$2 \cdot 10^{15}$ ($3 \cdot 10^{15}$)
NO_2 Vis dSCDs	477	$5 \cdot 10^{14}$ ($6 \cdot 10^{15}$)

[a] Only at positive EAs

Lambertian albedo (as implemented in RAPSODI) is not representative at least for negative EA observations with forest in the LOS.

On the one hand, it is desirable to obtain at least some sensitivity to altitudes below the MOHP, which is best achieved by including observations at negative EAs. On the other hand, test runs with negative EA observations indicated that the approximations discussed before bias the entire retrieval. For the retrievals presented in this thesis, we therefore go for a compromise by only including non-polarimetric dSCDs at negative EAs.

14.3 Model ground and vertical grid

In contrast to the real topography around the MOHP, the Earth's surface in the RAPSODI forward model is assumed to be flat. The horizontal sensitivity of MAX-DOAS observations decreases approximately exponentially with the horizontal distance x to the instruments with 1/e-lengths on the order of 10 km (Wagner and Beirle, 2016; Tirpitz et al., 2020). The model ground altitude was calculated applying a weighted average over the topography $h(x)$ along the elevation scan azimuthal direction according to:

$$h_{model} = \frac{\int_0^{50\,\mathrm{km}} h(x) \exp(-x/10\,\mathrm{km})}{\int_0^{50\,\mathrm{km}} \exp(-x/10\,\mathrm{km})} = 725\,\mathrm{m\ a.s.l.} \tag{14.1}$$

Consequently, in the model atmosphere, the PMAX-DOAS "levitates" at an altitude of 275 m above the ground. The topography and the model ground altitude are illustrated in Figure 12.2. We applied a custom vertical grid of 40 layers: the PMAX-DOAS is centered inside a layer of 50 m thickness, in the following referred to as the

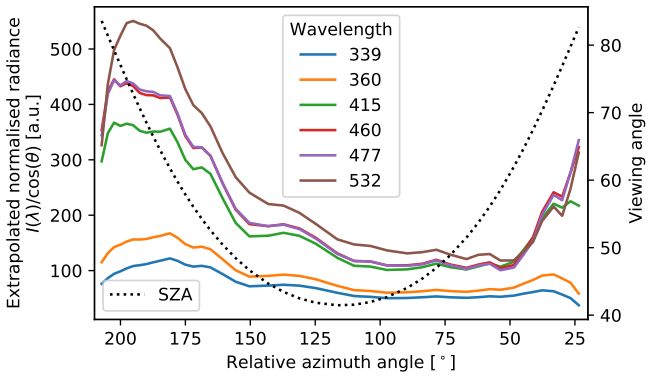

Figure 14.2: Radiances $I(\lambda)$ reflected from the ground towards the PMAX-DOAS instrument (2020-04-05), normalised by the cosine of the SZA $\cos(\theta)$. Assuming Lambertian reflection, $I(\lambda)/\cos(\theta)$ is an approximate measure for the ground's reflectivity. $I(\lambda)$ was inferred by extrapolating the radiances observed at all negative EAs (-1, -2 and -4°) to an EA of $-90°$ to remove the impact of atmospheric effects, e.g. light dilution between surface and instrument.

"PMAX-layer". Above and below, the layer thickness increases exponentially with vertical distance to the instrument. The grid is illustrated in Figure 14.3. Retrieved are the atmospheric parameters in the lowest 25 layers, spanning the altitude range between zero and 7.3 km above the ground. In the model atmosphere, the MOHP in-situ instruments are located at 265 m altitude, hence in the lower third of the PMAX-layer.

14.4 Static atmospheric parameters

Atmospheric parameters that are not retrieved with RAPSODI are O_3 concentrations, pressure, temperature and relative humidity. Profiles for all these quantities are provided by the DWD's O_3 sonde observations. The sonde profiles recorded closest in time served as the basis for the retrieval setup. Furthermore, for each evaluated elevation scan, the tropospheric O_3 amount was scaled with the coincident in-situ O_3 concentration observed at the MOHP. The scaling was applied with a weight of unity at the MOHP altitude, linearly decreasing with altitude h and falling to zero at $h = 10$ km. Below the MOHP, the O_3 concentration was assumed to be constant. Similar approaches were taken for pressure, temperature and relative humidity: here, profiles were scaled to agree with the coincident in-situ observations at MOHP and Altenstadt. For altitudes above the sonde's maximum altitude (≈ 35 km), a US-standard atmosphere was assumed. Example profiles of pressure, temperature, relative humidity, and O_3 are shown in the left panel of Figure 14.3.

Table 14.2: A priori settings for the state vector elements $\mathbf{x}$ applied for the evaluation of field data at the MOHP.

Kind	Parameter	A priori value	Apriori uncertainty	Correlation length
Profiles	c_{aer}	Exp. profile[a]	50 %	1 km
	c_{HCHO}	Exp. profile[b]	50 %	1 km
	c_{NO_2}	Exp. profile[b]	50 %	1 km
Surf. albedo	ω_{surf}	0.03	0.03	-
Aerosol properties	r_1	0.08 µm	25 %	-
	r_2	0.75 µm	40 %	-
	σ_1	0.5	15 %	-
	σ_2	0.6	10 %	-
	$\Re\, n(\lambda)$	1.47	0.06	400 nm
	$\Im\, n(\lambda)$	0.0017	100 %	400 nm
	f	0.9996	0.002	-

[a] 1 km scale height, VCD of $0.3 \cdot 10^8$ µm^2 cm^2
[b] 1 km scale height, VCD of $4 \cdot 10^{15}$ molec/cm^2

14.5 State vector

For the retrievals from field data, we limit most of our investigations to the Mie aerosol model, since the HG-model (with its simplifying assumptions) turned out to not accurately reproduce the real polarisation state of skylight (see Section 15.2). Further, in compliance with the data provided by the Sun photometer, we assume a common refractive index for both aerosol size modes, i.e. $\Re n_1$ and $\Re n_2$ as well as $\Im n_1$ and $\Im n_2$ are linked in the retrieval and in the following referred to as $\Re n$ and $\Im n$. An overview of the state vector elements is given in Table 14.2. The a priori aerosol VCD and properties represent approximate mean values and standard deviations as observed by the Sun photometer at MOHP over the year 2019. A priori trace gas VCDs were slightly reduced compared to the synthetic studies (compare Table 9.4), inspired by in-situ observations of NO_2 at the MOHP over the year 2019.

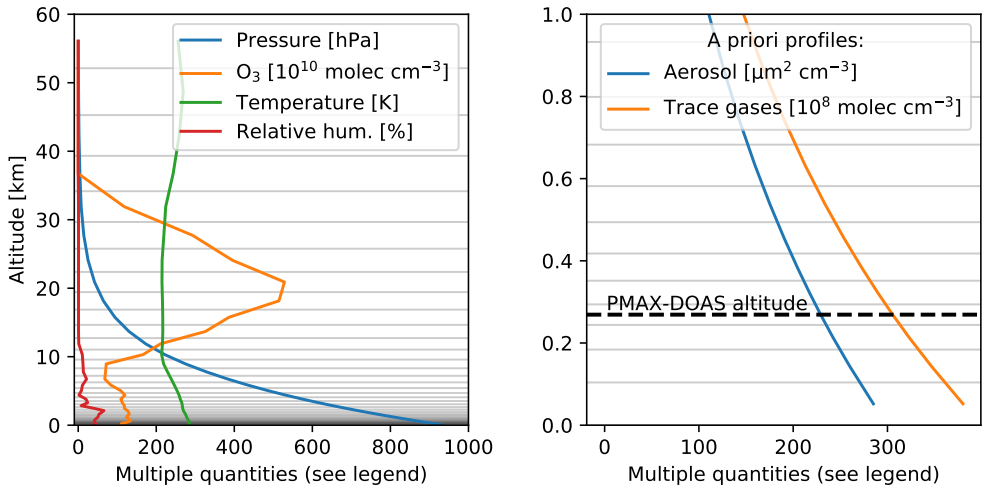

Figure 14.3: Illustration of the basic atmospheric settings. The left panel shows the entire grid (grey lines indicate model layer boundaries) with example profiles (noon on 2020-04-05) of parameters that are not retrieved. Right panel shows a zoom into the lowest kilometre, with the PMAX-DOAS instrument altitude and the a priori profiles for aerosol and trace gases (NO_2 and HCHO) indicated.

15 Comparison of measurements and forward model results

Before performing actual retrievals, it is illustrative to compare the field measurements to forward model simulations. For each real elevation scan we simulated the corresponding measurements in an atmosphere with aerosol profiles and properties as inferred from coincident ceilometer and Sun photometer observations. Below the vertical measurement range of the ceilometer (altitudes $< 460\,\mathrm{m}$ above the model ground), an exponential aerosol profile with a scale height of 1 km was assumed, which was scaled to obtain continuity at the transition between ceilometer and exponential profile. For trace gases, we assume the a priori profiles according to Table 14.2.

15.1 Differential slant column densities

Figure 15.1 and 15.2 compare measured and modelled O_4 dSCDs at 360 and 477 nm, respectively. In the MAX-DOAS community, it is not unusual to scale the measured O_4 dSCDs prior to the retrieval by a factor F_{O_4}. This was initially motivated by Wagner et al. (2009), who reported a significant mismatch between measured and simulated dSCDs in a relatively well-known atmosphere. The application of the scaling and the reason for its necessity are debated (e.g. Wagner et al., 2009; Clémer et al., 2010; Ortega et al., 2016; Wagner et al., 2019, and references therein). Scaling factors applied in former MAX-DOAS studies are $0.7 \leq F_{O_4} \leq 1$, typically with smaller values for the UV than the Vis. Also in the just presented comparison we found that a scaling of O_4 dSCDs by 0.85 and 0.9 in the UV and Vis, respectively, significantly improve the average agreement between measurement and model results. In Figure 15.1 and 15.2, these scalings are already applied and we will also use the scaled O_4 dSCDs in the retrievals in Section 16. This step is of course critical, as it entails the risk to conceal measurement artefacts or shortcomings of the model under the pretext of some "unknown physics". In the future, this should therefore be further investigated. The comparison between measurement and model for unscaled dSCDs is shown in Appendix D.

With this scaling applied, the overall agreement between measured and modelled dSCDs is satisfactory. As predicted in Section 6.4, the O_4 dSCDs recorded at different polariser orientations split up particularly at viewing geometries where high DOLPs are expected. For high EAs, the deviations are mostly in agreement with the measurement uncertainties and the basic observed daily patterns are well reproduced by the forward simulations. This changes for low EAs: here, the model

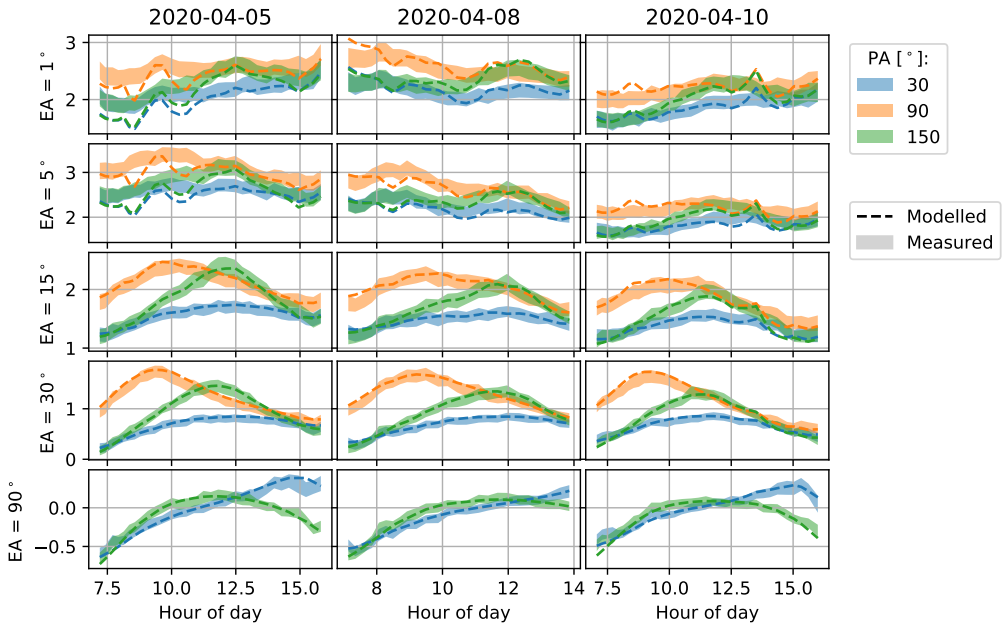

Figure 15.1: Comparison of measured and modelled O_4 dSCDs at 360 nm in units of 10^{43} molec^{2}cm^{-5} (vertical axis). The model atmosphere was set up to best knowledge from Sun photometer and ceilometer observations. For orientation regarding the geometries: the RAA changes over the day from 190° at 7:00h to 30° at 16:00h. The minimum SZA over the day is about 40°.

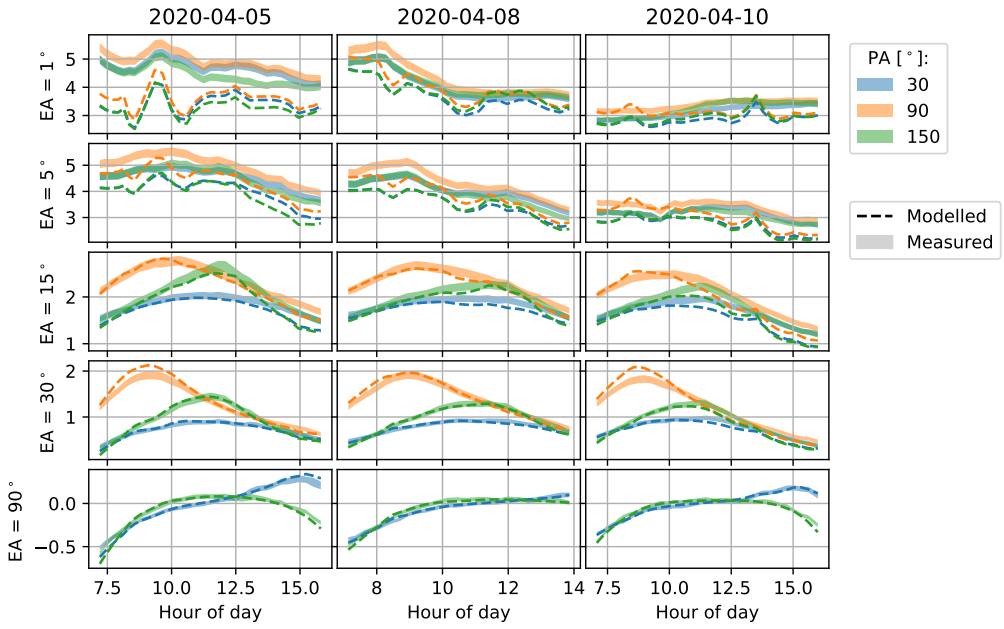

Figure 15.2: Same as Figure 15.1, but for O_4 at 477 nm

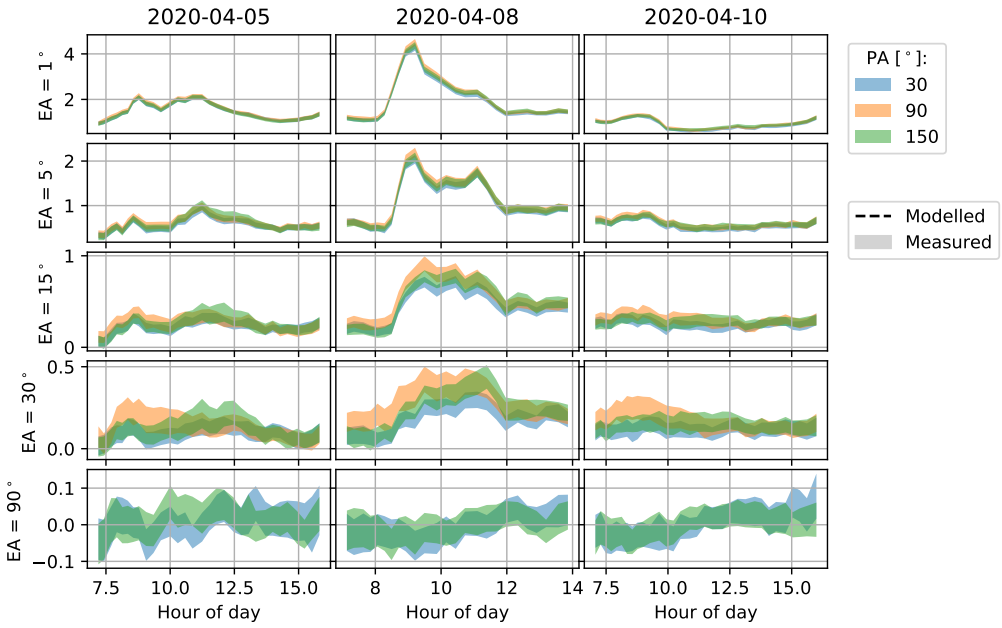

Figure 15.3: Same as Figure 15.1 but for HCHO dSCDs at 343 nm and without modelled data. DSCDs are in units of 10^{16} molec cm^{-2} (vertical axis).

at times strongly deviates from the measurements and shows large variability that coincide with the changes in aerosol properties as observed by the Sun photometer (compare Figure 12.5). Recall that aerosol profiles below the ceilometer's vertical measurement range are not known. The somewhat arbitrary assumption of an exponential profile in the lowest layers is therefore likely to explain large parts of the deviations. However, changes in aerosol properties with altitude might also be an issue, considering that MAX-DOAS observations become more sensitive to low altitudes with decreasing viewing elevation. Furthermore, the Sun photometer aerosol amounts and properties might not well represent the true aerosol conditions over the entire horizontal sensitivity range of MAX-DOAS observations at low EAs.

For HCHO and NO_2 there is no or not sufficient independent information available on their vertical distribution. Thus, a meaningful comparison between measurements and forward model results cannot be conducted. Figure 15.3 and 15.4 therefore only show the measured HCHO and NO_2 dSCDs. The HCHO dSCDs hardly exceed the PMAX-DOAS detection limit. A potential splitting with PA therefore gets lost in the noise. For NO_2 dSCDs, a splitting with PA is visible with similar patterns as for O_4. However, the splitting is significantly weaker than for O_4, which is in agreement with the predictions in Figure 6.7.

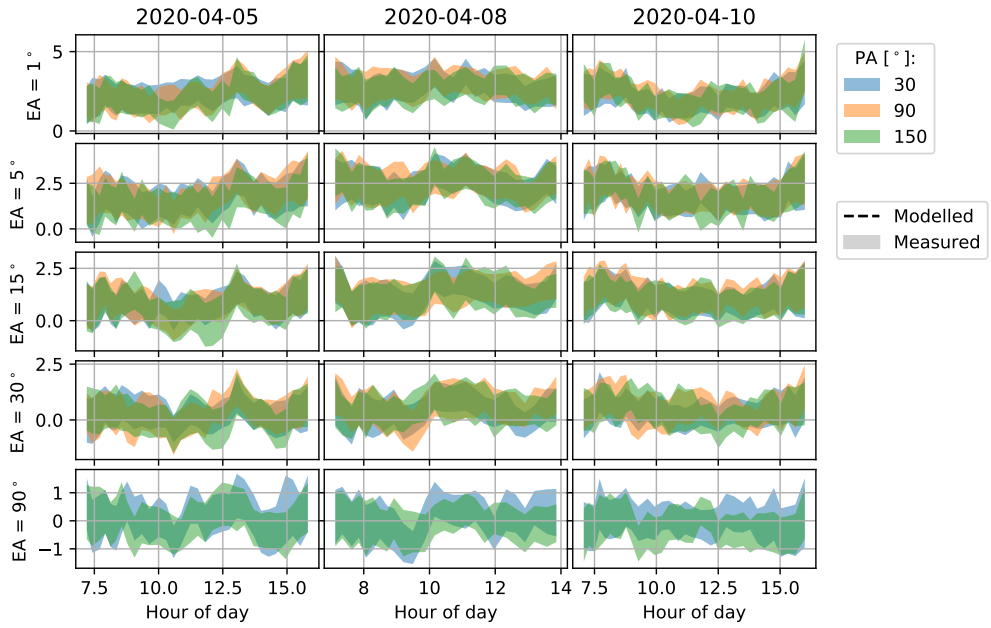

Figure 15.4: Same as Figure 15.1 but for NO_2 dSCDs at 460 nm and without modelled data. DSCDs are in units of 10^{16} molec cm^{-2} (vertical axis).

15.2 Differential slant optical thicknesses

Figure 15.5 and 15.6 show a comparison between modelled and measured dSOTs in the UV and the Vis respectively. Recall that, for field data, we focus on the incorporation of polarimetric information and therefore only consider two polariser angles ($\delta \in [30, 150]$) per viewing direction, both evaluated against the $\delta = 90°$ spectrum of the same viewing direction.

The agreement between model and measurement is reasonable in the sense that the basic temporal patterns are well reproduced. Significant deviations again coincide with changes in the aerosol properties observed by the Sun photometer (compare Figure 12.5), particularly on 2020-04-08 between 11:00 and 13:00h. Again, this indicates that the Sun photometer provided aerosol properties are at times not well representative for airmasses sampled by the PMAX-DOAS. The deviations increase with decreasing EA, probably for the same reasons as discussed in the context of O_4 dSCDs before. The decrease in DOLP with increasing aerosol load is directly visible here: the magnitude of the dSOTs is reduced on 2020-04-10 (AOT ≈ 0.2) compared to 2020-04-05 (AOT ≈ 0.06).

Figure 15.7 shows the same data as presented in Figure 15.1, 15.2, 15.5 and 15.6 but in the form of histograms. It does not provide new insights but is useful, since the same way of representation is applied to assess the convergence of the retrievals performed in Section 16.

For test purposes, we also applied the HG-aerosol model to perform forward simulations and compare them to the observations. Apart from the microphysical prop-

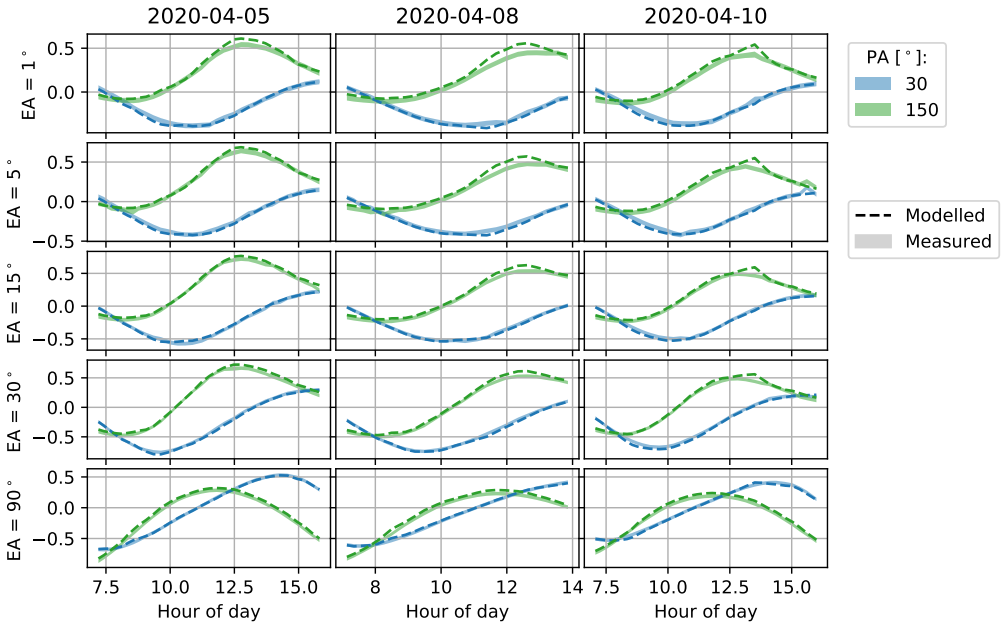

Figure 15.5: Same as Figure 15.1 but for dSOTs at 343 nm.

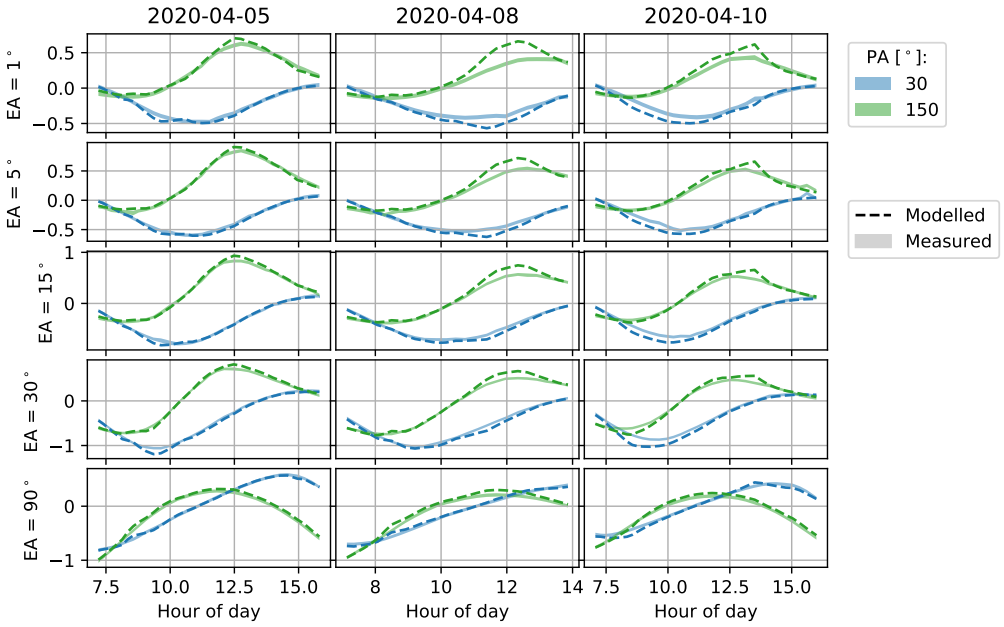

Figure 15.6: Same as Figure 15.1 but for dSOTs at 532 nm.

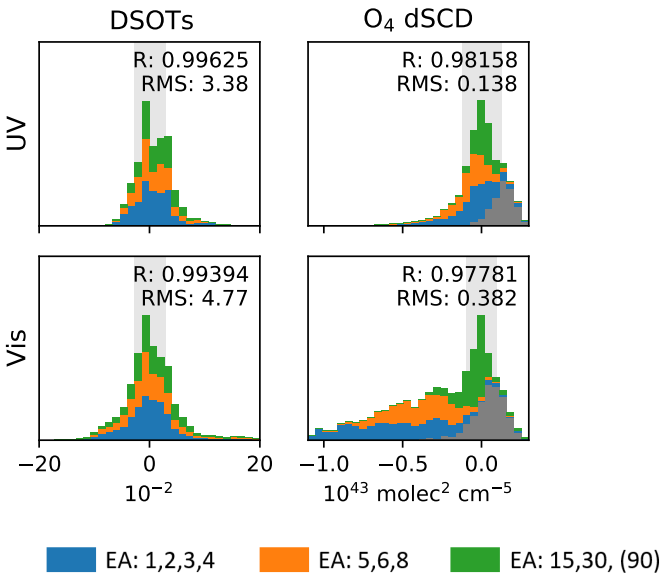

Figure 15.7: The same data as shown in Figure 15.1, 15.2, 15.5 and 15.6 but in the form of histograms, which indicate the difference $\mathbf{F}(\mathbf{x}) - \mathbf{y}$ between forward modelled results ($\mathbf{F}(\mathbf{x})$) and measurements ($\mathbf{y}$). Top row ("UV") shows data for dSOTs at $\lambda < 400\,\mathrm{nm}$, and O_4 dSCDs at 360 nm. Bottom row ("Vis") shows data for dSOTs at $\lambda > 400\,\mathrm{nm}$ and O_4 dSCDs at 477 nm. Grey shaded areas indicate the average measurement error. Numbers in the subplots indicate the correlation coefficient (R) and the RMS between measured and modelled data.

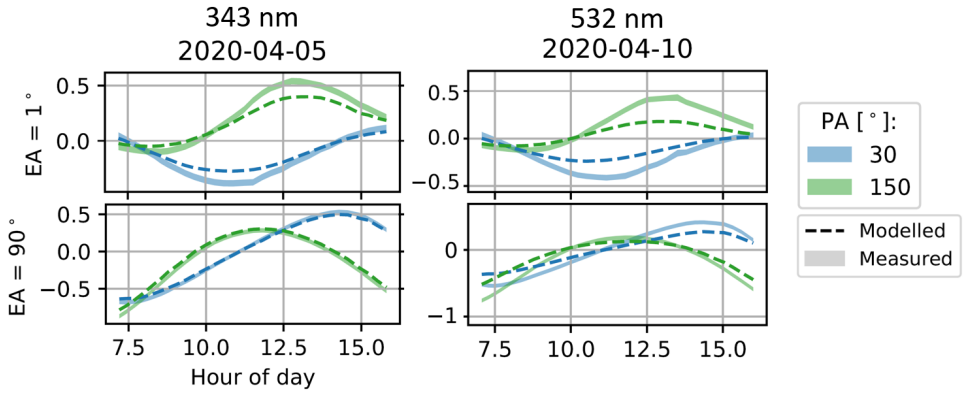

Figure 15.8: Comparison of modelled and measured dSOTs with HG-aerosol applied in the simulation. Left: day with low aerosol load (AOT of 0.06 at 440 nm) in the UV, i.e. low impact of aerosol scattering. Right: day with high aerosol load (AOT of 0.2 at 440 nm) in the Vis, i.e. high impact of aerosol scattering.

erties, the Sun photometer directly provides corresponding values for the asymmetry parameter, the single scattering albedo and the Ångstrom exponent, which were inserted for g_{hg}, ω_{hg} and $\mathring{a}$ in the forward model (spectrally interpolated to the corresponding wavelengths applying Equation 12.1). Figure 15.8 shows simulated dSOTs for selected days, wavelengths and EAs. Particularly in situations where aerosol scattering significantly contributes to the detected radiance field (large wavelengths, high aerosol load) the model significantly underestimates the dSOT magnitudes (hence, the DOLP). This is likely related to the simplifications taken in terms of the HG-phase matrix as defined in Section 3.3.3, which assumes aerosol scattering to be non-polarising. We conclude that the HG-approximation (at least in the form implemented in the RAPSODI algorithm) cannot fully reproduce the real SOP of skylight, and is therefore not a useful approximation for retrievals from polarimetric MAX-DOAS observations.

16 Retrieval results

Within this chapter, we present retrievals with RAPSODI on the basis of the dSOTs and dSCDs as inferred from the PMAX-DOAS spectra according to Section 13. As for synthetic data, we will show results from multiple retrieval runs with the composition of measurement and state vector being varied. In all retrievals, the species are retrieved simultaneously in a single model atmosphere and at multiple wavelengths.

Regarding the state vector $\hat{\mathbf{x}}$, we focus on two major cases:

- Profile retrieval only: we retrieve vertical profiles of aerosol, HCHO and NO_2, whereas surface albedo and aerosol microphysical properties are fixed to the values from coincident Sun photometer observations. The corresponding results are discussed in Section 16.1.

- Full state retrieval: we retrieve the full set of atmospheric parameters, including vertical profiles, surface albedo and aerosol microphysical properties. The corresponding results are shown in Section 16.2.

For the purpose of side studies, we occasionally implement further state vector compositions. These are discussed in more detail in the corresponding paragraphs. Regarding the measurement vector $\hat{\mathbf{y}}$, two cases are investigated:

- Retrieval from non-polarimetric observations: $\hat{\mathbf{y}}$ only consists of non-polarimetric dSCDs of O_4, HCHO and NO_2 at all available wavelengths according to Table 14.1. In the nomenclature introduced for synthetic data (see Table 9.5), this corresponds to the "Multi-S" mode.

- Retrieval from polarimetric observations: for positive EAs, all available polarimetric dSCDs and dSOTs are incorporated into $\hat{\mathbf{y}}$. At negative EAs, we keep the non-polarimetric dSCDs and exclude dSOTs for the reasons discussed in Section 14.1. This corresponds to the "Multi-S-P" mode.

16.1 Retrieval of vertical profiles only

In a first retrieval run we only retrieved vertical profiles of aerosol and trace gases, whereas surface albedo and aerosol microphysical properties were fixed to the values from coincident Sun photometer observations. The measurement vector contains non-polarimetric dSCDs of O_4, HCHO and NO_2 at all available wavelengths according to Table 14.1 (in the nomenclature introduced in Table 9.5 this corresponds to

the Multi-S mode). DSOTs were not included. Apart from the simultaneous retrieval of all species from data at multiple wavelengths and the application of the Mie-model, this setting is very similar to how a conventional MAX-DOAS retrieval would be performed.

Figure 16.1 shows the results over the three investigated days. The first six rows show aerosol profiles and aerosol vertical columns in comparison to the Sun photometer and ceilometer observations. Here, two comparisons are performed in terms of aerosol surface area concentration c_{aer} (first two rows) and in terms of the aerosol extinction coefficient K_{aer} (fourth to sixth row), respectively. Recall that AOTs are directly measured by the Sun photometer (determining the attenuation of direct sunlight), whereas the Sun photometer aerosol area VCD is a product of the AERONET retrieval algorithm and and strongly depends on the inferred aerosol microphysical properties. Therefore, the comparison of extinction profiles and AOTs should in the following be considered more meaningful.

The shown ceilometer profiles were convoluted with the PMAX-DOAS AVKs according to Eq. 5.23. They therefore represent how the PMAX-DOAS is expected to perceive the original ceilometer profiles (the latter are shown in Figure 12.6), given its sensitivity to the different atmospheric layers. For the calculation of PMAX aerosol VCDs and AOTs, only layers above the PMAX-DOAS (including the PMAX-layer) were considered to ensure comparability to the Sun photometer (which is located about 10 m below the PMAX-DOAS). The "partial" AOT and VCD represent the vertically integrated convoluted ceilometer profiles, i.e. they estimate the fraction of the total vertical column that the PMAX-DOAS is able to detect according to its AVKs.

The seventh row of Figure 16.1 shows the retrieved HCHO profiles. For HCHO, there are no supporting observations available for comparison. Also, HCHO dSCDs only slightly exceeded the detection limit over the investigated period. The following investigations and discussions therefore focus on aerosol and NO_2. The last two rows show retrieval results of NO_2. The bottom row compares the NO_2 concentration retrieved in the PMAX-layer with coincident MOHP in-situ observations.

Text labels in the very right indicate the average DOFS obtained for the respective species' profiles. Recall that at negative EAs (which are most sensitive to the layers below the PMAX-DOAS) we always feed non-polarimetric dSCDs to the retrieval (see Section 13.3). Therefore, for the calculation of DOFS, only the layers above the PMAX-DOAS are considered to better assess the gain in information achieved through the incorporation of polarimetric information at positive EAs in later retrieval runs. In each profile plot, the altitude of the PMAX-DOAS instrument is indicated by a white dashed line.

Shaded areas in the line plots indicate uncertainties. The PMAX-DOAS uncertainties, particularly for the vertical columns, are very small and unlikely to represent the real uncertainty. This is a well-known issue: as described in Section 5.4, the retrieval covariance $\hat{\mathbf{S}}$ is inferred by propagating the measurement uncertainties (assumed to be normally distributed) into the retrieval results but does not consider other (often prevailing) sources of uncertainties, e.g. horizontal inhomogeneity.

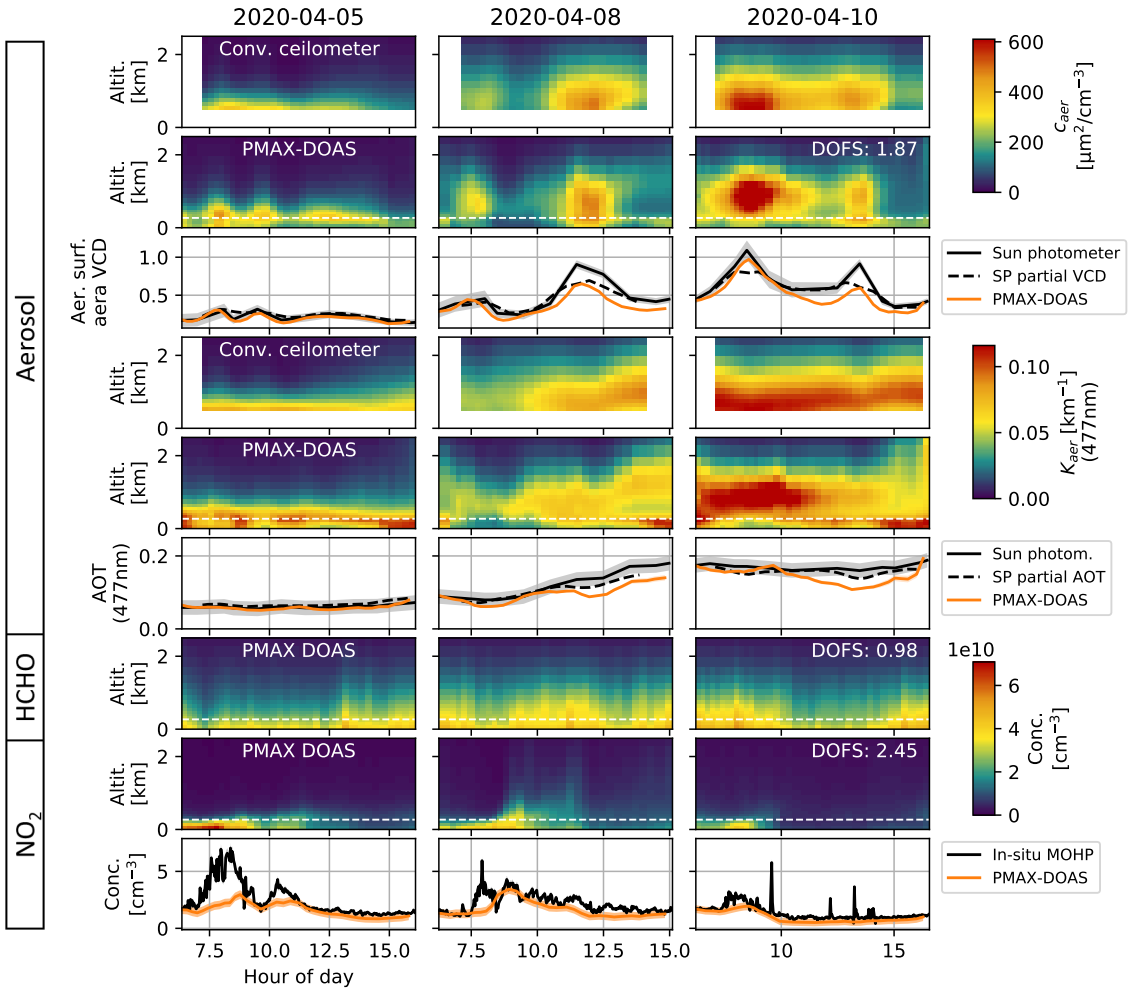

Figure 16.1: Profiles retrieved from non-polarimetric dSCDs of O_4, HCHO and NO_2. See text for further details.

Regarding aerosol profiles and vertical columns, the basic patterns of PMAX-DOAS, Sun photometer and ceilometer agree well. The observed deviations are comparable to those reported in former comparison studies using similar approaches (e.g. Frieß et al., 2016).

For layers below the PMAX-DOAS, there is no data for validation available. Here, some features in the aerosol profiles seem unlikely though: thin aerosol layers at the PMAX-DOAS altitude or features sharply confined to the layers below (in the evening of all three days). Their origin has not been identified but a priori biases or issues with the negative EA observations are potential candidates (see also Section 14.1). Similar issues appear also in some of the following retrievals. However, we will not further discuss this, since no supporting data exists on the corresponding altitudes and since the feasibility of retrievals from negative EAs requires thorough investigations that are out of the scope of this thesis.

The NO_2 profiles look realistic over the full altitude range. In the morning, the PBL typically rises due to convection driven by solar heating of the surface (Stull, 2012). It is very likely this rise that is observed in the NO_2 profiles, most pronounced on 2020-04-08. Regarding the NO_2 concentration in the PMAX-layer, the boundary layer might advect up the slopes of the Hohenpeissenberg, leading to very local increases in the NO_2 concentration at about 8:00h. The corresponding peaks in the in-situ concentration might therefore not be detected by the PMAX-DOAS. Later in the day, when the PMAX-layer is fully covered by the PBL and well mixed, the PMAX and in-situ observations show good agreement most of the time.

Figure 16.2 compares the modelled observations $\mathbf{F}(\hat{\mathbf{x}})$ for the retrieved state $\hat{\mathbf{x}}$ to the actual observations $\hat{\mathbf{y}}$, thereby indicating the quality of the retrieval's convergence. Positive offsets, i.e. overestimations by the model, are observed for O_4 and NO_2 dSCDs in the UV. Furthermore, the model slightly underestimates O_4 Vis dSCDs particularly at low EAs where O_4 dSCDs are large. In the case of NO_2 this is likely related to a priori biases: the average retrieved NO_2 concentrations over the three investigated days are rather small compared to the a priori values. For O_4, the rather uncertain scaling factors might be an issue but also the fixed aerosol properties from the Sun photometer might not be ideal, preventing the algorithm from bringing both UV and Vis observations into agreement. We will show in Section 16.2 that the retrieval of the full state vector including aerosol microphysical properties yields much better agreement.

In the next retrieval run, we incorporated polarimetric information, i.e. polarimetric dSCDs and dSOTs at all available wavelengths according to Table 14.1 were included in $\hat{\mathbf{y}}$ (in the nomenclature introduced in Table 9.5 this corresponds to the Multi-S-P mode). The results are shown in Figure 16.3 and 16.4.

Aerosol profiles and vertical columns strongly deviate from the ceilometer and Sun photometer data. Recalling the disagreement between measured and forward modelled dSOTs already observed e.g. in Figure 15.6, this might be expected to some extent. They are most likely a consequence of erroneous or non-representative aerosol properties provided by the Sun photometer. In the affected time intervals, RAPSODI obviously compensates those by introducing aerosol layers at high altitudes ($> 2\,\mathrm{km}$). This is rather successful regarding the convergence of the retrieval (see Figure 16.4) but not desired at all. Interestingly, the NO_2 profiles are not significantly affected compared to the retrieval from non-polarimetric dSCDs and the agreement of MAX-DOAS and in-situ instrument even slightly improves.

A striking finding was made when repeating the same retrieval, but this time including the surface albedo ω_{surf} in $\hat{\mathbf{x}}$ as an additionally retrieved parameter. The results are shown in Figure 16.5 and 16.7. The retrieved values for the surface albedo are shown in Figure 16.6.

Just by retrieving ω_{surf}, the agreement between PMAX-DOAS and supporting observations for aerosol profiles and columns is basically "restored" and the agreement of the vertical columns is even improved compared to the retrieval from non-

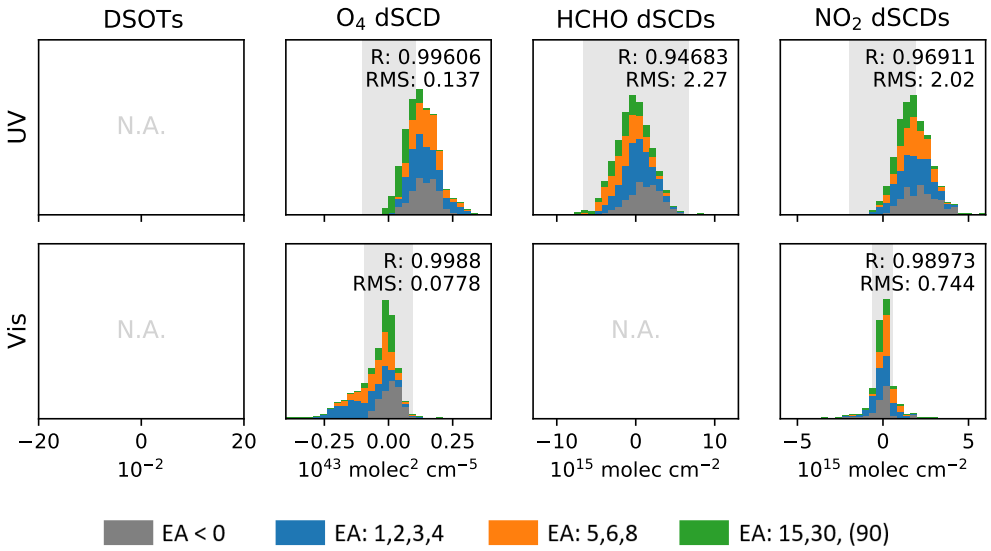

Figure 16.2: Comparison of modelled measurements $\mathbf{F}(\hat{\mathbf{x}})$ for the retrieved state $\hat{\mathbf{x}}$ to the actual observations $\hat{\mathbf{y}}$. Histograms show the difference $\mathbf{F}(\hat{\mathbf{x}})$ - $\hat{\mathbf{y}}$. Top row ("UV") shows data for dSOTs at $\lambda < 400\,\mathrm{nm}$, O_4 and NO_2 dSCDs at 360 nm and HCHO dSCDs at 343 nm. Bottom row ("Vis") shows data for dSOTs at $\lambda > 400\,\mathrm{nm}$, O_4 dSCDs at 477 nm and NO_2 dSCDs at 460 nm. Grey shaded areas indicate the average measurement error.

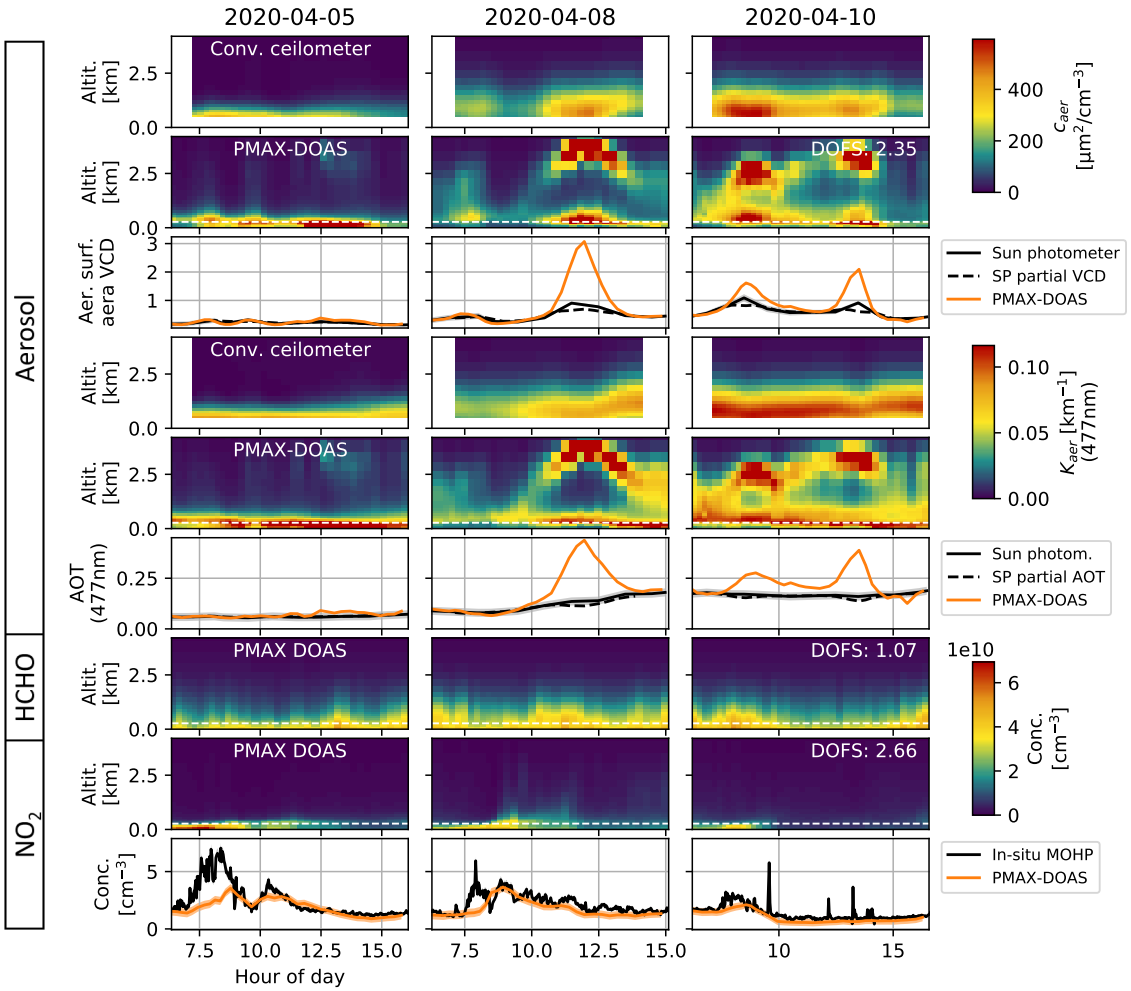

Figure 16.3: Same as Figure 16.1 but for profiles retrieved from the full set of polarimetric observations according to Table 14.1: this includes dSOTs and polarimetric dSCDs of O_4, HCHO and NO_2.

polarimetric dSCDs in Figure 16.1. Figure 16.7 furthermore indicates a significant improvement in the convergence of the retrieval in the sense that the biases between $\mathbf{F}(\hat{\mathbf{x}})$ and $\hat{\mathbf{y}}$ are reduced compared to Figure 16.2 and 16.4. The retrieved surface albedo varies strongly but does not show a consistent diurnal cycle as it would be expected if topography features or the BRDF of the real surface were the only issue. Instead ω_{surf} seems to correlate with changes in the Sun photometer aerosol properties and at times exhibits rather unlikely spectral dependencies (e.g. in the evening). We therefore assume that RAPSODI "exploits" ω_{surf} to compensate for two effects here: (1) the model's simplifying approximations regarding the topography and surface properties and (2) erroneous or non-representative aerosol properties from the Sun photometer. The incorporation of polarimetric information increases the DOFS for the retrieved profiles by about 0.5 for aerosol, 0.1 for HCHO and 0.2 for NO_2

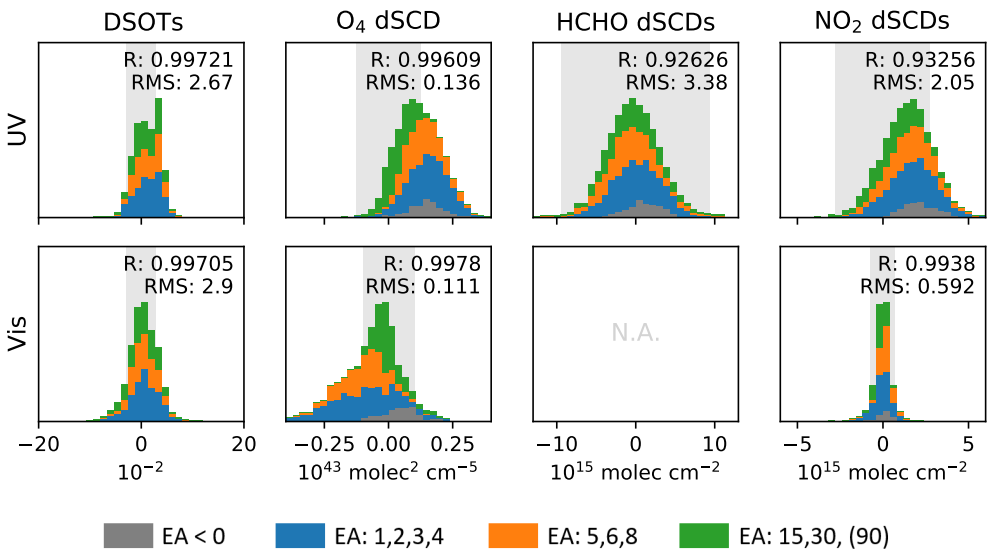

Figure 16.4: Same as Figure 16.2 but for the retrieval results shown in Figure 16.3.

compared to the retrieval from non-polarimetric dSCDs. This is qualitatively in line with the findings from the synthetic studies in Section 9, even though the conditions as well as the assumptions on a priori and measurement covariances are quiet different.

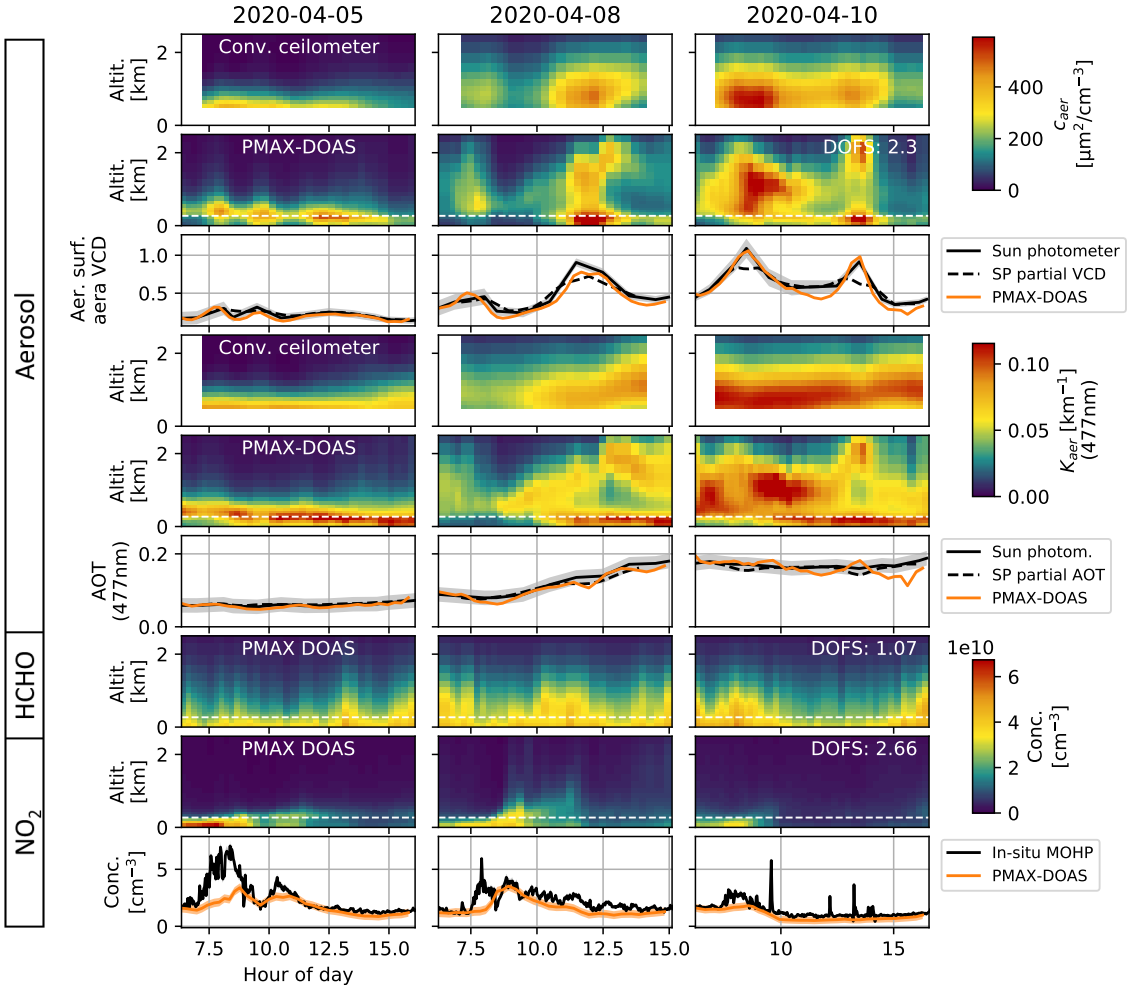

Figure 16.5: Same as Figure 16.3 but with the surface albedo being retrieved as additional parameter.

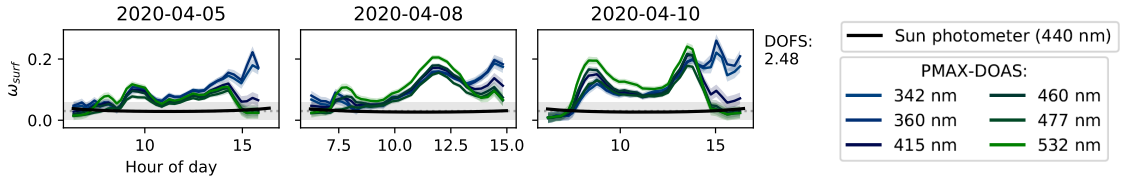

Figure 16.6: Retrieved surface albedo values for the profile results shown in Figure 16.5. Grey dashed lines and shaded rectangles indicate a priori values and uncertainties. DOFS on the right represent temporal averages summed over all six wavelengths.

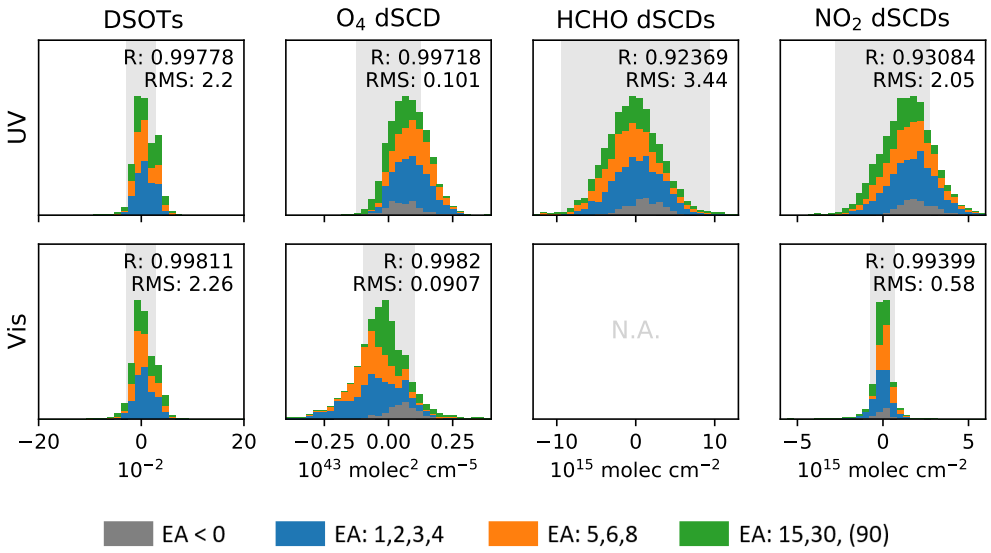

Figure 16.7: Same as Figure 16.2 but for the retrieval results shown in Figure 16.5 and 16.6.

16.2 Retrieval of the full atmospheric state

So far we limited the retrieval to vertical distributions of aerosol and trace gases. We will now go a step further and retrieve all parameters listed in Table 14.2, hence, vertical profiles, surface albedo and aerosol microphysical properties. Again we start by only incorporating non-polarimetric dSCDs of O_4, HCHO and NO_2 in $\hat{\mathbf{y}}$ (Multi-S mode). The retrieval results are shown in Figure 16.8, 16.9 and 16.10.

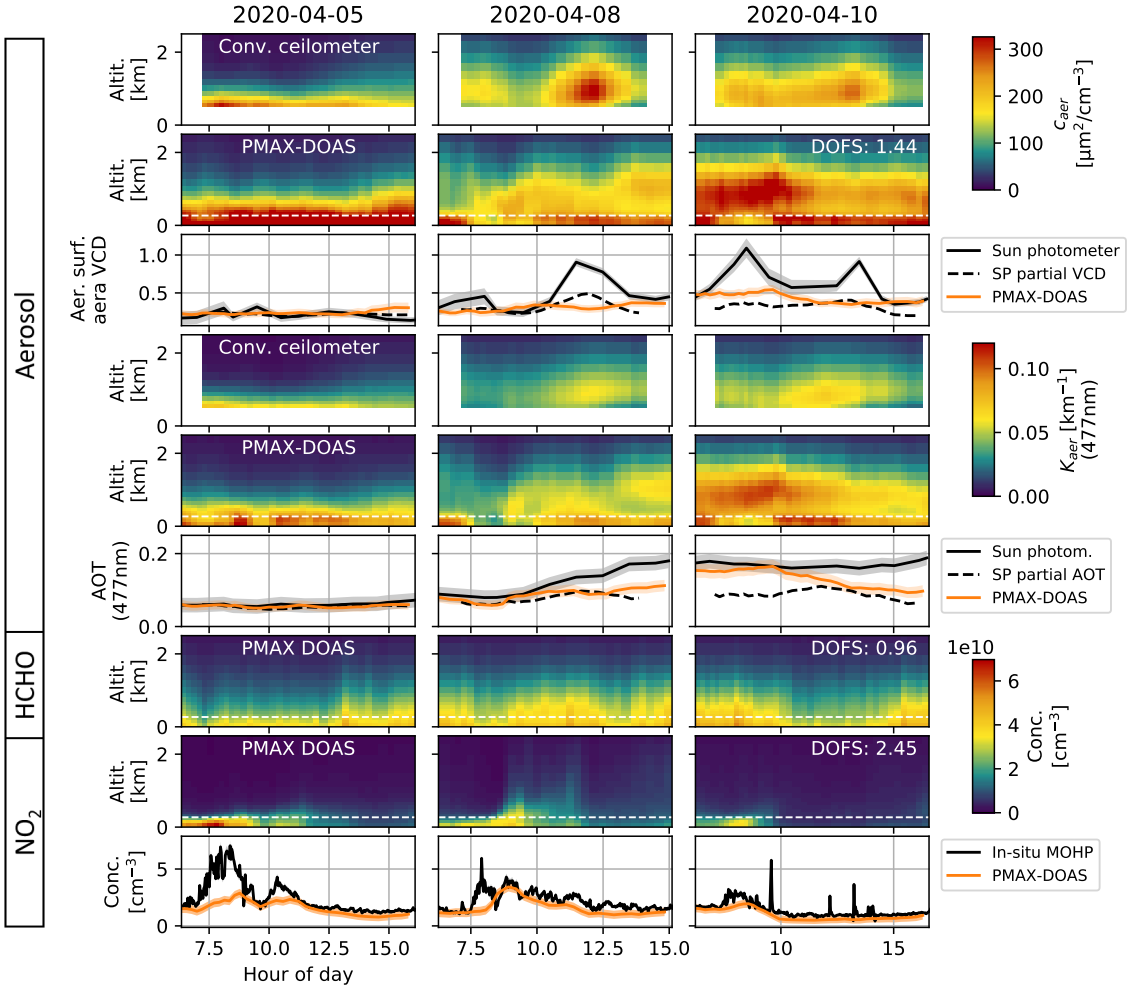

Figure 16.8: Same as Figure 16.1 but with surface albedo and all aerosol microphysical properties being retrieved from non-polarimetric dSCDs of O_4, HCHO and NO_2.

As indicated by the DOFS values in Figure 16.9, the information on surface albedo and aerosol properties is very limited. Significant information (DOFS > 0.2) is only inferred on the fine mode parameters r_1 and σ_1 as well as ω_{surf} and $\Re n$ (if DOFS are summed over all wavelengths). For r_2, σ_2, $\Im n$ and f, DOFS are below 0.15 and the retrieval basically resorts to the a priori values that significantly differ from

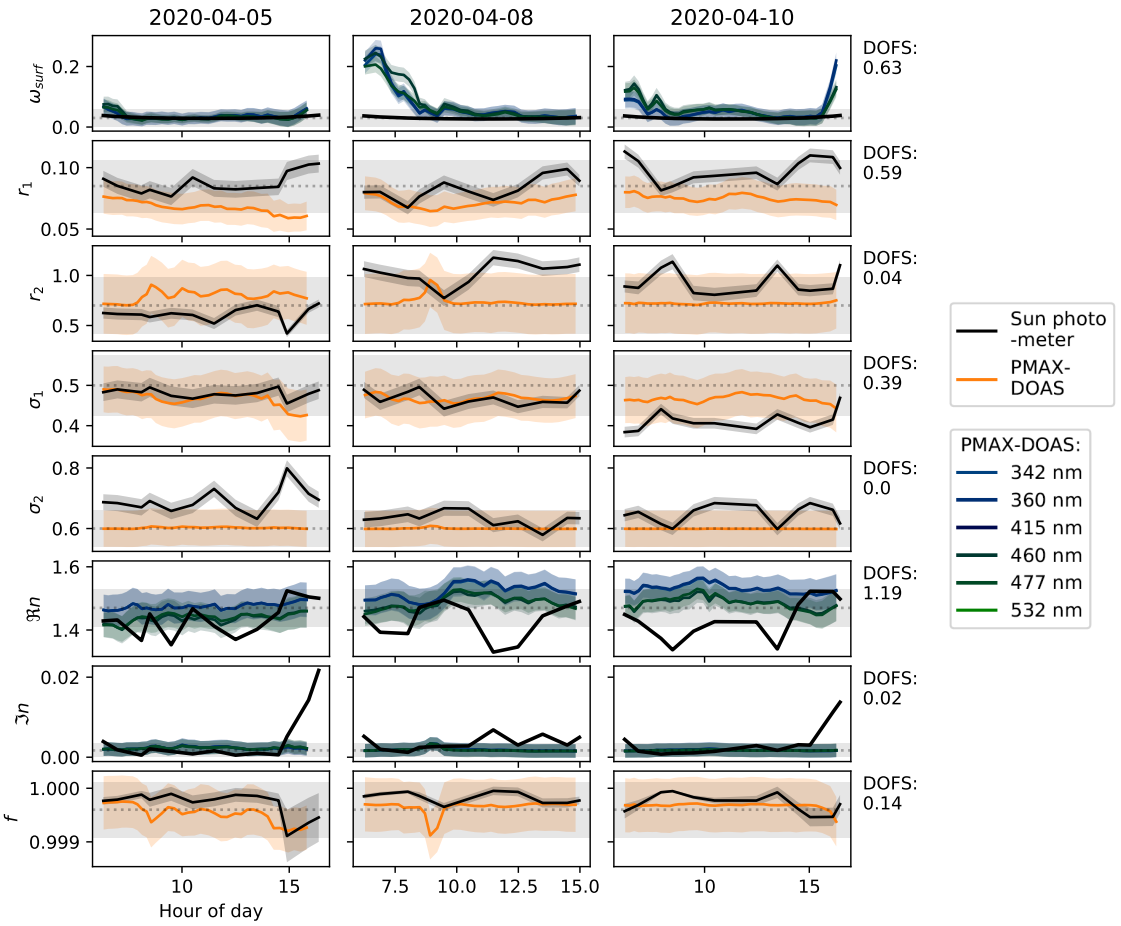

Figure 16.9: Retrieved surface albedo and aerosol properties for the profiling results shown in Figure 16.8 (retrieval from non-polarimetric dSCDs of O_4, HCHO and NO_2). Grey dashed lines and shaded rectangles indicate a priori values and uncertainties. DOFS on the right represent temporal averages. For spectrally resolved quantities (ω_{surf}, n), DOFS are summed up over all wavelengths.

the Sun photometer observations. As a consequence, PMAX-DOAS area surface concentrations and VCDs in Figure 16.8 strongly differ from the ceilometer and Sun photometer data, particularly when the differences between Sun photometer and a priori values are large. Now that the retrieval algorithm is "aware" of the limited information on aerosol properties, the DOFS for aerosol profiles (1.4) are significantly reduced compared to the former retrieval runs (between 1.9 and 2.3). Accordingly, the convolution of the ceilometer profiles (see Eq. 5.23) yields a apriori biased and thus much smaller values than in the comparisons before. Interestingly, the PMAX-DOAS extinction profiles are still rather in agreement with the unconvoluted ceilometer profiles (as shown in Figure 12.6) than with the convoluted ones. The results for trace gases do not seem to be much affected by the limited

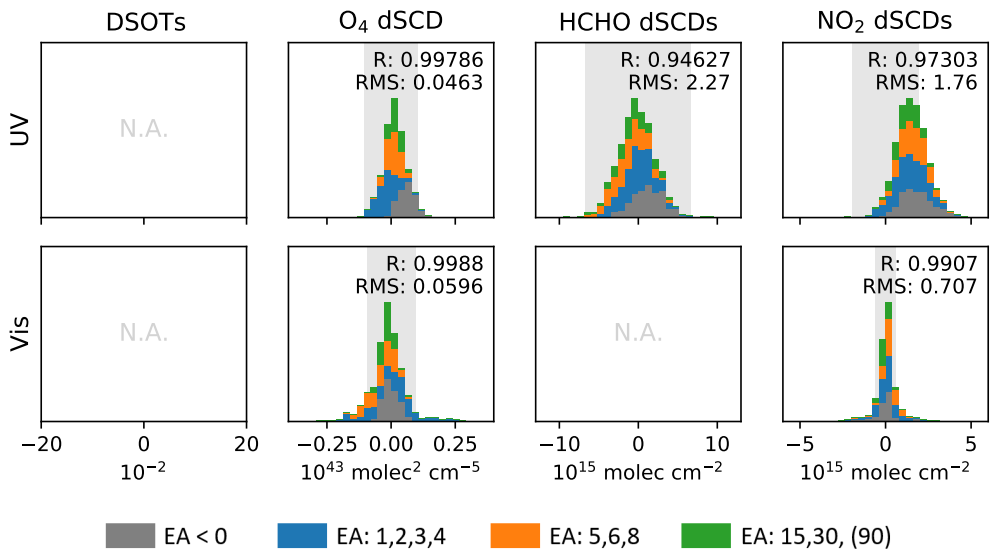

Figure 16.10: Same as Figure 16.2 but for the retrieval results shown in Figure 16.8 and 16.9.

information on the aerosol conditions. The retrieved surface albedo again lacks a consistent diurnal cycle, indicating that it still compensates for some aerosol related effects, probably horizontal or vertical gradients in the aerosol properties. As shown in Figure 16.10, the large set of retrieved parameters allows RAPSODI to achieve exceptional convergence. Compared to former retrieval runs, particularly the differences in modelled and measured O_4 dSCDs are significantly reduced to about half the measurement uncertainty.

We now incorporate all available polarimetric dSCDs and dSOTs according to Table 14.1 into $\hat{\mathbf{y}}$ (Multi-S-P mode) and perform another retrieval of the full atmospheric state. Figures 16.11, 16.12 and 16.13 show the corresponding results. Furthermore, Table 16.1 directly compares the DOFS obtained for the full atmospheric state retrievals from non-polarimetric and polarimetric data. Regarding surface albedo and aerosol properties, the information content significantly increases: the number DOFs for both more than doubles. Accordingly, the results in Figure 16.12 are now drawn away from the a priori assumptions, except for σ_2, where the information content remains very low (DOFS of 0.05). The agreement with the Sun photometer aerosol properties is rather poor with correlation coefficients below 0.2 for all parameters. From the available data it is hard to tell which observations are closer to reality, or to what extent the deviations are related to the sampling of different air-masses. While some of the retrieved parameters vary realistically smooth over the day, others at times exhibit rather unlikely outliers or variations. Particularly $\Im n$ shows unrealistically large values in the forenoon. Also, the DOFS of $\Im n$ are highly variable ranging from 0.05 to 1.5. A technical issue, probably related to the linking of the modes, cannot be fully excluded here but further investigations are

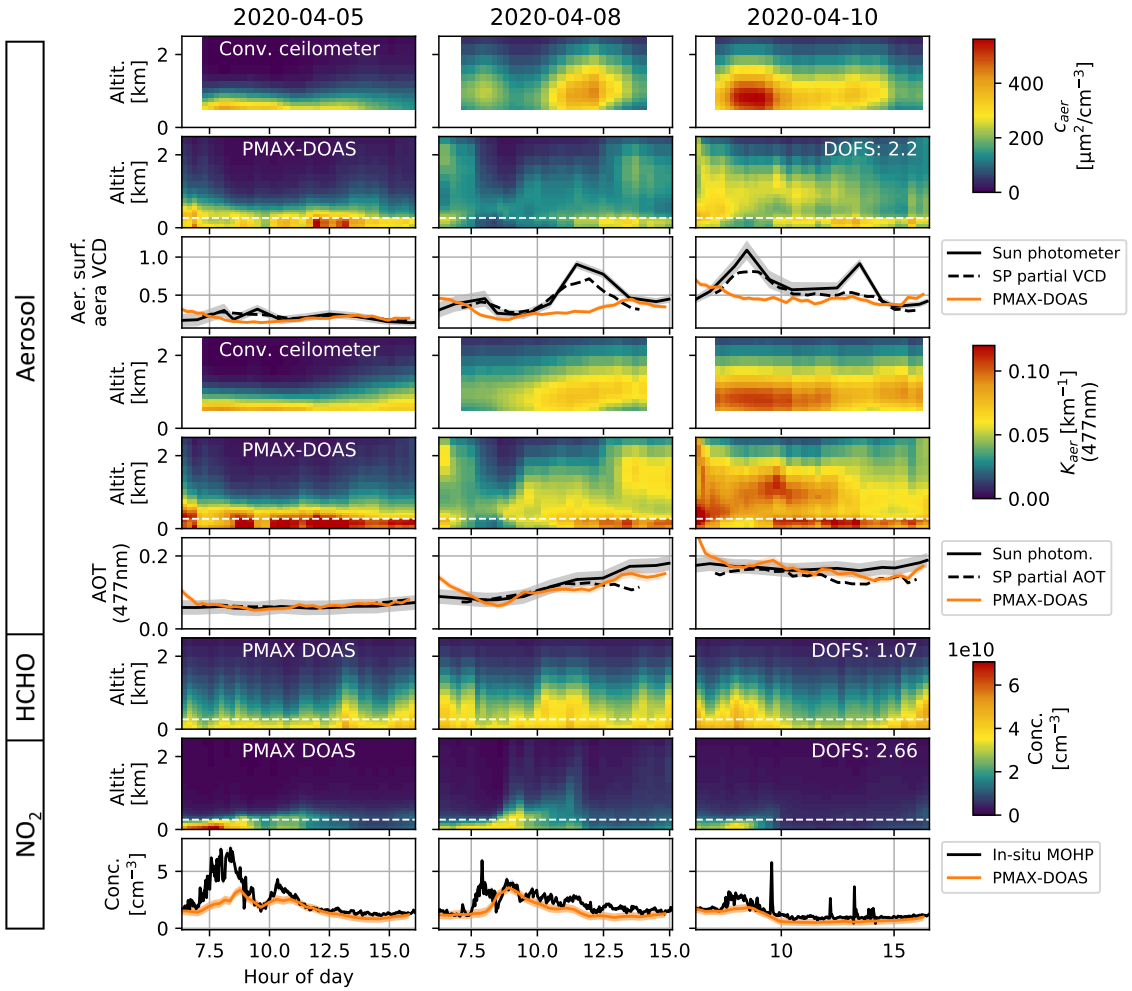

Figure 16.11: Same as Figure 16.1 but with surface albedo and all aerosol microphysical properties being retrieved from polarimetric dSCDs and dSOTs.

necessary to identify the actual reason. It shall be noted that also the Sun photometer values for $\Im n$ show very large values in the evening on two of the three days, indicating that the AERONET retrieval exhibits similar issues. The modal fraction f retrieved by the PMAX-DOAS tends to particularly low values (i.e. more coarse mode particles) in the morning. Light fog events at low altitudes (invisible to the Sun photometer) might a reason, even though nothing the like could be observed in the corresponding DWD webcam images.

Again, as a result of the disagreement in the aerosol properties, also the aerosol area concentration profiles and area-based VCDs of PMAX-DOAS and supporting observations disagree. Nevertheless, for reasons discussed before (e.g. Section 12.4.3), the Sun photometer VCD is arguable and it is well possible that the PMAX-DOAS VCD, with its low variability over the day (except of the early morning), is closer to reality. In contrast to the aerosol area concentration data, the aerosol

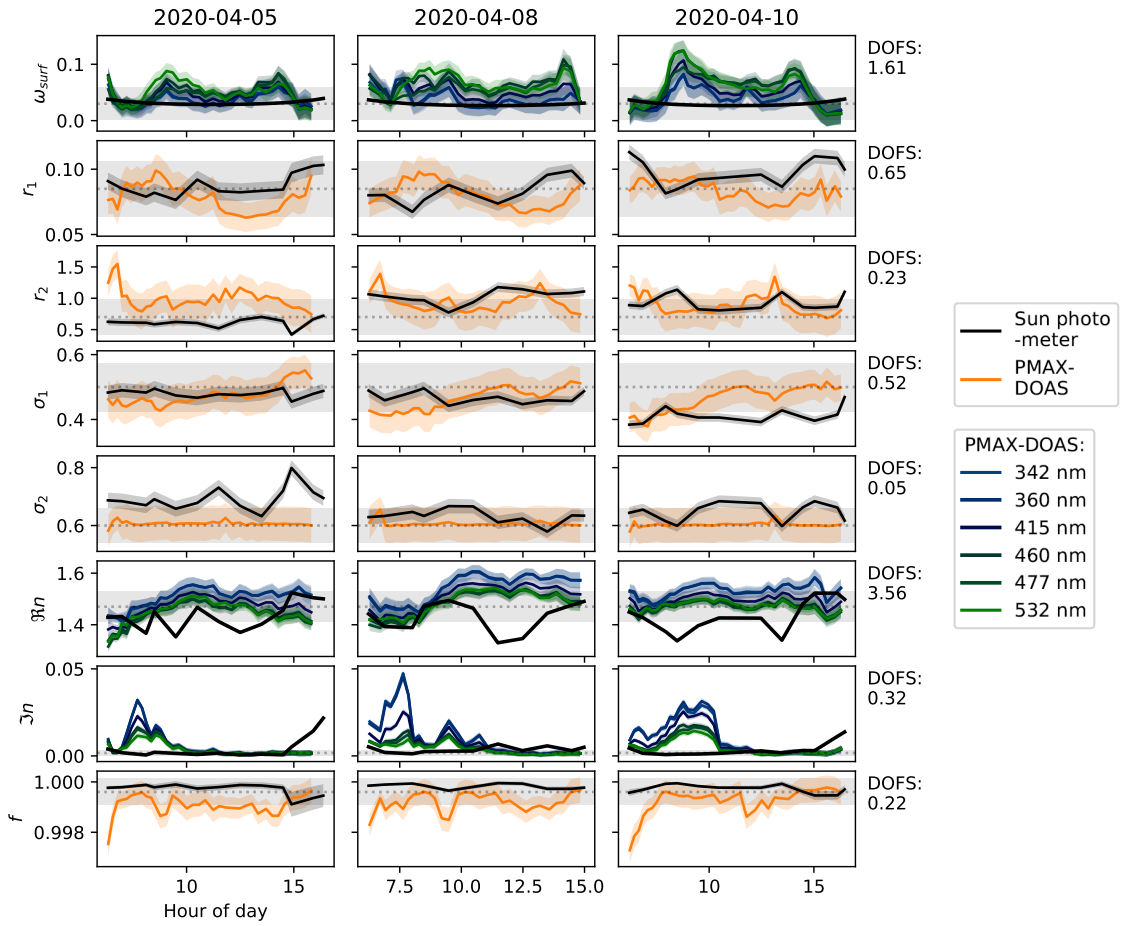

Figure 16.12: Retrieved surface albedo and aerosol properties for the profiling results shown in Figure 16.11 (retrieval from polarimetric dSCDs and dSOTs). Grey dashed lines and shaded rectangles indicate a priori values and uncertainties. DOFS on the right represent temporal averages. For spectrally resolved quantities (ω_{surf}, n), DOFS are summed up over all wavelengths.

extinction profiles and AOTs are in good agreement: when excluding scans before 7:00h, the RMSD between Sun photometer and PMAX-DOAS AOTs is 0.015. Compared to the full atmospheric state retrieval from non-polarimetric observations (RMSD of 0.035) the agreement improves by almost 60 %. Also the agreement between PMAX-DOAS and in-situ NO_2 concentrations (the latter averaged to half hour intervals to approximately account for the much larger spatial and temporal kernels of the PMAX-DOAS) slightly improves: The RMSDs after 8:30h reduce by about 10 %. Figure 16.13 again indicates a successful convergence over the entire period with deviations between modelled and measured DSCDs of the order or smaller than typical measurement uncertainties.

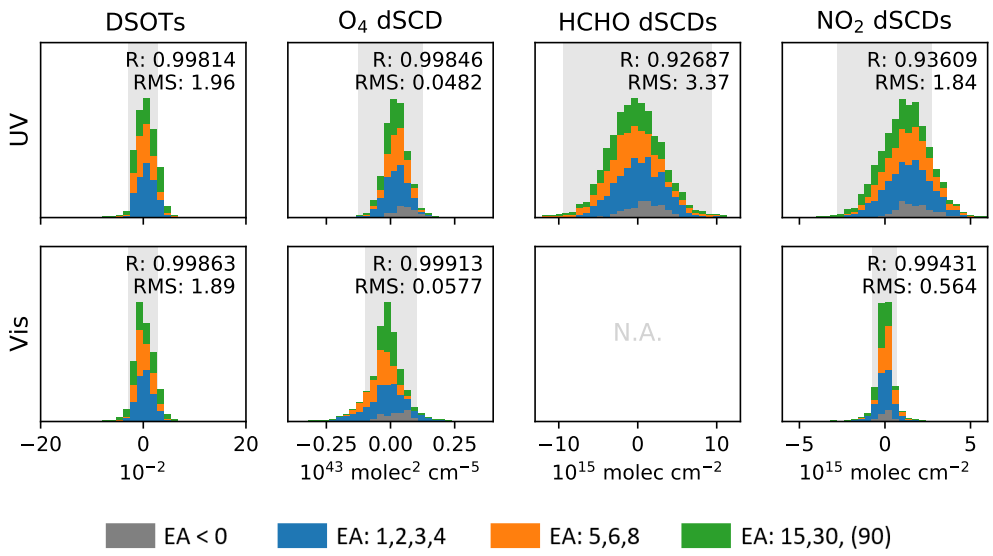

Figure 16.13: Same as Figure 16.2 but for the retrieval results shown in Figure 16.11 and 16.12.

Table 16.1: Average DOFS for the retrievals of the full atmospheric state from non-polarimetric (Multi-S) and polarimetric (Multi-S-P) data.

Parameter subgroup	Multi-S	Multi-S-P	Absolute increase	Relative increase
Aerosol profiles	1.44	2.2	0.76	53 %
HCHO profiles	0.96	1.07	0.11	11 %
NO_2 profiles	2.45	2.66	0.21	9 %
Surf. albedo	0.63	1.61	0.98	156 %
Aerosol properties	2.37	5.55	3.18	134 %
Total	7.85	13.09	5.24	67 %

In Section 12.4.3 we already discussed that large parts of the variations in the Sun photometer observed aerosol properties might be a result of strong correlations between them. Lastly, we therefore performed another retrieval run from the full set of polarimetric measurements but only retrieving profiles, ω_{surf} and the fine mode radius r_1. All other parameters were fixed to the values observed by the Sun photometer. Regarding those parameters, RAPSODI assimilates the potentially false variations in the Sun photometer data and is forced to adapt r_1 accordingly, which should bring r_1 from the PMAX-DOAS into better agreement with the Sun photometer values. The results for ω_{surf} and r_1 are shown in Figure 16.14. Indeed, for r_1 the agreement between PMAX-DOAS and Sun photometer improves significantly (correlation coefficient of 0.58) compared to the retrievals before, again indicating

that the variations in the Sun photometer aerosol properties are not real. On the other hand, it also suggests that the different air-masses sampled by PMAX-DOAS and Sun photometer are comparable at least to some extent.

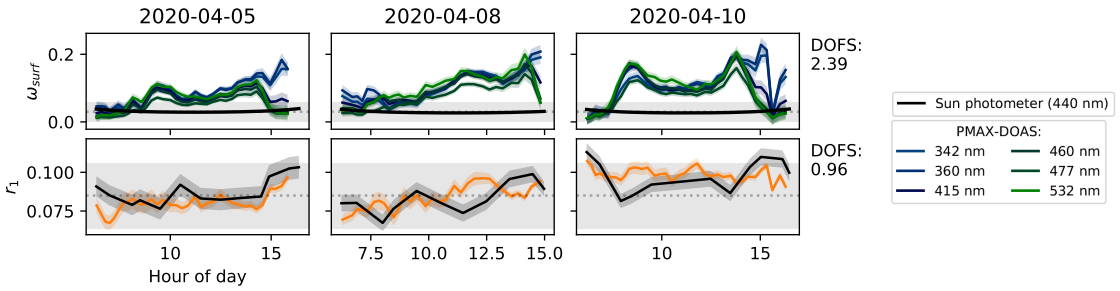

Figure 16.14: Retrieved surface albedo and fine mode radius if all other aerosol parameters are fixed to the values observed by the Sun photometer.

16.3 Concluding remarks

Even though a thorough statistical analysis on the basis of a long-term dataset has not yet been performed, the results presented in this chapter provide first insight regarding the potential, feasibility and challenges of polarimetric MAX-DOAS retrievals from field data. It shall also be pointed out that, for the first time, aerosol microphysical properties were retrieved from MAX-DOAS observations. The retrieval converges successfully and the results for most parameters are plausible, at least for the atmosphere above the PMAX-DOAS.

Polarimetric observations significantly increase the information content on the full atmospheric state by more than 60 % in terms of DOFS. The information on surface albedo and aerosol properties more than doubles. For aerosol profiles it increases by about 50 %. For trace gas profiles, the increase is small ($< 15\,\%$). Recall that the non-polarimetric data was calculated from the polarimetric dataset. A conventional instrument without polarising filter would perceive about twice the amount of light, thereby reducing the measurement uncertainties and increasing the DOFS in a "real" non-polarimetric retrieval. The numbers given above might therefore be slightly too optimistic. Generally, the observed increase in information is in qualitative agreement with the findings from synthetic studies in Section 9. In the details, however, the DOFS from synthetic data and field measurements cannot be directly compared, as they are based on different scenarios regarding atmospheric state and viewing geometries, as well as different assumptions on a priori and measurement covariances.

A thorough validation of the retrieval results, particularly regarding aerosol properties, turned out to be difficult. First of all, the supporting observations sample quiet different air-masses: ceilometer profiles are inferred along the zenith LOS

above the MOHP and the Sun photometer provides vertically integrated quantities inferred from almucantar scans at rather high viewing elevations over the day. In contrast, the PMAX-DOAS observations exhibit considerable horizontal sensitivity ranges (typically several kilometres) and are particularly sensitive to low altitudes. Therefore, horizontal inhomogeneities as well as vertical gradients in the aerosol properties potentially induce large deviations between the different observations. Second, the scaling of ceilometer profiles involves simplifying assumptions and there are severe indications that the Level 1.5 inversion data from the Sun photometer does not provide sufficiently reliable data. Also the rather uncertain O_4 scaling factors might introduce biases, however, side studies indicated that the aerosol properties are predominantly driven by information from the dSOT observations. For future validations, accurate and representative supporting observations are therefore highly desirable but likely associated with tremendous efforts.

Also the PMAX-DOAS results itself raise a number of questions to be further investigated in the future. While the strong increase in sensitivity to surface albedo and aerosol properties is encouraging, it comes along with the necessity for their accurate description within the model. While the HG-aerosol model has established as a useful approximation in conventional MAX-DOAS retrievals, we found that it is not suitable for polarimetric observations, as it fails to accurately reproduce the SOP of skylight. Furthermore, there are indications that the model assumption of a Lambertian surface is not appropriate and might be replaced by a BRDF approach in the future. Lastly, it might be necessary to allow vertical gradients in the aerosol properties. Regarding these aspects, diverse solutions are conceivable but all associated with an increased complexity of the retrieval and additional computational effort.

Regarding aerosol extinction profiles the patterns observed by the ceilometer and the PMAX-DOAS are still similar for most retrieval runs. Also the AOTs observed by Sun photometer and PMAX-DOAS agree quiet well most of the time (RMSD of 0.015 for the retrieval of the full atmospheric state from polarimetric observations). In contrast, for the surface albedo, aerosol area concentrations and aerosol properties, the correlation between PMAX-DOAS and Sun photometer is poor (correlation coefficients $\lesssim 0.2$) and deviations are sometimes even of the order of the a priori uncertainties. On the other hand, the results of the PMAX-DOAS appear plausible, in the sense that parameters change smoothly over the day. For the reasons discussed before, it is not fully clear whether the Sun photometer or the PMAX-DOAS observations are closer to reality. The retrieved NO_2 concentration in the PMAX-layer and the in-situ observations by the DWD agree well when the PBL presumably exceeds the MOHP altitude and the PMAX-layer is well mixed.

As shown during the investigations on synthetic data in Section 9, there is large potential to improve the retrieval results in the future by incorporating alternative viewing geometries (e.g. almucantar scans) and dSOTs between different viewing directions. Another aspect that we have avoided so far is the impact of clouds, which is generally an issue in passive remote sensing applications. However, for the retrieval of aerosol properties from polarimetric sky radiance measurements,

investigations in this direction have been performed by Grob et al. (2019). They find that retrievals are still feasible under moderate cloud fractions if the instrument points to cloud holes (either actively or by applying corresponding filters). To what extent such approaches are transferable to polarimetric MAX-DOAS observations remains to be investigated.

Part IV

Conclusions and outlook

In the course of this work, first important steps have been taken to integrate polarimetry into MAX-DOAS applications.

A major outcome is the RAPSODI retrieval algorithm, with the unique capability to process polarimetric MAX-DOAS observations and to utilise the corresponding information to retrieve vertical distributions of aerosol and trace gases as well as aerosol properties. Furthermore, in contrast to former algorithms, it retrieves all species of interest simultaneously in a shared model atmosphere thereby considering and exploiting corresponding synergetic effects. It is also the first MAX-DOAS retrieval algorithm that allows to infer aerosol microphysical properties. For this purpose RAPSODI makes use of a Mie aerosol model with the aerosol properties being described in terms of a bi-modal size distribution and material refractive indices.

The development and deployment of the PMAX-DOAS instrument resulted in a comprehensive dataset of polarimetric MAX-DOAS observations recorded at the Meteorological Observatory Hohenpeissenberg. Different viewing geometries (elevation scans, almucantar scans and direct-sun observations) were implemented in the measurement routine. The full dataset covers a period of more than one year and thus comprises various atmospheric conditions.

Prior to this work, it was already well known from former studies (e.g. Boesche et al., 2006; Emde et al., 2010; Xu and Wang, 2015) that polarimetric observations of skylight provide useful information, since aerosol alters the skylight's SOP compared to a pure Rayleigh atmosphere. In contrast, former studies paid little attention to the fact that light of different SOP arriving at the Earth's surface has taken different effective paths through the atmosphere. Polarimetry therefore allows to realise light path geometries inaccessible to conventional MAX-DOAS observations. This is an important aspect when aiming at the retrieval of spatial distributions of atmospheric constituents. We found that variations in the O_4 AMF up to 60 % can be achieved in a single viewing direction, just by regarding skylight of different polarisation orientations. For gases confined to lower altitudes, the effect is reduced (by a factor of ≈ 2 for gases with an exponential profile of 1 km scale height) but still significant. The DOLP and the O_4 excentricity (the maximum relative change of O_4 dSCDs achieved through different PAs in a single viewing direction) exhibit similar but not equal patterns in their dependence on viewing direction, wavelength and aerosol parameters. Polarimetric O_4 dSCDs can therefore be regarded to carry a "new kind" of information on aerosols that, to our knowledge, has not yet been considered by any other atmospheric remote sensing approach.

A crucial part of this work is based on investigations with synthetic data. Amongst others, measurements and weighting functions were simulated for a comprehensive set of different atmospheric scenarios and instrument viewing geometries. On the basis of this data, the potential of polarimetric MAX-DOAS observations compared to non-polarimetric observations could be assessed. The total information increase achieved in terms DOFS is about 50 %, when retrieving vertical distribu-

tions of aerosol, HCHO and NO_2 as well as aerosol microphysical properties from UV-Vis spectra recorded during typical elevation scans. Largest gain in information is obtained for aerosol properties (about 70 %) and aerosol area concentration profiles (50 %). In contrast, the increase for trace gas concentration profiles is rather small (about 10 %). Regarding aerosol microphysical properties, high sensitivity (0.7 DOFS per parameter) is achieved for the fine mode properties, whereas the sensitivity to coarse mode properties remains small (DOFS $\lesssim$ 0.2 per parameter). As discussed in detail in Section 9 the exact numbers vary, depending on the underlying assumptions. The numbers above represent approximate mean values.

Retrievals on the basis of the simulated observations show that the incorporation of polarimetric information significantly improves the accuracy of the results, particularly for aerosol related quantities. In an ideal atmosphere, the RMSD between retrieved and true values for aerosol VCDs and aerosol properties decreases by about 60 %. In contrast, for trace gas VCDs the decrease is below 20 % and even an increase is observed, if the loss of light due to the polariser is taken into account (detailed discussion in Section 9.6). Aerosol property results improve by about 40 %. The fine mode aerosol microphysical parameters can be retrieved to an accuracy of 30 % percent of the a priori uncertainty. Coarse mode results achieve only 70 % and, as a consequence of the little available information, remain strongly biased towards the a priori. The information in the measurements can be further enhanced by about 50 % (in DOFS, compared to the polarimetric elevation scan), by including almucantar scan geometries and the variation of radiances over the sky's hemisphere as additional source of information. In this case also the retrieval of coarse mode properties becomes feasible. Generally, these very promising results degrade if additional noise is added to the observations (noise magnitudes up to 10 %, to simulate atmospheric spatio-temporal variability) but remain below the a priori uncertainties for vertical columns, trace gas concentrations and aerosol fine mode properties.

Apart from the investigations on synthetic data, first polarimetric retrievals were performed on the basis of field data from the PMAX-DOAS instrument. Elevation scans on three selected clear sky days were evaluated. The increase in information achieved through the incorporation of polarimetric observations is in qualitative agreement with the findings from the synthetic studies above. Differences in the exact numbers are expected since the underlying atmospheric scenarios and retrieval settings were different. The average increase in total DOFS is about 65 %. For aerosol properties, aerosol profiles and trace gas profiles the increases are about 130 %, 50 % and 10 %. The comparison of the retrieval results with the supporting observations yielded mostly good agreement for AOTs and NO_2 concentrations. For the retrieval of vertical distributions of aerosol, HCHO and NO_2 as well as aerosol microphysical properties, an RMSD in AOTs of 0.035 was achieved by the non-polarimetric retrieval. The incorporation of polarimetric information yielded an improvement of almost 60 %, reducing the RMSD to 0.015. In contrast, the retrieved aerosol area VCDs and aerosol properties (also regarding the fine mode)

strongly disagreed with the Sun photometer observations: the correlation coefficients between PMAX-DOAS and Sun photometer were below 0.2 and the deviations were sometimes of the order of the a priori uncertainty. The reasons could not be unambiguously identified. On the one hand, there are indications that the limited accuracy and representativeness of the Sun photometer Level 1.5 observations are a major issue. On the other hand, there are indications that simplifications in the RAPSODI model atmosphere bias the PMAX-DOAS retrieval results. This comprises the assumption of a Lambertian flat surface, spatio-temporal homogeneity and constant aerosol properties over the full altitude range. But also the simplified bi-modal representation of the aerosol size distribution or the assumption of spherical particles might have some effect. Another critical aspect is the scaling of O_4 dSCDs prior to the retrieval, which is still not understood and debated within the community. In the future, a thorough validation of the field measurements is highly desirable but likely associated with tremendous efforts. Alternatively, studies addressing these issues might be performed on the basis of synthetic data from independent models (e.g. Monte Carlo RTMs) that allow to simulate observations in three dimensional atmospheres, including horizontal inhomogeneities or variable surface properties. Note that the three days of elevation scan data comprise only a very small subset of the PMAX-DOAS dataset. An extended evaluation will provide further insight not only regarding the statistics. Future activities might comprise combined retrievals from almucantar and elevation scan data as well as direct-sun observations. Furthermore, the feasibility of retrievals under less ideal conditions, in particular in the presence of clouds, is an important issue to investigate.

In the instrumental design of (polarimetric) MAX-DOAS instruments, particular care has to be taken regarding undesired polarisation sensitivities of various components. In the past, multimode optical fibres have been considered to be efficient polarisation scramblers and a useful tool to ensure equal sensitivity of the spectroscopic setup to arbitrary polarisation orientations. In contrast, investigations in the course of this thesis suggest that, at least in modern optical fibres, the DOP can be largely maintained over fibre lengths of several metres. In conjunction with the polarisation sensitivity of typical grating spectrometers, this can severely bias the measurements, with consequences for the spectral analysis and the retrieval results in both, polarimetric and non-polarimetric MAX-DOAS applications.

Apart from the investigations proposed above, diverse future activities are conceivable. Explicit additional features that might be implemented in the RAPSODI algorithm are:

- An improved model representation of surface properties in terms of a BRDF instead of a Lambertian albedo.

- A computationally feasible approach to account for vertical gradients in the aerosol properties.

- An improved parametrisation for the spectral dependence of surface albedo and aerosol refractive indices, for instance in terms of a polynomial.
- The consideration and propagation of uncertainties in those atmospheric parameters that are not retrieved.
- The capability to make use of narrow-band polarisation features originating from inelastic Raman scattering as well as strong trace gas absorption. Both are expected to carry additional information on the atmospheric state (Aben et al., 1999; Wagner et al., 2009).

Further studies might address the following aspects:

- As indicated in the course of our investigations on synthetic data, there is large potential in the optimisation of viewing geometries: the number of observations might be strongly reduced without significant loss in information, thereby improving the temporal resolution of the measurements.
- Most of our investigations focus on the wavelength range between 300 and 550 nm. Extending the range to the near IR is expected to further improve the results in particular regarding the sensitivity to coarse mode aerosol properties. Furthermore, it might help to disentangle those retrieved parameters that are strongly correlated.
- As discussed before, AMFs vary strongly with the polarisation orientation of the detected skylight. This might be utilised to retrieve AOTs and trace gas VCDs from observations in a single viewing direction.

In short, we found that the use of polarimetry in MAX-DOAS measurements is a promising approach in particular for applications focussing on aerosol. Yet, in the face of the numerous possibilities and questions regarding the detailed implementation of instruments and retrieval algorithms, many aspects remain to be investigated in further detail.

Part V

Appendix

A VLIDORT linearisations

The main results of VLIDORT (for our purposes) are the stokes parameters $\mathbf{I}$. For retrieval algorithms like RAPSODI, we also require the derivatives of $\mathbf{I}$ with respect to to the state vector $\mathbf{x}$ (see Section 5). For retrieval algorithms in general, these are often derived using *finite differences*: a small pertubation is applied to each parameter and the effect on the simulation results is evaluated. However, this approach is computational expensive as the forward model has to be run n additional times for this purpose. A great advantage of VLIDORT is that it can be configured to provide the desired derivatives (from internal calculations during the RTS) if it is configured accordingly.

Internally, the optical properties of each atmospheric layer in VLIDORT are described by three macroscopic quantities: the vertical extinction OT Δ, the single scattering albedo ω and the expansion coefficients $\mathbf{B}_p$ of the scattering matrix (the index p indicates the expansion order and will in the following be omitted). They describe the combined effects of molecules and aerosol on the radiative transport, hence:

$$\Delta = \tau_{gas} + \tau_{ray} + \tau_{aer} \tag{A.1}$$

$$\omega = \frac{\delta_{ray} + \delta_{aer}}{\Delta} \tag{A.2}$$

$$\mathbf{B} = \frac{\delta_{ray}\mathbf{B}_{ray} + \delta_{aer}\mathbf{B}_{aer}}{\delta_{ray} + \delta_{aer}} \tag{A.3}$$

with τ_{gas} being the layer's molecular absorption OT, τ_{ray} (τ_{aer}) being the Rayleigh (aerosol) extinction OT, δ_{ray} (δ_{aer}) being the Rayleigh (aerosol) scattering OT and $\mathbf{B}_{ray}$ ($\mathbf{B}_{aer}$) being the scattering matrix expansion coefficients for Rayleigh (aerosol) scattering. We further define the albedos

$$\omega_{ray} = \frac{\delta_{ray}}{\tau_{ray}} \qquad \text{and} \qquad \omega_{aer} = \frac{\delta_{aer}}{\tau_{aer}} \tag{A.4}$$

Normally, it is $\omega_{ray} = 1$, however, VLIDORT cannot not handle layer SAAs too close to unity and to avoid those, $\omega_{ray} = 1 - 10^{-5}$ is assumed.

To obtain the desired derivatives, the user must provide VLIDORT with normalised linearisations

$$\frac{1}{\Delta}\frac{\partial\Delta}{\partial z}, \qquad \frac{1}{\omega}\frac{\partial\omega}{\partial z} \qquad \text{and} \qquad \frac{1}{\mathbf{B}}\frac{\partial\mathbf{B}}{\partial z} \tag{A.5}$$

with respect to the desired parameters $\mathbf{z}$ (details can be found in the VLIDORT user guide). Particularly for the Mie model, these are not trivial and shall therefore

be reported here. $\mathbf{z}$ has a v-index, to indicate that the set of parameters discussed here is not exactly the same as the set of parameters $\mathbf{x}$ retrieved by RAPSODI: $\mathbf{z}$ basically contains the parameters as listed in Table 7.1, however, without the Ångstrom exponent and containing the layer molecular absorption optical depth α_{gas} instead of the trace gas concentrations. The following equations apply for each model layer. The layer index l will be omitted for convenience.

For a convenient representation we pre-calculate a few expressions. For the Mie model case, it is useful to define the variable ξ, relating the aerosol surface area concentration c_{aer} to the number concentration $c_{aer}^{(N)}$ according to

$$c_{aer}^{(N)} = \xi \cdot c_{aer} \tag{A.6}$$

From the equations for log-normal size distributions introduced in Section 3.3.3, it can be derived to

$$\xi = \frac{1}{4\pi} \left[f\, r_1^2\, \exp(2\sigma_1^2) + (1-f)\, r_2^2\, \exp(2\sigma_2^2) \right]^{-1} \tag{A.7}$$

Its derivatives with respect to the Mie model parameters (as listed in Table 7.1) are:

$$\frac{\partial \xi}{\partial r_1} = -8\pi\xi^2 f r_1 \exp(2\sigma_1^2) \tag{A.8}$$

$$\frac{\partial \xi}{\partial r_2} = -8\pi\xi^2 (1-f) r_2 \exp(2\sigma_2^2) \tag{A.9}$$

$$\frac{\partial \xi}{\partial \sigma_1} = -16\pi\xi^2 f r_1^2 \sigma_1 \exp(2\sigma_1^2) \tag{A.10}$$

$$\frac{\partial \xi}{\partial \sigma_2} = -16\pi\xi^2 (1-f) r_2^2 \sigma_2 \exp(2\sigma_2^2) \tag{A.11}$$

$$\frac{\partial \xi}{\partial f} = -4\pi\xi^2 \left[r_1^2 \exp(2\sigma_1^2) + r_2^2 \exp(2\sigma_2^2) \right] \tag{A.12}$$

$$\frac{\partial \xi}{\partial n_1} = \frac{\partial \xi}{\partial n_2} = 0 \tag{A.13}$$

With these, we can express the derivatives of τ_{aer} with respect to each Mie model parameter (indicated by the place-holder P) as

$$\frac{\partial \tau_{aer}}{\partial P} = c_{aer}\, h \left(\bar{\sigma}_{aer}^{(e)} \frac{\partial \xi}{\partial P} + \xi \frac{\partial \bar{\sigma}_{aer}^{(e)}}{\partial P} \right) \tag{A.14}$$

and with respect to the aerosol area surface concentration as

$$\frac{\partial \tau_{aer}}{\partial c_{aer}} = \xi\, \bar{\sigma}_{aer}^{(e)}\, h \tag{A.15}$$

$\bar{\sigma}_{aer}^{(e)}$ is the aerosol bulk extinction cross-section according to Equation 3.60 and h is the vertical extend of the model layer. The derivatives $\partial \bar{\sigma}_{aer}^{(e)} / \partial P$ are provided by the Mie model.

The equivalents of Eq. A.14 and A.15 for the HG model case are considerably simpler. Here, it is

$$\frac{\partial \tau_{aer}}{\partial c_{aer}} = \frac{1}{4} Q^{(hg)}\, h \qquad \text{and} \qquad \frac{\partial \tau_{aer}}{\partial P} = 0 \tag{A.16}$$

this time with P being a placeholder for $g^{(hg)}$ and $\omega^{(hg)}$, respectively, and $Q^{(hg)}$ being the aerosol extinction efficiency at the simulation wavelength. With these quantities introduced, we can give handy expressions for the required linearisations formulated in Eq. A.5.

The derivatives of the layer extinction OT Δ are:

$$\frac{1}{\Delta}\frac{\partial \Delta}{\partial \tau_{gas}} = \frac{1}{\Delta} \tag{A.17}$$

$$\frac{1}{\Delta}\frac{\partial \Delta}{\partial c_{aer}} = \frac{1}{\Delta}\frac{\partial \tau_{aer}}{\partial c_{aer}} \tag{A.18}$$

$$\frac{1}{\Delta}\frac{\partial \Delta}{\partial P} = \frac{1}{\Delta}\frac{\partial \tau_{aer}}{\partial P} \tag{A.19}$$

$$\tag{A.20}$$

For $\partial \tau_{aer}/\partial c_{aer}$ and $\partial \tau_{aer}/\partial P$, the precalculated expressions above have to be inserted, depending on which aerosol model is used.

The derivatives of the layer SSA ω are:

$$\frac{1}{\omega}\frac{\partial \omega}{\partial \tau_{gas}} = -\frac{1}{\Delta} \tag{A.21}$$

$$\frac{1}{\omega}\frac{\partial \omega}{\partial c_{aer}} = \frac{1}{\Delta}\left(\frac{\omega_{aer}}{\omega} - 1\right)\frac{\partial \tau_{aer}}{\partial c_{aer}} \tag{A.22}$$

$$\frac{1}{\omega}\frac{\partial \omega}{\partial P} = \frac{\tau_{aer}}{\omega\,\Delta}\frac{\partial \omega_{aer}}{\partial P} + \frac{1}{\Delta}\left(\frac{\omega_{aer}}{\omega} - 1\right)\frac{\partial \tau_{aer}}{\partial P} \tag{A.23}$$

Values inserted for ω_{aer} are either the Mie model bulk SSA $\bar{\omega}_{aer}$ (see Eq. 3.59) or the HG-SSA $\omega^{(hg)}$. The derivatives $\partial \bar{\omega}_{aer}/\partial P$ are provided by the Mie model. The derivatives $\partial \omega^{(hg)}/\partial P$ are trivial since

$$\frac{\partial \omega^{(hg)}}{\partial \omega^{(hg)}} = 1 \qquad \text{and} \qquad \frac{\partial \omega^{(hg)}}{\partial g^{(hg)}} = 0. \tag{A.24}$$

The derivatives for $\mathbf{B}$ will be given for a single matrix element β as they apply

equally for any element and expansion order:

$$\frac{1}{\beta}\frac{\partial\beta}{\partial\tau_{gas}} = 0 \tag{A.25}$$

$$\frac{1}{\beta}\frac{\partial\beta}{\partial c_{aer}} = \frac{1}{\beta}\frac{\partial\beta}{\partial\tau_{aer}}\frac{\partial\tau_{aer}}{\partial c_{aer}} \tag{A.26}$$

$$\frac{1}{\beta}\frac{\partial\beta}{\partial P} = \frac{1}{\beta}\left(\frac{\partial\beta}{\partial\omega_{aer}}\frac{\partial\omega_{aer}}{\partial P} + \frac{\partial\beta}{\partial\tau_{aer}}\frac{\partial\tau_{aer}}{\partial P} + \frac{\partial\beta}{\partial\beta_{aer}}\frac{\partial\beta_{aer}}{\partial P}\right) \tag{A.27}$$

with the outer derivatives

$$\frac{\partial\beta}{\partial\tau_{aer}} = \frac{\omega_{aer}}{\omega\Delta}(\beta_{aer} - \beta) \tag{A.28}$$

$$\frac{\partial\beta}{\partial\omega_{aer}} = \frac{\tau_{aer}\delta_{ray}}{\omega^2\Delta^2}(\beta_{aer} - \beta_{ray}) \tag{A.29}$$

$$\frac{\partial\beta}{\partial\beta_{aer}} = \frac{\delta_{aer}\delta_{ray}}{\omega\Delta} \tag{A.30}$$

The derivatives $\partial\beta_{aer}/\partial P$ are either provided by the Mie model, or vanish in the case of the HG model.

B Pointing calibration

A 2D water level was mounted on the PMAX-DOAS pedestal which allowed to install the instrument in the field with a nearly upright instrument azimuth axis. The calibration of the water level and the elevation motor offset is illustrated in the top panel of Figure B.1. Light from a laser pointer was coupled into the spectrometer side of the telescope fibre. By adjusting the elevation motor offset and the pedestal orientation, the emerging beam from the telescope was horizontally aligned with the beam of a laser level over a distance of 10 to 20 m in three azimuth directions (0, 90 and 180°). The water level allowed to install the reinstall the instrument in the field with tilting angles in the azimuthal axis less than 0.2°. As indicated in Figure 13.3, the accuracy of the EA is of particular importance in MAX-DOAS elevation scans. Therefore, at the MOHP, the pedestal orientation was fine adjusted in the elevation scan plane by scanning over a small light source (angular height as perceived by the telescope $< 0.003°$), positioned at an EA of 0° with the help of a laser level (see bottom panel of Figure B.1. The intensities perceived by the adjusted PMAX-DOAS during the scan are shown on the left. They indicate an EA accuracy better than 0.1° and also confirm the theoretically expected telescope vertical FOV of 0.25°.

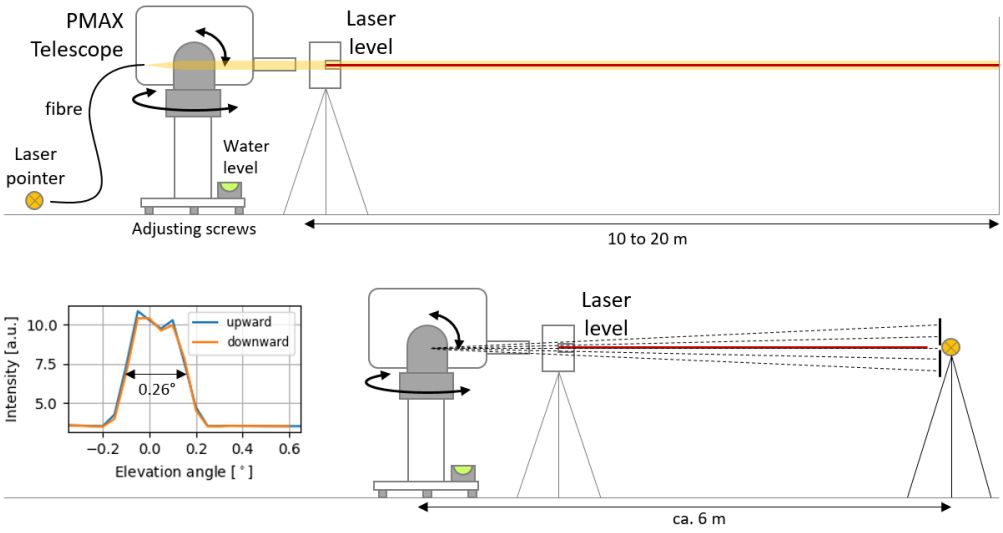

Figure B.1: Top: Simultaneous calibration of the water level on the PMAX-DOAS pedestal and the elevation motor offset. Bottom: field fine adjustment of the pedestal orientation in the elevation scan plane.

The alignment of the polariser is easiest, if light of a very well known polarisation orientation is available as reference. In the course of this thesis we used skylight in

the zenith viewing direction. However, a much simpler approach for lab calibrations in the future might be to use the specular reflection of light from a water surface close to the Brewster angle. The setup is illustrated in Figure B.2.

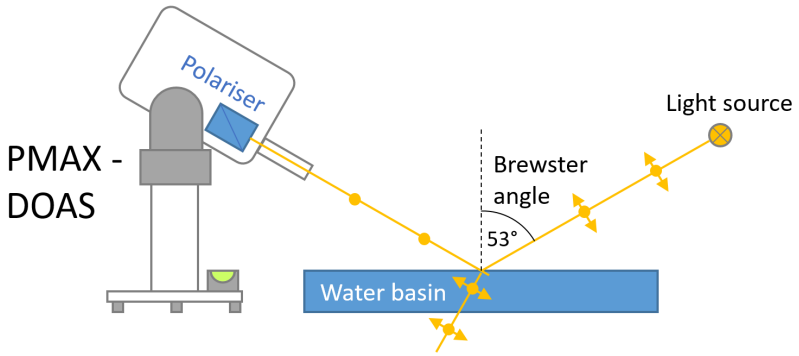

Figure B.2: Proposed setup for future accurate and simple calibration of the instrument's polariser orientation in the laboratory. Specular reflection on a water surface close to the Brewster angle is used to create a horizontally polarised beam as reference.

C Box airmass factors

Equation 4.20 can be derived as follows: consider an optically homogenous layer l with vertical optical depth $\tau_l^{(a)}$. The slant optical thickness is then given by $\tau_l^{(a)} \cdot A$ and the attenuation of the incident radiance I_0 along the slant light path is described by

$$I = I_0 \exp(-\tau_l^{(a)} \cdot A_l) \tag{C.1}$$

with I being the merging radiance. Accordingly, it is

$$\frac{\partial I}{\partial \tau_l^{(a)}} = -AI_0 \exp(-\tau_l^{(a)} A) = A \cdot I \tag{C.2}$$

Solving for A_l, yields Equation 4.20.

D Measured and forward modelled O_4 dSCDs

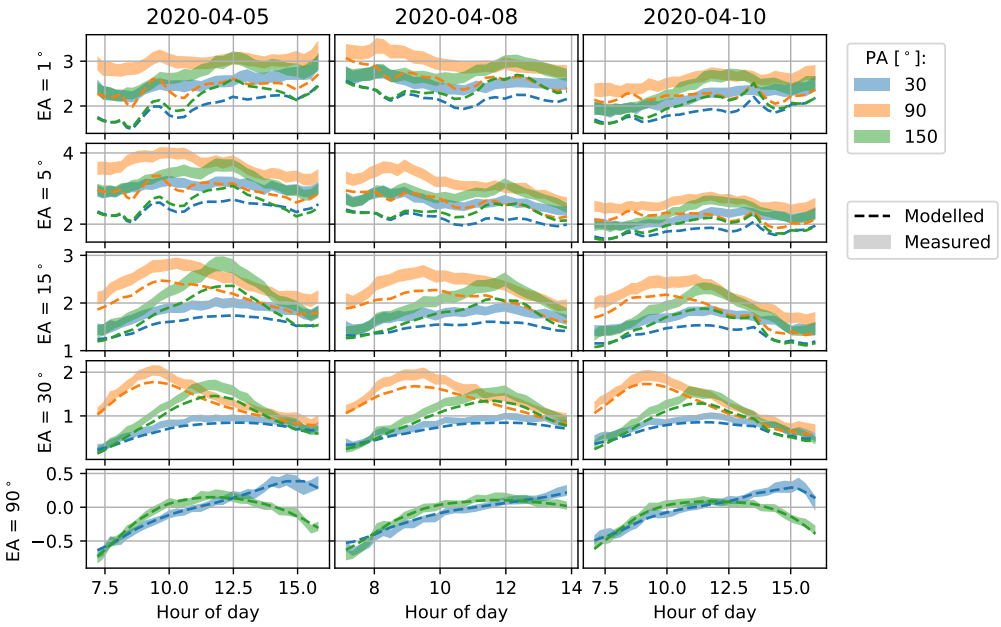

Figure D.1: Same as Figure 15.1, but with no O_4 scaling applied ($F_{O_4} = 1.0$ instead of 0.85).

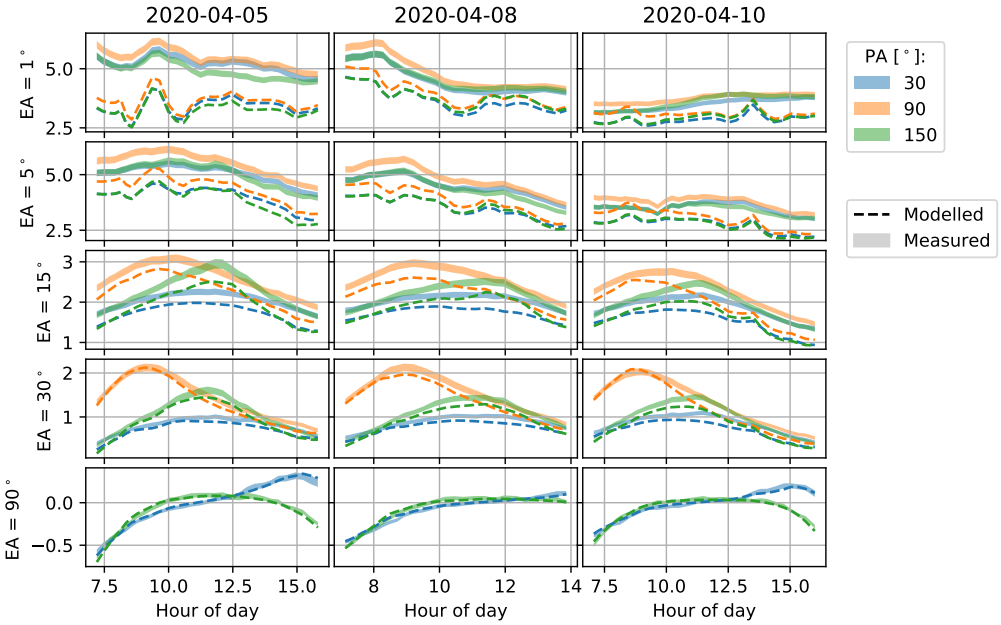

Figure D.2: Same as Figure 15.2, but with no O_4 scaling applied ($F_{O_4} = 1.0$ instead of 0.9).

E Lists

E.1 List of abbreviations

Abbreviation	Description
MAX-DOAS	Multi-Axis DOAS
DOAS	Differential Optical Absorption Spectroscopy
RAPSODI	Retrieval of Atmospheric Parameters from Spectroscopic Observations using DOAS Instruments
VMR	Volume mixing ratio
PBL	Planetary boundary layer
EM	Electromagnetic
RT	Radiative transfer
RTS	Radiative transfer model
RTE	Radiative transfer equation
TOA	Top of the atmosphere
UV	Ultra-violet spectral range
Vis	Visible spectral range
NIR	Near infra-red spectral range
SZA	Solar azimuth angle
VAA	Viewing azimuth angle
RAA	relative (viewing) azimuth angle
EA	(Viewing) elevation angle
PA	(Instrument) polariser angle
LOS	Line of sight
SOP	State of polarisation
DOP	Degree of polarisation
DOLP	Degree of linear polarisation
FOV	Field of view
SCD	Slant column density
dSCD	Differential slant column density
OT	Optical thickness
SOT	Slant optical thickness
dSOT	Differential slant optical thickness
ISF	Instrumntal slit function
VCD	Vertical column density
AOT	Aerosol optical thickness
AMF	Air mass factor
BAMF	Box air mass factor
RMS	Root mean square
RMSD	Root-mean-square difference
GT	Glan-Thompson (polarising filter)
UPS	Undesired polarisation sensitivity
HG	Henyey-Greenstein (approximation)

E.2 List of Figures

E.3 List of Tables

F Bibliography

Aben, I., Helderman, F., Stam, D. M., and Stammes, P.: Spectral fine-structure in the polarisation of skylight, Geophysical Research Letters, 26, 591–594, https://doi.org/10.1029/1999GL900025, URL https://agupubs.onlinelibrary.wiley.com/doi/abs/10.1029/1999GL900025, 1999.

AERONET: Aerosol Robotic Network (AERONET) Homepage, URL https://aeronet.gsfc.nasa.gov/, 2018.

Agrawal, G. P.: Fiber-optic communication systems, vol. 222, John Wiley & Sons, 2012.

Ambartsumian, V.: Diffusion of light by planetary atmospheres, Astron Zh, 19, 30–41, 1942.

Artifex-Engineering: Artifex Engineering Homepage, URL https://artifex-engineering.com/optics/polarization-optics/polarizers/glan-thompson-polarizers/, 2021.

Azzam, R. M. A.: Phase shifts that accompany total internal reflection at a dielectric–dielectric interface, Journal of the Optical Society of America, 21, 1559–1563, https://doi.org/10.1364/JOSAA.21.001559, URL http://josaa.osa.org/abstract.cfm?URI=josaa-21-8-1559, 2004.

Bates, D.: Rayleigh scattering by air, Planetary and Space Science, 32, 785–790, 1984.

Beirle, S., Dörner, S., Donner, S., Remmers, J., Wang, Y., and Wagner, T.: The Mainz profile algorithm (MAPA), Atmospheric Measurement Techniques, 12, 1785–1806, https://doi.org/10.5194/amt-12-1785-2019, URL https://www.atmos-meas-tech.net/12/1785/2019/, 2019.

Bernal, A.: Validation and application of SCIATRAN polarisation simulations for ground-based multi-axis DOAS measurements, Master's thesis, University of Bremen, 2017.

Boesche, E., Stammes, P., Ruhtz, T., Preusker, R., and Fischer, J.: Effect of aerosol microphysical properties on polarization of skylight: sensitivity study and measurements, Appl. Opt., 45, 8790–8805, https://doi.org/10.1364/AO.45.008790, URL http://ao.osa.org/abstract.cfm?URI=ao-45-34-8790, 2006.

Bohren, C. F. and Huffman, D. R.: Absorption and scattering of light by small particles, John Wiley & Sons, 2008.

Bösch, T., Rozanov, V., Richter, A., Peters, E., Rozanov, A., Wittrock, F., Merlaud, A., Lampel, J., Schmitt, S., de Haij, M., Berkhout, S., Henzing, B., Apituley, A., den Hoed, M., Vonk, J., Tiefengraber, M., Müller, M., and Burrows, J. P.: BOREAS – a new MAX-DOAS profile retrieval algorithm for aerosols and trace gases, Atmospheric Measurement Techniques, 11, 6833–6859, https://doi.org/10.5194/amt-11-6833-2018, URL https://www.atmos-meas-tech.net/11/6833/2018/, 2018.

Bucholtz, A.: Rayleigh-scattering calculations for the terrestrial atmosphere, Applied Optics, 34, 2765–2773, 1995.

Bussemer, M.: Der Ring-Effekt: Ursachen und Einfluß auf die spektroskopische Messung stratosphärischer Spurenstoffe., Master's thesis, University of Heidelberg, 1993.

Chami, M., Santer, R., and Dilligeard, E.: Radiative transfer model for the computation of radiance and polarization in an ocean–atmosphere system: polarization properties of suspended matter for remote sensing, Appl. Opt., 40, 2398–2416, https://doi.org/10.1364/AO.40.002398, URL http://ao.osa.org/abstract.cfm?URI=ao-40-15-2398, 2001.

Chan, K. L., Wang, Z., Ding, A., Heue, K.-P., Shen, Y., Wang, J., Zhang, F., Hao, N., and Wenig, M.: MAX-DOAS measurements of tropospheric NO_2 and HCHO in Nanjing and the comparison to OMI observations, Atmospheric Chemistry and Physics Discussions, 2019, 1–25, https://doi.org/10.5194/acp-2018-1266, URL https://www.atmos-chem-phys-discuss.net/acp-2018-1266/, 2019.

Chance, K. and Kurucz, R.: An improved high-resolution solar reference spectrum for earth's atmosphere measurements in the ultraviolet, visible, and near infrared, Journal of Quantitative Spectroscopy and Radiative Transfer, 111, 1289–1295, https://doi.org/https://doi.org/10.1016/j.jqsrt.2010.01.036, URL https://www.sciencedirect.com/science/article/pii/S0022407310000610, special Issue Dedicated to Laurence S. Rothman on the Occasion of his 70th Birthday., 2010.

Chandrasekhar, S.: The transfer of radiation in stellar atmospheres, Bulletin of the American Mathematical Society, 53, 641–711, 1947.

Chandrasekhar, S.: Radiative transfer, Courier Corporation, 2013.

Charnock, A.: Python-SRTM, URL https://pypi.org/project/python-srtm/, 2020.

Ciddor, P. E.: Refractive index of air: new equations for the visible and near infrared, Applied optics, 35, 1566–1573, 1996.

Clémer, K., Van Roozendael, M., Fayt, C., Hendrick, F., Hermans, C., Pinardi, G., Spurr, R., Wang, P., and De Mazière, M.: Multiple wavelength retrieval of tropospheric aerosol optical properties from MAXDOAS measurements in Beijing, Atmospheric Measurement Techniques, 3, 863–878, https://doi.org/10.5194/amt-3-863-2010, URL https://www.atmos-meas-tech.net/3/863/2010/, 2010.

Coulson, K. L., Dave, J. V., and Sckera, Z.: Tables related to radiation emerging from a planetary atmosphere with Rayleigh scattering, University of California Press, Berkeley, 1960.

Dahlback, A. and Stamnes, K.: A new spherical model for computing the radiation field available for photolysis and heating at twilight, Planetary and Space Science, 39, 671 – 683, https://doi.org/https://doi.org/10.1016/0032-0633(91)90061-E, URL http://www.sciencedirect.com/science/article/pii/003206339190061E, 1991.

De Rooij, W. and Van der Stap, C.: Expansion of Mie scattering matrices in generalized spherical functions, Astronomy and Astrophysics, 131, 237–248, 1984.

Deschamps, P., Breon, F., Leroy, M., Podaire, A., Bricaud, A., Buriez, J., and Seze, G.: The POLDER mission: instrument characteristics and scientific objectives, IEEE Transactions on Geoscience and Remote Sensing, 32, 598–615, https://doi.org/10.1109/36.297978, 1994.

Donner, S., Kuhn, J., Van Roozendael, M., Bais, A., Beirle, S., Bösch, T., Bognar, K., Bruchkousky, I., Chan, K. L., Drosoglou, T., Fayt, C., Frieß, U., Hendrick, F., Hermans, C., Jin, J., Li, A., Ma, J., Peters, E., Pinardi, G., Richter, A., Schreier, S. F., Seyler, A., Strong, K., Tirpitz, J.-L., Wang, Y., Xie, P., Xu, J., Zhao, X., and Wagner, T.: Evaluating different methods for elevation calibration of MAX-DOAS instruments during the CINDI-2 campaign, Atmospheric Measurement Techniques Discussions, 2019, 1–51, https://doi.org/10.5194/amt-2019-115, URL https://www.atmos-meas-tech-discuss.net/amt-2019-115/, 2019.

Dubovik, O. and King, M. D.: A flexible inversion algorithm for retrieval of aerosol optical properties from Sun and sky radiance measurements, Journal of Geophysical Research: Atmospheres, 105, 20 673–20 696, https://doi.org/10.1029/2000jd900282, 2000a.

Dubovik, O. and King, M. D.: A flexible inversion algorithm for retrieval of aerosol optical properties from Sun and sky radiance measurements, Journal of Geophysical Research: Atmospheres, 105, 20 673–20 696, https://doi.org/10.1029/2000JD900282, URL https://agupubs.onlinelibrary.wiley.com/doi/abs/10.1029/2000JD900282, 2000b.

Dubovik, O., Smirnov, A., Holben, B. N., King, M. D., Kaufman, Y. J., Eck, T. F., and Slutsker, I.: Accuracy assessments of aerosol optical properties

retrieved from Aerosol Robotic Network (AERONET) Sun and sky radiance measurements, Journal of Geophysical Research: Atmospheres, 105, 9791–9806, https://doi.org/https://doi.org/10.1029/2000JD900040, URL https://agupubs.onlinelibrary.wiley.com/doi/abs/10.1029/2000JD900040, 2000.

Dubovik, O., Holben, B., Eck, T. F., Smirnov, A., Kaufman, Y. J., King, M. D., Tanré, D., and Slutsker, I.: Variability of absorption and optical properties of key aerosol types observed in worldwide locations, Journal of the atmospheric sciences, 59, 590–608, 2002.

Edlén, B.: The refractive index of air, Metrologia, 2, 71, 1966.

Emde, C., Buras, R., Mayer, B., and Blumthaler, M.: The impact of aerosols on polarized sky radiance: model development, validation, and applications, Atmospheric Chemistry and Physics, 10, 383–396, https://doi.org/10.5194/acp-10-383-2010, URL https://acp.copernicus.org/articles/10/383/2010/, 2010.

Finlayson-Pitts, B. J. and Pitts Jr., J. N.: Chemistry of the upper and lower atmosphere: theory, experiments, and applications, Elsevier, 1999.

Frieß, U.: MS-DOAS Software, Personal communication, 2018.

Frieß, U.: HeiDOAS - Python library for DOAS spectral analysis, Personal communication, 2020.

Frieß, U., Monks, P., Remedios, J., Rozanov, A., Sinreich, R., Wagner, T., and Platt, U.: MAX-DOAS O4 measurements: A new technique to derive information on atmospheric aerosols: 2. Modeling studies, Journal of Geophysical Research: Atmospheres, 111, 2006.

Frieß, U., Klein Baltink, H., Beirle, S., Clémer, K., Hendrick, F., Henzing, B., Irie, H., de Leeuw, G., Li, A., Moerman, M. M., van Roozendael, M., Shaiganfar, R., Wagner, T., Wang, Y., Xie, P., Yilmaz, S., and Zieger, P.: Intercomparison of aerosol extinction profiles retrieved from MAX-DOAS measurements, Atmospheric Measurement Techniques, 9, 3205–3222, https://doi.org/10.5194/amt-9-3205-2016, URL https://www.atmos-meas-tech.net/9/3205/2016/, 2016.

Frieß, U., Beirle, S., Alvarado Bonilla, L., Bösch, T., Friedrich, M. M., Hendrick, F., Piters, A., Richter, A., van Roozendael, M., Rozanov, V. V., Spinei, E., Tirpitz, J.-L., Vlemmix, T., Wagner, T., and Wang, Y.: Intercomparison of MAX-DOAS vertical profile retrieval algorithms: studies using synthetic data, Atmospheric Measurement Techniques, 12, 2155–2181, https://doi.org/10.5194/amt-12-2155-2019, URL https://www.atmos-meas-tech.net/12/2155/2019/, 2019.

Garcia, R. D. M. and Siewert, C. E.: The FN method for radiative transfer models that include polarization effects, Journal of Quantitative Spectroscopy and Radiative Transfer, 41, 117–145, https://doi.org/https://doi.org/10.1016/0022-4073(89)90133-7, URL https://www.sciencedirect.com/science/article/pii/0022407389901337, 1989.

Gibbs, D. P., Betty, C. L., Bredow, J. W., and Fung, A. K.: Polarized and cross-polarized angular reflectance characteristics of saline ice and snow, Remote Sensing Reviews, 7, 179–195, 1993.

Gliß, J., Stebel, K., Kylling, A., Dinger, A. S., Sihler, H., and Sudbø, A.: Pyplis–A Python Software Toolbox for the Analysis of SO2 Camera Images for Emission Rate Retrievals from Point Sources, Geosciences, 7, https://doi.org/10.3390/geosciences7040134, URL https://www.mdpi.com/2076-3263/7/4/134, 2017.

Gölz, D.: Verfahren zur elektronischen Kompensation der Polarisationsmodendispersion in optischen Übertragungssystemen, Ph.D. thesis, Technische Universität, Darmstadt, URL http://tuprints.ulb.tu-darmstadt.de/3129/, 2012.

Grainger, J. and Ring, J.: Anomalous Fraunhofer line profiles, Nature, 193, 762–762, 1962.

Grainger, R. G.: Some useful formulae for aerosol size distributions and optical properties, Lect. Notes (University of Oxford), 2012.

Grattan, L. S. and Meggitt, B. T.: Optical Fiber Sensor Technology: Fundamentals, Springer Science & Business Media, New York, 2000.

Green, D. W. E.: Magnitude corrections for atmospheric extinction, International Comet Quarterly, 14, 55, 1992.

Greenblatt, G. D., Orlando, J. J., Burkholder, J. B., and Ravishankara, A. R.: Absorption measurements of oxygen between 330 and 1140 nm, Journal of Geophysical Research: Atmospheres, 95, 18 577–18 582, https://doi.org/https://doi.org/10.1029/JD095iD11p18577, URL https://agupubs.onlinelibrary.wiley.com/doi/abs/10.1029/JD095iD11p18577, 1990.

Grob, H., Emde, C., and Mayer, B.: Retrieval of aerosol properties from ground-based polarimetric sky-radiance measurements under cloudy conditions, Journal of Quantitative Spectroscopy and Radiative Transfer, 228, 57 – 72, https://doi.org/https://doi.org/10.1016/j.jqsrt.2019.02.025, URL http://www.sciencedirect.com/science/article/pii/S0022407318308781, 2019.

Hammad, A. and Chapman, S.: VII. The primary and secondary scattering of sunlight in a plane-stratified atmosphere of uniform composition, The London, Edinburgh, and Dublin Philosophical Magazine and Journal of Science, 28, 99–110, 1939.

Hansen, J. E.: Circular Polarization of Sunlight Reflected by Clouds, Journal of the Atmospheric Sciences, 28, 1515–1516, https://doi.org/10.1175/1520-0469(1971)028<1515:CPOSRB>2.0.CO;2, 1971.

Hansen, J. E. and Travis, L. D.: Light scattering in planetary atmospheres, Space science reviews, 16, 527–610, 1974.

Hasekamp, O. P. and Landgraf, J.: Retrieval of aerosol properties over land surfaces: capabilities of multiple-viewing-angle intensity and polarization measurements, Appl. Opt., 46, 3332–3344, https://doi.org/10.1364/AO.46.003332, URL http://ao.osa.org/abstract.cfm?URI=ao-46-16-3332, 2007.

Hasekamp, O. P., Landgraf, J., and van Oss, R.: The need of polarization modeling for ozone profile retrieval from backscattered sunlight, Journal of Geophysical Research: Atmospheres, 107, ACL 13–1–ACL 13–16, https://doi.org/https://doi.org/10.1029/2002JD002387, URL https://agupubs.onlinelibrary.wiley.com/doi/abs/10.1029/2002JD002387, 2002.

Heckel, A., Richter, A., Tarsu, T., Wittrock, F., Hak, C., Pundt, I., Junkermann, W., and Burrows, J. P.: MAX-DOAS measurements of formaldehyde in the Po-Valley, Atmospheric Chemistry and Physics, 5, 909–918, https://doi.org/10.5194/acp-5-909-2005, URL https://www.atmos-chem-phys.net/5/909/2005/, 2005.

Henyey, L. G. and Greenstein, J. L.: Diffuse radiation in the galaxy, The Astrophysical Journal, 93, 70–83, 1941.

Herman, B. M., Browning, S. R., and Curran, R. J.: The effect of atmospheric aerosols on scattered sunlight, Journal of the Atmospheric Sciences, 28, 419–428, 1971.

Herman, J., Cede, A., Spinei, E., Mount, G., Tzortziou, M., and Abuhassan, N.: NO_2 column amounts from ground-based Pandora and MFDOAS spectrometers using the direct-Sun DOAS technique: Intercomparisons and application to OMI validation, Journal of Geophysical Research: Atmospheres, 114, 2009.

Hönninger, G. and Platt, U.: Observations of BrO and its vertical distribution during surface ozone depletion at Alert, Atmospheric Environment, 36, 2481 – 2489, https://doi.org/https://doi.org/10.1016/S1352-2310(02)00104-8, URL http://www.sciencedirect.com/science/article/pii/S1352231002001048, air/Snow/Ice Interactions in the Arctic: Results from ALERT 2000 and SUMMIT 2000, 2002.

Holben, B. N., Eck, T. F., Slutsker, I., Tanre, D., Buis, J., Setzer, A., Vermote, E., Reagan, J., Kaufman, Y., Nakajima, T., et al.: AERONET—A federated instrument network and data archive for aerosol characterization, Remote sensing of environment, 66, 1–16, 1998.

Holben, B. N., Eck, T. F., Slutsker, I., Smirnov, A., Sinyuk, A., Schafer, J., Giles, D., and Dubovik, O.: Aeronet's Version 2.0 quality assurance criteria, in: Remote Sensing of the Atmosphere and Clouds, edited by Tsay, S.-C., Nakajima, T., Singh, R. P., and Sridharan, R., vol. 6408, pp. 134 – 147, International Society for Optics and Photonics, SPIE, https://doi.org/10.1117/12.706524, URL https://doi.org/10.1117/12.706524, 2006.

Hönninger, G., von Friedeburg, C., and Platt, U.: Multi axis differential optical absorption spectroscopy (MAX-DOAS), Atmospheric Chemistry and Physics, 4, 231–254, https://doi.org/10.5194/acp-4-231-2004, URL https://www.atmos-chem-phys.net/4/231/2004/, 2004.

Horbanski, M.: Emissions and Distribution of Reactive Iodine from Seaweed in Coastal Regions - Investigations using new mobile and in-situ DOAS techniques, Dissertation, University of Heidelberg, https://doi.org/10.11588/heidok.00020106, URL http://www.ub.uni-heidelberg.de/archiv/20106, 2015.

Horváth, G. and Varjú, D.: Principal Neutral Points of Atmospheric Polarization, pp. 23–31, Springer Berlin Heidelberg, Berlin, Heidelberg, https://doi.org/10.1007/978-3-662-09387-0_4, URL https://doi.org/10.1007/978-3-662-09387-0_4, 2004.

Hulst, H. C. and van de Hulst, H. C.: Light scattering by small particles, Courier Corporation, 1981.

IPCC: Climate Change 2014: Synthesis Report. Contribution of Working Groups I, II and III to the Fifth Assessment Report of the Intergovernmental Panel on Climate Change, techreport AR5, IPCC, Geneva, Switzerlan, Geneva, Switzerland, URL https://www.ipcc.ch/report/ar5/syr/, 2014.

Irie, H., Kanaya, Y., Akimoto, H., Iwabuchi, H., Shimizu, A., and Aoki, K.: First retrieval of tropospheric aerosol profiles using MAX-DOAS and comparison with lidar and sky radiometer measurements, Atmospheric Chemistry and Physics, 8, 341–350, https://doi.org/10.5194/acp-8-341-2008, URL https://www.atmos-chem-phys.net/8/341/2008/, 2008.

Johnston, P.: Making uv/vis cross sections, reference fraunhofer and synthetic spectra, unpublished manuscript, 1996.

Kattawar, G. W. and Plass, G. N.: Radiance and polarization of multiple scattered light from haze and clouds, Applied optics, 7, 1519–1527, 1968.

Kemp, J. C., Swedlund, J. B., MURPHY, R. E., and WOLSTENCROFT, R. D.: Physical sciences: circularly polarized visible light from Jupiter, Nature, 231, 169–170, 1971.

Kiesewetter, D. V.: Polarisation characteristics of light from multi-mode optical fibres, Quantum Electronics, 40, 519–524, https://doi.org/10.1070/qe2010v040n06abeh013514, URL https://doi.org/10.1070/qe2010v040n06abeh013514, 2010.

Koehler, U.: Image of the MOHP observatory, Personal communication, 2021.

Kraus, S.: DOASIS: a framework design for DOAS, Ph.D. thesis, University of Mannheim, URL http://d-nb.info/981351662, 2006.

Kreher, K., Van Roozendael, M., Hendrick, F., Apituley, A., Dimitropoulou, E., Frieß, U., Richter, A., Wagner, T., Abuhassan, N., Ang, L., Anguas, M., Bais, A., Benavent, N., Bösch, T., Bognar, K., Borovski, A., Bruchkouski, I., Cede, A., Chan, K. L., Donner, S., Drosoglou, T., Fayt, C., Finkenzeller, H., Garcia-Nieto, D., Gielen, C., Gómez-Martín, L., Hao, N., Herman, J. R., Hermans, C., Hoque, S., Irie, H., Jin, J., Johnston, P., Khayyam Butt, J., Khokhar, F., Koenig, T. K., Kuhn, J., Kumar, V., Lampel, J., Liu, C., Ma, J., Merlaud, A., Mishra, A. K., Müller, M., Navarro-Comas, M., Ostendorf, M., Pazmino, A., Peters, E., Pinardi, G., Pinharanda, M., Piters, A., Platt, U., Postylyakov, O., Prados-Roman, C., Puentedura, O., Querel, R., Saiz-Lopez, A., Schönhardt, A., Schreier, S. F., Seyler, A., Sinha, V., Spinei, E., Strong, K., Tack, F., Tian, X., Tiefengraber, M., Tirpitz, J.-L., van Gent, J., Volkamer, R., Vrekoussis, M., Wang, S., Wang, Z., Wenig, M., Wittrock, F., Xie, P. H., Xu, J., Yela, M., Zhang, C., and Zhao, X.: Intercomparison of NO_2, O_4, O_3 and HCHO slant column measurements by MAX-DOAS and zenith-sky UV-Visible spectrometers during the CINDI-2 campaign, Atmospheric Measurement Techniques Discussions, 2019, 1–58, https://doi.org/10.5194/amt-2019-157, URL https://www.atmos-meas-tech-discuss.net/amt-2019-157/, 2019.

Lacis, A. A., Chowdhary, J., Mishchenko, M. I., and Cairns, B.: Modeling errors in diffuse-sky radiation: Vector vs scalar treatment, Geophysical Research Letters, 25, 135–138, https://doi.org/https://doi.org/10.1029/97GL03613, URL https://agupubs.onlinelibrary.wiley.com/doi/abs/10.1029/97GL03613, 1998.

Lampel, J., Frieß, U., and Platt, U.: The impact of vibrational Raman scattering of air on DOAS measurements of atmospheric trace gases, Atmospheric Measurement Techniques Discussions, 8, 3423–3469, 2015.

Lampel, J., Wang, Y., Hilboll, A., Beirle, S., Sihler, H., Puķīte, J., Platt, U., and Wagner, T.: The tilt effect in DOAS observations, Atmospheric Measurement Techniques, 10, 4819, 2017.

Landgraf, J., Hasekamp, O., van Deelen, R., and Aben, I.: Rotational Raman scattering of polarized light in the Earth atmosphere: a vector radiative transfer model using the radiative transfer perturbation theory approach, Journal of

Quantitative Spectroscopy and Radiative Transfer, 87, 399 – 433, https://doi.org/https://doi.org/10.1016/j.jqsrt.2004.03.013, URL http://www.sciencedirect.com/science/article/pii/S0022407304000664, 2004.

Leighton, P. A.: Photochemistry of Air Pollution, Acad, Press, New York, 1961.

Lenoble, J., Remer, L., and Tanre, D.: Aerosol remote sensing, Springer Science & Business Media, 2013.

Levelt, P. F., van den Oord, G. H. J., Dobber, M. R., Malkki, A., Huib Visser, Johan de Vries, Stammes, P., Lundell, J. O. V., and Saari, H.: The ozone monitoring instrument, IEEE Transactions on Geoscience and Remote Sensing, 44, 1093–1101, https://doi.org/10.1109/TGRS.2006.872333, 2006.

Levenberg, K.: A method for the solution of certain non-linear problems in least squares, Quarterly of applied mathematics, 2, 164–168, 1944.

Li, Z., Goloub, P., Dubovik, O., Blarel, L., Zhang, W., Podvin, T., Sinyuk, A., Sorokin, M., Chen, H., Holben, B., Tanré, D., Canini, M., and Buis, J.-P.: Improvements for ground-based remote sensing of atmospheric aerosol properties by additional polarimetric measurements, Journal of Quantitative Spectroscopy and Radiative Transfer, 110, 1954 – 1961, https://doi.org/https://doi.org/10.1016/j.jqsrt.2009.04.009, URL http://www.sciencedirect.com/science/article/pii/S002240730900154X, 2009.

Marcuse, D.: Coupled-Mode Theory for Anisotropic Optical Waveguides, Bell System Technical Journal, 54, 985–995, https://doi.org/https://doi.org/10.1002/j.1538-7305.1975.tb02878.x, URL https://onlinelibrary.wiley.com/doi/abs/10.1002/j.1538-7305.1975.tb02878.x, 1975.

Marquardt, D. W.: An algorithm for least-squares estimation of nonlinear parameters, Journal of the society for Industrial and Applied Mathematics, 11, 431–441, 1963.

Maystre, D.: Theory of Wood's Anomalies, pp. 39–83, Springer Berlin Heidelberg, Berlin, Heidelberg, https://doi.org/10.1007/978-3-642-28079-5_2, URL https://doi.org/10.1007/978-3-642-28079-5_2, 2012.

McGuire Jr., J. P. and Chipman, R. A.: Analysis of spatial pseudodepolarizers in imaging systems, Optical Engineering, 29, 1478 – 1484, https://doi.org/10.1117/12.55756, URL https://doi.org/10.1117/12.55756, 1990.

Meller, R. and Moortgat, G. K.: Temperature dependence of the absorption cross sections of formaldehyde between 223 and 323 K in the wavelength range 225–375 nm, Journal of Geophysical Research: Atmospheres, 105, 7089–7101, https://doi.org/10.1029/1999JD901074, URL https://agupubs.onlinelibrary.wiley.com/doi/abs/10.1029/1999JD901074, 2000.

Mie, G.: Beiträge zur Optik trüber Medien, speziell kolloidaler Metallösungen, Annalen der physik, 330, 377–445, 1908.

Mishchenko, M., Lacis, A., and Travis, L.: Errors induced by the neglect of polarization in radiance calculations for rayleigh-scattering atmospheres, Journal of Quantitative Spectroscopy and Radiative Transfer, 51, 491 – 510, https://doi.org/https://doi.org/10.1016/0022-4073(94)90149-X, URL http://www.sciencedirect.com/science/article/pii/002240739490149X, 1994.

Mishchenko, M. I. and Travis, L. D.: Satellite retrieval of aerosol properties over the ocean using polarization as well as intensity of reflected sunlight, Journal of Geophysical Research: Atmospheres, 102, 16 989–17 013, https://doi.org/10.1029/96JD02425, URL https://agupubs.onlinelibrary.wiley.com/doi/abs/10.1029/96JD02425, 1997.

Mitschke, F.: Fiber Optics, Springer, 2016.

Nag, S., Gatebe, C. K., and Hilker, T.: Simulation of Multiangular Remote Sensing Products Using Small Satellite Formations, IEEE Journal of Selected Topics in Applied Earth Observations and Remote Sensing, 10, 638–653, https://doi.org/10.1109/JSTARS.2016.2570683, 2017.

Nasse, J.-M.: Halogens in the coastal boundary layer of Antarctica, Dissertation, University of Heidelberg, https://doi.org/10.11588/heidok.00026489, URL http://www.ub.uni-heidelberg.de/archiv/26489, 2019.

Nasse, J.-M., Eger, P. G., Pöhler, D., Schmitt, S., Frieß, U., and Platt, U.: Recent improvements of Long-Path DOAS measurements: impact on accuracy and stability of short-term and automated long-term observations, Atmospheric Measurement Techniques Discussions, 2019, 1–36, https://doi.org/10.5194/amt-2019-69, URL https://www.atmos-meas-tech-discuss.net/amt-2019-69/, 2019.

Öhmke, V.: Depolarisation of light in optical multimode fibres, Bachelor thesis, University of Heidelberg, 2019.

Ortega, I., Berg, L. K., Ferrare, R. A., Hair, J. W., Hostetler, C. A., and Volkamer, R.: Elevated aerosol layers modify the O2–O2 absorption measured by ground-based MAX-DOAS, Journal of Quantitative Spectroscopy and Radiative Transfer, 176, 34 – 49, https://doi.org/https://doi.org/10.1016/j.jqsrt.2016.02.021, URL http://www.sciencedirect.com/science/article/pii/S0022407315301746, 2016.

Palmer, C.: Diffraction grating handbook, Newport Corporation New York, 5th edition edn., 2002.

Perner, D. and Platt, U.: Absorption of light in the atmosphere by collision pairs of oxygen (O2)2, Geophysical Research Letters, 7, 1053–1056, https://doi.org/https:

//doi.org/10.1029/GL007i012p01053, URL https://agupubs.onlinelibrary.wiley.com/doi/abs/10.1029/GL007i012p01053, 1980.

Petty, G. W.: A first course in atmospheric radiation, Sundog Pub, 2006.

Platt, U. and Stutz, J.: Differential Optical Absorption Spectroscopy, vol. 1, Springer Berlin Heidelberg, https://doi.org/10.1007/978-3-540-75776-4, 2008.

Platt, U., Marquard, L., Wagner, T., and Perner, D.: Corrections for zenith scattered light DOAS, Geophysical Research Letters, 24, 1759–1762, https://doi.org/https://doi.org/10.1029/97GL01693, URL https://agupubs.onlinelibrary.wiley.com/doi/abs/10.1029/97GL01693, 1997.

Preusker, R., Boettger, U., and Fischer, J.: Spectral and bidirectional measurements of the Stokes vector in the O2A band and their interpretation, in: Atmospheric Sensing and Modeling II, edited by Santer, R. P., vol. 2582, pp. 13 – 20, International Society for Optics and Photonics, SPIE, https://doi.org/10.1117/12.228544, URL https://doi.org/10.1117/12.228544, 1995.

Raman, C. V.: A new radiation, Indian Association for the Cultivation of Science, 1928.

Remer, L. A. and Kaufman, Y. J.: Dynamic aerosol model: Urban/industrial aerosol, Journal of Geophysical Research: Atmospheres, 103, 13 859–13 871, 1998.

Riesing, K. M., Yoon, H., and Cahoy, K. L.: Rapid telescope pointing calibration: a quaternion-based solution using low-cost hardware, Journal of Astronomical Telescopes, Instruments, and Systems, 4, 1 – 10, https://doi.org/10.1117/1.JATIS.4.3.034002, URL https://doi.org/10.1117/1.JATIS.4.3.034002, 2018.

Rodgers, C. D.: Inverse methods for atmospheric sounding : theory and practice, World Scientific Publishing, 2000.

Roedel, W. and Wagner, T.: Strahlung und Energie in dem System Atmosphäre/Erdoberfläche, in: Physik unserer Umwelt: Die Atmosphäre, pp. 1–65, Springer, 2017.

Rogers, A. J.: Polarization in optical fibers, Artech House, 2008.

Rothman, L. S., Gordon, I. E., Barber, R. J., Dothe, H., Gamache, R. R., Goldman, A., Perevalov, V. I., Tashkun, S. A., and Tennyson, J.: HITEMP, the high-temperature molecular spectroscopic database, Journal of Quantitative Spectroscopy and Radiative Transfer, 111, 2139–2150, https://doi.org/https://doi.org/10.1016/j.jqsrt.2010.05.001, URL https://www.sciencedirect.com/science/article/pii/S002240731000169X, xVIth Symposium on High Resolution Molecular Spectroscopy (HighRus-2009), 2010.

Scheffler, H. and Elsässer, H.: Physik der Sterne und der Sonne, Mannheim: Bibliographisches Institut-Wissenschaftsverlag, 1974.

Seidler, T.: PMAX-DOAS - Eine neue Methode zur Bestimmung von Aerosolprofilen mittels polarisationsabhängiger MAX-DOAS Messungen, Master's thesis, University of Heidelberg, 2008.

Seinfeld, J. H. and Pandis, S. N.: Atmospheric chemistry and physics: from air pollution to climate change, John Wiley & Sons, 2016.

Serdyuchenko, A., Gorshelev, V., Weber, M., Chehade, W., and Burrows, J. P.: High spectral resolution ozone absorption cross-sections - Part 2: Temperature dependence, Atmospheric Measurement Techniques, 7, 625–636, https://doi.org/10.5194/amt-7-625-2014, URL https://amt.copernicus.org/articles/7/625/2014/, 2014.

Shettle, E. P. and Fenn, R. W.: Models for the aerosols of the lower atmosphere and the effects of humidity variations on their optical properties, vol. 79 of *214*, Optical Physics Division, Air Force Geophysics Laboratory, 1979.

Siewert, C. E.: A concise and accurate solution to Chandrasekhar's basic problem in radiative transfer, Journal of Quantitative Spectroscopy and Radiative Transfer, 64, 109–130, https://doi.org/https://doi.org/10.1016/S0022-4073(98)00144-7, URL https://www.sciencedirect.com/science/article/pii/S0022407398001447, 2000.

Sihler, H., Lübcke, P., Lang, R., Beirle, S., de Graaf, M., Hörmann, C., Lampel, J., Penning de Vries, M., Remmers, J., Trollope, E., Wang, Y., and Wagner, T.: In-operation field-of-view retrieval (IFR) for satellite and ground-based DOAS-type instruments applying coincident high-resolution imager data, Atmospheric Measurement Techniques, 10, 881–903, https://doi.org/10.5194/amt-10-881-2017, URL https://www.atmos-meas-tech.net/10/881/2017/, 2017.

Sinyuk, A., Holben, B. N., Eck, T. F., Giles, D. M., Slutsker, I., Korkin, S., Schafer, J. S., Smirnov, A., Sorokin, M., and Lyapustin, A.: The AERONET Version 3 aerosol retrieval algorithm, associated uncertainties and comparisons to Version 2, Atmospheric Measurement Techniques, 13, 3375–3411, https://doi.org/10.5194/amt-13-3375-2020, URL https://amt.copernicus.org/articles/13/3375/2020/, 2020.

Solomon, S., Schmeltekopf, A. L., and Sanders, R. W.: On the interpretation of zenith sky absorption measurements, Journal of Geophysical Research: Atmospheres, 92, 8311–8319, https://doi.org/https://doi.org/10.1029/JD092iD07p08311, URL https://agupubs.onlinelibrary.wiley.com/doi/abs/10.1029/JD092iD07p08311, 1987.

Spurr, R.: LIDORT and VLIDORT: Linearized pseudo-spherical scalar and vector discrete ordinate radiative transfer models for use in remote sensing retrieval problems, pp. 229–275, Springer Berlin Heidelberg, Berlin, Heidelberg, https://doi.org/10.1007/978-3-540-48546-9_7, URL https://doi.org/10.1007/978-3-540-48546-9_7, 2008.

Spurr, R.: VLIDORT Version 2.8 User's Guide, RT Solutions, Inc., 9 Channing Street, Cambridge, MA 02138, USA, 2018.

Spurr, R.: VLIDORT Version 2.8.3 Beta, Personal communication, 2021.

Spurr, R., Wang, J., Zeng, J., and Mishchenko, M.: Linearized T-matrix and Mie scattering computations, Journal of Quantitative Spectroscopy and Radiative Transfer, 113, 425–439, 2012.

Spurr, R. J.: VLIDORT: A linearized pseudo-spherical vector discrete ordinate radiative transfer code for forward model and retrieval studies in multilayer multiple scattering media, Journal of Quantitative Spectroscopy and Radiative Transfer, 102, 316 – 342, https://doi.org/https://doi.org/10.1016/j.jqsrt.2006.05.005, URL http://www.sciencedirect.com/science/article/pii/S0022407306001191, 2006.

Stull, R. B.: An introduction to boundary layer meteorology, vol. 13, Springer Science & Business Media, 2012.

Stutz, J. and Platt, U.: Numerical analysis and estimation of the statistical error of differential optical absorption spectroscopy measurements with least-squares methods, Applied Optics, 35, 6041–6053, https://doi.org/10.1364/AO.35.006041, URL http://ao.osa.org/abstract.cfm?URI=ao-35-30-6041, 1996.

Stutz, J. and Platt, U.: Improving long-path differential optical absorption spectroscopy with a quartz-fiber mode mixer, Appl. Opt., 36, 1105–1115, https://doi.org/10.1364/AO.36.001105, URL http://ao.osa.org/abstract.cfm?URI=ao-36-6-1105, 1997.

Thalman, R. and Volkamer, R.: Temperature dependent absorption cross-sections of O2–O2 collision pairs between 340 and 630 nm and at atmospherically relevant pressure, Phys. Chem. Chem. Phys., 15, 15 371–15 381, https://doi.org/10.1039/C3CP50968K, URL http://dx.doi.org/10.1039/C3CP50968K, 2013.

Tikhonov, A. N.: Solution of incorrectly formulated problems and the regularisation method, Dokl. Akad. Nauk. SSSR, 151, 501–504, 1963.

Tirpitz, J.-L., Frieß, U., Hendrick, F., Alberti, C., Allaart, M., Apituley, A., Bais, A., Beirle, S., Berkhout, S., Bognar, K., Bösch, T., Bruchkouski, I., Cede, A., Chan, K. L., den Hoed, M., Donner, S., Drosoglou, T., Fayt, C., Friedrich, M. M., Frumau, A., Gast, L., Gielen, C., Gomez-Martín, L., Hao, N., Hensen,

A., Henzing, B., Hermans, C., Jin, J., Kreher, K., Kuhn, J., Lampel, J., Li, A., Liu, C., Liu, H., Ma, J., Merlaud, A., Peters, E., Pinardi, G., Piters, A., Platt, U., Puentedura, O., Richter, A., Schmitt, S., Spinei, E., Stein Zweers, D., Strong, K., Swart, D., Tack, F., Tiefengraber, M., van der Hoff, R., van Roozendael, M., Vlemmix, T., Vonk, J., Wagner, T., Wang, Y., Wang, Z., Wenig, M., Wiegner, M., Wittrock, F., Xie, P., Xing, C., Xu, J., Yela, M., Zhang, C., and Zhao, X.: Intercomparison of MAX-DOAS vertical profile retrieval algorithms: studies on field data from the CINDI-2 campaign, Atmospheric Measurement Techniques Discussions, 2020, 1–49, https://doi.org/10.5194/amt-2019-456, URL https://amt.copernicus.org/preprints/amt-2019-456/, 2020.

Twomey, S.: On the numerical solution of Fredholm integral equations of the first kind by the inversion of the linear system produced by quadrature, Journal of the ACM (JACM), 10, 97–101, 1963.

Van de Hulst, H. and Grossman, K.: Multiple light scattering in planetary atmospheres, avm, p. 35, 1968.

van Zyl, J. J.: The Shuttle Radar Topography Mission (SRTM): a breakthrough in remote sensing of topography, Acta Astronautica, 48, 559–565, https://doi.org/https://doi.org/10.1016/S0094-5765(01)00020-0, URL https://www.sciencedirect.com/science/article/pii/S0094576501000200, 2001.

Vandaele, A., Hermans, C., Simon, P., Carleer, M., Colin, R., Fally, S., Mérienne, M., Jenouvrier, A., and Coquart, B.: Measurements of the NO2 absorption cross-section from 42 000 cm^{-1} to 10 000 cm^{-1} (238–1000 nm) at 220 K and 294 K, Journal of Quantitative Spectroscopy and Radiative Transfer, 59, 171 – 184, https://doi.org/https://doi.org/10.1016/S0022-4073(97)00168-4, URL http://www.sciencedirect.com/science/article/pii/S0022407397001684, atmospheric Spectroscopy Applications 96, 1998.

Veefkind, J., Aben, I., McMullan, K., Förster, H., de Vries, J., Otter, G., Claas, J., Eskes, H., de Haan, J., Kleipool, Q., van Weele, M., Hasekamp, O., Hoogeveen, R., Landgraf, J., Snel, R., Tol, P., Ingmann, P., Voors, R., Kruizinga, B., Vink, R., Visser, H., and Levelt, P.: TROPOMI on the ESA Sentinel-5 Precursor: A GMES mission for global observations of the atmospheric composition for climate, air quality and ozone layer applications, Remote Sensing of Environment, 120, 70–83, https://doi.org/https://doi.org/10.1016/j.rse.2011.09.027, URL https://www.sciencedirect.com/science/article/pii/S0034425712000661, the Sentinel Missions - New Opportunities for Science, 2012.

Vlemmix, T., Piters, A. J. M., Berkhout, A. J. C., Gast, L. F. L., Wang, P., and Levelt, P. F.: Ability of the MAX-DOAS method to derive profile information for NO_2: can the boundary layer and free troposphere be separated?, Atmospheric Measurement Techniques, 4, 2659–2684, https://doi.org/

10.5194/amt-4-2659-2011, URL https://www.atmos-meas-tech.net/4/2659/2011/, 2011.

Vlemmix, T., Hendrick, F., Pinardi, G., De Smedt, I., Fayt, C., Hermans, C., Piters, A., Wang, P., Levelt, P., and Van Roozendael, M.: MAX-DOAS observations of aerosols, formaldehyde and nitrogen dioxide in the Beijing area: comparison of two profile retrieval approaches, Atmospheric Measurement Techniques, 8, 941–963, https://doi.org/10.5194/amt-8-941-2015, URL https://www.atmos-meas-tech.net/8/941/2015/, 2015.

Wagner, T.: Satellite observations of atmospheric halogen oxides, Ph.D. thesis, University of Heidelberg, 1999.

Wagner, T. and Beirle, S.: Estimation of the horizontal sensitivity range from MAX-DOAS O_4 observations, Tech. rep., QA4ECV, URL http://www.qa4ecv.eu/sites/default/files, 2016.

Wagner, T., Chance, K., Frieß, U., Gil, M., Goutail, F., Hönninger, G., Johnston, P., Karlsen-Tørnkvist, K., Kostadinov, I., Leser, H., et al.: Correction of the Ring effect and I0-effect for DOAS observations of scattered sunlight, in: 1st DOAS Workshop, Heidelberg, Germany, pp. 13–14, 2001.

Wagner, T., Dix, B. v., Friedeburg, C. v., Frieß, U., Sanghavi, S., Sinreich, R., and Platt, U.: MAX-DOAS O_4 measurements: A new technique to derive information on atmospheric aerosols—Principles and information content, Journal of Geophysical Research: Atmospheres, 109, 2004.

Wagner, T., Deutschmann, T., and Platt, U.: Determination of aerosol properties from MAX-DOAS observations of the Ring effect, Atmospheric Measurement Techniques, 2, 495–512, https://doi.org/10.5194/amt-2-495-2009, URL https://www.atmos-meas-tech.net/2/495/2009/, 2009.

Wagner, T., Beirle, S., Brauers, T., Deutschmann, T., Frieß, U., Hak, C., Halla, J. D., Heue, K. P., Junkermann, W., Li, X., Platt, U., and Pundt-Gruber, I.: Inversion of tropospheric profiles of aerosol extinction and HCHO and NO_2 mixing ratios from MAX-DOAS observations in Milano during the summer of 2003 and comparison with independent data sets, Atmospheric Measurement Techniques, 4, 2685–2715, https://doi.org/10.5194/amt-4-2685-2011, URL https://www.atmos-meas-tech.net/4/2685/2011/, 2011.

Wagner, T., Beirle, S., Benavent, N., Bösch, T., Chan, K. L., Donner, S., Dörner, S., Fayt, C., Frieß, U., García-Nieto, D., Gielen, C., González-Bartolome, D., Gomez, L., Hendrick, F., Henzing, B., Jin, J. L., Lampel, J., Ma, J., Mies, K., Navarro, M., Peters, E., Pinardi, G., Puentedura, O., Puķīte, J., Remmers, J., Richter, A., Saiz-Lopez, A., Shaiganfar, R., Sihler, H., Van Roozendael, M., Wang, Y., and Yela, M.: Is a scaling factor required to obtain clo-

sure between measured and modelled atmospheric O_4 absorptions? An assessment of uncertainties of measurements and radiative transfer simulations for 2 selected days during the MAD-CAT campaign, Atmospheric Measurement Techniques, 12, 2745–2817, https://doi.org/10.5194/amt-12-2745-2019, URL https://www.atmos-meas-tech.net/12/2745/2019/, 2019.

Wang, X., Reagan, J. A., Dobler, J., and Rubio, M.: Cabannes versus Rayleigh scattering and terrestrial backscatter ratio revisited in LITE in support of CALIPSO, in: IGARSS 2003. 2003 IEEE International Geoscience and Remote Sensing Symposium. Proceedings (IEEE Cat. No. 03CH37477), vol. 7, pp. 4407–4409, IEEE, 2003.

Wang, Y., Li, A., Xie, P.-H., Chen, H., Xu, J., Wu, F.-C., Liu, J.-G., and Liu, W.-Q.: Retrieving vertical profile of aerosol extinction by multi-axis differential optical absorption spectroscopy, Acta Physica Sinica, 62, 180705, https://doi.org/10.7498/aps.62.180705, URL http://wulixb.iphy.ac.cn/EN/abstract/article_55526.shtml, 2013.

Whitby, K. T.: The physical characteristics of sulfur aerosols, in: Sulfur in the Atmosphere, pp. 135–159, Elsevier, 1978.

Wiegner, M. and Geiß, A.: Aerosol profiling with the Jenoptik ceilometer CHM15kx, Atmospheric Measurement Techniques, 5, 1953–1964, https://doi.org/10.5194/amt-5-1953-2012, URL https://www.atmos-meas-tech.net/5/1953/2012/, 2012.

Wiscombe, W. J.: The Delta–M Method: Rapid Yet Accurate Radiative Flux Calculations for Strongly Asymmetric Phase Functions, Journal of the Atmospheric Sciences, 34, 1408–1422, https://doi.org/10.1175/1520-0469(1977)034<1408:TDMRYA>2.0.CO;2, URL https://doi.org/10.1175/1520-0469(1977)034<1408:TDMRYA>2.0.CO;2, 1977.

Wood, R.: XLII. On a remarkable case of uneven distribution of light in a diffraction grating spectrum, The London, Edinburgh, and Dublin Philosophical Magazine and Journal of Science, 4, 396–402, https://doi.org/10.1080/14786440209462857, URL https://doi.org/10.1080/14786440209462857, 1902.

Xu, X. and Wang, J.: Retrieval of aerosol microphysical properties from AERONET photopolarimetric measurements: 1. Information content analysis, Journal of Geophysical Research: Atmospheres, 120, 7059–7078, https://doi.org/https://doi.org/10.1002/2015JD023108, URL https://agupubs.onlinelibrary.wiley.com/doi/abs/10.1002/2015JD023108, 2015.

Yilmaz, S.: Retrieval of atmospheric aerosol and trace gas vertical profiles using multi-axis differential optical absorption spectroscopy, Ph.D. thesis, Heidelberg, Univ., Diss., 2012, URL http://archiv.ub.uni-heidelberg.de/volltextserver/volltexte/2012/13128, 2012.

Young, A. T.: Rayleigh scattering, Phys. Today, 35, 42–48, 1982.

Zebner, H., Zambelli, P., Taylor, S., Nwaogaidu, S. O., Michelsen, T., and Little, J.: Pysolar python library: staring directly at the sun since 2007, Online, URL https://pysolar.readthedocs.io/, 2017.

Zhang, Z.: TMAX-DOAS on measurement of Aerosols and NO_2 in Heidelberg, Bachelor thesis, University of Heidelberg, 2014.

Zielcke, J.: Observations of reactive bromine, iodine and chlorine species in the Arctic and Antarctic with Differential Optical Absorption Spectroscopy, Ph.D. thesis, University of Heidelberg, https://doi.org/10.11588/heidok.00018932, URL http://www.ub.uni-heidelberg.de/archiv/18932, 2015.

Acknowledgements

An erster Stelle danke ich herzlich Prof. Dr. Ulrich Platt, der mir als Doktorvater diese interessante Arbeit ermöglicht und mich mit zahlreichen Anregungen und Ratschlägen unterstützt hat.

Ein ganz besonderer Dank gilt auch Dr. Udo Frieß, der das Projekt angestoßen sowie den Großteil der Betreuungsarbeit übernommen hat und mir in allen möglichen Aspekten der Arbeit mit Rat und Tat zur Seite stand.

Weiterhin danke ich Prof. Dr. Andreas Quirrenbach für die Übernahme der Zweitbegutachtung.

Ich danke allerherzlichst meinen Kollegen für die gute Atmosphäre und Zusammenarbeit, die schöne Zeit auf verschiedenen Kampagnen und Tagungen, sowie die mentale Unterstützung in den härteren Phasen der Arbeit. Besonders hervorheben möchte ich in diesem Zusammenhang die ehrenwerten "Maischda" Jonas Kuhn und Stefan Schmitt. Außerdem meine Büro-Mitbewohner Marleen Lausecker und Moritz Schöne sowie Christopher Fuchs, Simon Warnach, James Barry, Florian Dinger, Katja Bigge, Holger Sihler, Lara Penth, Martin Horbanski, Ralph Kleinschek und Nicole Bobrowski.

Weiterhin danke ich:

- Prof. Dr. André Butz und Prof. Dr. Klaus Pfeilsticker für die zahlreichen Gespräche und Ratschläge bezüglich Strahlungstransport- und Inversionsfragen.

- Dem Team von der Airyx GmbH, insbesondere Denis Pöhler und Johannes Lampel, unter anderem für die Unterstützung bei der Entwicklung des PMAX-DOAS Instruments.

- Dem Werkstatt-Team des IUPs, ganz besonders Heribert Sommer, der den feinmechanischen Part des Instrumentenbaus übernommen und mit vielen Ideen zu dessen Verbesserung beigetragen hat.

- Dem deutschen Wetterdienst und AERONET, ganz besonders Robert Holla aber auch Ina Mattis, Wolfgang Steinbrecht und Dagmar Kubistin, für die Möglichkeit am Hohenpeissenberg zu messen, für die Pflege des PMAX-DOAS und die Bereitstellung der Vergleichsdaten.

- Dem Sekretariat und er Verwaltung im IUP.

- Dem MetPVNet-Team und der Hochschule Kempten (insbesondere Frank Fischer) für die Möglichkeit erster Einsätze des PMAX-DOAS im Feld.

- Martina Friedrich vom Royal Belgian Institute for Space Aeronomy für Tipps und Ratschläge zu VLIDORT

- Der Heidelberg Graduate School for Physics, Prof. Dr. André Butz, Prof. Dr. Ulrich Platt und Udo Frieß für die finanzielle Unterstützung in den letzten Monaten der Arbeit.

- Robert Spurr von RT solutions Inc. für die Unterstützung rund um VLIDORT.

Ein dickes Dankeschön geht auch an meine Familie und verschiedene Freunde, die mir vor allen Dingen die zermürbende Schreibphase im Covid-Winter-Lockdown erträglicher gemacht haben und dabei viel Gejammer ertragen mussten.

Der meiste Dank geht an meine Frau Mareike, die immer für mich da war. Sie hat mich in den richtigen Momenten aufgebaut oder auch auf den Boden zurückholt und mich in den letzten Jahren in allerlei Gemütszuständen mit viel Geduld und Humor ertragen. Außerdem hat sie mir ziemlich oft erfolgreich den Rücken frei gehalten. Eigentlich wollte ich hier immer reinschreiben: "I thank my wife, for organising my life", aber das passt schlecht in eine Danksagung auf Deutsch.